Advanced Nanomaterials and Their Applications toward Sustainable Electrochemical Energy Conversion

by

Yifan Liu

A dissertation submitted to Johns Hopkins University in conformity with the requirements for the degree of Doctor of Philosophy.

Baltimore, Maryland

April, 2019

Abstract

Electrochemical reactions represent a promising energy conversion route yet its large scale application had always been hindered by large overpotential and low selectivity. This dissertation aims to investigate the catalysis of alcohol electro-oxidation and hydrogen evolution reaction, which are crucial reactions in direct alcohol fuel cells (DAFCs) and water electrolyzers.

Nanomaterials with various compositions, morphologies and structures were investigated for electro-oxidation of ethanol and ethylene glycol. All catalysts exhibited enhance activity while sphere-like Pt_3Sn/C exhibited enhanced CO_2 activity. By conducting a carefully designed KOH treatment to remove surface SnO_x species, the dual role of Sn species in Pt_3Sn/C was revealed.

The electro-oxidation of glycerol on Pt was also investigated combining sum frequency generation (SFG) and electrochemistry. Adsorbed CO, which is the crucial reaction intermediate for CO_2, was observed by SFG on Pt surface at as low as 0.05 V and persisted until 0.7 V. However, CO_2 selectivity was characterized to be below 4 % by GC-MS. Such difference could be ascribed to facility of C-C bond cleavage in glycerol while hindered *CO oxidative removal on Pt surface at low potential region. Isotopically labelled glycerol experiment also revealed that middle carbon contributes a minor portion of produced CO_2, indicating cleavage of C-C bond in remaining C2 moiety is more challenging than that in initial C3 molecule.

In addition to alcohol electro-oxidation, we also investigated hydrogen evolution reaction (HER). Novel two dimensional MoS_2 nanosheets were successfully synthesized and their HER activity were demonstrated to be merely moderately lower than Pt/C.

The results of this dissertation provide mechanism insight about catalysis of alcohol electro-oxidation and hydrogen evolution reaction, and suggest promising directions for the development of DAFCs and water electrolyzers.

Advisor: Prof. Chao Wang

Reader: Prof. Jonah Erlebacher

Prof. David H. Gracias

Acknowledgement

I would like to acknowledge my PhD advisor Prof. Chao Wang for his generous support during the past six years. He spent a lot of time discussing with me that helped me build up insightful understanding of electrocatalysis. It is under his supervision that I became capable of handling scientific research independently.

Many thanks are also due to my defense committee members: Prof. David Gracias, Prof. Mike Tsapatsis, Prof. Mike Bevan, Prof. Jonah Erlebacher, Prof. Howard Fairbrother and Prof. Tim Mueller. Their time spent on my dissertation is much appreciated.

Five undergraduate students and two master students worked with me since 2016. I would like to express my acknowledgement to each and every one of them: Mr. Jonathan Chen, Mr. Jeff Peng, Mr. Miaojin Wei, Mr. Alex Alessi, Mr. Pingfan Hu, Mr. Zhongyu Liu and Ms. Wenqi Zhou. They did excellent experimental work and working with them is also a great learning process for me that taught me how to take responsibility and manage.

Lastly and most importantly, I would like to express my gratitude to my parents Mr. Liu and Mrs. Wang, as well as my significant other Ms. Tang. Thank you for your love and tolerance that supported me all the way along this journey.

Dedication

To my family

Contents

List of Figures

Chapter 1. Introduction

1.1 Background and motivation

The human society has been relying on fossil fuel combustion as the primary energy source for more than one century and it had brought technology, industrialization and prosperities. Yet now, human beings are facing the unsustainability of fossil fuel. The global consumption of fossil fuels has been increasing rapidly and the reserves are expected to exhaust as early as 2088, as presented in Figure 1.1.1. Therefore searching for sustainable energy sources and developing relevant techniques is an urgent task for researchers.

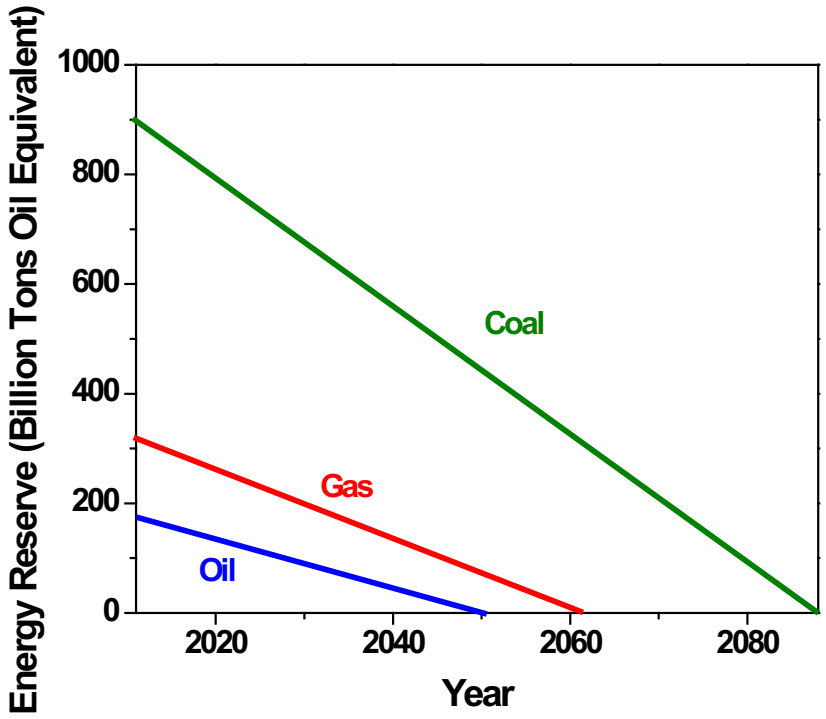

Figure 1.1.1. Estimated global fossil fuel reserve from 2011-2088. Source: http://www.americancoalcouncil.org/page/natural_resources

Alcohol is a promising energy resource due to its sustainability, high energy density and clean products[1]. Ethanol is the most widely used alcohol since it could be produced from crops including corns, sugarcanes etc.[2] United States produces over half of global ethanol, as is shown in Figure 1.1.2. Ethanol has been added into gasoline for cars in Brazil for decades[3] and is now being increasingly used for same purpose in the United States.

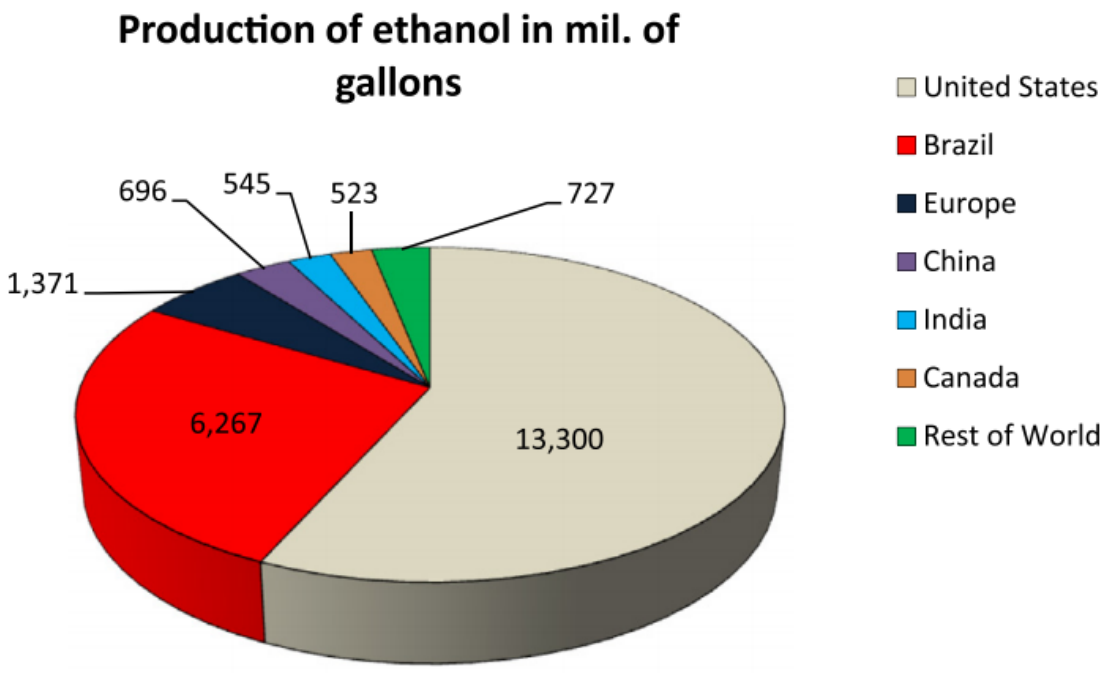

Figure 1.1.2. Production of ethanol in 2013 by countries. Adapted with permission from Ref 4.[4] Copyright 2016 Elsevier.

Instead of combustion, ethanol could also be utilized by feeding into Direct Ethanol Fuel Cells (DEFCs). DEFCs are challenged by the missing of ideal electrocatalysts for Ethanol Oxidation Reaction (EOR). Platinum has been mostly used and investigated but its activity and selectivity is still pending improvement. This work

aimed to design and synthesize nanomaterials for the electrocatalysis of EOR for enhanced activity as well as selectivity toward complete oxidation. Alcohols other than ethanol, e.g. ethylene glycol and glycerol, were also investigated to help understand the mechanism of alcohol electro-oxidation. Three electrode system was implemented for the investigation of surface property and alcohol electro-oxidation activity of catalysts. Gas Chromatography-Mass Spectrometry (GCMS) and Nuclear Magnetic Resonance (NMR) was adopted for product characterization. In addition, Sum Frequency Generation (SFG) was implemented for characterizing the species adsorbed on Pt during alcohol electro-oxidation. With the understanding of activity, selectivity and mechanism, catalysts were further improved to enhance their performance. The ultimate goal of this work is to develop catalysts that could be implemented in a real Direct Alcohol Fuel Cell (DAFC). Figure 1.1.3 describes the overview of this work.

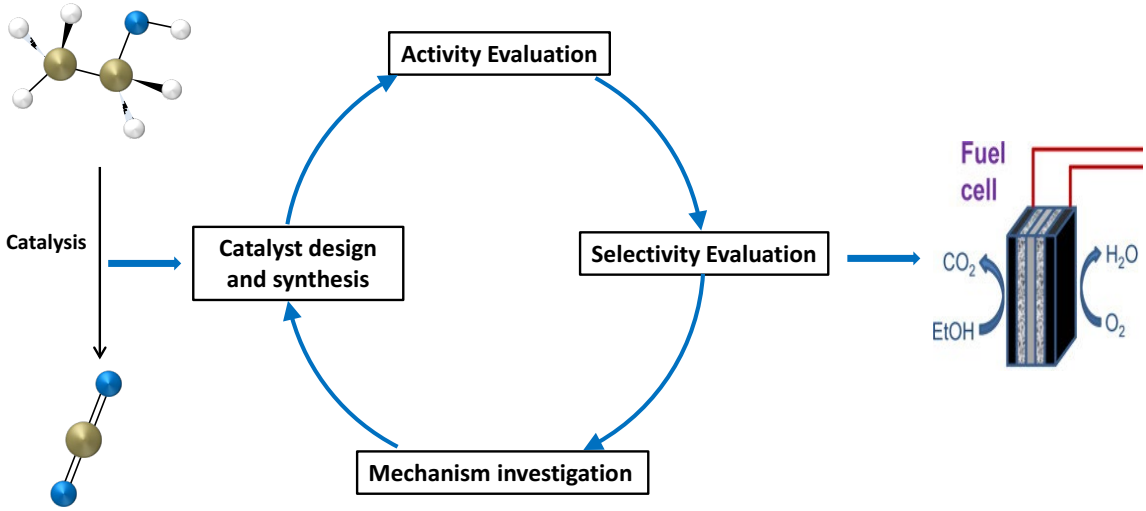

Figure 1.1.3. Overview of this work on catalysts exploration of alcohol electro-oxidation.

Hydrogen is another promising renewable energy source yet its production is challenging[5]. Water electrolysis is a feasible method and its large scale application is prohibited by high cost and scarcity of Pt catalyst for Hydrogen Evolution Reaction

(HER). This work also explores inexpensive and abundant HER catalysts as alternative for Pt.

1.2 Introduction of Nanomaterials

The study of nanomaterials has a long history and extensively boomed with the maturity of microscope techniques. Their small size (1-100 nm) endowed them with unique optical and mechanical properties that could be designed and engineered for various purposes[6]. The synthesis methods of nanomaterials could be divided into two categories: "Bottom Up" and "Top Down". Top down methods breaks down bulk materials into nanometer scale, including: mechanical exfoliation[7], chemical exfoliation[8-10], ball milling[11] etc. Top down methods usually result in a broad distribution of size and shape in product. Bottom up methods, on the other hand, make atoms self-assemble into nanomaterials and the size and shape of product could be better controlled. Typical bottom up method include Chemical Vapor Deposition (CVD)[12] and solvothermal method[13-14] while solvothermal method is most widely adopted for application because of its excellent control in product size and shape.

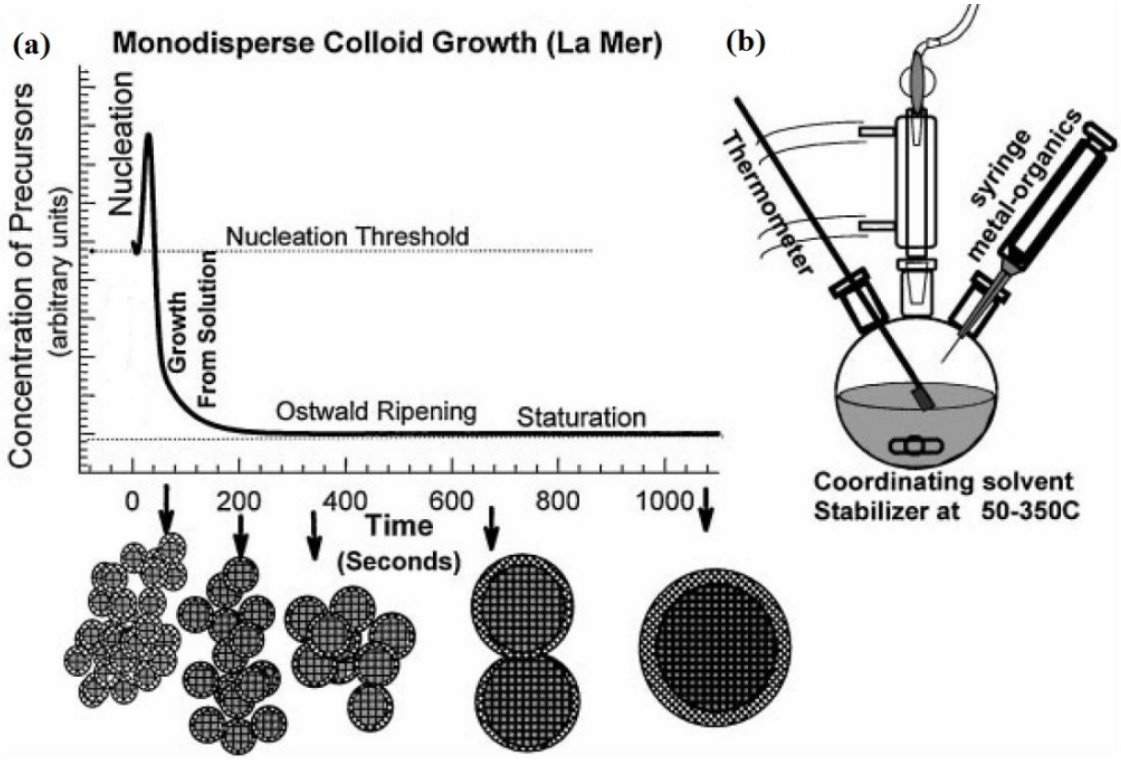

Figure 1.2.1. (a) La Mer Plot and (b) Sketch of typical solvothermal experimental setup of nanoparticle synthesis. Adapted with permission from Ref 14.[14] Copyright 2009 Royal Society of Chemistry.

In solvothermal method, atoms provided from salt precursors go through nucleation and Ostwald ripening before forming uniform size and shape nanomaterials (see figure 1.2.1a)[15]. Quick nuclei formation is triggered by sufficient concentration of precursor and appropriate temperature. The nucleation process is typically rather fast and consumes all metal precursors in a short period of time. During this process the nuclei concentration increases significantly and the nuclei sizes grow slightly. Then the nuclei and small nanoparticles go through Ostwald ripening, a process induced by the competition of volume free energy and surface energy, resulting in the sacrifice of small

nanoparticles and growth of bigger nanoparticles[16]. After that, the nanoparticles will slowly reach uniform size and shape.

The final size and shape of product is related to initial concentration of precursors, growth temperature, type and amount of organic surfactant etc. Figure 1.2.1b shows a sketch of typical experimental setup of nanomaterials solvothermal synthesis with thermometer, certain atmosphere and stirring. The solvent in this method could be organic or aqueous solution. Typically, glass flasks are adopted for organic solvothermal reactions while autoclaves with Teflon liners are implemented for hydrothermal synthesis, as is shown in Figure 1.2.2.

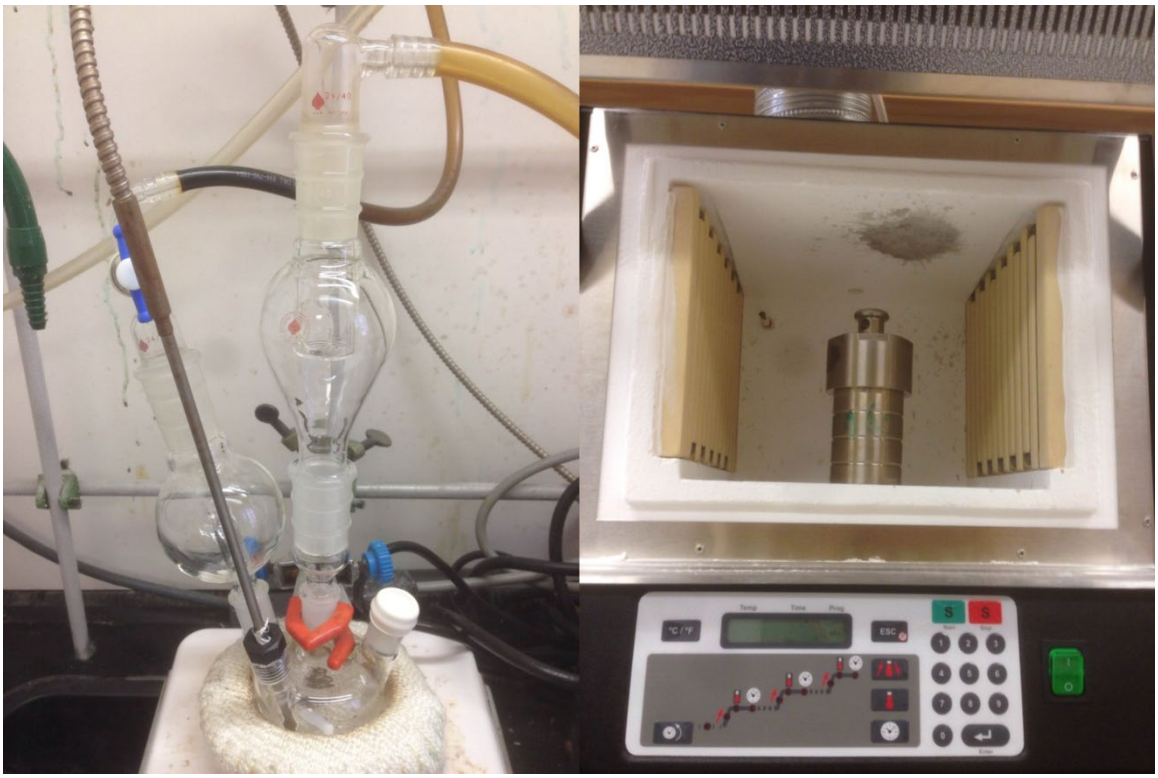

Figure 1.2.2. Photo of (a) organic solvothermal and (b) hydrothermal synthesis experimental setup

Characterization is a crucial and essential component in the field of nanomaterial research. It is important to investigate and determine the properties of synthesized

nanomaterials. Common characterization techniques include Transmission Electron Microscopy (TEM) and Scanning Electron Microscopy (SEM) for morphology observation, Energy Dispersive X-ray Spectroscopy (EDS or EDX) for composition determination, X-ray Diffraction (XRD) for crystal structure determination, X-ray Photoelectron Spectroscopy (XPS) for surface oxidation state investigation, Ultraviolet-visible spectroscopy (UV-Vis) for optical property study, Dynamic Light Scattering (DLS) for size distribution quantification, Extended X-ray Absorption Fine Structure (EXAFS) and X-ray Absorption Near Edge Structure (XANES) for bond property investigation etc.

Numerous nanomaterials had been successfully synthesized and characterized. Their compositions vary from precious metal (e.g. Pt[17-20], Au[21-22], Ag[23]), to transition metal oxides/nitrides/carbides/sulfides/phosphides (MnO_6[24], FeP[25], CoP[26-27], Co_2P[26], MoS_2[28-31], Mo_2C[32], WC[33], CdS[34], Co_9S_8[35], Co_3S_4[35-36], $Co_{1-x}S$[37], SnO_2[38], Co_3O_4[39-40], $W_{18}O_{49}$[41] etc.), and binary metal alloy nanomaterials (e.g., PtNi alloy[42-44], PtSn alloy[45-46], PtFe alloy[47]). These nanomaterials exhibit various shape and morphology, including zero-dimensional nanospheres[13], one-dimensional nanorods[48], two-dimensional nanoplates and nanosheets[49-50] etc.

The spike in nanomaterial synthesis and characterization techniques around millennium year motivated the application of nanoparticles. Their small size and unique property have endowed them potential application toward nanomedicine and drug delivery[51-52], heterogeneous catalysis[53-54] as well as electrochemical catalysis[55-56]. This dissertation aims to take advantage of unique property of nanomaterial and investigate their applications toward electrochemical catalysis.

1.3 Introduction of thermodynamics and kinetics of electrochemical reactions

Electrochemical reactions are redox reactions induced by the gain or loss of electrons near electrode. Typical electrochemical reactions could be written as:

$$O + ne^- \rightarrow R \quad (1.3.1)$$

$$R - ne^- \rightarrow O \quad (1.3.2)$$

Where O represents oxidant and R represents reductant. Like other chemical reactions, electrochemical reactions are governed by thermodynamic and kinetic laws.

For electrochemical reaction, the change of Gibbs free energy is defined as:

$$\Delta G = -nFE \quad (1.3.3)$$

where n is electron transfer number during reaction, F is faraday constant (≈ 96485 $C \cdot mol^{-1}$), E is the reaction potential.

According to general thermodynamics, change of Gibbs free energy is also governed by:

$$\Delta G = \Delta G^{\ominus} + RTlnQ \quad (1.3.4)$$

where $\Delta G^{\ominus}$ is the change of Gibbs free energy under standard state, R is gas constant (8.314 $J \cdot mol^{-1} \cdot K^{-1}$), T is temperature, Q is reaction quotient.

If the $\Delta G^{\ominus}$ is substituted with

$$\Delta G^{\ominus} = -nFE^{\ominus} \quad (1.3.5)$$

It is easy to derive:

$$E = E^{\ominus} - \frac{RT}{nF} lnQ \quad (1.3.6a)$$

For oxidation half reactions, this equation could be written as:

$$E = E_{ox}^{\ominus} - \frac{RT}{nF} ln \frac{a_{ox}}{a_{red}} \quad (1.3.6b)$$

While for reduction half reactions, the equation becomes:

$$E = E_{red}^{\ominus} - \frac{RT}{nF} ln \frac{a_{red}}{a_{ox}} \tag{1.3.6c}$$

Equation (1.3.6) is called Nernst Equation. As a basic electrochemical thermodynamics equation, it describes the relationship of reactant activity and reaction potentials.

Apart from thermodynamics, reaction kinetics is also a key factor influencing electrochemical reactions. The rate constant k_m could be described by Arrhenius equation:

$$k_m = Aexp\left(-\frac{E_A}{RT}\right) \tag{1.3.7}$$

here pre-exponential factor A and activation energy E_A are both empirical values and usually determined by experiment. The activation energy could be calculated from derivative of equation (1.3.7):

$$E_A = RT^2 \frac{dlnk_m}{dT} \tag{1.3.8}$$

To illustrate the energy change and concept of activation energy, potential energy-distance curves are adopted[57]. As is shown in Figure 1.3.1, vertical axis is enthalpy (potential energy) and horizontal axis is distance (within reaction coordinate). Activation energy equals to the difference of $H^{\ddagger}$ (highest enthalpy along reaction pathway) and H_x (reactant enthalpy). If $-T\Delta S$ term is added to ΔH, the potential energy-distance could be represented by Gibbs free energy. It has been reported that rate constants could be expressed as[58]:

$$k_m = \kappa_m \frac{kT}{h} \exp(-\frac{\Delta G_m^{\ddagger}}{RT}) \tag{1.3.9}$$

with k being Boltzmann constant, κ_m being dimensionless coefficient and h being Planck constant.

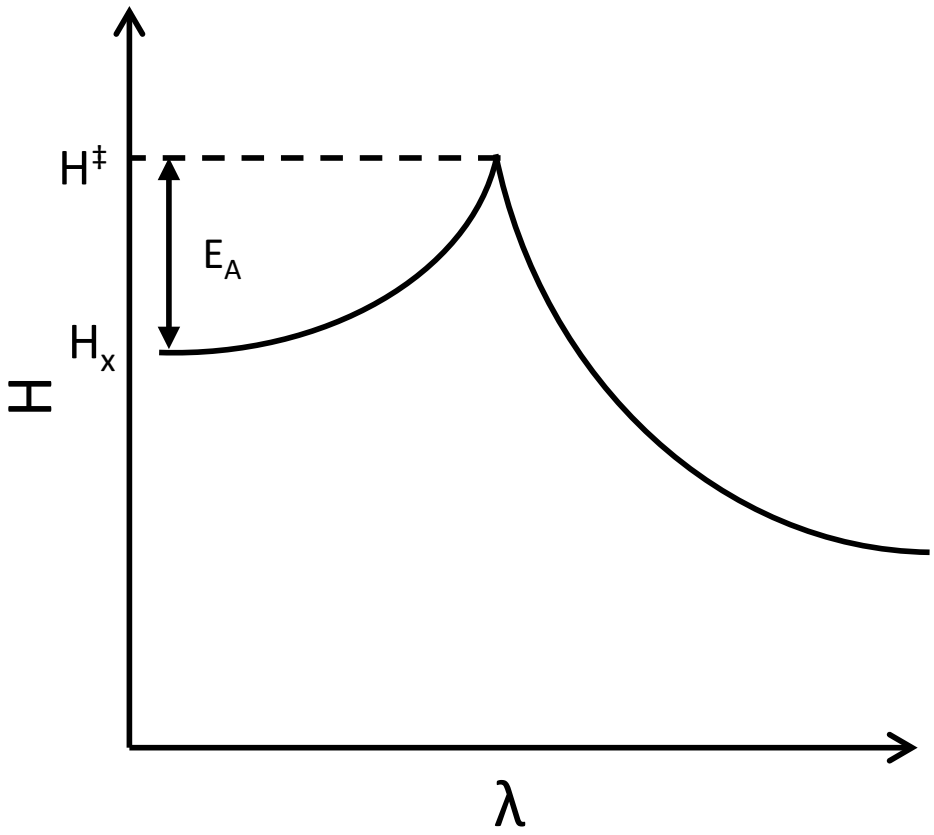

Figure 1.3.1. Example of potential energy-distance curves for a simple reaction X→Y

Equations (1.3.8) and (1.3.9) could be utilized to measure and calculate activation energy for non-electrochemical reactions by changing temperature and measuring rate constant. However, it is not feasible for electrochemical reactions. The measurement has to be conducted under same Galvani potential, which is the potential difference between electrode and electrolyte. When the temperature is varied, the Galvani potential will change simultaneously and the relationship between temperature change and Galvani potential change is unknown. To solve this obstacle the concept real activation energy E_A' was invented[57]:

$$E_A' = E_A \pm \alpha T \Delta S \tag{1.3.10}$$

α is the coefficient implementing the change of Galvani potential with temperature. In addition, considering the net charge transfer between electrode and electrolyte, the total Gibbs free energy should also be corrected:

$$-\Delta G^0 = -\Delta G_0^0 \pm nFE \tag{1.3.11}$$

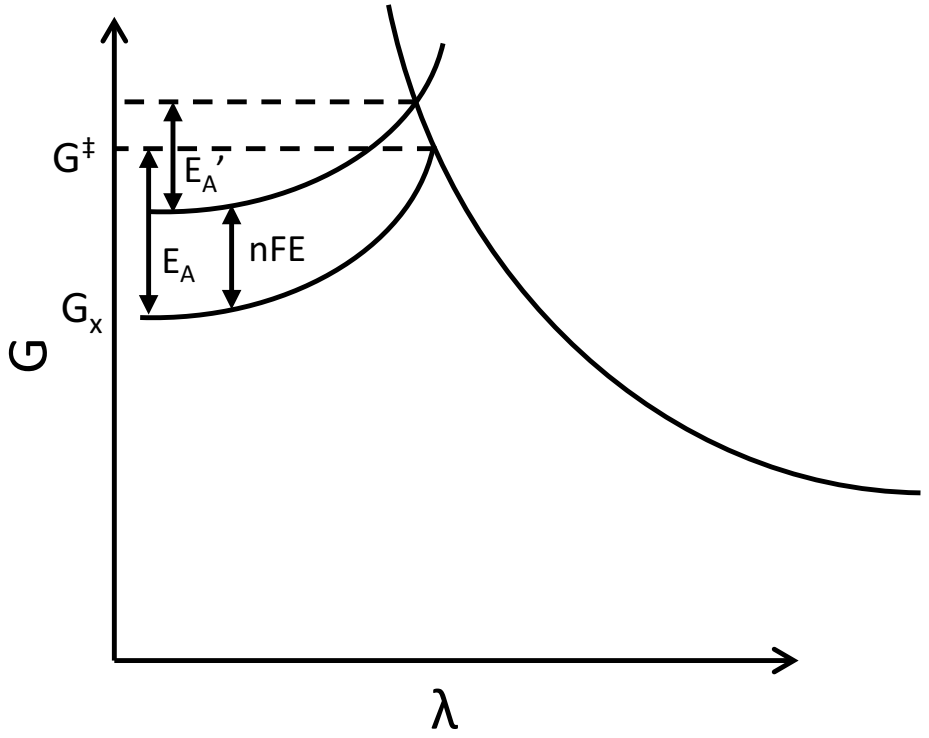

Figure 1.3.2. Change of activation energy with potential change

Correspondingly, activation energy would be corrected to below as is shown in Figure 1.3.2:

$$E_A' = E_A^0 - (\pm \alpha nFE) \tag{1.3.12}$$

Substituting (1.3.12) into the Arrhenius equation, the overall rate constant could be expressed as:

$$h_m = k_m exp\left(\pm \frac{n\alpha FE}{RT}\right) \tag{1.3.13}$$

The equation between potentials and rate constant is helpful for the description of relationship between overpotential η and nominal current. It is found by experiment that current and overpotential follow empirical equation as:

$$i = a' exp\left(\frac{\eta}{b'}\right) \tag{1.3.14}$$

or, if written in Tafel form (Tafel equation)

$$\eta = a + blogi \tag{1.3.15}$$

Theoretical derivation could prove that current and overpotential does follow this equation. Consider an electrochemical reaction between oxidant and reductant

$$O + ne^- \rightleftharpoons R \tag{1.3.16}$$

The reaction could proceed forward and backward simultaneously with both v_f and v_b

$$v_f = h_f C_O(t) = \frac{i_c}{nFA} \tag{1.3.17}$$

$$v_b = h_b C_R(t) = \frac{i_a}{nFA} \tag{1.3.18}$$

Here h_f and h_b are rate constants of forward and backward reaction, $C_O(t)$ and $C_R(t)$ are concentration of oxidant and reductant at time t at electrode surface, i_a and i_c are anodic and cathodic component of nominal current, A is the surface area of electrode. Therefore the overall current will be

$$i = i_c - i_a = nFA\left[h_f C_O(t) - h_b C_R(t)\right] \tag{1.3.19}$$

By substituting h with equation (1.3.13)

$$i = FAk_m\left[C_O(t) exp\left(-\frac{\alpha F\eta}{RT}\right) - C_R(t) exp\left(\frac{(1-\alpha)F\eta}{RT}\right)\right] \tag{1.3.20}$$

The above equation is a precise description between current and overpotential in electrochemical reactions.

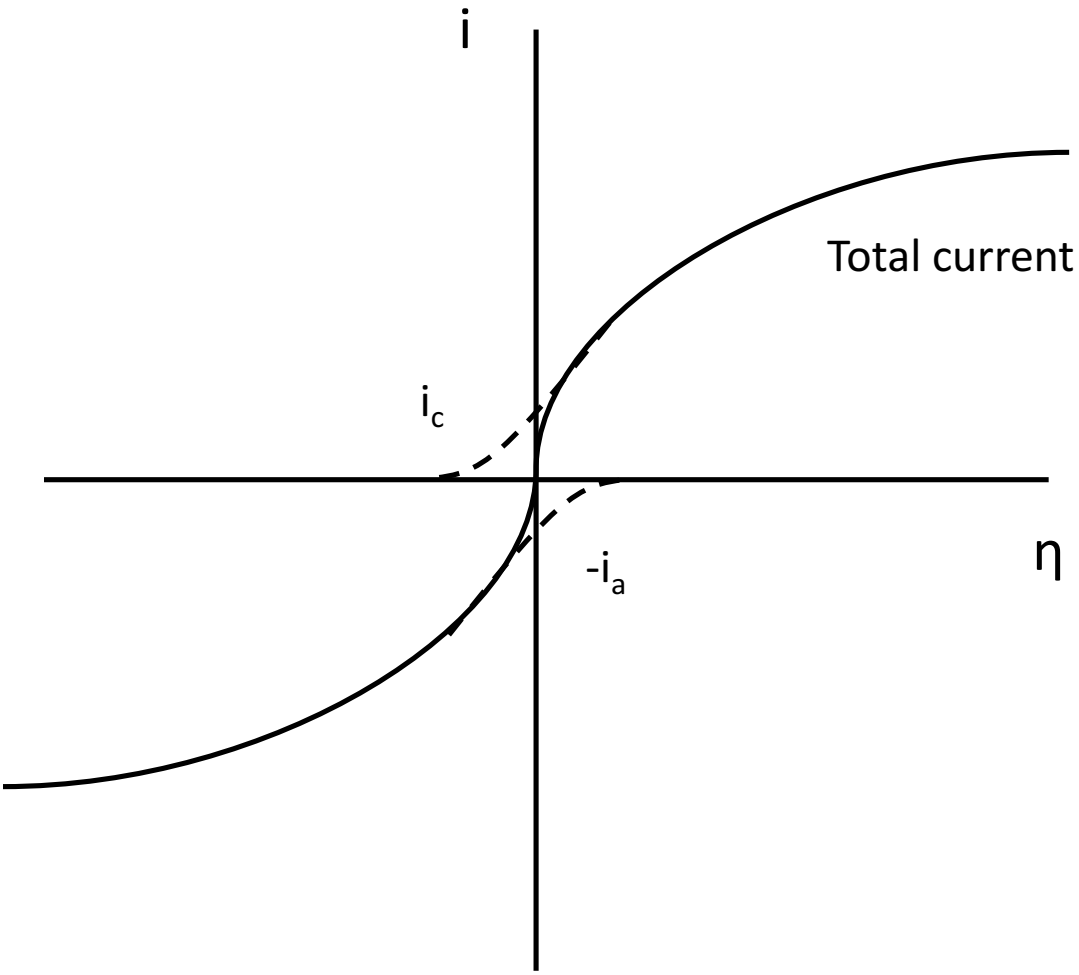

Figure 1.3.3. Sample total current-overpotential curve

Figure 1.3.3 is a typical current-overpotential curve for ordinary electrochemical reaction. Dashed line in Figure 1.3.3 show the corresponding i_c and i_a. When the electrolyte is well stirred or the reaction kinetic is sluggish compared to diffusion rate, the reaction is not limited by diffusion. Under such condition the concentration of oxidant and reductant could be treated as constant and equation (1.3.20) could be simplified to:

$$i = i_0 \left[exp\left(-\frac{\alpha F \eta}{RT}\right) - exp\left(\frac{(1-\alpha) F \eta}{RT}\right) \right] \tag{1.3.21}$$

Where i_0 is the current at zero overpotential. This equation is known as Butler-Volmer equation. In such condition the overpotential will be mostly determined by the activation energy of electrochemical reaction. Take Figure 1.3.4 as an example, since the onset potential of curve b is lower than curve a, reaction b possess activation energy lower than reaction a.

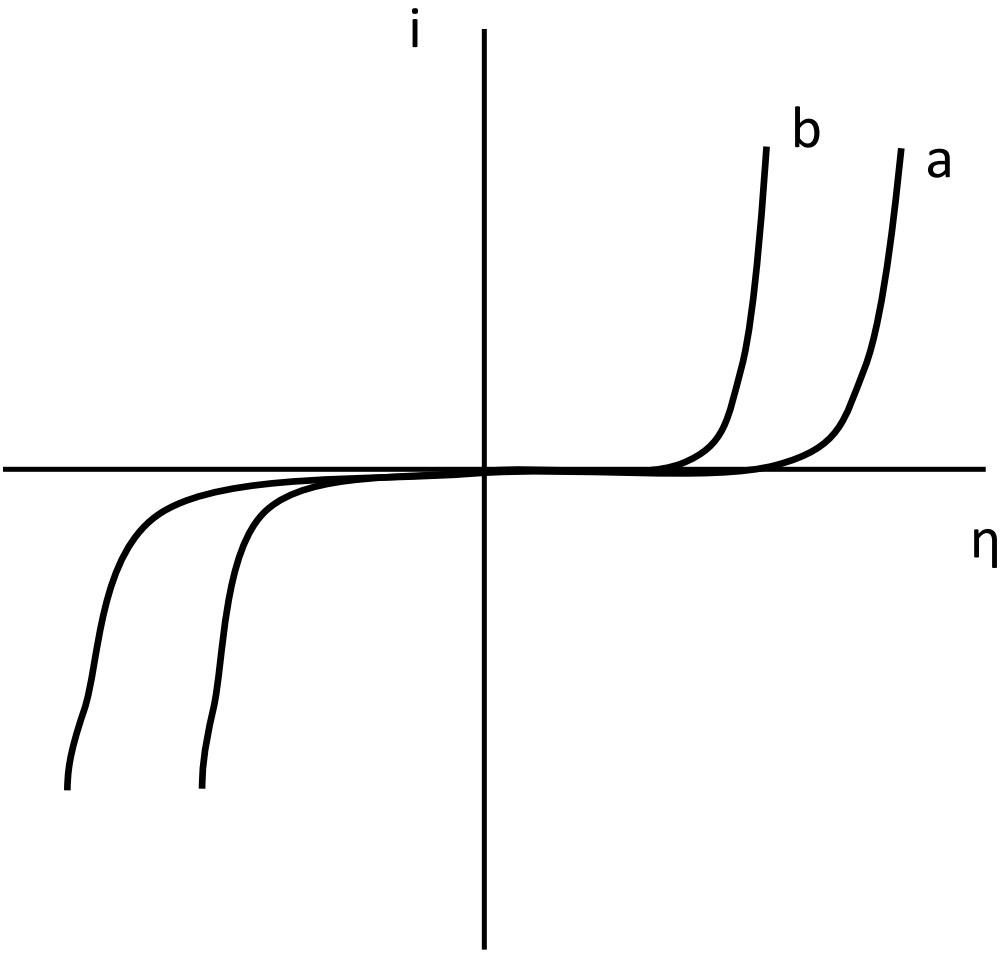

Figure 1.3.4. current-overpotential curve of electrochemical reactions with different activation energy

According to the mathematical relationship

$$e^x = 1 + x \; when \; x \to 0 \tag{1.3.22}$$

it is straightforward to derive a linear relationship between current and overpotential at small over potentials:

$$i = -i_0 \frac{\alpha F \eta}{RT} \; when \; \eta \to 0 \tag{1.3.23}$$

When overpotential is large, one of the two exponentials in equation (1.3.21) would be negligible. Take large negative overpotential as an example. With $exp\left(-\frac{\alpha F \eta}{RT}\right) \gg exp\left(\frac{(1-\alpha)F\eta}{RT}\right)$ equation (1.3.21) could be approximated as:

$$i = i_0 exp\left(-\frac{\alpha F \eta}{RT}\right) \tag{1.3.24}$$

Or taking log on both sides:

$$\eta = \frac{RT}{\alpha F} lni_0 - \frac{RT}{\alpha F} lni \tag{1.3.25}$$

Therefore the theoretical proof of Tafel equation is achieved. The a and b terms in equation (1.3.15) are $\frac{2.3RT}{\alpha F} logi_0$ and $\frac{-2.3RT}{\alpha F}$ respectively. Following Tafel equation, plot of log i vs. η (known as Tafel plot) is always implemented for kinetic analysis. As is shown in Figure 1.3.6, a Tafel plot in ideal situation would be linear at large overpotential region.

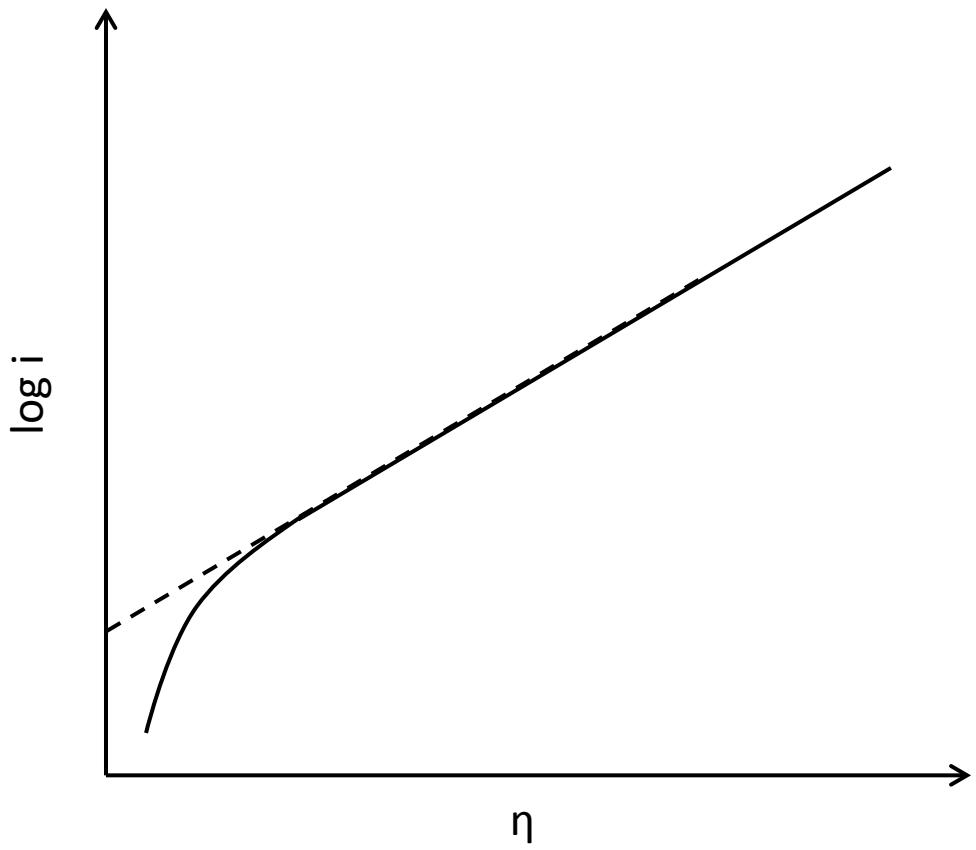

Figure 1.3.5. Tafel plot in ideal condition

Above are the fundamental thermodynamics and kinetics of electrochemical reaction. These analysis and conclusions construct the base of our evaluation for electrocatalysts.

1.4 Introduction of electrochemistry experiments and related theories

Current electrochemistry experiments are typically conducted in a three electrode setting. Figure 1.4.1 shows a sketch of typical three electrode set up. These three electrodes are working electrode, counter electrode and reference electrode respectively. Working electrode and reference electrode form a circuit for potential measurement and control. Working electrode and counter electrode constitute another parallel circuit for controlling and measuring current. The purpose of separating potential and current circuit

is to avoid potential change of single electrode with current passing through. Reference electrode is a half cell with determined and stable potential. Typically various commercial reference electrodes are implemented for different electrolyte.

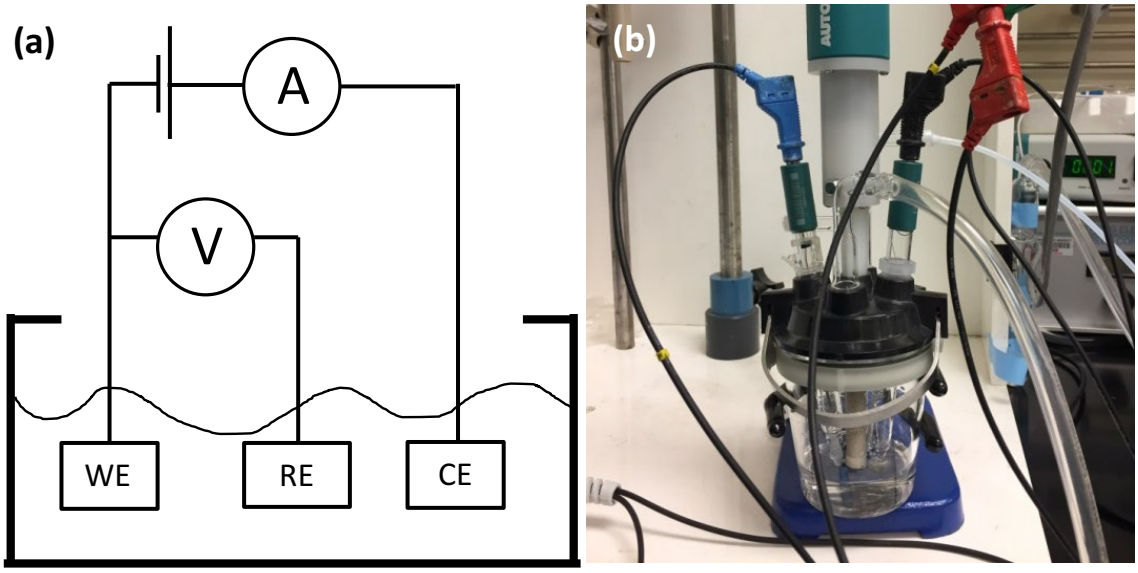

Figure 1.4.1. (a) Illustration of three electrodes experimental set up[59]. (b) Photo of a typical three electrodes electrochemical device.

For example, Ag/AgCl electrode for acidic electrolyte, Hg/Hg_2Cl_2 and $Hg/HgSO_4$ electrode for alkali electrolyte etc. Counter electrode could be any stable and conductive material. Pt wire or mesh is adopted as counter electrode very often due to its stability in various electrolyte and excellent conductivity. Working electrode could be bulk electrode or powder loaded onto commercial glassy carbon Rotating Disk Electrode (RDE). Electrolyte composition vary from aqueous solution (including $HClO_4$[60], H_2SO_4[61], $KHCO_3$[62], KOH[63] etc.), organic solution and solid electrolyte.

Cyclic voltammetry (CV) is the most common scanning technique. Potential is changed back and forth continuously while current is recorded, as is shown in Figure

1.4.2. Data is presented in E-I curve, i.e. voltammogram. Current measured during CV could be devided into three categories: (i) charge current (double layer capacitance current), (ii) adsorption/desorption current and (iii) faradaic current (redox current). They will be introduced and discussed below.

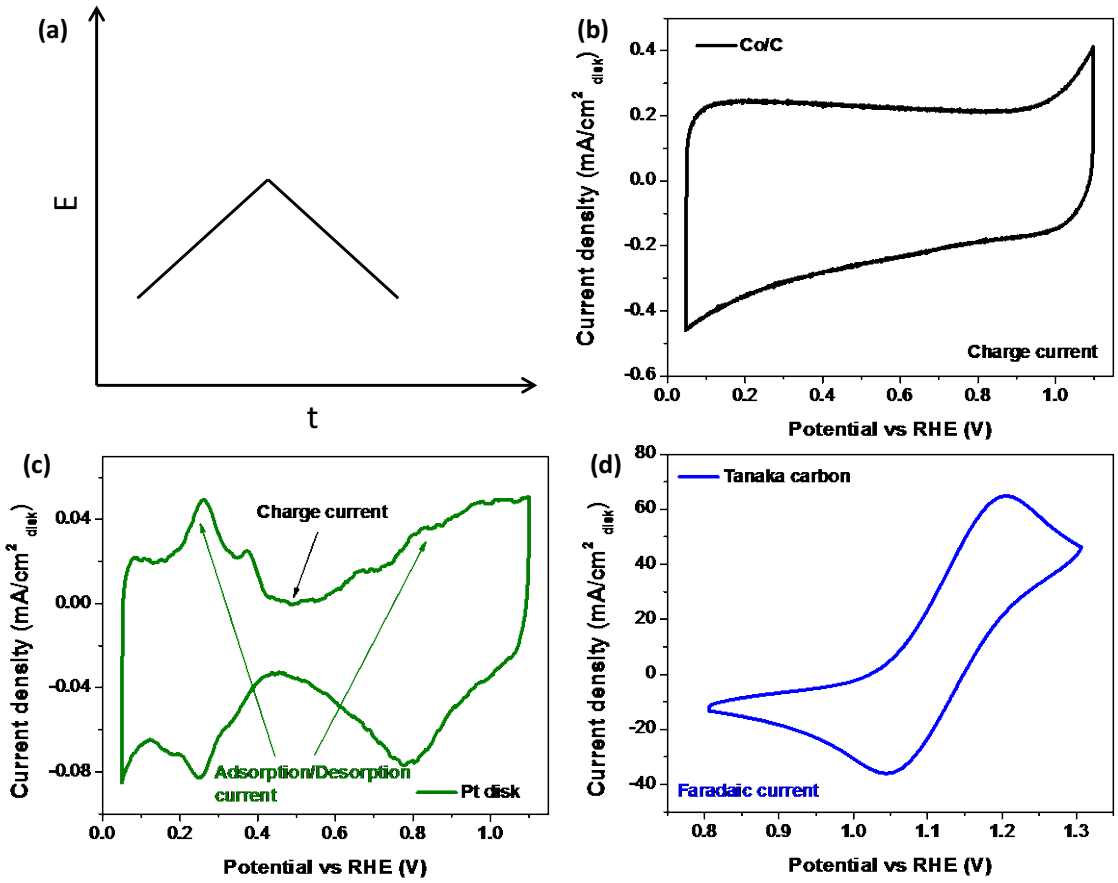

Figure 1.4.2. (a) Sample of potential change with time during cyclic voltammetry measurement. Sample voltammograms: (b) Co loaded on carbon in 0.1M KOH, (c) commercial Pt disk electrode in 0.1M KOH, (d) carbon in 2.5M H_2SO_4 + 2M $VOSO_4$.

(i) Charge current

Not all electrodes possess the capability to let charge cross electrode-electrolyte interface smoothly. Under some circumstances, charge would be hindered from passing between electrode and electrolyte and accumulate at the interface. This process is called

polarization[64]. Working electrode is polarizable under many conditions regardless of material and loaded catalyst. When net charge crossing electrode-electrolyte interface is zero, the electrode is considered ideal polarizable. Under such circumstance, there will be positive charge accumulating on electrode side and double layer dominated by negative charge in electrolyte near electrode (or the opposite way) as is shown in Figure 1.4.3.

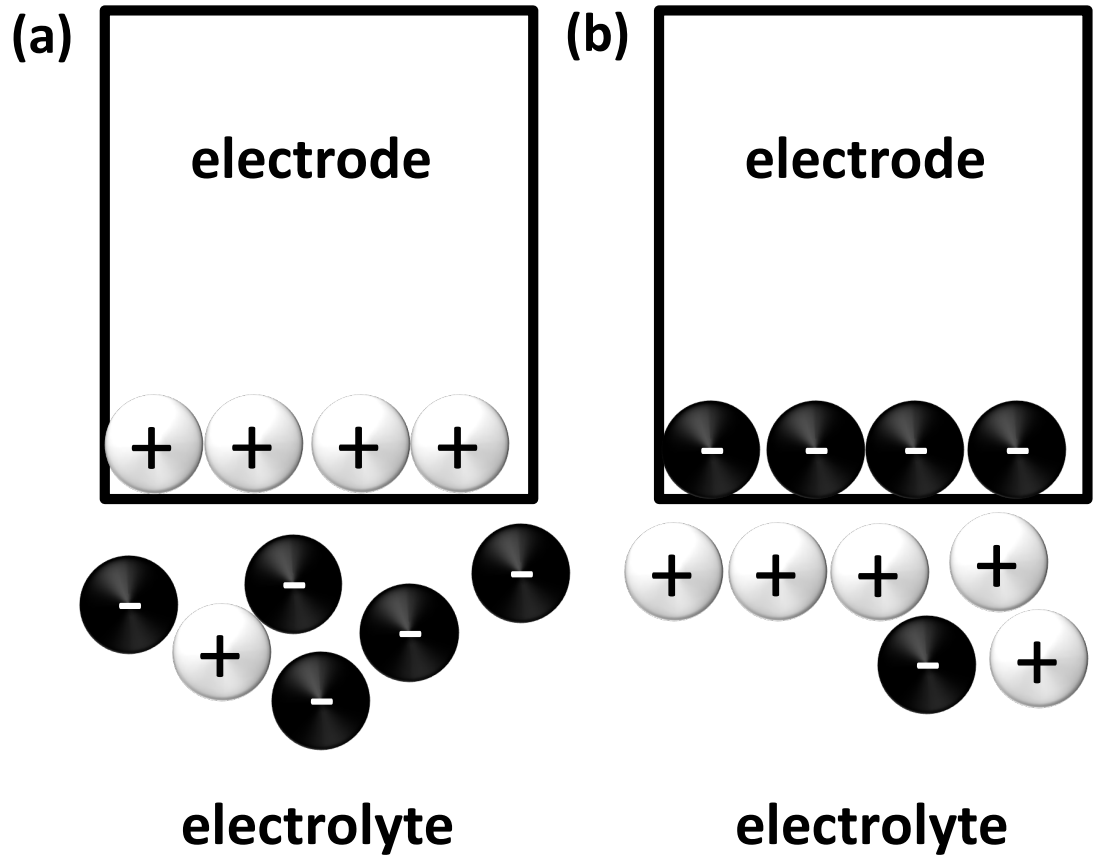

Figure 1.4.3. Illustration of double layer near electrode

This electrode-electrolyte interface with double layer behaves similarly as capacitors in electric circuits. The capacitance volume C_d (herein C_d refers to capacitance per unit area) depends on potential but in most cases an average C_d is adopted through the whole potential range of interest. The electrolyte between working electrode and counter electrode possess resistance. Therefore the electrochemistry cell could be simplified as an

analogy to a circuit with resistance R_e and capacitance C_d. When potential is applied via potentiostat (electrochemistry apparatus), the relation between potential, resistance and capacitor is:

$$E = iR_e + \frac{q}{C_d} \tag{1.4.1}$$

Here i and q are current and charge per unit area. In the positive scan or negative scan of CV, potential could simply be expressed as:

$$E = vt \tag{1.4.2}$$

where v is the scan rate. Therefore an equation between q and t could be acquired:

$$vt = iR_e + \frac{q}{C_d} \tag{1.4.3}$$

Equation (1.4.3) could be solved by changing i to dq/dt with fixed initial condition. Assuming there is no initial charge on capacitor, the solution would be:

$$i = vC_d\left[1 - exp\left(-\frac{t}{R_sC_d}\right)\right] \tag{1.4.4}$$

Equation (1.4.4) depicts the relation between charging current and time. Current increase to equilibrium during positive scan (decrease during negative scan) in initial charging process and would be constant before change of scan direction. Usually R_sC_d is small compared to t so equilibrium could be reached in a very short time (<10 s). The total equilibrium charging current would be

$$|i_c| = AC_dv \tag{1.4.5}$$

where A is electrode surface area. Equation (1.4.5) depicts a positive linear relationship between scan rate and total charge current. Namely, the higher scan rate, the higher

charge current. When scan direction changes, equation (1.4.3) is still effective and current will reach equilibrium of the other direction quickly. Figure 1.4.2b is a sample CV curve with mostly charge current and negligible faradaic current. By varying the scan rate, the total capacitance and relative electrochemically active surface area (ECSA) could be determined[65-66]. As is shown in Figure 1.4.4, by varying scan rate from 5 mV/s to 50 mV/s in ideal polarizable region (i.e. negligible faradaic current) the total double layer capacitance of reduced graphene oxide and tanaka carbon is 0.4 mF and 1.18 mF respectively. Therefore the ECSA of tanaka carbon is roughly 2.95 times of reduced graphene oxide.

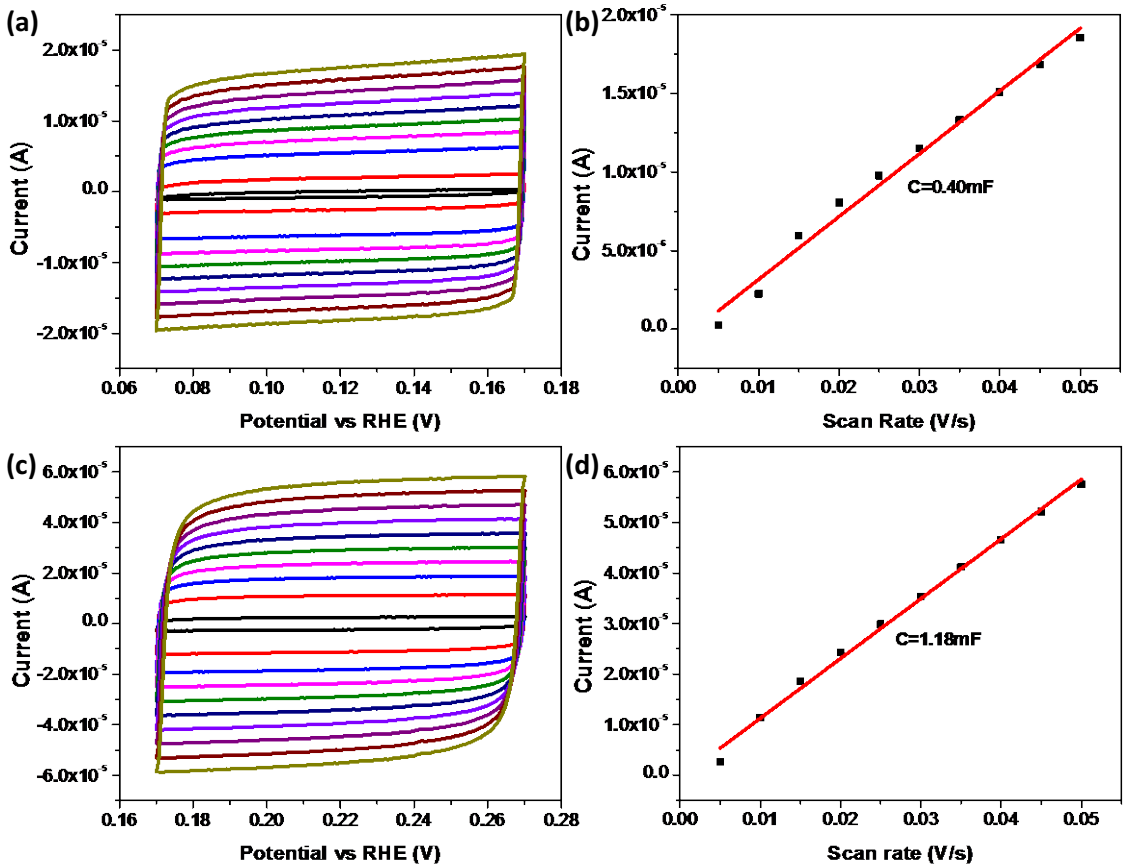

Figure 1.4.4. Charge current in ideal polarizable region of (a) reduced graphene oxide and (c) tanaka carbon with scan rates from 5 mV/s to 50 mV/s measured in 2.5M H_2SO_4 and 2M $VOSO_4$. (b) and (d) are corresponding current-scan rate plot.

(ii) Adsorption/desorption current

Figure 1.4.2c shows a voltammogram of platinum disk electrode measured in 0.1M KOH. Two pairs of anodic and cathodic peaks are exhibited in potential region of 0.05-0.4 V and 0.7-1.0 V. These two pairs of peaks could be attributed to H^+ adsorption/desorption peaks (Hupd peak) and OH^- adsorption/desorption peaks[17]. The adsorption/desorption of H^+ and OH^- results in a current change yet this is not induced by reduction or oxidation. The Hupd peak area is related to amount of absorbed H^+ and could be used to determine ECSA of Pt[67]. It should be pointed out that the current is almost flat in the potential region of 0.4 – 0.6 V in Figure 1.4.2c, this is a near ideal polarizable region and the current is dominated by capacitance charge current.

(iii) Faradaic current

Current attributed to redox reaction at electrode-electrolyte interface is defined as faradaic current. The voltammogram in Figure 1.4.2d is an example of faradaic current and peak. The anodic peak at 1.18 V corresponds to $VO^{2+} + H_2O - e^- \rightarrow VO_2^+ + 2H^+$ and the cathodic peak at 1.05 V corresponds to its reverse reaction. In electrocatalytic measurements, faradaic current is the main evaluation for catalytic activity.

Apart from CV, chrono methods are also common measurement techniques. To avoid interference from charge current and adsorption/desorption current, the potential could be held at a certain value when current is measured against time (chrono-amperometry). Or

the current could be set to constant while the potential is measured (chrono-potentiometry). Figure 1.4.5a and b illustrates the applied potential or current on three electrode system. Figure 1.4.5c and d are sample chrono-amperometry and chrono-potentiometry curves of commercial MoS_2 in 0.1M $HClO_4$ measured for Hydrogen Evolution Reaction (HER).

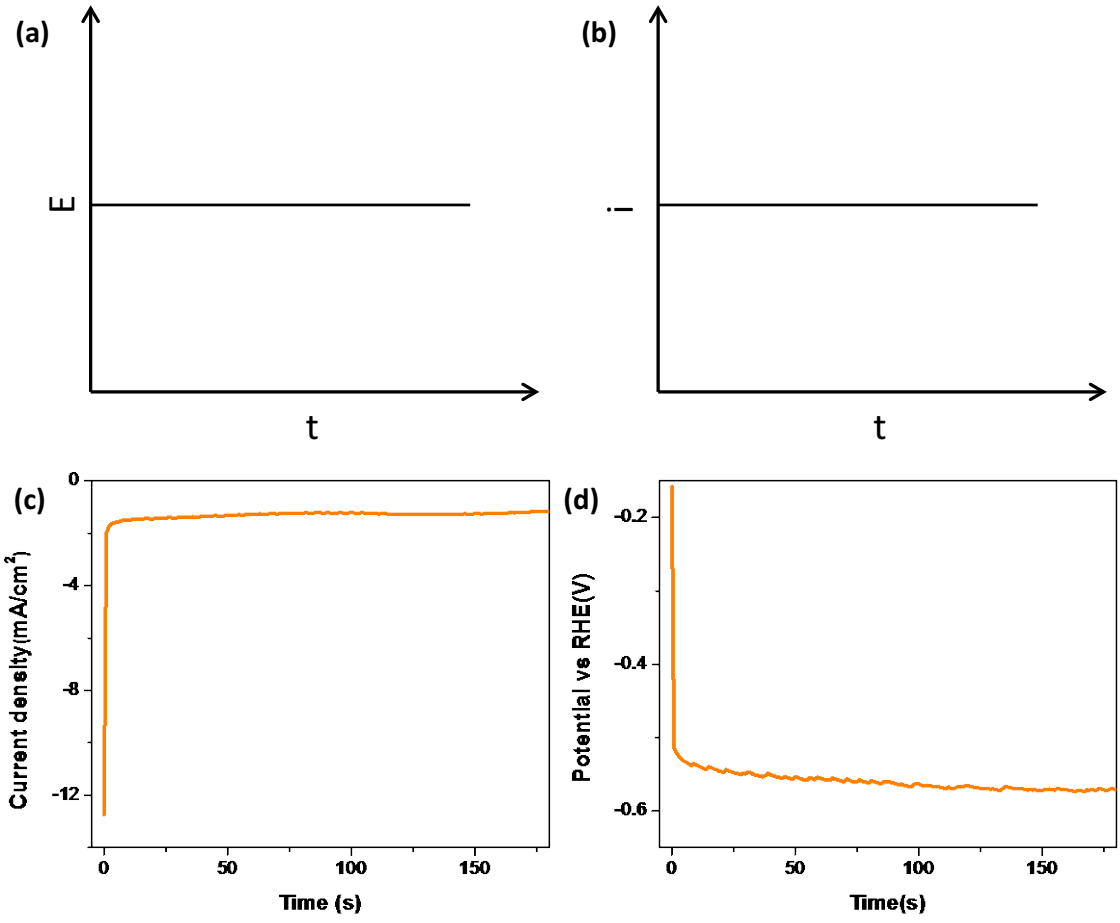

Figure 1.4.5. Illustration of (a) chrono-amperometry and (b) chrono-potentiometry method and sample curve of (c) chrono-amperometry at -0.3 V and (d) chrono-potentiometry at 10 mA/cm^2 of commercial MoS_2 measured in 0.1M $HClO_4$.

There is a sharp decrease of |i| in amperometry and increase of |E| in potentiometry in the first three seconds. This is due to the charging process of double

layer and possible adsorption/desorption process. The charging and adsorption/desorption would saturate in a very short time, in this case <2 seconds, and current or potential will be stable with slow change. The slow change (usually decrease in activity) could be attributed to decomposition or poisoning of active sites.

1.5 Direct Ethanol Fuel Cells (DEFCs) and Ethanol Oxidation Reaction (EOR)

Fuel cells are devices that directly convert chemical energy into electricity. With energy efficiency up to 50 % at room temperature[69], it is more efficient than combustion based energy conversion techniques since the heat loss is negligible[68]. As is listed in table 1.5.1[68], there are many types of fuel cells with different feed material and structure and most of them rely on hydrogen for anodic oxidation reaction. The wide application of hydrogen is limited by its low energy density and difficulty to store[2]. Ethanol is a promising feed for fuel cells due to its many advantages: it possess energy density as high as 8.01 kWh/kg[1], its oxidation product is clean and it could be produced renewably from

Table 1.5.1. Various types of fuel cell and their parameters overview. Reprinted with permission from Ref 68[68]. Copyright 2001 John Wiley & Sons Inc.

	AFC (Alkaline)	PEMFC (Polymer Electrolyte Membrane)	DMFC (Direct Methanol)	PAFC (Phosphoric Acid)	MCFC (Molten Carbonate)	SOFC (Solid Oxide)
Operating temp. (°C)	<100	60–120	60–120	160–220	600–800	800–1000 low temperature (500–600) possible
Anode reaction	$H_2 + 2OH^- \rightarrow 2H_2O + 2e^-$	$H_2 \rightarrow 2H^+ + 2e^-$	$CH_3OH + H_2O \rightarrow CO_2 + 6H^+ + 6e^-$	$H_2 \rightarrow 2H^+ + 2e^-$	$H_2 + CO_3^{2-} \rightarrow H_2O + CO_2 + 2e^-$	$H_2 + O^{2-} \rightarrow H_2O + 2e^-$
Cathode reaction	$½\,O_2 + H_2O + 2e^- \rightarrow 2OH^-$	$½\,O_2 + 2H^+ + 2e^- \rightarrow H_2O$	$3/2\,O_2 + 6H^+ + 6e^- \rightarrow 3H_2O$	$½\,O_2 + 2H^+ + 2e^- \rightarrow H_2O$	$½\,O_2 + CO_2 + 2e^- \rightarrow CO_3^{2-}$	$½\,O_2 + 2e^- \rightarrow O^{2-}$
Applications	Transportation Space Military Energy storage systems			Combined heat and power for decentralised stationary power systems	Combined heat and power for stationary decentralised systems and for transportation (trains, boats, ...)	
Realised Power	Small plants 5–150kW modular	Small plants 5–250 kW modular	Small plants 5 kW	Small – medium sized plants 50kW – 11MW	Small power plants 100-kW- 2 MW	Small power plants 100–250kW
Charge Carrier in the Electrolyte	OH^-	H^+	H^+	H^+	CO_3^{2-}	O^{2-}

corns/sugar canes[70-71] etc. Direct Ethanol Fuel Cells (DEFCs) take advantage of above and convert chemical energy in ethanol into electricity. The working principle of a DEFC is shown in Figure 1.5.1. The cathodic reaction is typically Oxygen Reduction Reaction (ORR), its reaction formula and standard reaction potential in acidic environment is:

$$O_2 + 4H^+ + 4e^- \rightarrow 2H_2O \qquad E^{\ominus} = 1.229\,V\ (vs\ SHE)$$

The anodic reaction is Ethanol Oxidation Reaction (EOR). The reaction pathway and product of EOR is more complicated compared to ORR. Ethanol could be completely oxidized into CO_2 or partially oxidized into acetaldehyde and acetic acid. The reactions in acidic condition are listed below:

$$C_2H_5OH + 3H_2O \rightarrow 2CO_2 + 12H^+ + 12e^- \qquad E^{\ominus} = 0.084V\ (vs\ SHE)$$

$$C_2H_5OH \rightarrow CH_3CHO + 2H^+ + 2e^- \qquad E^{\ominus} = -0.02V\ (vs\ SHE)$$

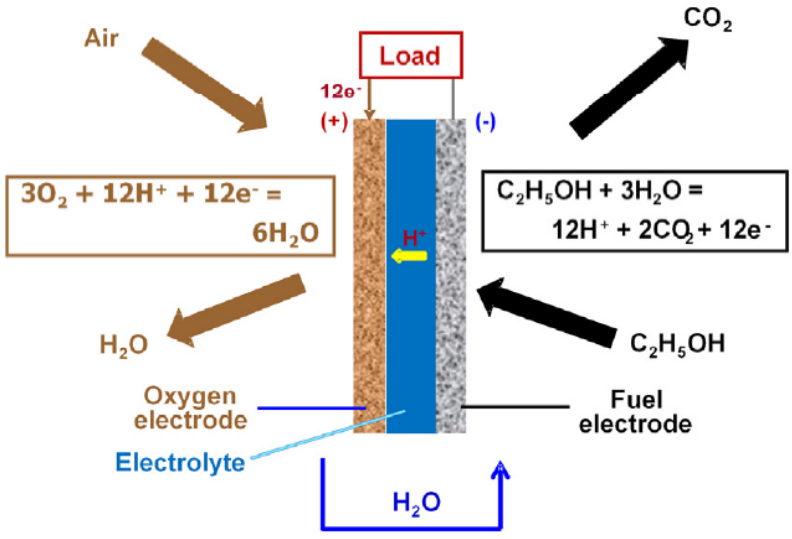

Figure 1.5.1. Schematic illustration of DEFC working principle. Reprinted with permission from Ref 2[2]. Copyright 2015 Elsevier.

$$C_2H_5OH + H_2O \rightarrow CH_3COOH + 4H^+ + 4e^- \qquad E^{\ominus} = 0.058V\ (vs\ SHE)$$

One major technical barrier of DEFC is the sluggish kinetic and low complete oxidation selectivity of EOR. Although the standard potential of EOR is merely $-0.02 \sim +0.084$V, high overpotential is usually required for observation of significant current. For example, with platinum as catalyst, the onset potential of EOR is typically 0.5-0.6 V[72-73]. The CO_2 selectivity of EOR has also been problematic. The faradaic efficiency of CO_2 when implementing platinum catalyst has been low (not exceeding 5%[72]). Therefore developing catalysts with high activity and high CO_2 selectivity has been an ongoing task for researchers.

There have been many reported studies about the mechanism of EOR on Pt surface, both theoretically and experimentally. It is commonly agreed that the first step is ethanol molecules adsorb on Pt surface and dehydrogenate to form CH_3CO* or CH_2CO* intermediates[74-78]. Kavanagh et al. proposed a feasible mechanism (Figure 1.5.2) and calculated the energy change and activation energy of various reaction pathways on pure platinum surface. Their results showed that the critical step influencing CO_2 selectivity on platinum surface is the competition between dissociation and hydrolysis of CH_3CO^*. The activation energy for CH_3CO^* to dissociate into CH_x^* and CO^* is higher for CH_3CO^* to form CH_3COOH[74]. This is the reason for low CO_2 selectivity on Pt. Wang et al. calculated the activation energy for C-C bond cleavage on various Pt sites and found that C-C bond breaking is relatively more favorable on low coordinated Pt sites[75], for example, C-C bond breaks more easily on Pt (211) compared to Pt (100).

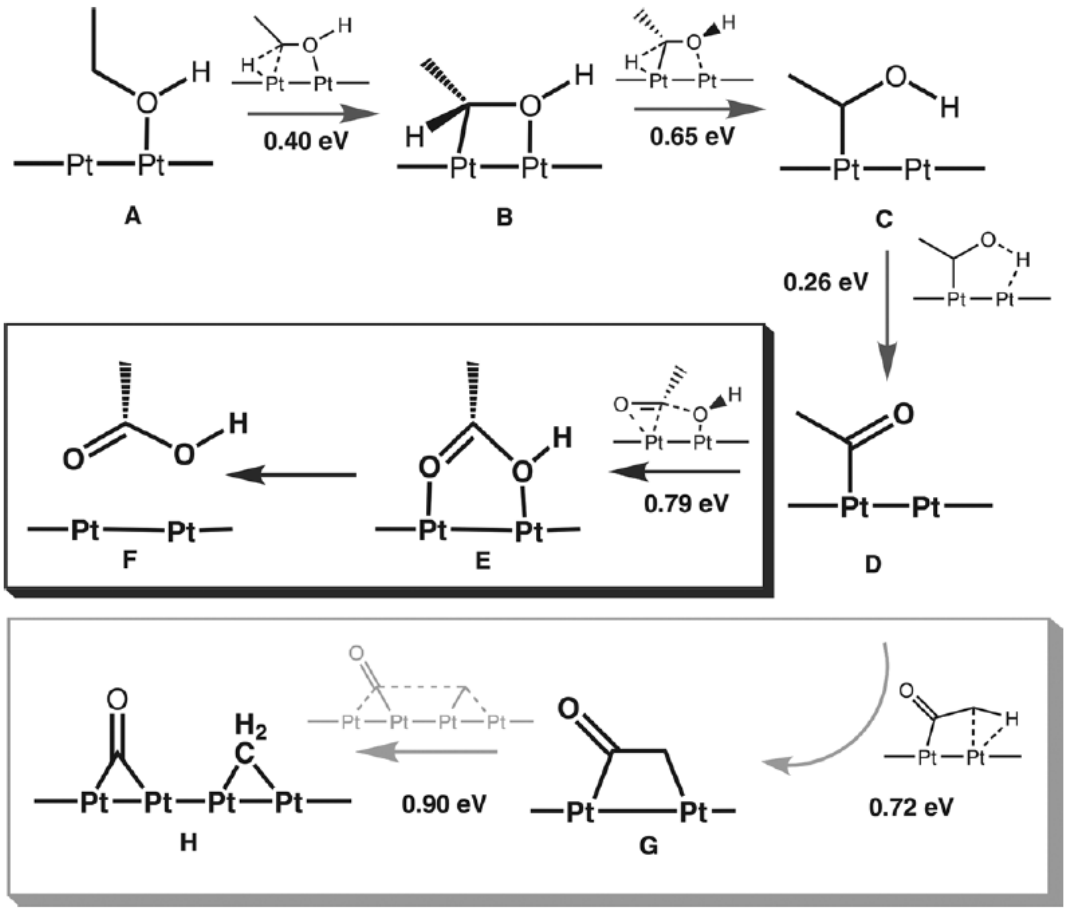

Figure 1.5.2. EOR Reaction pathway with calculated activation energy of each critical step on Pt surface. Reprinted with permission from reference 74[74]. Copyright 2012 John Wiley & Sons Inc.

There was also significant amount of experimental work done to detect CO_2 during EOR and reveal its mechanism. Wang et al. reported the investigation of EOR product on Pt surface utilizing Differential Electrochemical Mass Spectroscopy (DEMS) and they found that the signal of CO_2 is two order of magnitude lower than the signal of acetaldehyde and acetic acid[72]. Lai et al. implemented Surface Enhanced Raman Spectroscopy (SERS) and reported that CO^* and CH_x^* signal could be observed as low as 0.1 V, indicating the capability of Pt to cleave C-C bond at low voltage[77]. Yet CO^* and

CH_x^* signal would disappear only at 0.525 V and 0.325 V respectively, indicating their poisoning effect on Pt surface. Kowal et al. used *in situ* Infrared Reflection-Adsorption Spectroscopy (IRRAS) to investigate the product adsorbed on catalyst surface. They were able to observe CO_2 vibration peak on Pt (111) electrode at a quite high potential (>0.78 V)[79].

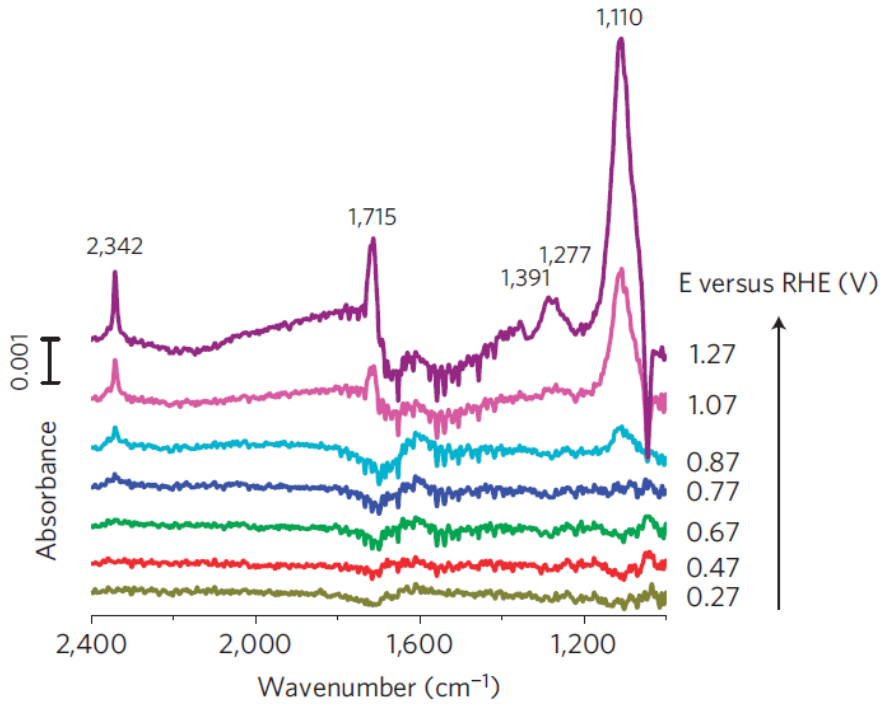

Figure 1.5.4. *in situ* IRRAS spectra recorded during EOR on Pt (111). Reprinted with permission from Ref 79[79]. Copyright 2009 Nature Publishing Group.

To summarize, researchers have found that due to intermediate poisoning and obstacle in C-C bond cleavage, Pt exhibit sluggish kinetic and weak selectivity toward full oxidation during EOR. There are also significant amount of effort of tuning composition and structure of Pt catalyst to enhance EOR activity and selectivity. They

will be introduced in the following chapters. In fact, the focus of this work is improving EOR activity and selectivity by developing advanced nanomaterial as catalysts.

1.6 Water electrolysis and Hydrogen Evolution Reaction (HER)

Water electrolysis is a feasible method of producing hydrogen[80]. Hydrogen Evolution Reaction (HER) is the cathodic reaction during electrolysis. Due to the simplicity of hydrogen molecules, the mechanism of HER is relatively simple, especially in acidic environment. It is generally agreed that HER in acidic environment could be divided into three steps[81]:

First its Volmer reaction $H_3O^+ + e^- \rightarrow H_{ads} + H_2O$

then it's either Heyrovsky reaction $H_{ads} + H_3O^+ \rightarrow H_2 + H_2O$

or Tafel reaction $H_{ads} + H_{ads} \rightarrow H_2$

Platinum is very active toward HER[82] but developing substitute catalyst for Pt that is more abundant and inexpensive will provide the potential for industrial scale applications. Many materials had been reported to be active for HER and MoS_2 is a particularly interesting one among them. Bulk MoS_2 is inert but nano-scaled MoS_2 is highly active. Jaramillo et al. reported that the active site of MoS_2 is on the edge of sheets (presented in Figure 1.6.1)[83]. In this work, a significant amount of effort was devoted to the rational synthesis of two dimensional MoS_2 nanosheets for the catalysis of HER.

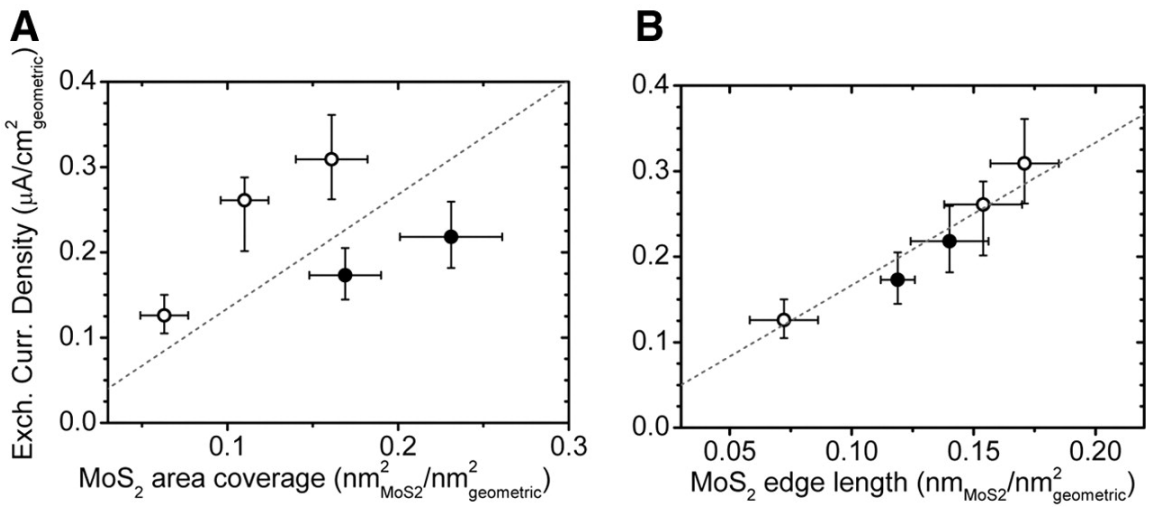

Figure 1.6.1. (a) MoS_2 area and (b) MoS_2 edge length correlation with HER activity. Reprinted with permission from Ref 83[83]. Copyright 2007 American Association for the Advancement of Science.

Chapter 2. Electro-oxidation of Ethanol Using Sphere-like Pt_3Sn Nanoparticles

Adapted with permission of from Liu,Y. *et al.* ACS Catal., 2018, 8, 11, 10931-10937

2.1 Introduction

Ethanol is a promising alternative to fossil fuels.[3] It has a specific energy of 8.3 kWh/kg and an energy density of 6.7 kWh/L, which are comparable to the values of gasoline (12.9 kWh/kg and 9.5 kWh/L).[84] Compared to combustion, it is potentially more efficient to utilize the energy stored in ethanol by feeding it into a fuel cell. In a direct ethanol fuel cell (DEFC), the electro-oxidation of ethanol can be coupled to the oxygen reduction reaction and deliver 12 electrons per molecule at an equilibrium potential of 0.084 V (versus the standard hydrogen electrode, SHE), with the theoretical energy efficiency being as high as 96% (at 80 ^{o}C).[84-85]

One major challenge for DEFCs is the sluggish kinetics of the ethanol oxidation reaction (EOR) toward the complete-oxidation product, CO_2. Carbon-supported platinum (Pt/C) has been widely used for the EOR, but the partial oxidation toward acetic acid is found to be the dominant pathway on Pt surfaces.[86-89] Spectroscopic studies show that cleavage of the C-C bond in ethanol is feasible on Pt at low electrode potentials (e.g., <0.3 V versus the reversible hydrogen electrode (RHE), which is also used in the following discussion unless otherwise specified), but it is likely limited to specific surface sites (e.g., steps or defects) of low abundance.[90-92] The dissociation of ethanol generates strongly binding C_1 intermediates such as $*CH_x$ (x = 1, 2 or 3) and *CO (* denotes an adsorption site on catalyst surface), which require higher potentials (e.g., >0.5

V) to oxidize. At elevated potentials, however, the partial oxidation pathway becomes more favorable, either due to the presence of more surface sites (such as (111) terrace sites) that are active for the oxidation of ethanol to acetic acid, or because of the rise of energy barrier for C-C bond cleavage when the surface is covered by adsorbed hydroxide (*OH).[93-95]

To alleviate the poisoning effect of *CO, Pt-bimetallic electrocatalysts such as Pt-Sn have been intensively studied for the EOR.[96-100] It is expected that Sn (or SnO_2 on the surface) could promote the adsorption of *OH and thus facilitate the oxidative removal of *CO from nearby Pt sites. Despite the commonly observed catalytic activity enhancements, controversial results are however present about the selectivity toward CO_2.[101-105] Moreover, the electrocatalytic performance of Pt-Sn electrocatalysts is found to vary substantially depending on the catalyst structures (particle size, extended surfaces vs. nanoparticles, etc.),[99, 106] concentration, surface coverage and chemical nature of Sn (Pt-Sn alloy vs. Pt-SnO_2 interface),[99, 102-103] electrolyte,[107-110] or experimental methods (e.g., *in situ* Fourier-transform infrared spectroscopy (FTIR)[98, 105, 111] vs. differential electrochemical mass spectrometry (DEMS)[97, 105] vs. (quasi)steady-state electrochemical studies[96, 109, 111]). It remains largely elusive whether the introduction of Sn, or more strictly speaking, what kind of tin sites, improves the complete oxidation of ethanol on Pt-based electrocatalysts.

We report on the electrocatalytic study of EOR on monodisperse and homogeneous Pt_3Sn alloy nanoparticles. These nanoparticles were synthesized by co-reduction of platinum and tin chloride in organic solutions (see the Methods in SI). The obtained nanoparticles were supported on carbon black, with the organic surfactants removed by applying a mild

thermal treatment in air.[112] Electrochemical properties of the derived Pt_3Sn/C catalysts were examined by combining cyclic voltammetry, CO stripping and chronoamperometry, with comparative studies performed on commercial Pt/C. Catalytic selectivity for the EOR was evaluated in a H-type cell under potentiostatic conditions, with the generated CO_2 analyzed by using an gas chromatography-mass spectrometer (GC-MS). In addition, the Pt_3Sn/C catalyst was treated in an alkaline electrolyte to remove the tin species exposed on the surface, which served as control for revealing the role of Sn in the EOR electrocatalysis.

2.2 Experimental method

Materials. Oleylamine (70%, Sigma), oleic acid (90%, Aldrich), platinum tetrachloride (Acros Organic), tin(II) chloride (Strem Chemicals), borane tert-butylamine complex (Sigma), trisodium citrate (Alfa Aesar), tin (IV) chloride (Strem), Sn (II) sulfate (Sigma), Polyvinylpyrrolidone (MW 8,000, Alfa Aesar), Sodium borohydride (Sigma), commercial Pt/C (Tanaka Inc.) and perchloric acid (70%, 99.999% trace metal basis from Sigma) were purchased and used as received.

Synthesis of 6 nm Pt_3Sn nanoparticles. Sphere-like Pt_3Sn nanoparticles were synthesized using an organic solution method. 9 ml of oleylamine and 0.4 ml of oleic acid were mixed and heated to 140 °C. At this temperature the solution was evacuated for 10 minutes before purged with Ar for another 10 minutes. The evacuation and Ar flow were repeated twice before the solution was cooled down to 50 °C. Then 101 mg $PtCl_4$ and 19 mg $SnCl_2$ dissolved in 0.5 ml ethanol was injected into solution. After stirring under argon flow at 50 °C for 10 minutes, the solution was heated up to 120 °C where 300 mg

of borane tert-butylamine complex dissolved in 2 ml of oleylamine was quickly injected. The dark brown solution was kept at 120 °C for 20 minutes before cooling down to room temperature. The product was precipitated by adding ethanol and centrifuging at 4,000 rpm for 5 minutes. After washing with toluene and ethanol, the final product was dispersed in toluene for storage and further usage.

Synthesis of Sn nanoparticles. Sn nanoparticles were grown by modifying a reported protocol.[113] Briefly, 171.2 mg of tin (II) sulfate, 100 mg of polyvinylpyrrolidone and 10 ml of de-ionized water were mixed together. To the above solution, a mixture of 400 mg of sodium borohydride and 10 ml of water were added. The mixture was stirred in air for 2 hours before centrifugation at 10, 000 rpm for 10 minutes. Precipitate was washed with water again before further usage.

Synthesis of SnO_2 nanoparticles. Briefly, 0.5 mmol of trisodium citrate, 0.5 mmol of $SnCl_4$ and 30 ml of water were mixed and put in a 50 ml Teflon liner in an autoclave. The autoclave was heated to 160 °C with a ramp rate of 10 °C/min before being held at 160 °C for 12 hours. After being cooled down to room temperature, the product was acquired by centrifugation and washed with water before further usage.

Catalyst Preparation. The as-synthesized Pt_3Sn nanoparticles dispersed in toluene were mixed with carbon black (KETJENBLAC, >900 m^2/g) in a roughly 2:1 mass ratio. After ultra-sonication for 30 minutes the suspension was centrifuged at 10,000 rpm for 5 minutes. The sediment was re-dispersed in hexane by sonication and centrifuged at 6,000

rpm for 3 minutes. The collected product was dried at 80 °C and then annealed at 185 °C in air for overnight. Inductively Coupled Plasma-Mass Spectrometry (ICP-MS) was conducted to determine the loading of Pt in the catalyst as well as the Pt/Sn ratio. See Figure 2.2.1 for ICP calibration curve.

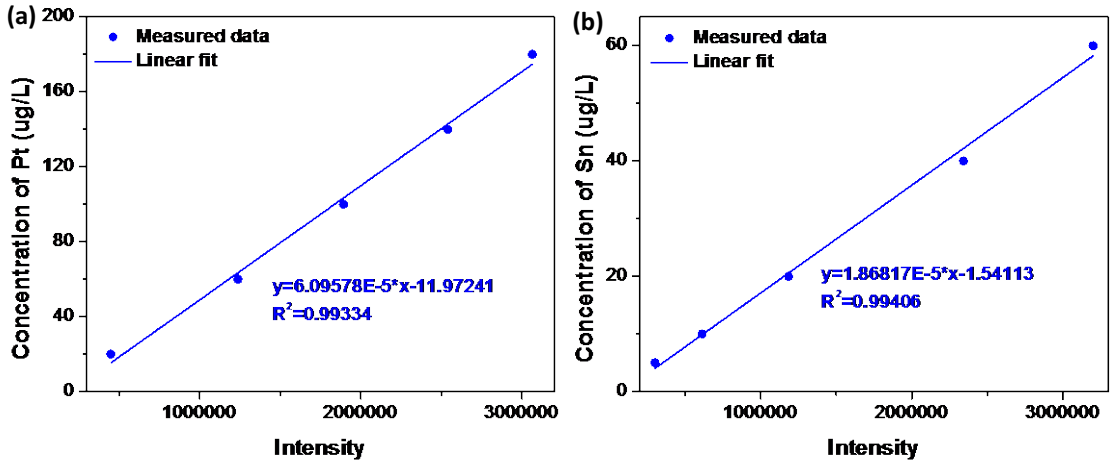

Figure 2.2.1. ICP calibration curve of (a) Pt and (b) Sn.

Characterization. Transmission Electron Microscopy (TEM) images were acquired on an FEI Tecnai 12 microscope operated at 100 kV. X-ray diffraction (XRD) patterns were collected on a PANalytical X'Pert^3 Powder X-Ray Diffractometer equipped with a Cu Kα radiation source (λ=0.15406). Scanning transmission electron microscopy (STEM) imaging and energy-dispersive X-ray spectroscopy (EDX)-based element maps were acquired on a JEOL JSM-6700F Field Emission Scanning Electron Microscope. X-ray Photoelectron Spectroscopy (XPS) measurements were done on a PHI 5600 Multi-technique photoelectron spectrometer using a Mg Kα X-ray source. Inductively Coupled Plasma Mass Spectrometry (ICP-MS) was collected with a PerkinElmer Elan DRC II Quadrupole. Nuclear Magnetic Resonance (NMR) was conducted using a Bruker Fourier 300 MHz spectrometer.

Electrochemical studies. A Metrohm PGSTAT302N potentiostat was used for the electrochemical studies. For the rotating disk electrode (RDE) measurements, a piece of glassy carbon (5 mm in diameter) was used as the working electrode, a Ag/AgCl redox couple as the reference electrode and a Pt wire as the counter electrode (no Pt contamination is noted for the anodic reaction of ethanol). For electrode preparation, the nanoparticles/carbon catalysts were dispersed in 10% iso-propanol (with 0.025 % Nafion) aqueous solutions at 1 mg/ml. The mixtures were sonicated for about 30 minutes to allow formation of uniform ink. Typically, 20 ul of ink was dropped onto the surface of glassy carbon and was dried in air. Cyclic voltammogram was recorded at 50 mV/s after ~10 cycles of scan for surface cleaning. Chronoamperometry was conducted at each potential for 30 minutes. The transient signals within the first two seconds were discarded in the calculation of average amperometric currents. All specific currents were normalized by mass of Pt acquired from ICP.

For product analysis, the electrocatalytic studies were conducted in an air-tight electrochemical cell previously developed by our group (see Figure 2.2.2 for its photo).[114] A piece of glassy carbon disk (2x2 cm^2) was used as the working electrode, on which 1-2 ml of catalyst ink (1 mg/ml) was deposited on. The electrolyte was 0.1 M of $HClO_4$, to which 0.1 M of ethanol was added. Helium was purged into the anodic compartment at a rate of 10 sccm and induced into the sampling valve of GC-MS. The gas-phase products were analyzed by using a GCMS-QP2010SE (Shimadzu) equipped with a Plot-Q column (Restek). Each potential was applied and held for 30 minutes. Liquid products were analyzed by using NMR.

Figure 2.2.2. Photo of (a) electrolysis cell and (b) whole experimental setup.

KOH Treatment. The selection of KOH treatment to remove the surface tin oxide species is based on the Pourbaix diagram of tin.[115] Tin and tin (hydro)oxides are rather stable over the pH range from ~1 to ~10, but become soluble at higher pH (e.g., in 0.1 M KOH with pH = 13). The alkaline treatment to remove surface tin oxides was conducted by scanning the electrocatalysts in Ar-saturated 0.1 M of KOH between 0.05 and 0.8 V for 5 cycles. The upper limit of potential was set to 0.8 V to avoid Pt dissolution and leaching of subsurface tin. The CV became stable in the alkaline electrolyte after 5 scans, indicating the accomplishment of removing surface tin oxides. The catalyst on RDE was scanned at 50 mV/s, versus 5 mV/s for the catalyst loaded on graphite plate. Lower scan rate was used in the latter case considering the much thinker catalyst layer on the graphite plate, which has about 50 – 100 times higher loading than on the RDE.

Calculation of Faradaic efficiency (FE) toward CO_2. Given the concentrations of generated CO_2 (ppm) measured by the MS detector and the flow rate of Helium, mass flow rates of CO_2 generated from the EOR can be calculated by using the ideal gas law. For each CO_2 molecule produced, the electrode delivers 6 electrons. The Faradaic efficiency toward CO_2 is thus calculated by

$$FE\ (\%) = \frac{I_{CO2}}{I_{total}}$$

$$= \frac{\frac{CO_2\ concentration\ (ppm)}{10^6} \times flow\ rate \times \frac{P}{R \times T} \times F \times 6}{average\ total\ current} \times 100\%$$

where P is the atmospheric pressure, R is the ideal gas constant, T is the room temperature and F is the Faraday constant.

2.3 Results and Discussion

Figure 2.3.1a shows a TEM image of the as-synthesized Pt_3Sn nanoparticles. They possess a sphere-like shape with the average particle size determined to be 6.3 (±0.4) nm. Scanning transmission electron microscopy (STEM) images show (111) lattice fringes (with a spacing of 0.23 nm) of face-centered cubic (fcc) crystals throughout the nanoparticles, indicating a single-crystal nature of the material (Figures 1b and c). The crystal structure was confirmed by X-ray diffraction (XRD) analysis (Figure 2.3.2). Element distribution in the Pt_3Sn nanoparticles was mapped by using STEM-based energy-dispersive X-ray spectroscopy (EDX) (Figures 2.3.1d-f). Both Pt and Sn were found to be homogeneously distributed across the nanoparticles. The elemental ratio between Pt and Sn was determined by inductively coupled plasma mass spectrometry

(ICP-MS) to be 3.04, close to the targeted composition of Pt_3Sn. It should be pointed out that our synthesis of the Pt_3Sn nanospheres is distinct from the previously reported methods using formic acid,[116] potassium bromide,[117] citric acid[118] or ethylene glycol[96] as reducing agents. The use of borane tert-butylamine as reducing agent is believed to be more advantageous for simultaneous reduction of the Pt and Sn salts to obtain monodisperse and homogeneous nanoparticles in organic solution synthesis, as also seen in the previous reports.[119-121]

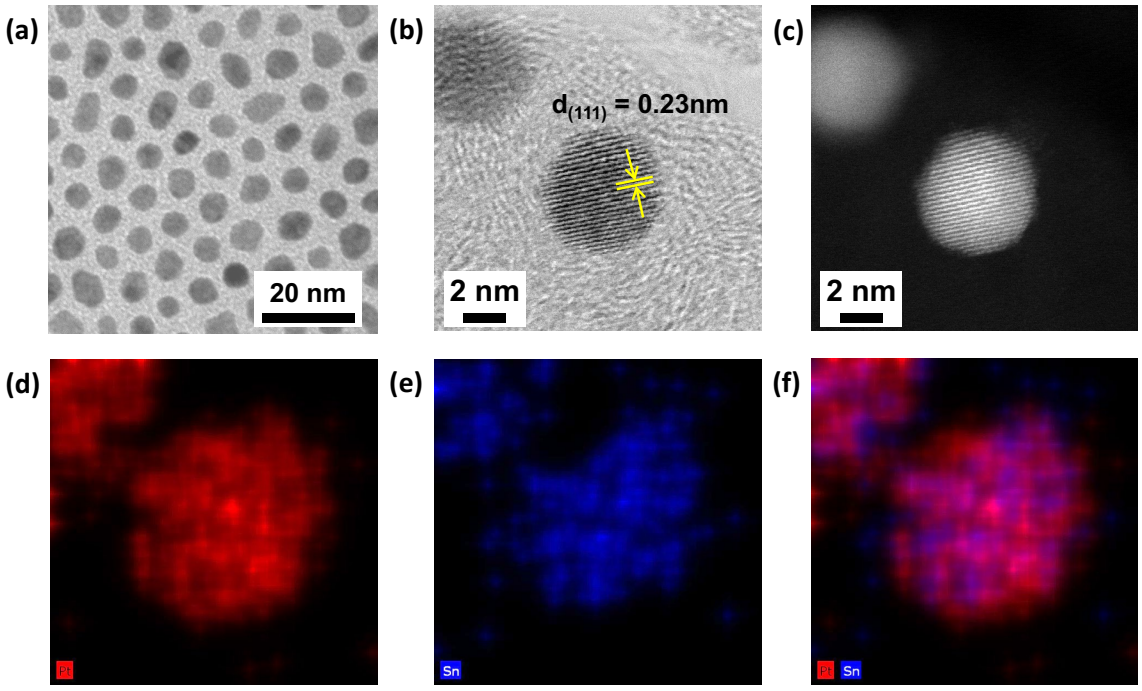

Figure 2.3.1. (a) TEM, (b) Bright-field and (c) dark-field STEM images of the as-synthesized Pt_3Sn nanoparticles. (d-f) Element maps showing the distribution of Pt (red) and Sn (blue) across a Pt_3Sn alloy nanoparticle.

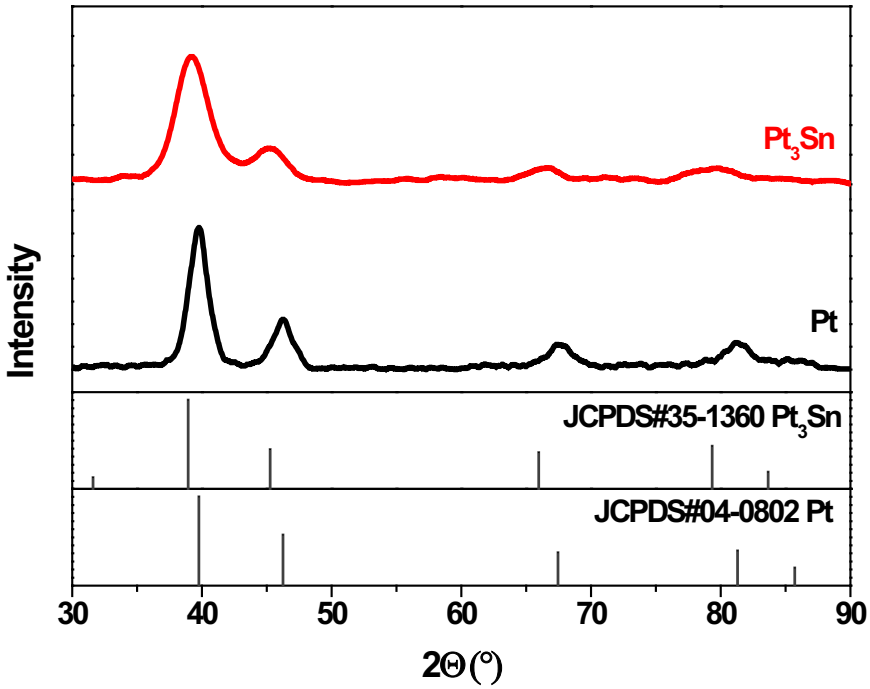

Figure 2.3.2. XRD patterns of the Pt_3Sn nanoparticles in comparison to Pt.

The acquired Pt_3Sn nanoparticles were loaded on carbon black (KETJENBLAC, >900 m^2/g) and, after the removal of surfactants, evaluated as electrocatalysts for the EOR. Figure 2.3.3a presents the cyclic voltammogram (CV) recorded in 0.1 M $HClO_4$ for the Pt_3Sn/C catalyst, in comparison to the commercial Pt/C (~6 nm, obtained from Tanaka Inc.; see Figure 2.3.4 for the TEM image). Pt/C exhibits the H_{upd} peak from ~0.05 V to ~0.4 V and OH adsorption peak onset at ~0.7 V in the voltammogram. Pt_3Sn/C possesses substantially suppressed H_{upd} features as compared to Pt/C, with the associated charges calculated to be only ~6.46 C/g_{Pt} (versus 91.8 C/g_{Pt} for Pt/C). The suppressed H_{upd} features for Pt_3Sn can be attributed to the coverage of surface sites by tin species (likely present as tin oxides on the nanoparticle surface, see Figure 2.3.5 for the X-ray photoemission spectroscopy (XPS) spectra) and/or the weakening of Pt-H binding on the alloy catalyst.[17] Pt_3Sn/C also exhibits downshift in the onset potential

for hydroxide adsorption (OH_{ad}), namely from ~0.7 V for Pt/C to ~0.5 V. Noticeably the CVs recorded on Sn or SnO_2 do not exhibit any significant features in the potential region of 0.05 – 1.05 V (Figures 2.3.6 and 2.3.7). It has been suggested that water dissociation can be facilitated at the Pt-SnO_2 interface.[98] While this effect could explain the lower onset potential for OH_{ad} in the anodic scan, it would not give rise to the negative shift of the hydroxide desorption peak exhibited in the cathodic scan (from ~0.8 V for Pt/C to 0.5 – 0.6 V for Pt_3Sn, Figure 2.3.3). We thus attribute the downshift of OH_{ad} peaks observed on Pt_3Sn/C to the enhanced adsorption of hydroxide on the platinum-tin oxide interface.[122]

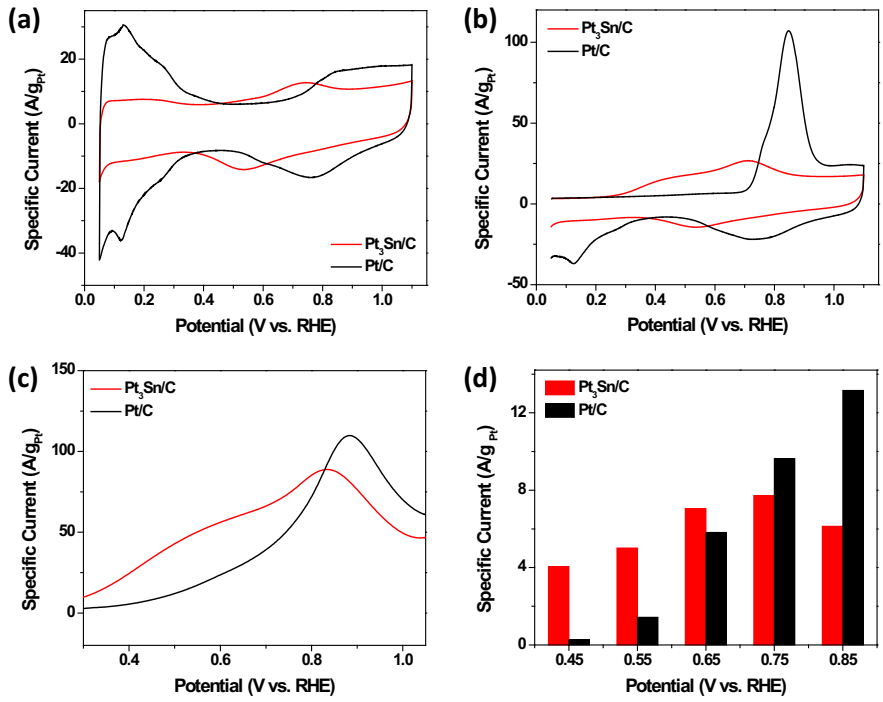

Figure 2.3.3. (a) CV and (b) CO stripping patterns recorded on Pt_3Sn/C and Pt/C in 0.1 M of $HClO_4$. (c) Polarization curves and (d) amperometric currents measured in 0.1 M of $HClO_4$ + 0.1 M of ethanol. Scan rate was 50 mV/s in (a-c).

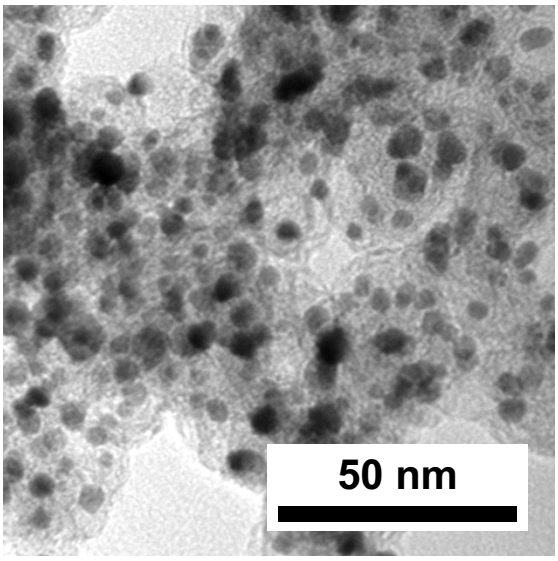

Figure 2.3.4. Representative TEM image of the commercial Pt/C catalyst employed in this study.

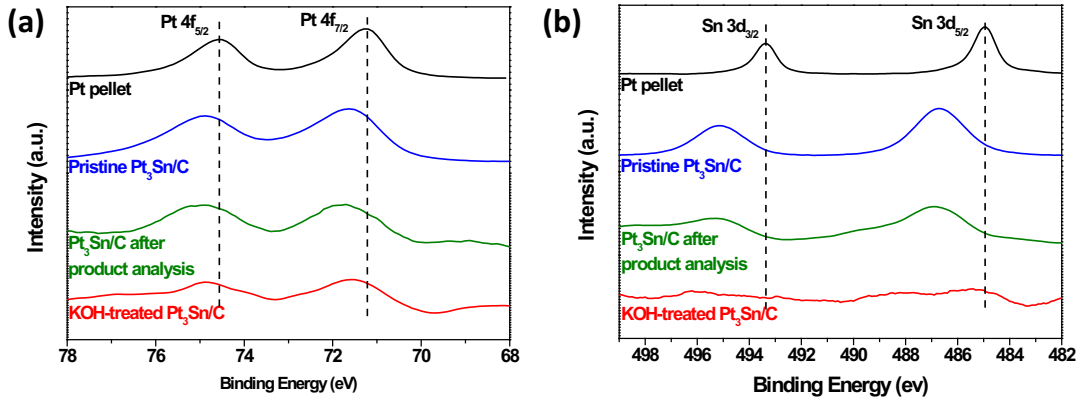

Figure 2.3.5. (a) Pt 4f- and (b) Sn 3d-edge spectra of the pristine Pt_3Sn/C, Pt_3Sn/C after 2.5 h of electrochemical reactions for product analysis and KOH-treated Pt_3Sn/C. All Pt_3Sn/C samples show Pt $4f_{7/2}$ peak at 71.6 – 71.7 eV (vs 71.2 eV for Pt pellet), indicating Pt on the catalyst surface was partially oxidized. The pristine Pt_3Sn/C and the Pt_3Sn/C after reaction possess Sn $3d_{5/2}$ peak at 486.7 – 486.8 eV (vs 485.0 eV for the metallic Sn pellet), indicating the surface Sn species was also oxidized.[123] KOH-treated Pt_3Sn/C has

nearly invisible Sn signal, confirming the successful removal of most tin oxides from the surface. The atomic ratio of Pt/Sn estimated from the XPS is 4.2 for the pristine Pt_3Sn/C.

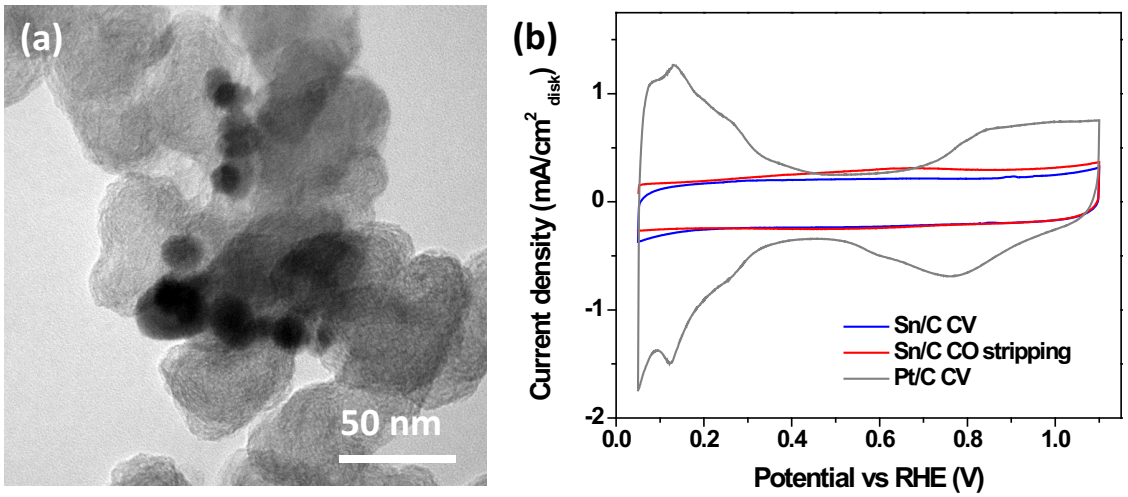

Figure 2.3.6. (a) TEM image of Sn/C used for the control experiments. (b) CV and CO stripping profile recorded on Sn/C. CV of Pt/C was put in (b) for comparison.

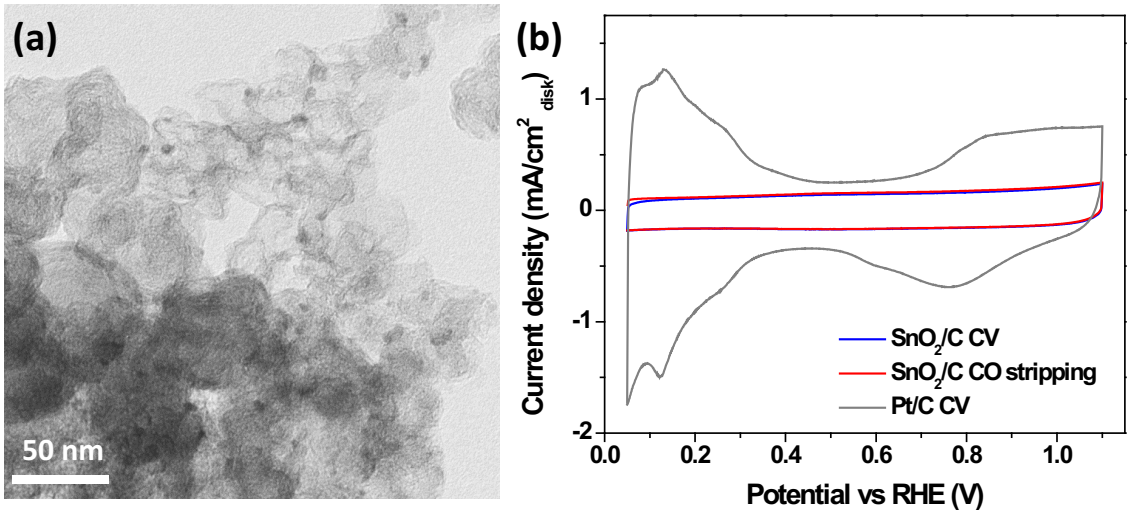

Figure 2.3.7. (a) TEM image of SnO_2/C prepared as a control for the electrochemical studies. (b) CV and CO stripping profile recorded on SnO_2/C. CV of Pt/C was put in (b) for comparison.

The surface properties of Pt_3Sn nanoparticles were further probed by oxidative stripping of pre-adsorbed CO monolayers (Figure 2.3.3b). The CO stripping pattern recorded on Pt_3Sn/C is featured with two broad peaks at ca. 0.45 and 0.71 V, whereas the pattern for Pt/C only exhibits one strong peak around 0.85 V. The peak at 0.71 V for Pt_3Sn overlaps with the OH_{ad} peak as shown in Figure 2.3.3a, but still discernible after subtracting the blank CVs from the CO stripping patterns (Figure 2.3.8). Since neither Sn nor SnO_2 nanoparticles adsorb CO (Figures 2.3.6 and 2.3.7), we assign the two CO stripping peaks on Pt_3Sn/C to be associated with the Pt sites on surface, of which the adsorption properties are modified by surface tin oxide or subsurface metallic tin. We notice the discussions of CO oxidation at low potentials (<0.7 V) associated with low-coordinated Pt sites such as steps[124] and adislands[125]. In our study, the Pt/C control has similar particle size to the Pt_3Sn nanoparticles, but do not exhibit any low-potential features in CO stripping. We are thus inclined to the interpretation through modified surface properties for the alloy nanoparticles, as previously reported on Pt-bimetallic electrocatalysts.[17, 126] The much lower potentials of the CO stripping peaks for Pt_3Sn indicate the facilitated oxidative removal of *CO on the alloy catalyst as compared to Pt/C. The presence of two peaks could be ascribed to two types of Pt sites on the surface, e.g., (111) vs. (100), or being nearby vs. being away from the tin oxide species. Despite the quite dissimilar shapes of the CO stripping pattern, the integrated charges associated with CO stripping are actually in the same magnitude, i.e., 128 and 202 C/g_{Pt} for Pt_3Sn/C and Pt/C, respectively, with the difference much smaller than in the situation of H_{upd}. Considering that *CO typically can access more surface sites than *H on alloy catalysts,[17, 127], our finding suggests that, other than the coverage of surface sites by tin species, the

weakened hydrogen binding is probably the main cause for the suppressed H_{upd} features for Pt_3Sn/C as observed in Figure 2.3.3a.

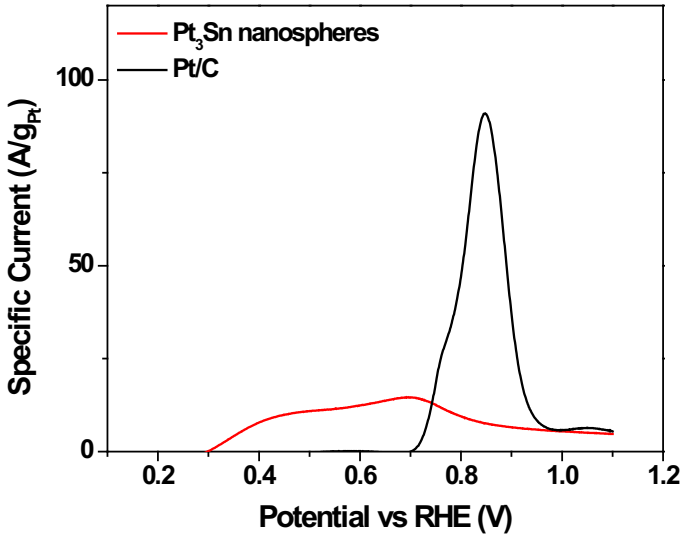

Figure 2.3.8. CO stripping patterns with the corresponding blank CVs subtracted.

Examination of the EOR electrocatalysis was first performed in a rotating disk electrode (RDE) apparatus by loading the carbon supported nanoparticles on glassy carbon. Figure 2.3.3c shows the polarization curves recorded in 0.1 M of $HClO_4$ with 0.1 M of ethanol added. Pt_3Sn/C exhibits much lower onset potential for the EOR, at ca. 0.3 V in comparison to ~0.5 V for Pt/C. Pt_3Sn/C reaches the peak current of ~90 A/g_{Pt} at 0.83 V, while Pt/C has a slightly higher peak current of ~110 A/g_{Pt} at 0.88 V. The polarization curve of Pt_3Sn/C is particularly featured with a shoulder peak around 0.5 – 0.6 V at a specific current of 40 – 50 A/g_{Pt}, which is absent in the case of Pt/C. This low-potential feature seems to correlate to the onset of OH_{ad} observed in the blank CV (Figure 2.3.3a) and the first peak exhibited in the CO stripping pattern (Figure 2.3.3b). We consider it as the sign of high EOR activity on the alloy catalyst.

Besides voltammetric polarization, we also performed chronoamperometry measurements on the RDEs, which allows for us to evaluate the electrocatalytic activity under potentiostatic conditions and without being subjected to the transient capacitance effects. Figure 2.3.3d summarizes the measured specific currents in the potential region of 0.45 – 0.85 V, with the amperometry curves presented in Figure 2.3.9. Consistent with the finding from the linear polarization curves (Figure 2.3.3c), Pt_3Sn/C is much more active than Pt/C in the low-potential region (<0.7 V). At 0.55 V, the measured specific currents are 5.0 and 1.4 A/g_{Pt} for Pt_3Sn/C and Pt/C, respectively. Pt/C outperforms Pt_3Sn/C at potentials more positive than 0.7 V, but as we will reveal below, it can be attributed to its high activity for the partial oxidation of ethanol. We also normalized the amperometric currents by the electrochemically active surface areas (ECSAs) estimated from the CO stripping charges (Figure 2.3.10). Pt3Sn/C exhibits much higher specific activities as evaluated in this way than Pt/ C for potentials up to 0.75 V, confirming the intrinsically enhanced catalytic activity of the surface of the bimetallic electrocatalyst.

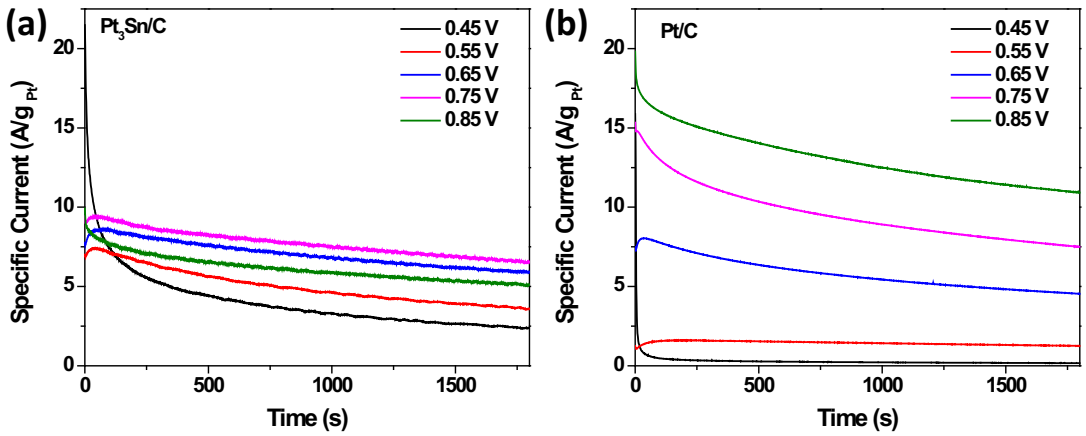

Figure 2.3.9. I-t curves recorded in the chronoamperometry studies for (a) Pt_3Sn/C and (b) Pt/C.

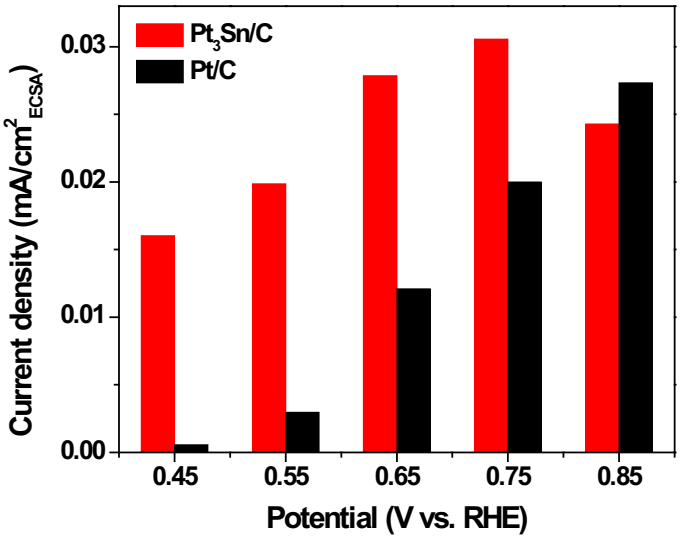

Figure 2.3.10. Amperometric current densities normalized against ECSA calculated from CO stripping charge measured in 0.1 M of $HClO_4$ + 0.1 M of ethanol.

To analyze the products for the EOR, we conducted additional electrocatalytic studies under potentiostatic conditions in an H-type electrochemical cell, in which a He flow is introduced to the anode compartment and carries out the generated CO_2 for quantitative analysis (Figures 2.3.11a and b).[95] Pt_3Sn/C is found to be much more selective than Pt/C for the oxidation of ethanol to CO_2, with the Faradaic efficiency (FE_{CO2}) achieving 12% at 0.55 V (Figure 2.3.11c). Pt/C has no more than 3% of FE_{CO2} throughout the investigated potential region, with no CO_2 signal detected at 0.45 V. For both catalysts, FE_{CO2} drops as the potential increases above 0.6 V. The superior catalytic selectivity of Pt_3Sn/C is better visualized by comparing the partial currents for CO_2 production (J_{CO2}) (Figure 2.3.11d). The value of J_{CO2} achieves 0.16 A/g_{Pt} at 0.55 V for Pt_3Sn/C, which represents ~5 times of improvement versus Pt/C at this potential. Similar to the trend for FE_{CO2}, J_{CO2} of Pt_3Sn/C drops as the potential becomes more positive, but

it is not the case for Pt/C, which reaches the highest J_{CO2} of 0.07A/g_{Pt} at 0.75 V. The C_2 products detected in the electrolyte (by using a nuclear magnetic resonance (NMR) spectrometer) after the EOR are mainly acetic acid and acetaldehyde (Figure 2.3.11).

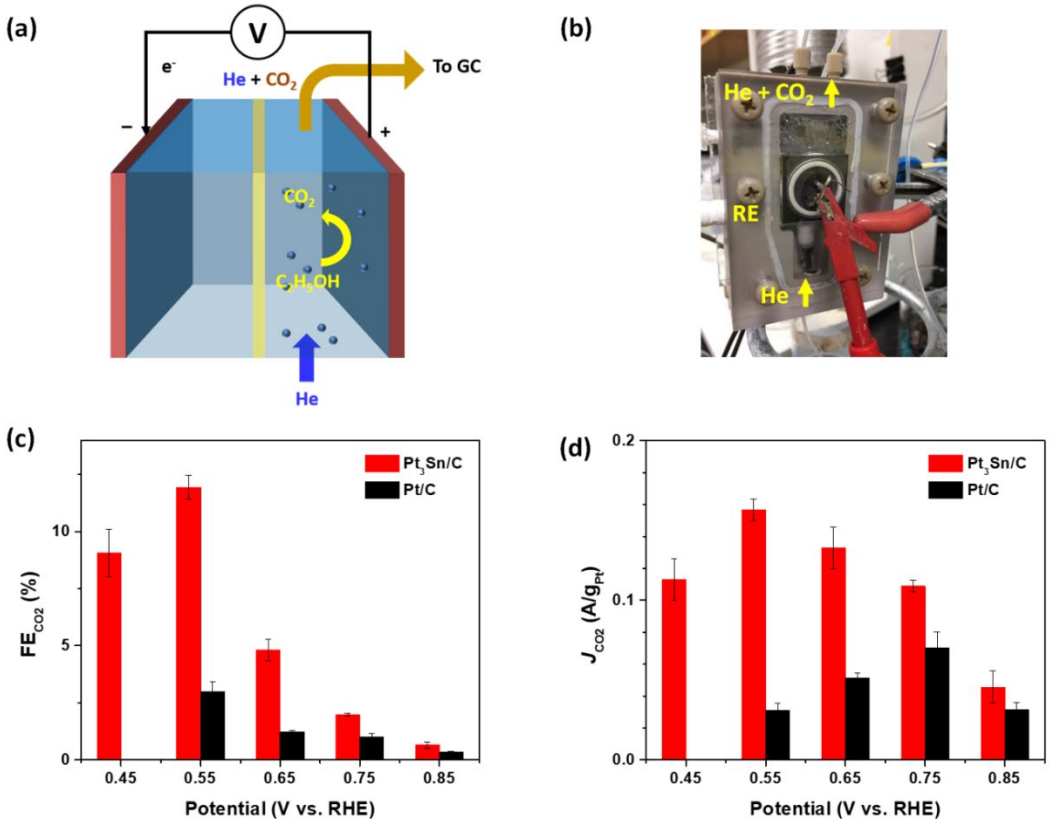

Figure 2.3.11. (a) Scheme and (b) photo of the electrochemical cell used for product-resolved electrocatalytic studies of the EOR under potentiostatic conditions. Note that the reaction (now shown in a) at the counter electrode is hydrogen evolution in the present three-electrode configuration, where the reference electrode (RE labeled in b) is placed in the anode compartment. (c, d) Comparison of Faradaic efficiency (FE_{CO2}) and partial current (J_{CO2}) toward CO_2 between Pt_3Sn/C and Pt/C.

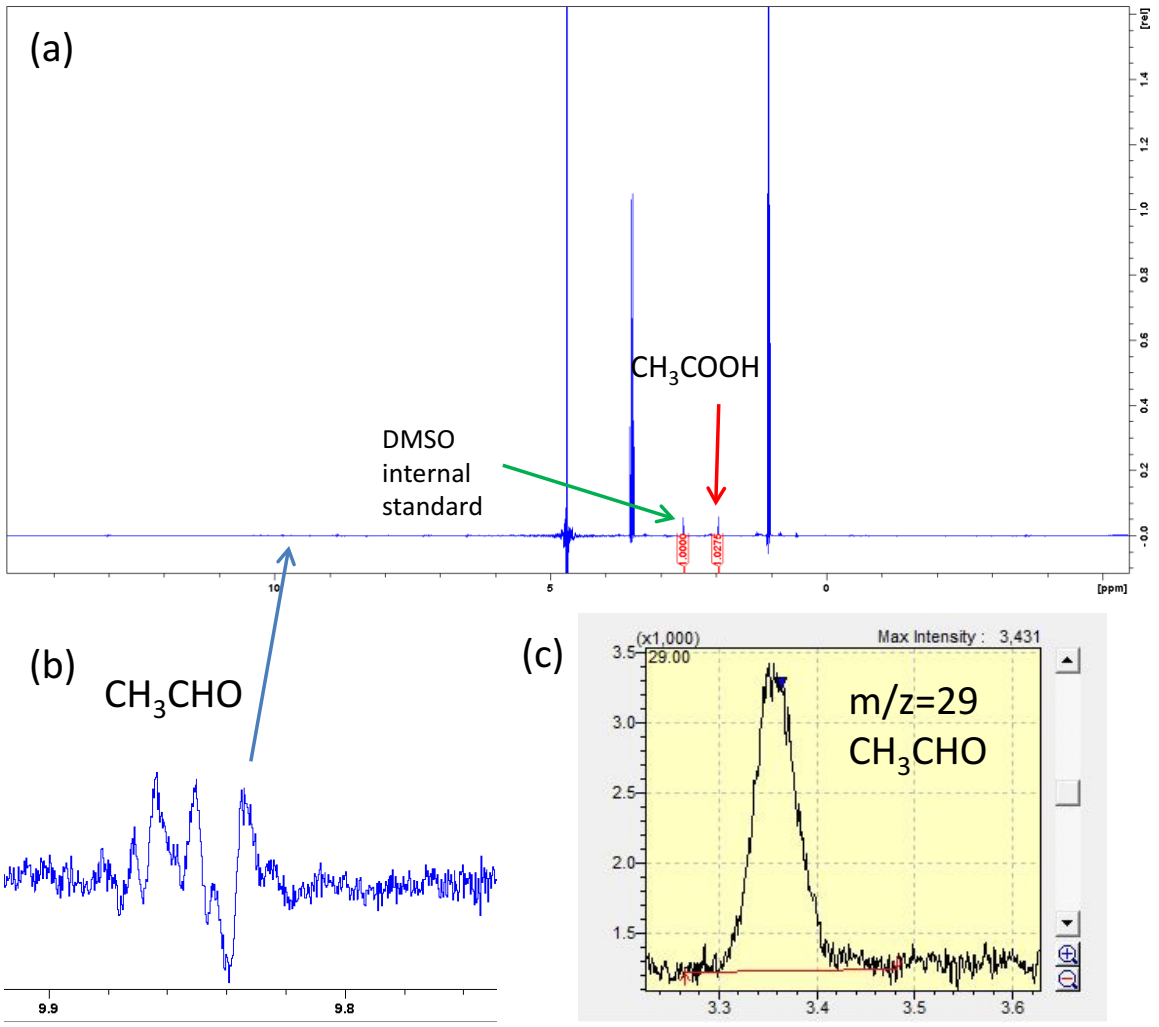

Figure 2.3.12. NMR spectra containing signals of (a) acetic acid and (b) acetaldehyde. (c) GC-MS signal of gaseous acetaldehyde.

Our results point to the Pt_3Sn alloy nanoparticles as a superior electrocatalyst for the EOR. Both the surface tin oxide and subsurface metallic tin species could modify the adsorption and catalytic properties of Pt sites on the alloy catalyst, contributing to the catalytic activity and selectivity enhancements. To discern the exact role of tin, we have treated Pt_3Sn/C in alkaline to remove the surface tin oxides and also investigated the EOR electrocatalysis on the treated catalyst. The removal of tin species from the alloy catalyst surface by the KOH treatment was confirmed by X-ray photoemission spectroscopy

(XPS) (Figure 2.3.5) and supported by the control experiment on SnO_2 nanoparticles (Figure 2.3.13). EDX analysis shows that the content of tin in the Pt_3Sn/C catalyst is reduced by ~25%, with the resulted Pt/Sn ratio being ~4.3 (Figure 2.3.14). The size and morphology of Pt3Sn/C remained nearly unchanged after the KOH treatment (Figure 2.3.15). Figure 2.3.16a compares the CVs recorded (in 0.1 M $HClO_4$) before and after the KOH treatment. The KOH-treated Pt_3Sn/C catalyst exhibits much more pronounced H_{upd} peaks and positive potential shift for the OH_{ad} adsorption peaks. While the CV becomes more like Pt/C, CO stripping pattern of the treated catalyst largely preserves the features of the pristine Pt_3Sn/C, albeit that the two peaks at 0.45 and 0.71 V become a little sharper and slightly lower in intensities (Figure 2.3.16b). These observations indicate that the oxidative removal of *CO is still feasible at relatively low potentials (<0.5 V) on the KOH-treated Pt_3Sn/C catalyst, on which most of the surface tin oxides have been removed and the behavior of OH_{ad} is more like Pt/C. The decoupling of low-potential oxidation of *CO from the enhanced adsorption of *OH has previously been seen on Pt-Ni alloy nanoparticles with a Pt-skin surface, and can be attributed to the weakening of CO binding on Pt by the non-noble metal (metallic Sn in the case of Pt_3Sn alloy) present in the subsurface layer.[17]

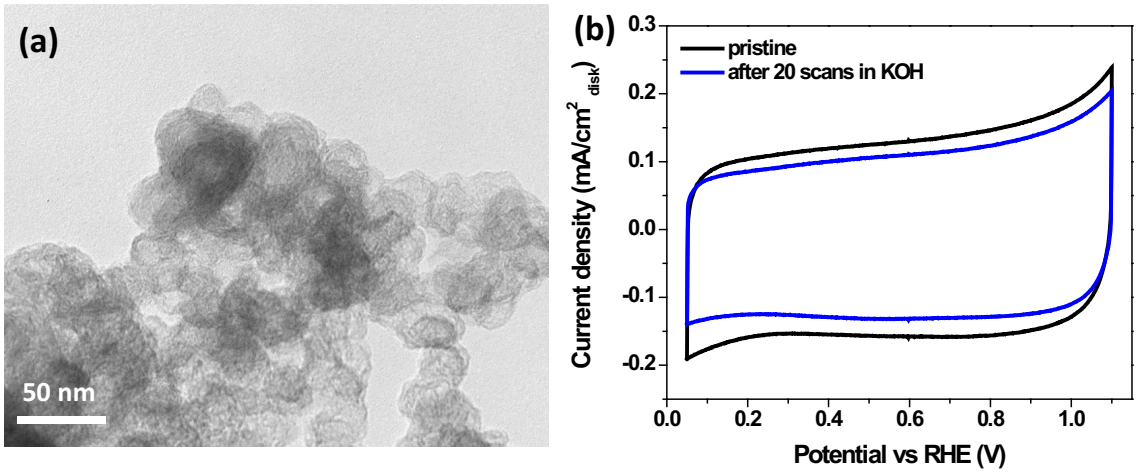

Figure 2.3.13. (a) TEM image of SnO_2/C after 20 scans in 0.1 M KOH, which shows no visible SnO_2 nanoparticles left. (b) CVs of pristine and KOH-treated SnO_2/C in 0.1 M $HClO_4$, both show no significant Faradaic features.

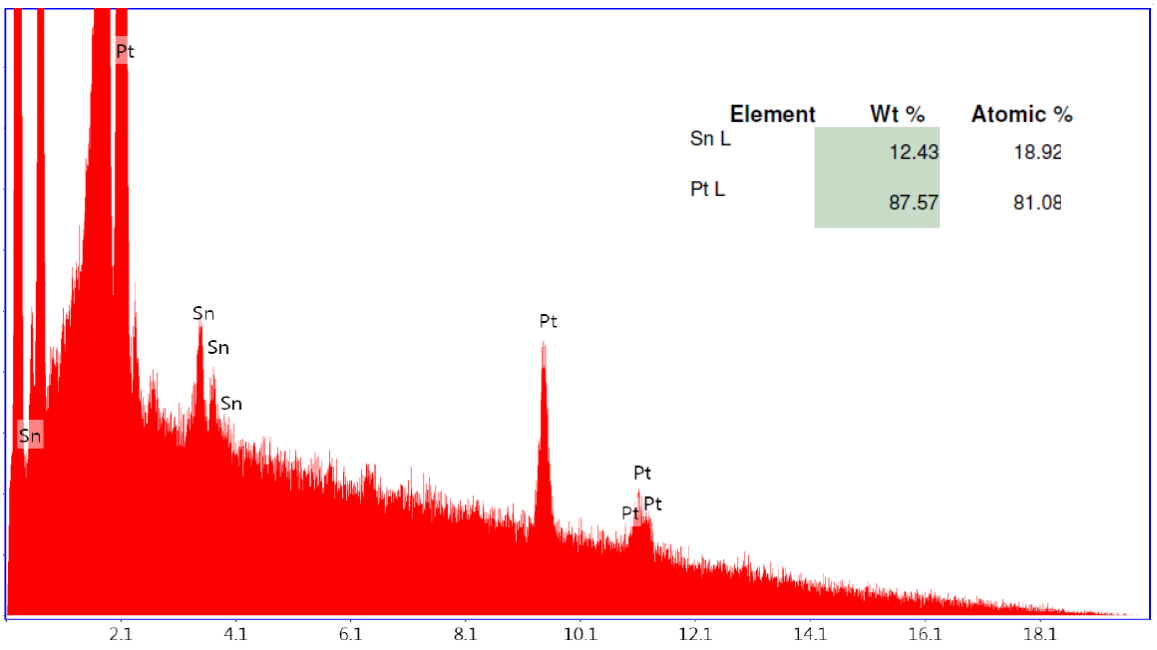

Figure 2.3.14. EDX spectrum recorded on the KOH-treated Pt_3Sn/C catalyst.

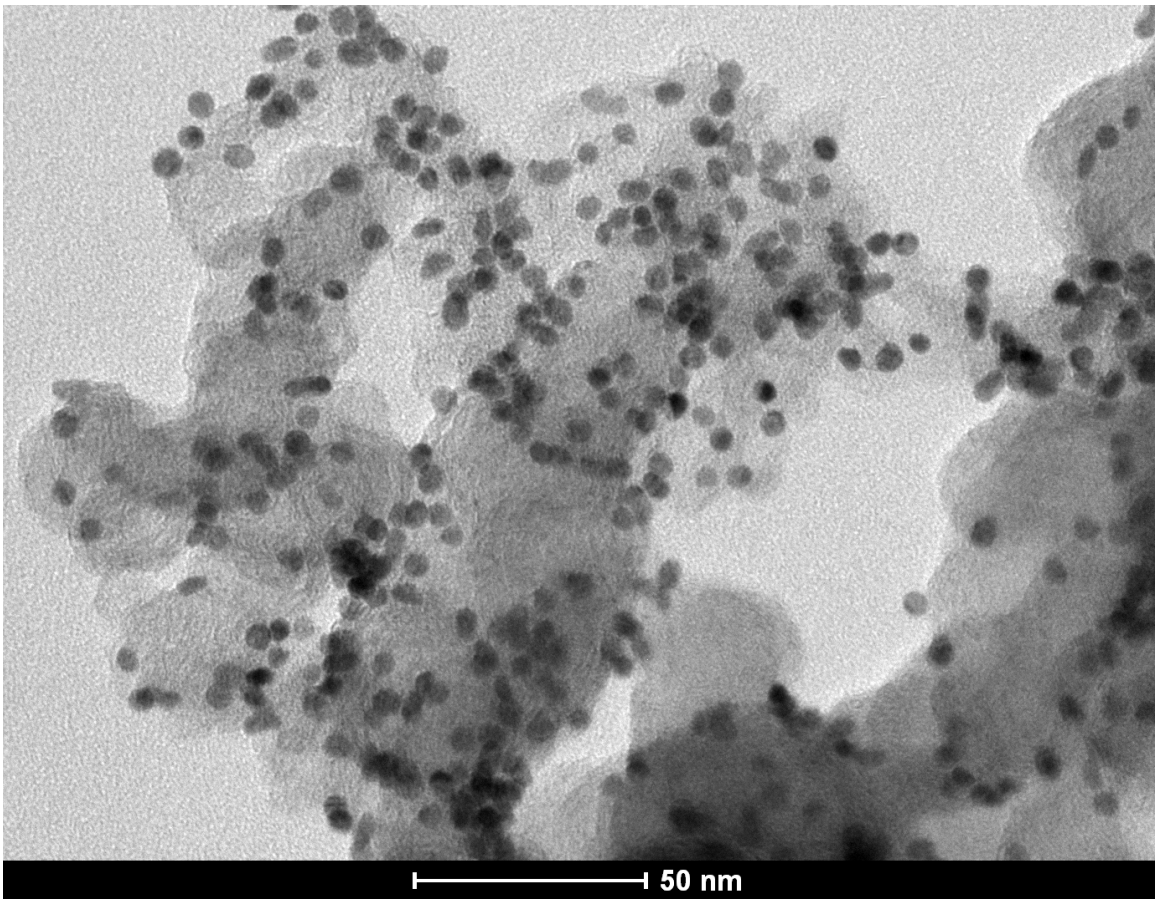

Figure 2.3.15. TEM image of KOH-treated Pt_3Sn/C.

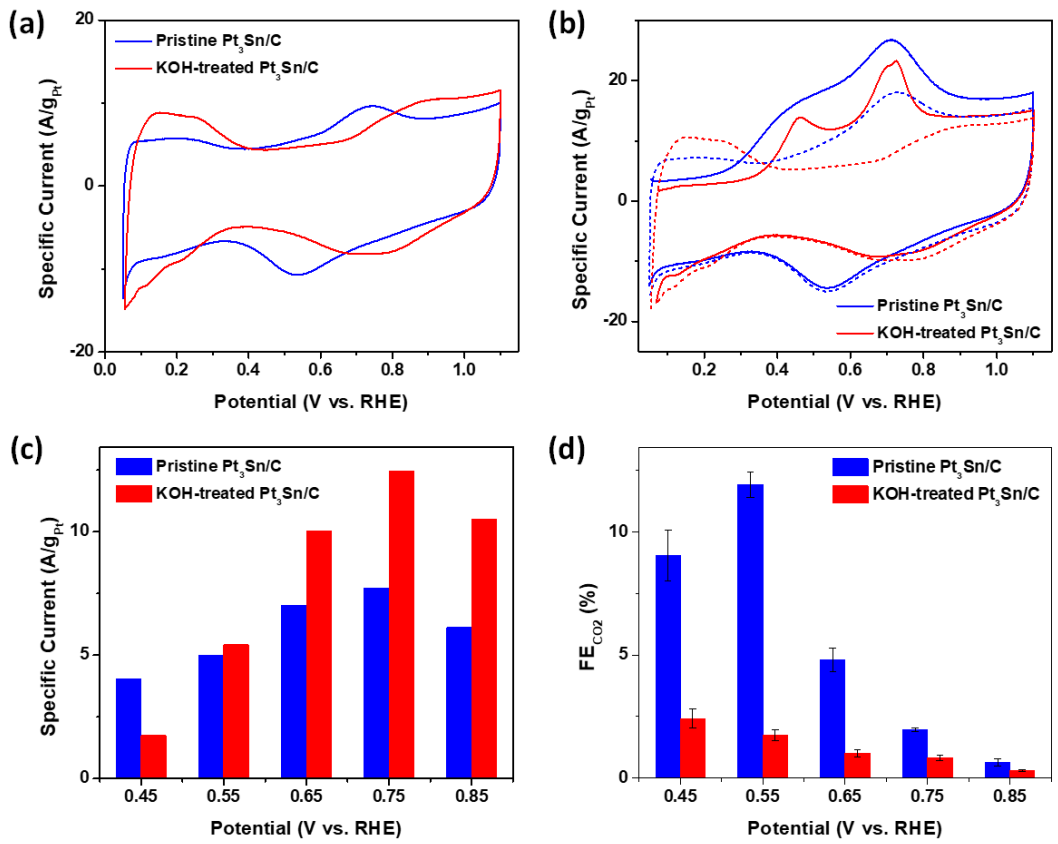

Figure 2.3.16. (a) CV and (b) CO stripping pattern of Pt_3Sn/C in 0.1 M $HClO_4$ after scans in 0.1 M KOH. (c) Amperometric specific currents and (d) CO_2 faradaic efficiency of pristine and KOH-treated Pt_3Sn/C.

The KOH-treated Pt_3Sn/C catalyst exhibits similar catalytic activity and selectivity to Pt/C. They give higher amperometric currents than the untreated Pt_3Sn/C at potentials above 0.5 V (Figure 2.3.16c). Similar to the discussion above for the comparison between untreated Pt_3Sn/C and Pt/C, it may not only be due to the exposure of more Pt sites on the surface of KOH-treated catalyst, but also caused by the higher activity for partial oxidation. The latter postulation is corroborated by the low FE_{CO2} measured on the KOH-treated Pt_3Sn/C, which is merely <3% throughout the investigated potential region and resembles the performance of Pt/C (Figure 2.3.16d). The

comparative studies of pristine and KOH-treated Pt_3Sn/C catalysts thus reveal that the surface tin oxide species plays a crucial and indispensable role in the complete oxidation of ethanol, whereas subsurface metallic tin, albeit facilitating the oxidative removal of *CO, does not improve the EOR selectivity toward CO_2 by itself.

Our findings suggest that the complete oxidation of ethanol is not limited by the oxidative removal of *CO on Pt_3Sn/C. The consistent observation of CO_2 throughout the electrocatalytic studies, albeit with the selectivity being dependent on the potential and whether tin oxide species is present on the surface, signifies the presence of surface sites cleaving the C-C bond in ethanol. After excluding these two possibilities, it becomes compelling to consider the oxidation of $*CH_x$ to *CO as the rate-limiting factors for the complete oxidation of ethanol. The α and β carbon in ethanol generate *CO and $*CH_x$, respectively, from the C-C bond cleavage. The sluggish kinetics of oxidative conversion of $*CH_x$ to *CO on Pt was initially proposed by Lai *et al.*[90] based on a surface-enhanced Raman spectroscopy (SERS) study, and later confirmed by Kutz *et al.*[128] in their investigation of isotopically labelled ethanol using SFG spectroscopy. More recently, our group has combined spectroelectrochemical studies using the sum frequency generation (SFG) technique and product-resolved electrocatalytic measurements to compare the electro-oxidation of ethanol and ethylene glycol on Pt, and identified the role of β carbon in hindering the complete oxidation of ethanol toward CO_2.[95] In the present work, both the pristine and the KOH-treated Pt_3Sn/C catalysts are capable of oxidizing *CO at relatively low potentials, but only the catalyst with tin oxide species present on the surface possesses enhanced the selectivity toward CO_2. The more favorable kinetics of complete ethanol oxidation on the pristine Pt_3Sn/C catalyst is further supported by the

detection of less methane (a minor product generated from the cathodic reduction of *CH_3)[86, 95] in the mass spectrometer than on the KOH-treated Pt_3Sn/C (Figure 2.3.17). We thus conclude with the role of tin oxides on the surface of Pt_3Sn nanoparticles to be enhancing the oxidation of *CH_x to *CO in the EOR electrocatalysis, whereas subsurface metallic Sn facilitates the oxidative removal of *CO. Considering that no improvement in CO_2 selectivity was found in the previous studies of Pt-SnO_2 (without subsurface metallic Sn in the Pt nanoparticles) electrocatalysts,[129-130] we believe it is the synergy of these two effects in the Pt_3Sn alloy nanoparticles for improving the electrooxidation of ethanol toward CO_2.

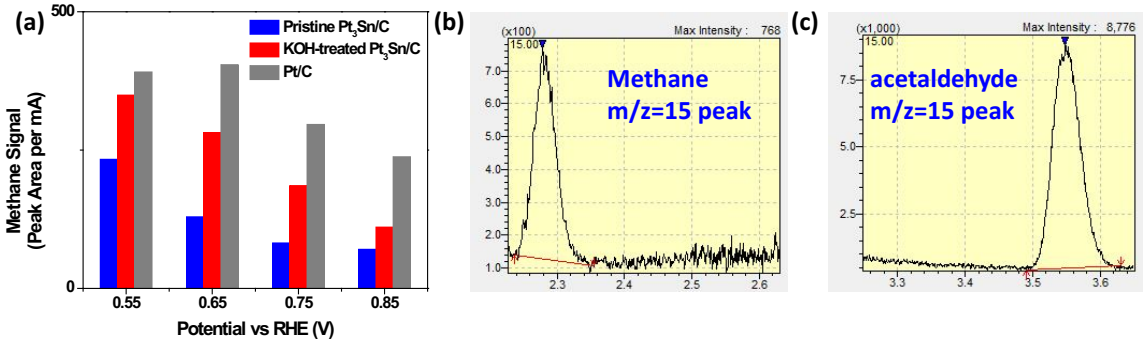

Figure 2.3.17. Detected MS signal for methane (m/z = 15; with elution time <2.5 min, versus >3.5 min for acetaldehyde), expressed as the integrated peak areas normalized by the corresponding electrode currents.

2.4 Conclusion

Here we report the investigation of ethanol electro-oxidation on monodisperse and homogeneous Pt_3Sn alloy nanoparticles. Electrochemical studies were conducted comparatively on the Pt_3Sn nanoparticles supported on carbon (Pt_3Sn/C), a commercial Pt/C catalyst, as well as KOH-treated Pt_3Sn/C with the surface tin species removed. Our

studies reveal the dual role of Sn in the EOR electrocatalysis on Pt_3Sn/C: the surface Sn, likely in the form of tin oxides, enhances the oxidation of $*CH_x$ intermediate to *CO; the subsurface metallic Sn weakens the binding of *CO and facilitates its oxidative removal. A synergy of these two roles, plus the presence of Pt surface sites capable of cleaving the C-C bond, give rise to the enhanced complete oxidation of ethanol.

Chapter 3. Electrocatalytic Study of Ethylene Glycol Oxidation on Pt_3Sn Alloy Nanoparticles

Adapted with permission of Liu, Y. *et al.* Chemelectrochem, **2019**, 6, 1004-1008

3.1 Introduction

Ethylene glycol possesses an energy density of 5.9 kWh/L (5.0 kWh/kg),[131-132] making it a promising fuel for direct alcohol fuel cells (DAFCs).[133] It can be chemically produced from ethylene or carbon monoxide,[134-136] or biologically via degradation of polyethylene.[137-138] Upon complete oxidation to CO_2, each ethylene glycol molecule can deliver 10 electrons at an equilibrium potential of ~+0.01 V, giving rise to a theoretical cell voltage of 1.22 V and an energy efficiency as high as 94 % for DAFCs.[84, 139] Motivated by its great potential as a liquid fuel, the electrocatalysis for ethylene glycol oxidation (EGO) has been studied intensively.[140-144] Similar to ethanol, the EGO can undergo parallel pathways toward partially oxidized C_2 species (glycolaldehyde, glyoxal, glycolic acid, glyoxylic acid, oxalic acid etc.[145]) or CO_2.[146] However, the absence of -CH_3 group in ethylene glycol makes its complete oxidation more feasible than for ethanol. Both spectroscopic and electrocatalytic studies have shown that the oxidative removal of $^*CH_x$ (* denotes an adsorption site on catalyst surfaces) intermediates generated from the C-C bond cleavage in ethanol oxidation requires higher potentials than for $^*CO$, which is the C_1 intermediate derived from α carbon in both ethylene glycol and ethanol oxidation.[95, 147] Also, density functional theory (DFT) calculations suggest that it only needs single binding sites for C-C bond cleavage in the EGO,[145, 148] as compared to the bidentate adsorption configuration of C_2 intermediates involved in ethanol oxidation.[74, 76]

Nonetheless, partial oxidation pathways are still dominant in the EGO and the Faradaic efficiency toward CO_2 (FE_{CO2}) is commonly found to be lower than 10% on platinum (Pt) based electrocatalysts.[145] For its implementation in DAFCs, it is important to develop selective electrocatalysts for complete oxidation of ethylene glycol.

It has been reported that $^{*}CO$ was observed during the spectro-electrochemical studies of EGO on Pt at potentials as low as 0.1 V, indicating the presence of active sites on Pt for cleaving the C-C bond in ethylene glycol.[95, 145] In their studies of EGO electrocatalysis by combining *in situ* infrared spectroscopy and online mass spectrometry, Schnaidt *et al.* suggest 2-hydroxyacetyl ($^{*}COCH_2OH$) as the intermediate to form $^{*}CO$ at relatively low potentials, which is then oxidized to CO_2 at more elevated potentials (e.g., >0.5 V).[145, 149-150] In addition, they found that C-C bond cleavage is not the rate limiting step in the electro-oxidation of ethylene glycol.[149] Thereby, the low selectivity of EGO toward CO_2 is likely due to the poisoning of surface active sites by $^{*}CO$ at low potentials and the favorable kinetics of partial oxidation pathway at high potentials.[74, 94] Bimetallic catalysts such as Pt-Ru, Pt-Cu, Pt-Co, Pt-Pd and Pt-Sn have thus been investigated for the EGO.[142, 151-154] In particular, Sn has attracted intensive attention for the sake of enhancing the adsorption of $^{*}OH$ and thereby the oxidative removal of $^{*}CO$.[79, 96] It has been reported that Pt-Sn bimetallic electrocatalysts could moderately enhance the selectivity of EGO toward CO_2,[155] but contrary results are also present in the literature[142]. The exact role of tin in the bimetallic Pt-Sn electrocatalysts remains largely elusive for the EGO.

Here we report a comprehensive electrocatalytic study of EGO on Pt_3Sn alloy nanoparticles. We have recently developed an organic solution method to synthesize

monodisperse and homogeneous Pt_3Sn alloy nanoparticles.[156] We examined the electrochemical properties of the derived Pt_3Sn/C catalysts and compared their electrocatalytic performance for the EGO with Pt/C. In particular, catalytic selectivity toward CO_2 was evaluated under potentiostatic conditions in a H-type cell equipped with a gas chromatography-mass spectrometer (GC-MS). Alkaline treatment was also applied to the alloy catalyst to remove surface tin (oxide) species, and comparative study of the pristine and treated catalysts has allowed us to reveal the role of tin in the EGO electrocatalysis.

3.2 Experimental Methods

Materials. perchloric acid (70%, 99.999% trace metal basis from Sigma), oleylamine (70%, Sigma), oleic acid (90%, Aldrich), platinum tetrachloride (Acros Organic), tin(II) chloride (Strem Chemicals), borane tert-butylamine complex (Sigma), Pt/C (Tanaka Inc.) were purchased and used as received.

Synthesis. Sphere-like Pt_3Sn nanoparticles were synthesized in organic solvent. Briefly, 9 ml of oleylamine and 0.4 ml of oleic acid were mixed in a round bottom flask and heated to 140 °C. The solution was then evacuated for 10 minutes before purged with Ar for another 10 minutes. The evacuation and Ar flow were repeated twice before cooling down to 50 °C. Then a mixture of 0.3 mmol $PtCl_4$, 0.1 mmol $SnCl_2$ and 0.5 ml ethanol was injected. After stirring at 50 °C for 10 minutes, the solution was heated to 120 °C at which temperature 300 mg borane tert-butylamine complex dissolved in 2 ml oleylamine was quickly injected. The dark brown solution was kept at 120 °C for 20 minutes and cooled down to room temperature. The product was acquired by adding ethanol and centrifuging at 4,000 rpm for 5 minutes. The sediment was dispersed in

toluene again and added ethanol for centrifugation one more time. The final product was dispersed in toluene.

The synthesized Pt_3Sn nanoparticles were mixed with carbon black (KETJENBLAC, >900 m^2/g) in a roughly 2:1 mass ratio and dispersed in toluene. The suspension was ultrasonicated for 30 minutes and centrifuged at 10,000 rpm for 5 minutes. Sediment were dispersed in hexane again by sonication and precipitated again by centrifugation at 6,000 rpm for 3 minutes. The collected black solid was then annealed at 185 °C in air for overnight. Pt loading in catalyst was determined via Inductively Coupled Plasma-Mass Spectrometry (ICP-MS).

Characterization. FEI Tecnai 12 microscope operated at 100 kV was used to acquire Transmission Electron Microscopy (TEM) images. X-ray diffraction (XRD) were conducted with a PANalytical X'Pert^3 Powder X-Ray Diffractometer equipped with a Cu Kα radiation source (λ=0.15406). X-ray Photoelectron Spectroscopy (XPS) measurements were conducted on a PHI 5600 Multi-technique photoelectron spectrometer using a Mg Kα X-ray source. Inductively Coupled Plasma Mass Spectrometry (ICP-MS) was measured with a PerkinElmer Elan DRC II Quadrupole.

Electrochemical studies. Electrochemical studies were conducted with a Metrohm PGSTAT302N potentiostat. A 5 mm diameter glassy carbon rotating disk electrode was used as the working electrode, Ag/AgCl and Pt was implemented as reference and counter electrode. Both Pt_3Sn/C and Pt/C catalysts were dispersed in aqueous solution contain 10% iso-propanol and 0.025 % Nafion with concentration of 1 mg/ml. The mixtures were ultrasonicated for about 30 minutes to form uniform ink. Typically, 20 ul of the above ink was dropped onto the glassy carbon surface and was dried in air. Cyclic

voltammograms (CVs) and EGO polarization curves were conducted at a scanning rate of 50 mV/s. Chronoamperometry was held at each potential for 30 minutes. The transient signals during the first two seconds were discarded in average amperometric currents calculations. All specific currents were normalized by mass of Pt determined by ICP.

Product-resolved electrochemical studies were conducted in an air-tight cell reported by our group.[114] 1-2 ml of catalyst ink mentioned in previous section was deposited onto a 2x2 cm^2 glassy carbon disk to be used as the working electrode. Helium was purged into the anodic compartment at a rate of 10 sccm in order to induce produced gas phase products into the sampling valve of GC-MS, which is a GCMS-QP2010SE (Shimadzu) equipped with a Plot-Q column (Restek). Each potential was held for 30 minutes.

3.3 Results and Discussion

Figure 3.3.1a shows a representative TEM image of the Pt_3Sn nanoparticles (also see Figure 3.3.2 for high-resolution TEM images). They have a sphere-like shape and an average diameter of ~6 nm. After supporting on carbon black, the organic surfactants were removed by annealing in air at 185 ^oC.[112] The derived Pt_3Sn/C catalyst possess uniform distribution of nanoparticles on the carbon support (Figure 3.3.1b). X-ray diffraction (XRD) analysis show that the derived Pt_3Sn/C catalyst possesses a face-centered cubic (fcc) crystal structure, which is consistent with the commercial Pt/C used in this study (Figures 3.3.1c and d). Figures 3.3.1e and f show the XPS spectra recorded at the Sn 3d and Pt 4f edges, respectively, for the Pt_3Sn/C catalyst. Pt_3Sn/C exhibits Sn $3d_{3/2}$ and $3d_{5/2}$ peaks at 495.1 eV and 486.7 eV, respectively, as compared to 493.4 eV and 484.9 eV for Sn metal, indicating the oxidation of surface tin species during the catalyst preparation. The peak positions for Pt $4f_{5/2}$ and $4f_{7/2}$ are more consistent between

Pt_3Sn/C and metallic Pt, and the lower extent of surface oxidation is expected for Pt as a noble metal. The surface composition estimated from the XPS spectra gives an atomic ratio of Pt/Sn ~ 4.2, which is close to the overall composition (3.04) measured from ICP.

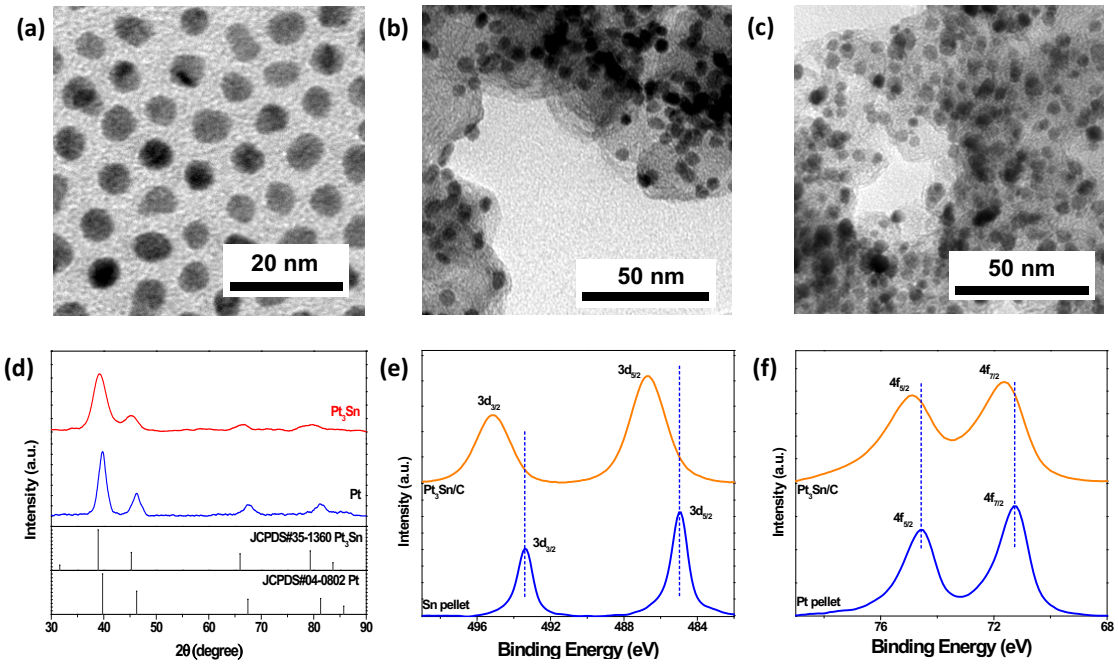

Figure 3.3.1. TEM images of (a) Pt_3Sn nanoparticles, (b) Pt_3Sn/C catalyst and (c) commercial Pt/C catalyst. (d) XRD pattern. (e) Sn 3d edge and (f) Pt 4f edge XPS spectra of Pt_3Sn/C catalyst.

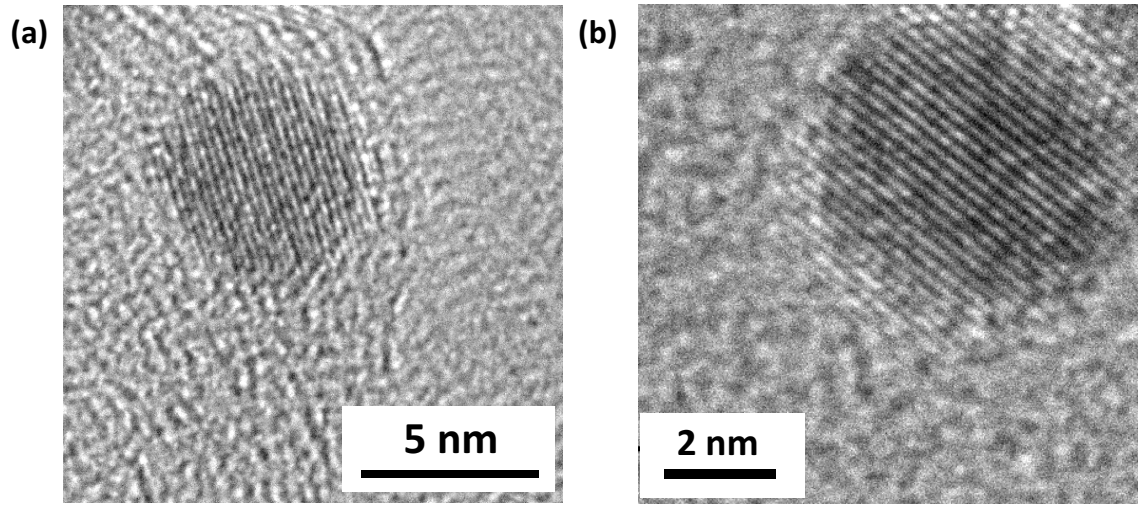

Figure 3.3.2. HRTEM images of Pt_3Sn.

Cyclic voltammograms (CVs) and CO stripping patterns were recorded on the Pt_3Sn/C catalyst in 0.1 M of $HClO_4$ (Figure 3.3.3a). Compared to Pt/C, Pt_3Sn/C exhibits significantly suppressed H_{upd} peaks at E < 0.4 V. The hydroxide adsorption peak of Pt_3Sn/C has a much lower onset potential than Pt/C, namely downshift from ~0.7 V to ~0.5 V. These features can be attributed to the weakened binding of hydrogen and enhanced adsorption of *OH on Pt due to the modification of surface property by tin. The CO stripping pattern recorded for Pt_3Sn/C exhibits two peaks at 0.45 V and 0.71 V, whereas Pt/C only shows one primary peak at 0.85 V. The lower peak potentials indicates that the oxidative removal of *CO is more facile on the bimetallic catalyst as compared to monometallic Pt, and the presence of two peaks could be attributed to two types of Pt sites, e.g. close to and far away from tin, or simply different crystal facets of the alloy nanoparticles. Noticeably, the calculated CO stripping charge for Pt_3Sn/C is about 63% of that for Pt/C (128 C/g_{Pt} vs 202 C/g_{Pt}), albeit that the H_{upd} charge of Pt_3Sn/C is 14 times smaller (6.5 C/g_{Pt} vs 91.8 C/g_{Pt}) (see Figure 3.3.4). While it is known that CO stripping can access more Pt sites then H_{upd} on Pt-bimetallic electrocatalysts,[17, 157] the results here

do indicate that the surface coverage of tin oxide is not significant on the Pt_3Sn/C catalyst, distinguishing it from the previously reported Pt-tin oxide core-shell nanostructures.[96]

According to the charges associated with CO stripping, the electrochemically active surface areas (ECSAs) of Pt_3Sn/C and Pt/C were estimated to be 30.4 and 48.2 m^2/g_{Pt}, respectively, by assuming an area-specific charge density of 420 $\mu C/cm^2$. It should be pointed out that debates are still present in the literature about this conversion factor, and accurate measurement of the ECSAs could be even more challenging for the Pt-Sn bimetallic electrocatalysts owing to the presence of both tin oxide on the surface and metallic tin in the subsurface.[17, 157-161] For simplicity, we will focus on mass-specific activities in the following discussion, while present the ECSA-specific results in the Supporting Information.

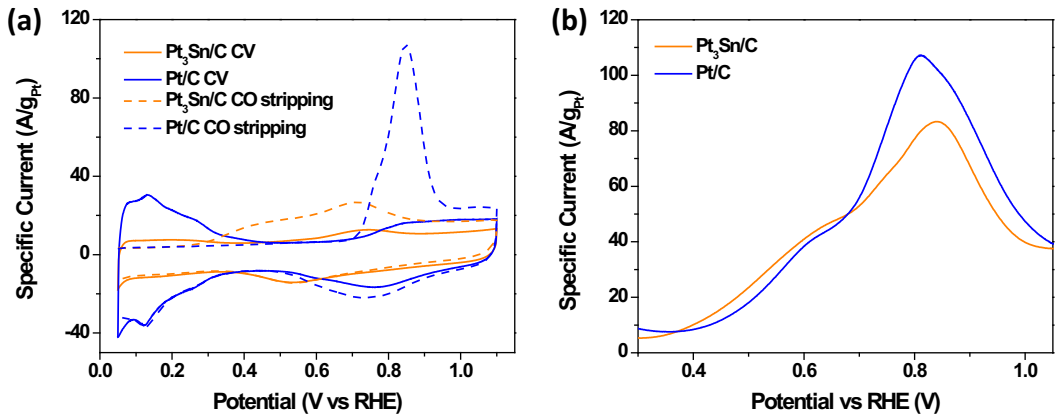

Figure 3.3.3. (a) CV and CO stripping pattern of Pt_3Sn/C and Pt/C in 0.1 M $HClO_4$. (b) polarization curve of Pt_3Sn/C and Pt/C in 0.1 M $HClO_4$ + 0.1 M ethylene glycol.

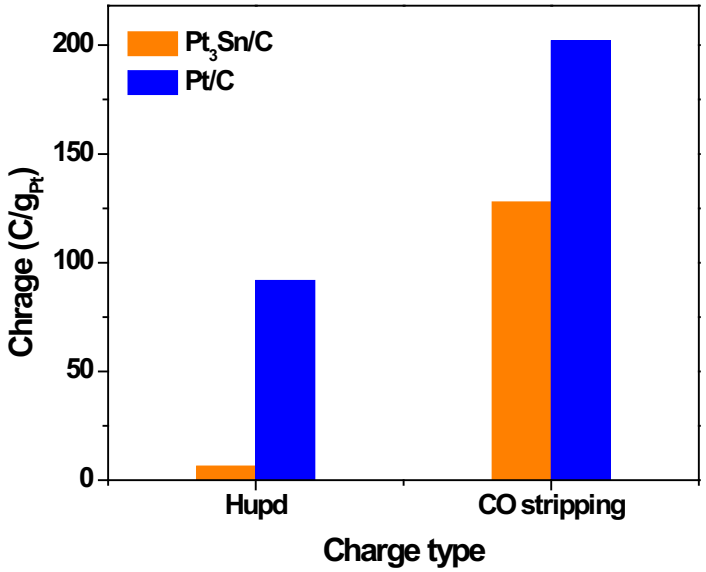

Figure 3.3.4. Comparison of H_{upd} charge and CO stripping charge of Pt_3Sn/C and Pt/C.

The polarization curves for EGO were recorded in the same electrolyte (0.1 M of $HClO_4$) by adding 0.1 M of ethylene glycol (Figure 3.3.3b). Pt_3Sn/C exhibits onset potential at ca. 0.33 V, slightly lower than Pt/C (~0.38 V). Both Pt_3Sn/C and Pt/C possess a shoulder peak at 0.5 – 0.7 V, with similar specific currents of ~40 A/g_{Pt} at 0.6 V. Both catalysts give a major peak at 0.8 – 0.85 V, with the peak currents read to be 83 and 107 A/g_{Pt} for Pt_3Sn/C and Pt/C, respectively. The rather similar catalytic activities of Pt_3Sn/C and Pt/C for the EGO is in contrary to the quite dissimilar behaviors shown in the blank CVs and CO stripping (Figure 3.3.3a), which is also distinct from the electro-oxidation of ethanol.[96, 116, 129, 162] While such divergences can be attributed to the different reaction mechanisms, they also suggest that the role of tin species in the Pt_3Sn electrocatalyst may vary in the electro-oxidation of *CO, ethanol and ethylene glycol.[95, 163-165]

Despite having similar catalytic activities to Pt/C, Pt_3Sn/C is much more selective for the EGO toward CO_2. Under potentiostatic conditions, CO_2 was detected at potentials

as low as 0.45 V for Pt_3Sn/C, with the maximal FE_{CO2} of 28% reached at 0.55 V (Figure 3.3.5a). In comparison, no CO_2 was detected at 0.45 V for Pt/C and the value of FE_{CO2} is merely <1% at 0.55 V. At more positive potentials, the FE_{CO2} of Pt_3Sn/C drops, but yet comparable to that for Pt/C, e.g., both at about 10 – 11% toward CO_2 at 0.75 V. Figure 3.3.5b shows the comparison of partial current for CO_2 production (J_{CO2}). Pt_3Sn/C delivers 0.18 A/g_{Pt} for CO_2 production at 0.45 V, versus zero by Pt/C at this potential. At 0.55 V, J_{CO2} of Pt_3Sn/C reaches 0.24 A/g_{Pt}, which is about 20 times of that measured for Pt/C. J_{CO2} of Pt_3Sn/C does not increase substantially until 0.75 V, where it reaches 0.71 A/g_{Pt}. Noticeably, Pt/C has higher values of J_{CO2} at 0.65 V and more positive potentials, reaching the maximum of 1.1 A/g_{Pt} at 0.75 V.

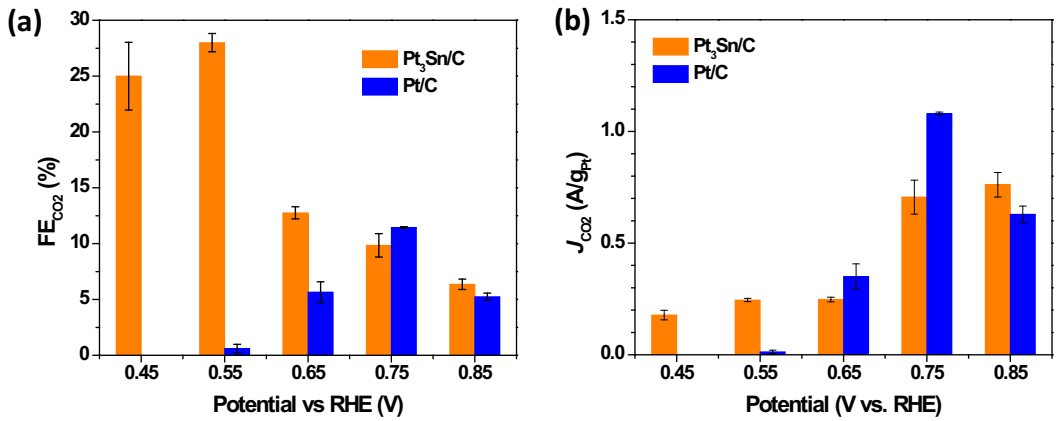

Figure 3.3.5. (a) CO_2 faradaic efficiency and (b) CO_2 partial current during product analysis in H-cell.

To examine the role of tin in the bimetallic electrocatalyst for the EGO, we have further performed control experiments to treat the Pt_3Sn/C catalyst in alkaline (0.1 M KOH). The alkaline treatment removed tin oxide (SnO_x) from the catalyst surface, as revealed by comparing the XPS spectra recorded before and after the treatment (Figures

3.3.6a and b). The Pt/Sn ratio estimated from XPS rise to 23.8, which is much higher than the overall composition (Pt/Sn ~ 4.3) measured by EDX, indicating the preservation of metallic Sn in the subsurface or bulk of the alloy nanoparticles. CVs recorded on the KOH-treated Pt_3Sn/C catalyst show expansion of the H_{upd} region and positive shift of the *OH onset potential, suggesting that the enhanced adsorption of *OH on the pristine Pt_3Sn/C is due to the SnO_x species present on the catalyst surface (Figure 3.3.6c). The features of CO stripping were however largely preserved on the KOH-treated catalyst, indicating that the facilitated oxidative removal of *CO on the pristine Pt_3Sn/C is due to subsurface metallic Sn (Figure 3.3.6d). In contrary to the behaviors in CO stripping, the KOH-treated catalyst has much lower selectivity toward CO_2 than the pristine one, with FE_{CO2} being no more than 3% (Figure 3.3.6e). It is noticed that the KOH-treated Pt_3Sn/C catalyst is even less selective for the complete oxidation of ethylene glycol than Pt/C (Figure 3.3.5a). The partial current for CO_2 production also dropped significantly after the KOH treatment, e.g., from 0.22 to 0.01 A/g_{Pt} at 0.55 V (Figure 3.3.6f).

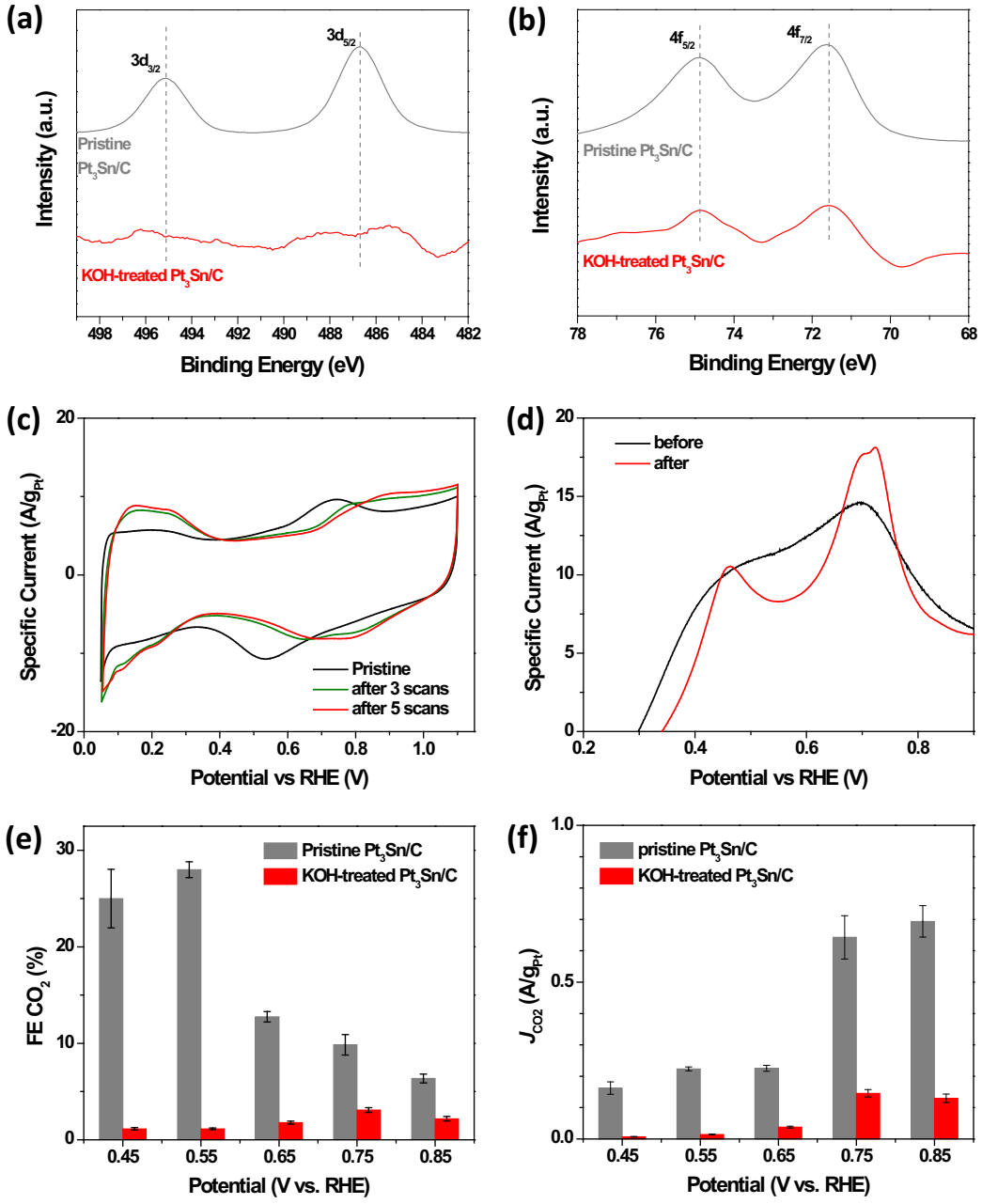

Figure 3.3.6. (a) Sn 3d edge and (b) Pt 4f edge XPS spectra of KOH-treated Pt_3Sn/C. (c) CV and (d) CO stripping (with CV signal subtracted) of Pt_3Sn/C before and after KOH-treatment. (e) CO_2 faradaic efficiency and (f) CO_2 partial current of KOH-treated Pt_3Sn/C during product analysis.

In a first glance, the enhanced CO_2 selectivity of the pristine Pt_3Sn/C in the low-potential region (0.45 – 0.65 V) is in line with the enhanced adsorption of *OH and facilitated oxidative removal of $^*CO$ (Figures 3.3.3a and 3.3.5a). One might thus assign the role of tin in the alloy catalyst to be relief of *CO poisoning during the EGO. However, our comparative studies of pristine and KOH-treated Pt_3Sn/C catalysts reveals a more sophisticated scenery. Although the metallic Sn present in the subsurface can facilitate the oxidative removal of *CO (Figure 3.3.6d), it does not promote the selectivity toward CO_2. The SnO_x present on the catalyst surface plays a more essential role than oxidizing *CO in enhancing the complete oxidation of ethylene glycol. Based on the reaction pathways reported by Schnaidt *et al.*,[145, 149-150] we propose a synergistic mechanism at the Pt-SnO_x interface for the EGO. Assuming $^*COCH_2OH$ is the intermediate for C-C bond cleavage, SnO_x could stabilize this adsorbate and reduce the energy barrier for its dissociation, possibly through binding to the β carbon via oxygen (by, for example, dehydration between the hydroxyl group and *OH on the SnO_x surface; see Figure 3.3.7). The alteration of single-site adsorption of $^*COCH_2OH$ on pure Pt surface to such a bidentate configuration, plus the facilitated oxidative removal of *CO by subsurface Sn (and/or surface SnO_x), give rise to the enhanced complete oxidation of ethylene glycol on the Pt_3Sn/C alloy catalyst than on Pt/C. Hereby we want to point out that the subsurface metallic Sn itself may weaken the adsorption of $^*COCH_2OH$, as this species binds to Pt via the carbonyl group that resembles the case of $^*CO$. Such an effect could make the desorption of 2-hydroxyacetyl more favorable and favor the partial oxidation pathways toward C_2 products such as glycolaldehyde, which can explain the lower CO_2 selectivity on the KOH-treated Pt3Sn/C catalyst than on Pt/C. Our work thus emphasizes the

importance of controlling the surface structures in developing advanced Pt-bimetallic electrocatalysts for selective oxidation of ethylene glycol and other multi-carbon alcohols.

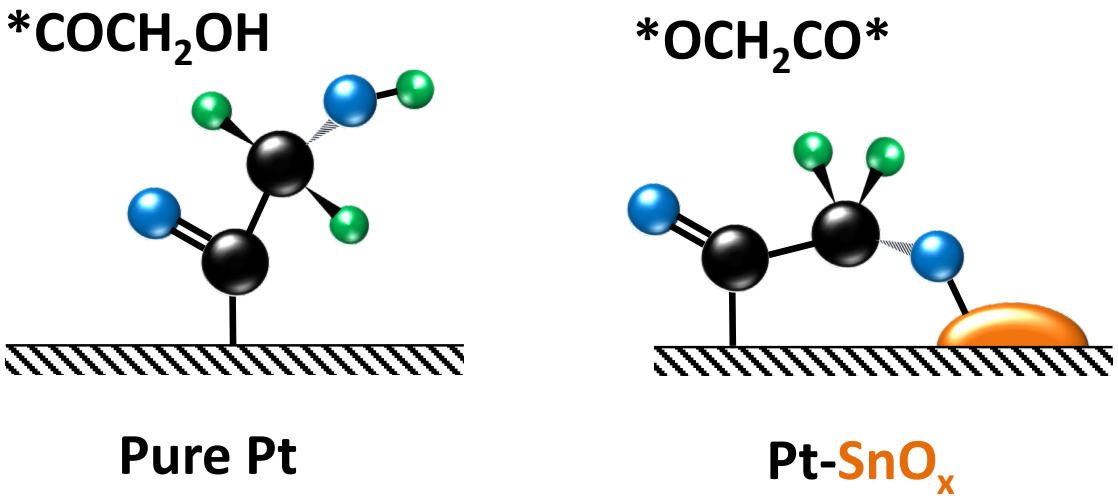

Figure 3.3.7. Hypothesized intermediate configuration on pure Pt and Pt-SnO_x interfaces.

3.4 Conclusion

Here we report on the electrocatalytic study of ethylene glycol oxidation (EGO) on monodisperse and homogeneous Pt_3Sn alloy nanoparticles. Catalytic activity and selectivity toward CO_2 were evaluated under potentiostatic conditions using a H-type cell equipped with a gas chromatography-mass spectrometer (GC-MS). An alkaline treatment was developed to remove surface tin (oxide) species from the alloy catalyst surface. By comparing the electrocatalytic performances of the pristine and treated Pt_3Sn catalysts, as well as commercial Pt/C, we were able to reveal the distinct roles of surface tin oxide and subsurface metallic tin species in the bimetallic electrocatalyst for complete oxidation of ethylene glycol: the former enhances the cleavage of C-C bond and the later felicitates the oxidative removal of $^*CO$ oxidative.

Chapter 4. Surface Modification of Sphere-like Pt3Sn Nanoparticles during Alcohol Electro-oxidation

4.1 Introduction

We have reported the surface property, alcohol electro-oxidation activity and selectivity of sphere-like Pt_3Sn/C. They exhibited significantly superior activity and CO_2 selectivity compared to Pt/C during both Ethanol Oxidation Reaction (EOR) and Ethylene Glycol Oxidation (EGO). The Sn species in Pt_3Sn/C exhibited dual role for EOR and EGO: subsurface metallic Sn species facilitates *CO oxidation while surface SnO_x substantially enhance CO_2 selectivity. To the best of our knowledge, there has been no report on the change and modification of Pt3Sn/C surface property, which was discovered by us. The surface change and modification during alcohol electro-oxidation was investigated in detail and this behavior was correlated to CO_2 selectivity during alcohol electro-oxidation.

4.2 Experimental methods

Materials. perchloric acid (70%, 99.999% trace metal basis from Sigma), Oleylamine (70%, Sigma), oleic acid (90%, Aldrich), platinum tetrachloride (Acros Organic), tin(II) chloride (Strem Chemicals), borane tert-butylamine complex (Sigma), Pt/C (Tanaka Inc.) were purchased and used as received.

Synthesis. Sphere-like Pt_3Sn nanoparticles were synthesized in organic solvent. Briefly, 9 ml of oleylamine and 0.4 ml of oleic acid were mixed in a round bottom flask and heated to 140 °C. The solution was then evacuated for 10 minutes before purged with

Ar for another 10 minutes. The evacuation and Ar flow were repeated twice before cooling down to 50 °C. Then a mixture of 0.3 mmol $PtCl_4$, 0.1 mmol $SnCl_2$ and 0.5 ml ethanol was injected. After stirring at 50 °C for 10 minutes, the solution was heated to 120 °C at which temperature 300 mg borane tert-butylamine complex dissolved in 2 ml oleylamine was quickly injected. The dark brown solution was kept at 120 °C for 20 minutes and cooled down to room temperature. The product was acquired by adding ethanol and centrifuging at 4,000 rpm for 5 minutes. The sediment was dispersed in toluene again and added ethanol for centrifugation one more time. The final product was dispersed in toluene.

The synthesized Pt_3Sn nanoparticles were mixed with carbon black (KETJENBLAC, >900 m^2/g) in a roughly 2:1 mass ratio and dispersed in toluene. The suspension was ultrasonicated for 30 minutes and centrifuged at 10,000 rpm for 5 minutes. Sediment were dispersed in hexane again by sonication and precipitated again by centrifugation at 6,000 rpm for 3 minutes. The collected black solid was then annealed at 185 °C in air for overnight. Pt loading in catalyst was determined via Inductively Coupled Plasma-Mass Spectrometry (ICP-MS).

Characterization. FEI Tecnai 12 microscope operated at 100 kV was used to acquire Transmission Electron Microscopy (TEM) images. X-ray diffraction (XRD) were conducted with a PANalytical X'Pert^3 Powder X-Ray Diffractometer equipped with a Cu Kα radiation source (λ=0.15406). X-ray Photoelectron Spectroscopy (XPS) measurements were conducted on a PHI 5600 Multi-technique photoelectron spectrometer using a Mg Kα X-ray source. Inductively Coupled Plasma Mass Spectrometry (ICP-MS) was measured with a PerkinElmer Elan DRC II Quadrupole.

Electrochemical studies. Electrochemical studies were conducted with a Metrohm PGSTAT302N potentiostat. A 5 mm diameter glassy carbon rotating disk electrode was used as the working electrode, Ag/AgCl and Pt was implemented as reference and counter electrode, and no Pt contamination is noted for the anodic reaction of ethanol. Both Pt_3Sn/C and Pt/C catalysts were dispersed in aqueous solution contain 10% iso-propanol and 0.025 % Nafion with concentration of 1 mg/ml. The mixtures were ultrasonicated for about 30 minutes to form uniform ink. Typically, 20 ul of above ink was dropped onto the glassy carbon surface and was dried in air. Cyclic voltammogram (CV) was conducted with a scan rate of 50 mV/s after about 10 cycles of scan for surface cleaning. Chronoamperometry was held at each potential for 30 minutes. The transient signals during the first two seconds were discarded in average amperometric currents calculations. All specific currents were normalized by mass of Pt determined by ICP.

4.3 Results and discussion

Figures 4.3.1a and b show the TEM images of as-synthesized Pt_3Sn nanoparticles and Pt_3Sn/C catalysts. As is written in Chapter 2, its crystal structure is face-centered cubic as revealed by XRD pattern in Figure 4.3.1c.

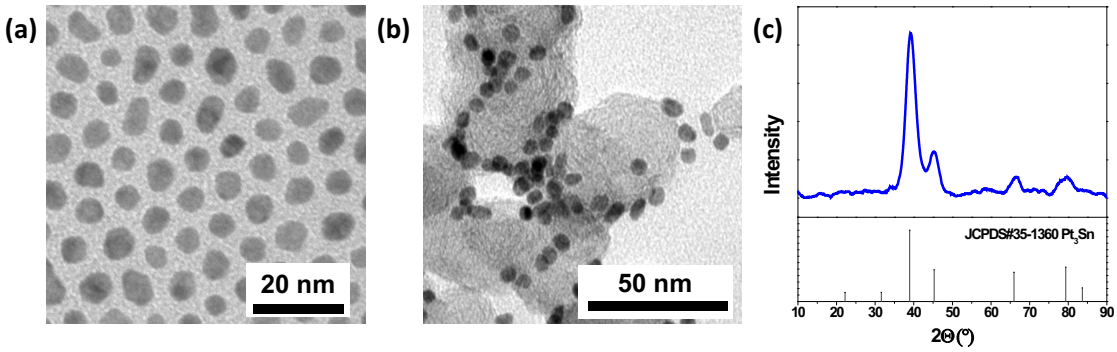

Figure 4.3.1. TEM images of (a) Pt_3Sn nanoparticles and (b) Pt_3Sn/C catalyst. (c) XRD pattern.

We observed change of CV and CO stripping pattern of sphere-like Pt_3Sn/C during scanning in 0.1 M $HClO_4$ + 0.1 M ethanol or 0.1 M $HClO_4$ + 0.1 M ethylene glycol. As is shown in Figure 4.3.2, CV exhibited increasing Hupd region and shrinking OH adsorption region when being scanned, and possessed CV extremely similar or identical to Pt/C after 20 scans. CO stripping pattern, however, still possessed two peaks at ~ 0.45 V and ~ 0.71 V, vs one peak at 0.85 V of Pt/C. The change process of CV and CO stripping pattern was similar in both ethanol oxidation reaction (EOR) and ethylene glycol oxidation (EGO).

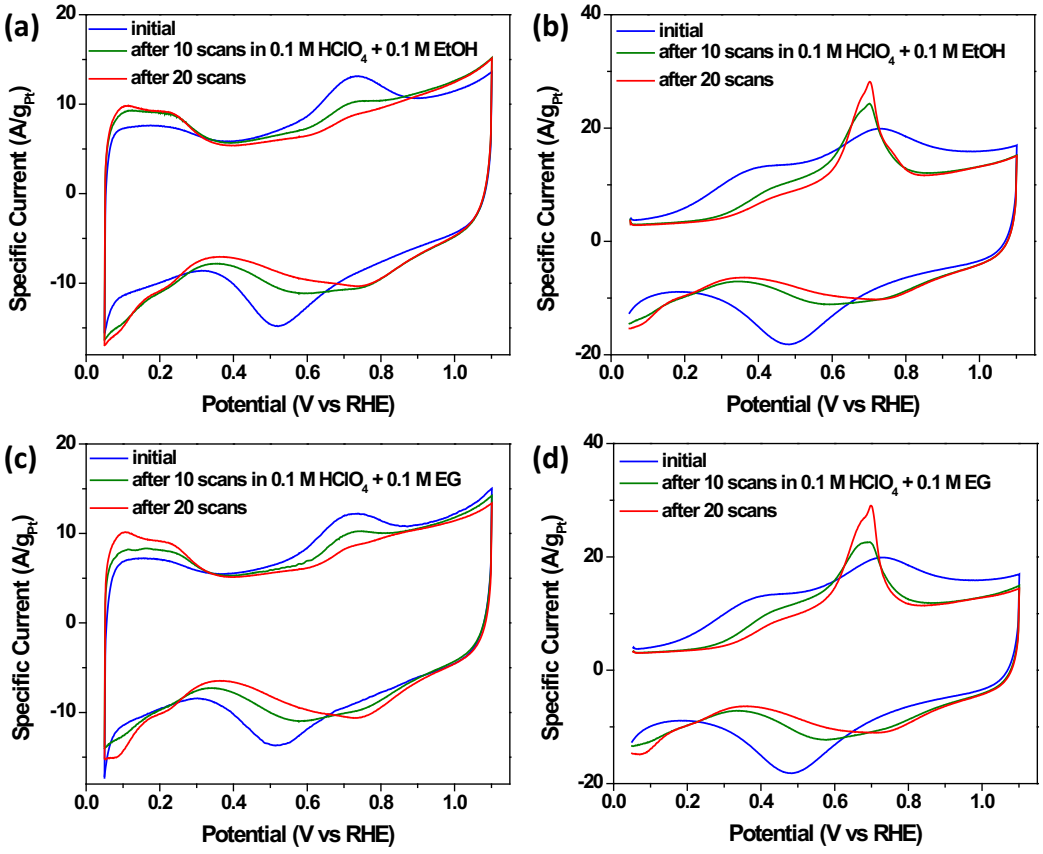

Figure 4.3.2. (a, c) CV and (b, d) CO stripping pattern of Pt_3Sn/C after certain cycles in 0.1 M $HClO_4$ + 0.1 M ethanol and 0.1 M $HClO_4$ + 0.1 M ethylene glycol respectively

Considering EOR and EGO would produce *CO adsorbed on Pt_3Sn/C surface, it is natural to attribute the change of surface to outward migration of Pt atoms due to *CO, which was observed previously on Pt-Co binary alloy nanoparticles.[166] However, our comparative study of scanning Pt_3Sn/C in argon and CO saturated 0.1 M $HClO_4$ did not support this hypothesis. As is shown in Figure 4.3.3, the CV and CO stripping exhibited identical pattern change when being scanned in argon and CO saturated 0.1 M $HClO_4$, which indicates negligible role played by *CO.

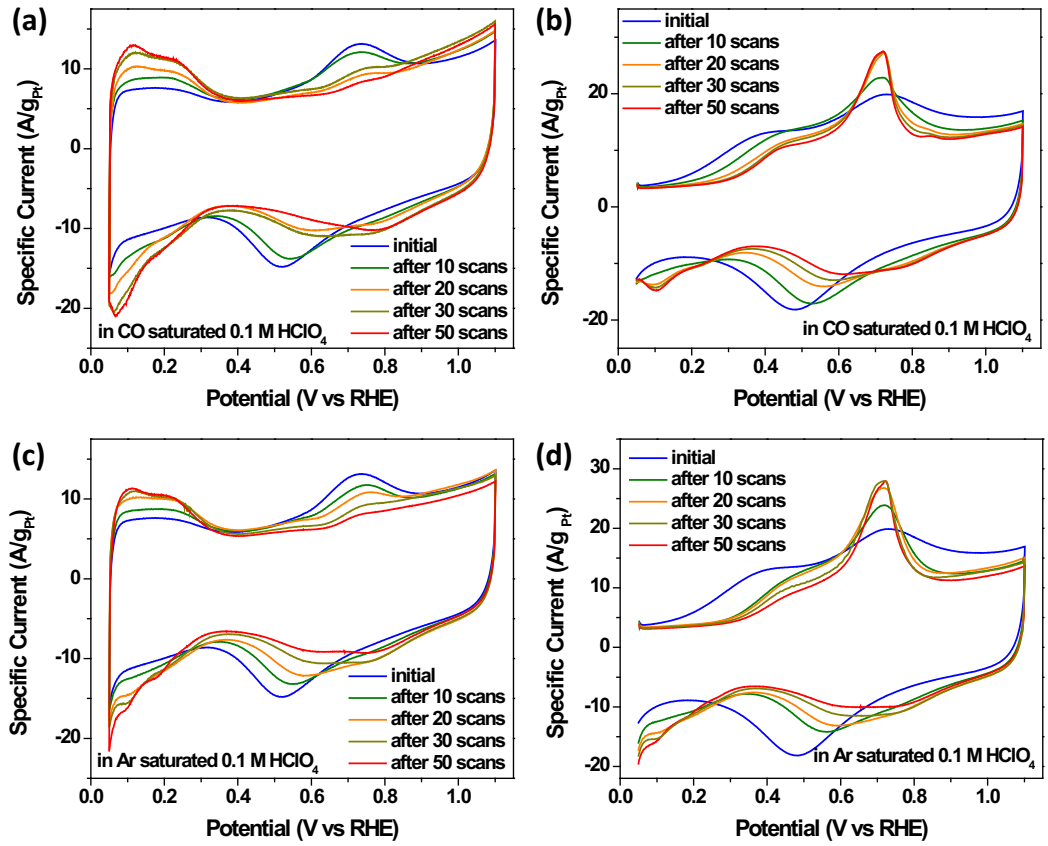

Figure 4.3.3. (a, c) CV and (b, d) CO stripping pattern of Pt_3Sn/C after certain cycles in carbon monoxide or argon saturated 0.1 M $HClO_4$

In order to quantify Pt occupation on surface, Hupd area of Pt_3Sn/C were integrated and compared to its final CV. The percentage of Hupd area was considered as electrochemical surface occupation and presented in Figure 4.3.4a. Pt surface occupation reaches 100 % when being scanned 20 cycles with ethanol or ethylene glycol in electrolyte, versus 50 cycles when scanned in electrolyte free of ethanol or ethylene glycol. This indicates that while surface SnO_x dissolution in $HClO_4$ slowly contributes to surface change of Pt_3Sn, existence of ethanol or ethylene glycol could expedite the surface SnO_x dissolution process, likely via $*OCH_2CH_2*$ or $*OCH_2CO*$ intermediates (see Figures 4.3.4b and 4.3.4c). Despite the significant change of CV pattern, total Pt:Sn ratio did not exhibit noticeable change after various scanning procedures (Figure 4.3.4d), which is distinct from the case of KOH treatment (see Chapter 2 and 3) and agrees well with higher stability of Sn in acidic environment.

We conducted surface property investigation of Pt_3Sn/C catalyst during EOR and EGO selectivity test. Figure 4.3.5 summarizes CV and CO stripping pattern of Pt_3Sn/C catalyst after each potential. CV pattern exhibited gradually revealing Hupd peak and suppressed OH adsorption peak. As is shown in Figure 4.3.5e, the surface Pt occupation slowly increases as potential increase and went above 60 % after 0.65 V. We hypothesize the surface Pt occupation of Pt_3Sn/C catalyst are correlated to CO_2 selectivity: Pt occupation below 0.55 V is low, representing a distinctly different surface property from Pt and resulted in substantially higher CO_2 selectivity in both EOR and EGO. Whereas surface property became similar to Pt beyond 0.65 V and CO_2 selectivity was similar to that of Pt/C.

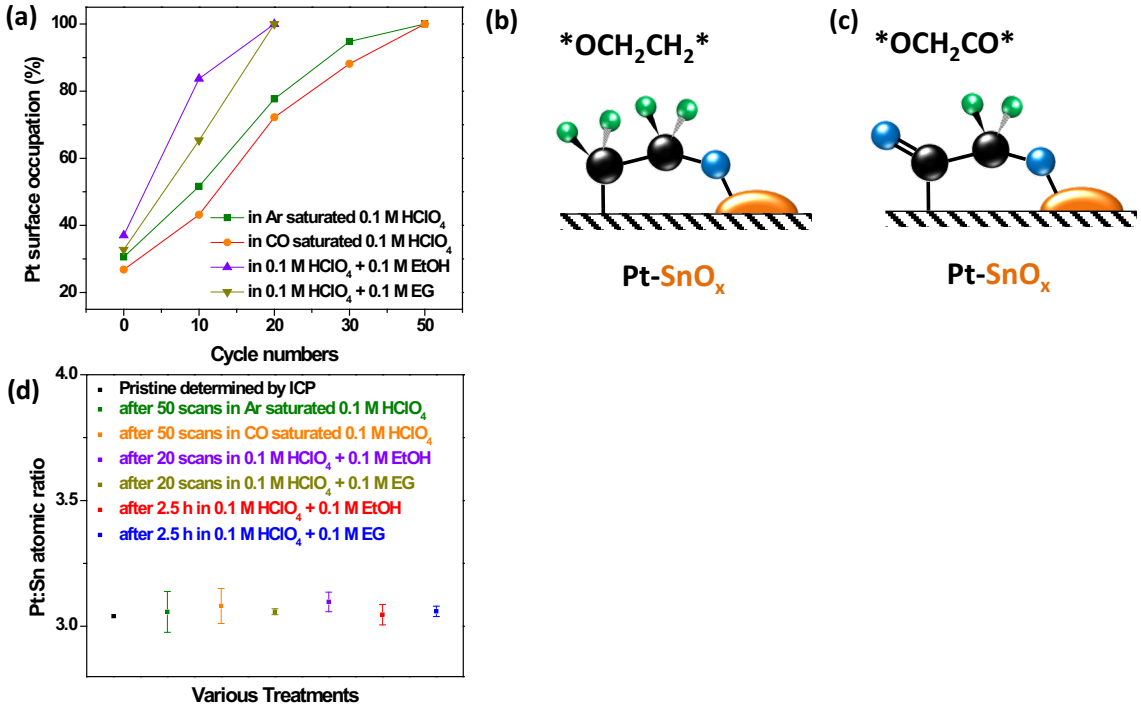

Figure 4.3.4. (a) Pt surface occupation calculated from Hupd peak area. (b, c) hypothesized mechanism for expedited surface SnO_x dissolution of ethanol and ethylene glycol. (d) Pt:Sn atomic ratio after various treatment determined by EDX.

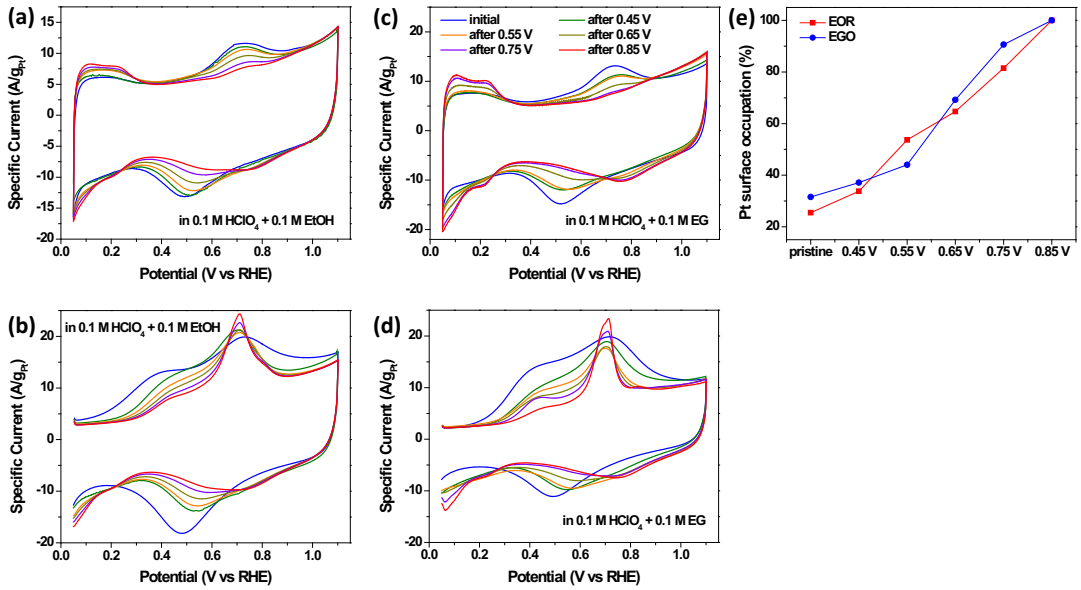

Figure 4.3.5. (a, c) CV, (b, d) CO stripping pattern change and (e) Pt surface occupation after 30 minutes chrono-amperometric EOR and EGO at various potentials

4.4 Conclusion

We have investigated in detail the change of surface property via CV and CO stripping. The surface change of Pt_3Sn/C in acidic electrolyte is inevitable due to slow dissolution of surface SnO_x species. We quantified the surface Pt occupation via Hupd peak area and hypothesize that the CO_2 selectivity might be correlated to electrochemical surface Pt occupation.

Chapter 5. Electro-oxidation of Ethanol and Ethylene Glycol with Cubic Pt_3Sn/C

5.1 Introduction

The previous chapters had investigated the alcohol electro-oxidation behavior of sphere-like Pt_3Sn/C in detail. In this chapter, cubic shaped Pt_3Sn nanoparticles synthesized following reported method were investigated for its activity and selectivity for electro-oxidation of ethanol and ethylene glycol. The surface terrace Pt sites on these Pt_3Sn/C were correlated to the catalytic behavior toward EOR and EGO.

5.2 Experimental Methods

Materials. 1-octadecene (90%, Alfa Aesar), dodecylamine (98%, Acros Organic), 1,2-hexadecanediol (90%, Aldrich), perchloric acid (70%, 99.999% trace metal basis from Sigma), Oleylamine (70%, Sigma), oleic acid (90%, Aldrich), platinum tetrachloride (Acros Organic), tin(II) chloride (Strem Chemicals), borane tert-butylamine complex (Sigma), Pt/C (Tanaka Inc.) were purchased and used as received.

Synthesis. Sphere-like Pt_3Sn nanoparticles were synthesized in organic solvent. Briefly, 9 ml of oleylamine and 0.4 ml of oleic acid were mixed in a round bottom flask and heated to 140 °C. The solution was then evacuated for 10 minutes before purged with Ar for another 10 minutes. The evacuation and Ar flow were repeated twice before cooling down to 50 °C. Then 101 mg $PtCl_4$ and 19 mg $SnCl_2$ dissolved in 0.5 ml ethanol was injected into solution. After stirring under argon flow at 50 °C for 10 minutes, the solution was heated up to 120 °C where 300 mg of borane tert-butylamine complex dissolved in 2 ml of oleylamine was quickly injected. The dark brown solution was kept

at 120 °C for 20 minutes and cooled down to room temperature. The product was acquired by adding ethanol and centrifuging at 4,000 rpm for 5 minutes. The sediment was dispersed in toluene again and added ethanol for centrifugation one more time. The final product was dispersed in toluene.

15nm Pt_3Sn nanoparticles are synthesized following a slightly modified reported method[46]. In short, 6ml of 1-octadecene, 560mg of dodecylamine and 200mg of 1,2-hexadecanediol was heated to 300 °C under inert atmosphere. A mixture of 0.025mmol $PtCl_4$, 0.01mmol $SnCl_2$, 0.5ml iso-propanol and 1.5ml of 1-octadecene was slowly injected into the solution at 300 °C. After injection the solution was kept at 300 °C for another 10 minutes before cooling down to room temperature. The nanoparticles were precipitated by adding iso-propanol and centrifuge at 4,000 rpm for 5 minutes. After the sediment was dispersed in toluene, it was centrifuged again with ethanol at 4,000 rpm for 5 minutes. Final product was dispersed in toluene for storage further usage.

The synthesized Pt_3Sn nanoparticles were mixed with carbon black (KETJENBLAC, >900 m^2/g) in a roughly 2:1 mass ratio and dispersed in toluene. The suspension was ultrasonicated for 30 minutes and centrifuged at 10,000 rpm for 5 minutes. Sediment were dispersed in hexane again by sonication and precipitated again by centrifugation at 6,000 rpm for 3 minutes. The collected black solid was then annealed at 185 °C in air for overnight. Pt loading in catalyst was determined via Inductively Coupled Plasma-Mass Spectrometry (ICP-MS).

Characterization. FEI Tecnai 12 microscope operated at 100 kV was used to acquire Transmission Electron Microscopy (TEM) images. X-ray diffraction (XRD) were conducted with a PANalytical X'Pert^3 Powder X-Ray Diffractometer equipped with a Cu

Kα radiation source (λ=0.15406). X-ray Photoelectron Spectroscopy (XPS) measurements were conducted on a PHI 5600 Multi-technique photoelectron spectrometer using a Mg Kα X-ray source. Inductively Coupled Plasma Mass Spectrometry (ICP-MS) was measured with a PerkinElmer Elan DRC II Quadrupole.

Electrochemical studies. Electrochemical studies were conducted with a Metrohm PGSTAT302N potentiostat. A 5 mm diameter glassy carbon rotating disk electrode was used as the working electrode, Ag/AgCl and Pt was implemented as reference and counter electrode, and no Pt contamination is noted for the anodic reaction of ethanol. Both Pt_3Sn/C and Pt/C catalysts were dispersed in aqueous solution contain 10% iso-propanol and 0.025 % Nafion with concentration of 1 mg/ml. The mixtures were ultrasonicated for about 30 minutes to form uniform ink. Typically, 20 ul of above ink was dropped onto the glassy carbon surface and was dried in air. Cyclic voltammogram (CV) was conducted with a scan rate of 50 mV/s after about 10 cycles of scan for surface cleaning. Chronoamperometry was held at each potential for 30 minutes. The transient signals during the first two seconds were discarded in average amperometric currents calculations. All specific currents were normalized by mass of Pt determined by ICP.

5.3 Results and Discussion

Figures 5.3.1a and 5.3.1b show the TEM images of as-synthesized Pt_3Sn nanocubes and Pt_3Sn/C catalysts. They possess face-centered cubic structure of intermetallic Pt_3Sn as revealed by XRD pattern in Figure 5.3.1c. Above characterization results are consistent with reported data by Wang et al.[46] The as-synthesized Pt_3Sn nanocubes were loaded on high surface area carbon and treated under mild thermal condition to remove surface organic surfactants.[112] The surface Pt species were slightly oxidized after treatment, as

indicated by XPS spectra of cubic Pt_3Sn/C catalyst---Cubic Pt_3Sn/C possessed Pt 4f peaks at 71.5 eV and 74.7 eV for $4f_{7/2}$ and $4f_{5/2}$ versus 71.2 eV and 74.5 eV of metallic Pt pellet. While for Sn edge spectra, cubic Pt_3Sn/C possessed Sn 3d peaks at 486.4 eV and 494.8 eV for $3d_{5/2}$ and $3d_{3/2}$ respectively vs 485.0 eV and 493.4 eV of Sn pellet, which indicates Sn species on the surface of cubic Pt_3Sn/C are mostly oxidized.

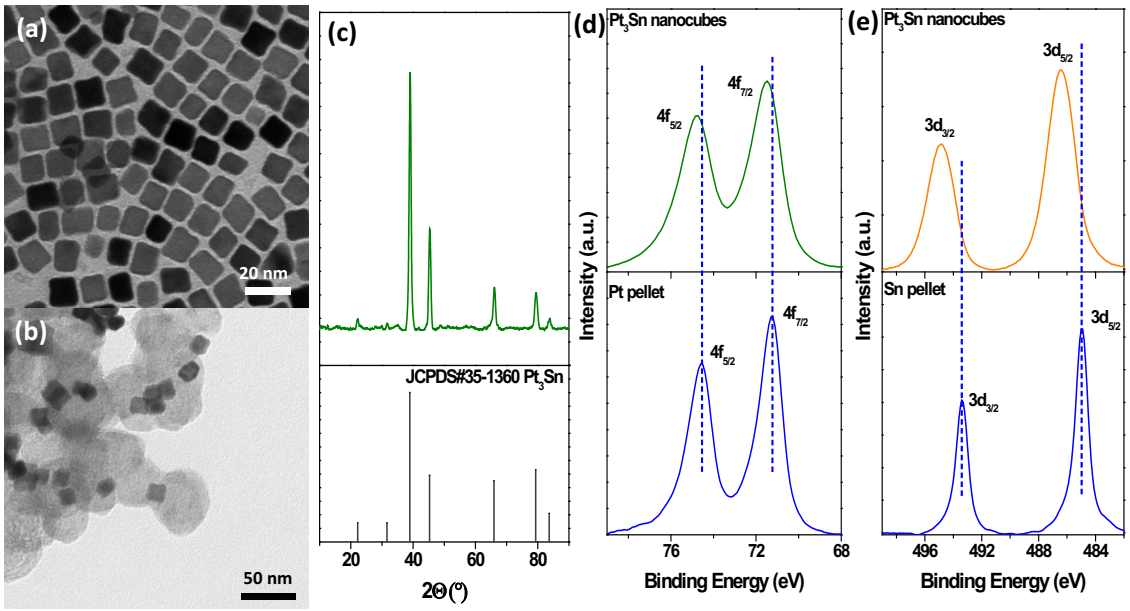

Figure 5.3.1. TEM images of (a) as-synthesized cubic Pt_3Sn and (b) cubic Pt_3Sn/C. (c) XRD pattern. (d) Pt edge and (e) Sn edge of cubic Pt_3Sn/C XPS spectra.

The acquired cubic Pt_3Sn/C catalyst were loaded on rotating disk electrode and examined for their surface properties and EOR and EGO catalytic activities. Comparison was made between cubic and sphere-like Pt_3Sn/C (reported in Chapter 2 - 4) to reveal the correlation between surface facets and catalytic behavior. The electrochemical surface area (ECSA) of tested cubic and sphere-like Pt_3Sn/C was 2.02 cm^2 and 1.68 cm^2 calculated from CO stripping pattern, while ECSA calculated from Hupd 0.63 cm^2 and 0.21 cm^2 respectively. Considering CO could access more surface sites than H^+, CO

stripping charge is a more accurate method of evaluation ECSA. In addition, Hupd charge:CO stripping charge was 0.19 and 0.05 for cubic and sphere-like Pt_3Sn/C respectively. The drastic difference indicates cubic Pt_3Sn/C showed much less weakened proton binding energy compared to sphere-like Pt_3Sn/C. Calculation from XPS spectra show that cubic Pt_3Sn/C only showed slightly higher Pt:Sn atomic ratio than sphere-like Pt_3Sn/C (4.7 vs 4.2). Therefore the difference should be mostly ascribed to terrace Pt sites on surface.

Considering the difference sizes and shapes of two types of Pt_3Sn/C, current densities were normalized against ECSA rather than mass of Pt as calculated in previous chapters. Figure 5.3.2a shows the CV of cubic and sphere-like Pt_3Sn/C in 0.1 M $HClO_4$. When normalized by ECSA, cubic Pt_3Sn/C possess significantly larger Hupd and OH adsorption region area, which indicates terrace Pt sites on surface of cubic Pt_3Sn/C exhibit property more similar to Pt. This is consistent with CO stripping pattern, where both Pt_3Sn/C exhibited two peaks while cubic Pt_3Sn/C shows larger peak at higher potential, reaching 0.12 mA/cm^2_{ECSA} vs (0.09 mA/cm^2_{ECSA} of sphere-like Pt_3Sn/C). The cubic Pt_3Sn/C were further scanned in 0.1 M $HClO_4$ + 0.1 M EtOH and 0.1 M $HClO_4$ + 0.1 M EG for evaluation of EOR and EGO activity. For EOR, although reaching higher peak current density at ca. 0.83 V than sphere-like Pt_3Sn/C (0.5 mA/cm^2_{ECSA} vs 0.45 mA/cm^2_{ECSA}), cubic Pt_3Sn/C lack the oxidation feature in potential region 0.4 – 0.6 V. The situation was consistent during EGO, whereas cubic Pt_3Sn/C showed even slightly lower peak current at ca. 0.78 V (0.51 mA/cm^2_{ECSA} vs 0.53 mA/cm^2_{ECSA}) with no oxidation feature in low potential region. Above results indicate suppressed activity

toward EOR and EGO, which could be ascribed to terrace sites of (100) lack the capability of cleaving C-C bond.[76-77]

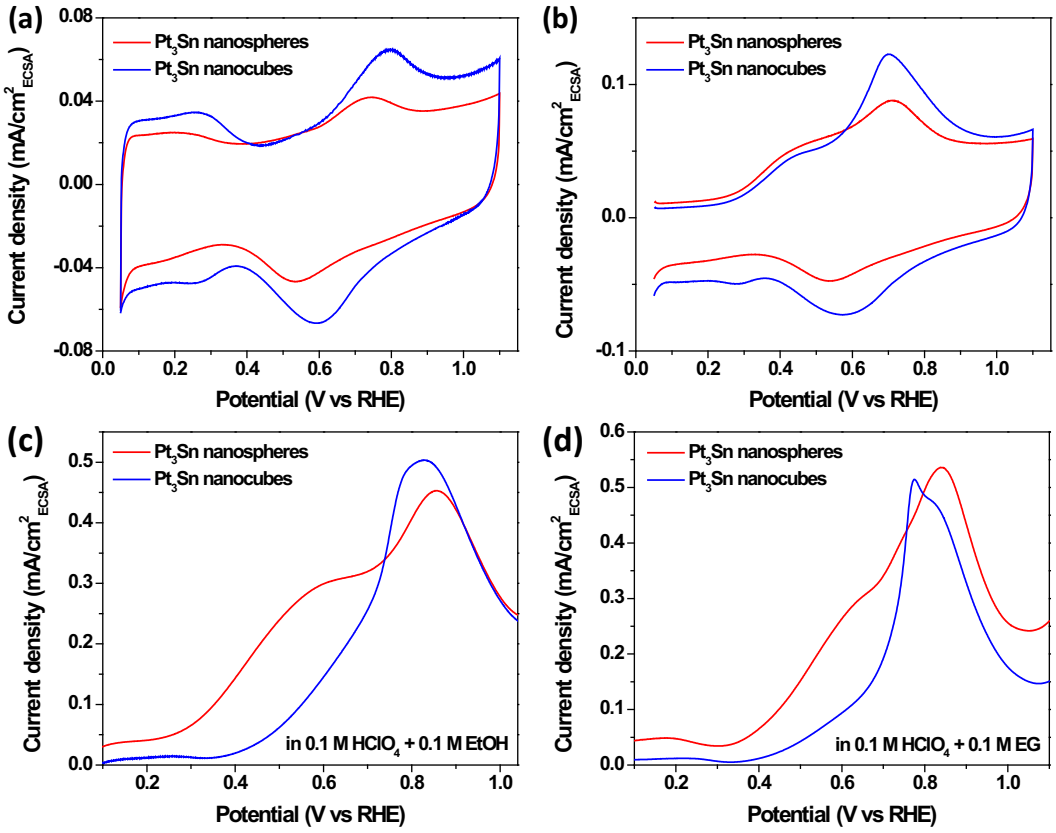

Figure 5.3.2. (a) CV and (b) CO stripping pattern of cubic Pt_3Sn/C and comparison with sphere-like Pt_3Sn/C in 0.1 M $HClO_4$. Polarization curve in 0.1 M $HClO_4$ + 0.1 M EtOH and 0.1 M $HClO_4$ + 0.1 M EG

Chronoamperometry tests were further carried out in 0.1 M $HClO_4$ + 0.1 M EtOH and 0.1 M $HClO_4$ + 0.1 M EG to evaluate EOR and EGO catalytic activity without double layer capacitance current. Cubic Pt_3Sn/C exhibited lower current density than sphere-like Pt_3Sn/C throughout potential region 0.45 V – 0.85 V for both EOR and EGO, as is shown in Figure 5.3.3. This is consistent with polarization curves in Figures 5.3.2c and 5.3.2d and confirms the lower activity of terrace Pt sites of Pt_3Sn.

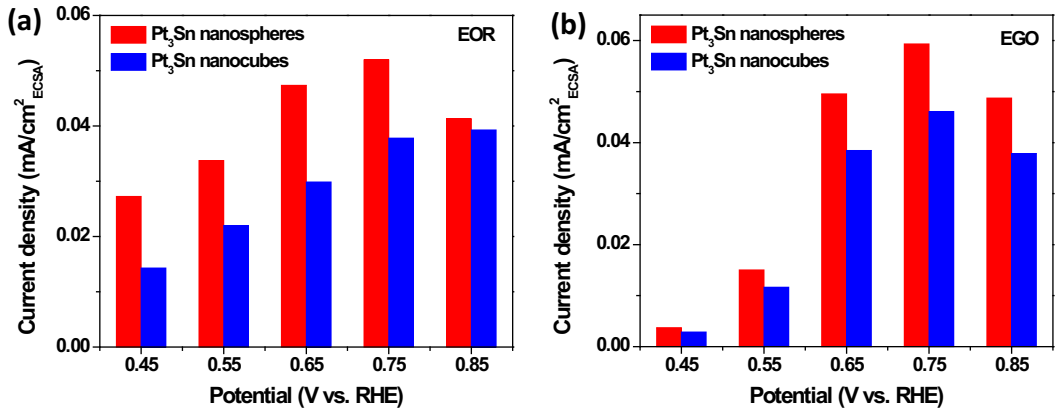

Figure 5.3.3. Average current density during 30 minutes chrono amperometry for (a) EOR and (b) EGO.

The CO_2 selectivity of cubic Pt_3Sn/C was examined in a novel H-type electrolysis cell. Cubic Pt_3Sn/C exhibited significantly lower selectivity toward CO_2 than sphere-like Pt_3Sn/C for both EOR and EGO (Figures 5.3.4a and 5.3.4b). The faradaic efficiency of CO_2 is below 3 % throughout the potential range of 0.45 V – 0.85 V for cubic Pt_3Sn/C during EOR and EGO, compared to 12 % and 27 % reached in EOR and EGO by sphere-like Pt_3Sn/C. The comparison between cubic and sphere-like Pt_3Sn/C is better visualized by CO_2 partial current (Figures 5.3.4c and 5.3.4d). Cubic Pt_3Sn/C exhibited CO_2 partial current 1/5 of sphere-like Pt_3Sn/C or lower.

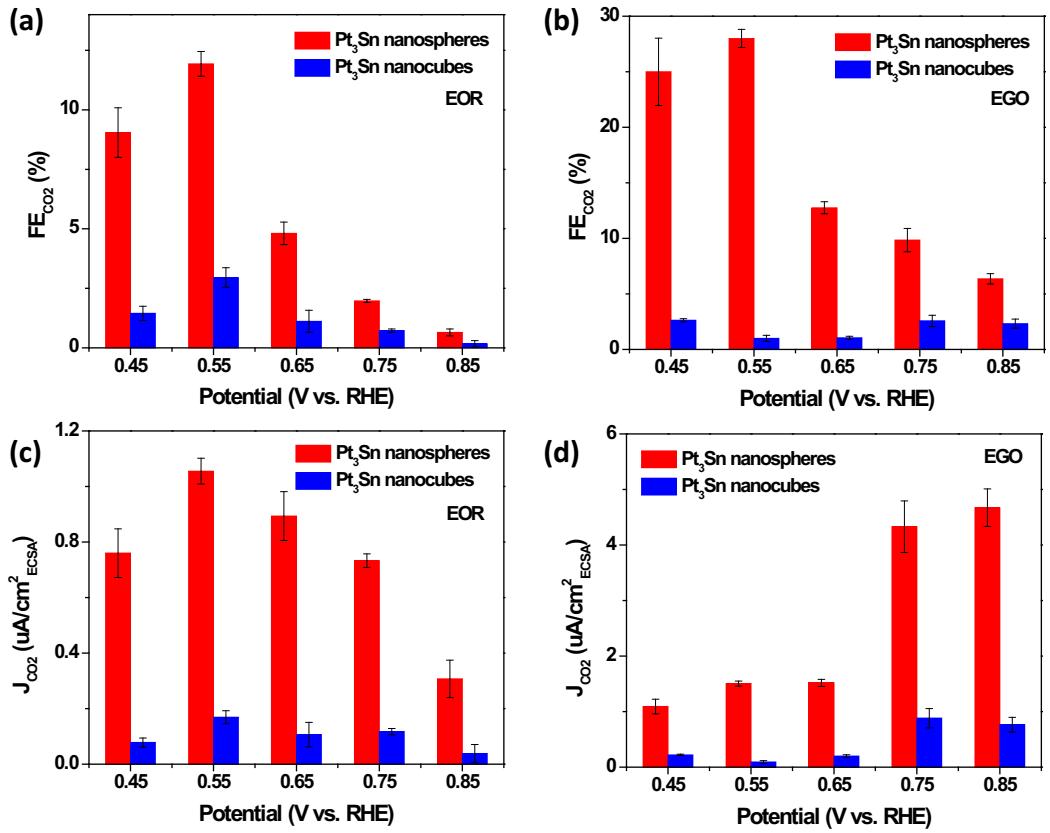

Figure 5.3.4. (a, b) carbon dioxide faradaic efficiency during EOR and EGO. (c, d) carbon dioxide partial current during EOR and EGO.

The lower selectivity toward CO_2 of cubic Pt_3Sn/C could likely be attributed to lack of C-C bond cleavage of terrace sites.[76] This postulation is further supported by selectivity toward acetic acid and methane (Figure 5.3.5). Cubic Pt_3Sn/C exhibited significantly higher acetic acid selectivity and lower methane signal compared to sphere-like Pt_3Sn/C, which indicates its lower capability of cleaving C-C bond.

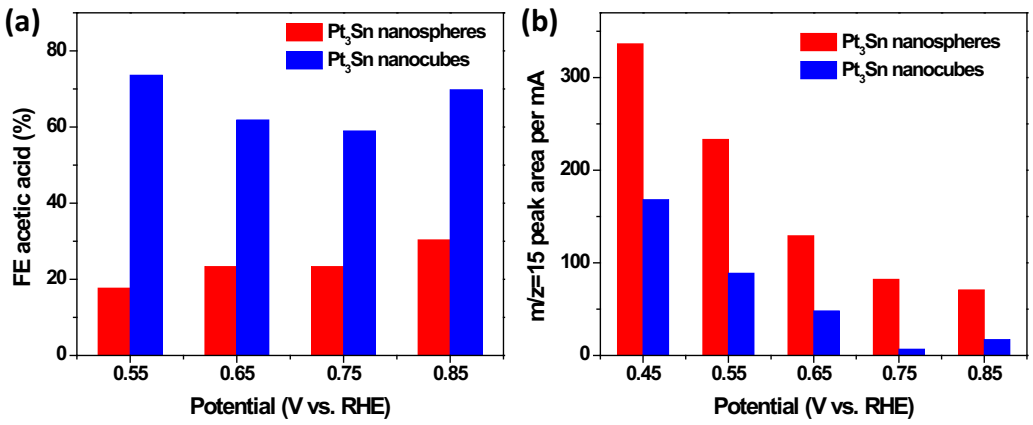

Figure 5.3.5. (a) acetic acid faradaic efficiency comparison. (b) methane signal detected by MS.

5.4 Conclusion

We have investigated the activity and selectivity of cubic Pt_3Sn/C during EOR and EGO. Compared to sphere-like Pt_3Sn/C, cubic shape catalysts exhibited slightly lower activity and CO_2 selectivity during both EOR and EGO. Our findings resembles the reported results that terrace Pt sites possess lower capability of cleaving C-C bond.

Chapter 6. Pt-SnOx heterodimer and Their Catalytic Behavior for Ethanol Electro-oxidation

6.1 Introduction

The benefits of Pt/Sn binary catalysts for alcohol electro-oxidation had been discussed in Chapter 2---Sn provide adsorbing sites for OH groups to assist with CO_{ads} and $CH_{x,ads}$ removal on Pt surface[96]. In Pt/Sn alloy catalysts, the tuning of composition and atomic structure had been proved to be difficult. For example, the amount of Sn that could be implemented is limited----too much Sn would decrease the amount of Pt ensemble on surface thus decrease total activity. Also, a significant portion of Sn might be buried in inner layers of catalyst, limiting the number of Pt-Sn(O_x) interface. As a matter of fact, in some reports Pt/Sn alloy catalyst exhibited minor or no enhancement for CO_2 selectivity[167-168]. Therefore non-alloy Pt-Sn(O_x) structure is interesting for researchers. Du et al. reported core shell structure with SnO_2 rich shell and Pt rich core and demonstrated their higher activity and CO_2 selectivity during EOR[96]. Jiang et al. synthesized non-alloy Pt/SnO_x with various Pt/Sn composition and confirmed their enhancement of EOR activity and CO_2 selectivity[129, 169]. Antolini et el. reported a complicated structure of $(PtSn)_{alloy}/SnO_2$ and demonstrated it superior catalytic activity in real DEFC[170]. Silva et al. constructed SnO_2@Pt core shell structure (with Pt shell) with enhanced EOR activity[171]. Above are the studies that claim Pt-Sn(O_x) non-alloy structure exhibit superior performance for alcohol electro-oxidation. There are also some reports claiming weaker performance of Pt-Sn(O_x) non-alloy structure compared to Pt/Sn alloy. For example, De Souza et al. reported that Pt_3Sn/C catalysts exhibit higher performance

than non-alloy PtSn/C catalyst in DEFC[118]. Godoi et al. investigated the EOR activity of Pt-Sn/C catalyst with various portion of alloy and found that higher alloy degree would result in higher EOR activity[172]. Silva et al. compared EOR activity and product selectivity of 92 % alloy and 6 % alloy Pt-Sn/C in another of their works and reported 92% alloy Pt-Sn/C exhibit higher EOR activity while 6 % alloy showed higher CO_2 selectivity[173]. It could be seen from above that non-alloyed Pt-Sn(O_x) catalysts showed various and controversial performance for alcohol electro-oxidation. In this chapter, various morphology of Pt-Sn heterodimer with Pt-Sn interface was designed and synthesized. Their structure is illustrated below in Figure 6.1.1. Their EOR activity and selectivity was also investigated.

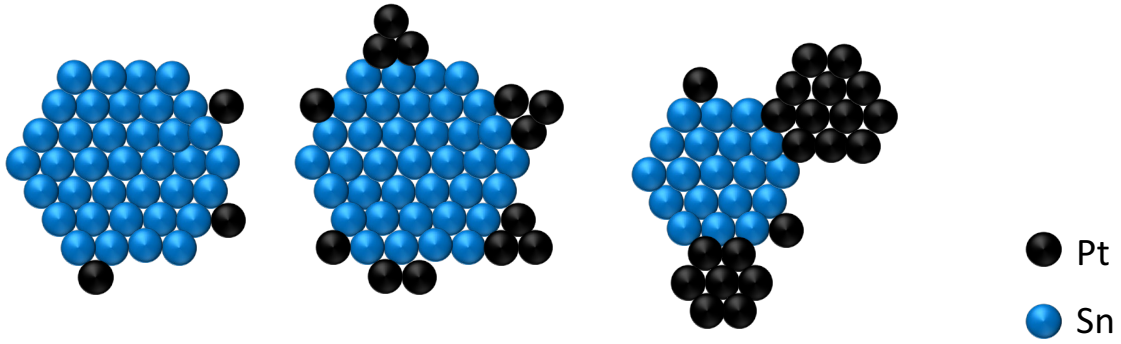

Figure 6.1.1. Illustration of Pt-Sn heterodimer of various structures.

6.2 Experimental method

Materials

Tin Sulfate (>95%, Sigma), polyvinylpyrrolidone (PVP, MW 8000, Alfa Aesar), Sodium borohydride (Sigma), platinum(II) chloride (98%, alfa aear), 1-octadecene (90%, Alfa Aesar), dodecylamine (98%, Acros Organic), 1,2-hexadecanediol (90%, Aldrich), oleylamine (70%, Sigma), oleic acid (90%, Aldrich), platinum tetrachloride (Acros Organic), tin(II) chloride (Strem Chemicals), borane tert-butylamine complex (Sigma)

and perchloric acid (70%, 99.999% trace metal basis from Sigma) were purchased and used as received.

Sn seed synthesis

Tin seed nanoparticles could be grown in aqueous or organic solvent. Aqueous solution method was modified from reported synthetic protocol[113]. Briefly, 0.4 mmol $SnSO_4$, 50 mg PVP (MW 8,000) were dissolved in 10 ml de-ionized water. Then 200 mg $NaBH_4$ dissolved in 10 ml water was slowly poured into the $SnSO_4$ and PVP solution. The mixture was stirred in ambient air at room temperature for 2 hours. Product was collected by centrifugation at 10,000 rpm for 20 minutes. The brown sediment was re-dispersed in de-ionized water and centrifuged again at 10,000 rpm for 20 minutes twice to wash off extra PVPs. Acquired product was dispersed in ethanol for further use and storage. Sn seed could also be synthesized in organic solvent with a novel method. In this method, 9 ml of oleylamine and 0.4 ml of oleic acid was heated to 140 – 160 °C and evacuated for 10 minutes in round bottom flask. Then the reaction container was purged with argon for 10 minutes. The evacuation and purging was repeated twice to remove impurities in solvent. The yellow solvent was then cooled down to 50 °C when the flask was opened and 300 mg of BTB was added. When all BTB dissolved, 0.2 mmol of $SnCl_2$ was added into solution. The mixture was quickly heated to 120 °C and was held at there for 5 minutes before cooling down to room temperature. The product was acquired by centrifugation after adding ethanol and washed with ethanol again to remove excess amount of oleylamine.

Pt-Sn heterodimer synthesis

Platinum was grown onto Sn seed via galvanic replacement. For a typical synthesis of $Pt_{3.3}Sn$ heterodimer, 20 mg of the above Sn nanoparticles were dispersed in 23 ml of ethanol and heated to ~65 °C under inert atmosphere. Then 11 mg of $PtCl_2$ dissolved in 2 ml of ethanol was injected dropwise into the Sn dispersion. The molar ratio of Sn:Pt was controlled to be 4:1. The mixture was held at 65 °C for 1 hour. The product was acquired by centrifugation at 10,000 rpm for 5 minutes. The product was then washed by water twice to remove excess amount of $PtCl_2$. After washing, product was dispersed in ethanol for further use and storage. Pt-Sn heterodimer with different composition was grown with different amount of $PtCl_2$. For example, $Pt_{1.3}Sn$ heterodimer was synthesized by controlling Sn:Pt molar ratio to be 8:1. Precise Pt:Sn molar ratio were determined by ICP-MS.

Catalyst Preparation

The catalyst preparation process for Pt-Sn heterodimers was similar to Pt/Sn alloys. The as-synthesized Pt-Sn heterodimers dispersed in ethanol were mixed with carbon black (Ketjenblack, ~900 m^2/g) in a roughly 2:1 mass ratio. After ultra-sonication for 30 minutes the suspension was centrifuged at 10,000 rpm for 5 minutes. To wash away more organic surfactants on the surface of nanoparticles the sediment was re-dispersed in hexane by sonication and centrifuged at 6,000 rpm for 3 minutes. Then the sediment was dispersed in hexane again and dried out in air at 80 °C before being annealed at 185 °C in air overnight. Inductively Coupled Plasma-Mass Spectrometry (ICP-MS) was conducted to determine the precise loading of Pt and Sn in catalyst.

Characterization

Characterization methods were similar to Pt/Sn alloys. Transmission Electron Microscopy (TEM) images were acquired on an FEI Tecnai 12 microscope operating at 100 kV. X-ray diffraction (XRD) patterns were collected on a PANalytical X'Pert^3 Powder X-Ray Diffractometer equipped with a Cu Kα radiation source (λ=0.15406). Energy-dispersive X-ray spectroscopy (EDX) was acquired on a JEOL JSM-6700F Field Emission Scanning Electron Microscope. X-ray Photoelectron Spectroscopy (XPS) measurements were done on a PHI 5600 Multi-technique photoelectron spectrometer using a Mg Kα X-ray source. Inductively Coupled Plasma Mass Spectrometry (ICP-MS) was collected with a PerkinElmer Elan DRC II Quadrupole. Nuclear Magnetic Resonance (NMR) was conducted using a Bruker Fourier 300 MHz spectrometer.

Electrochemistry test on Rotating Disk Electrode (RDE)

The EOR activities were measured with same method as Pt/Sn. 5mm glassy carbon rotation disk electrode (RDE) with a Metrohm PGSTAT302N potentiostat was implemented. The reference electrode was an Ag/AgCl electrode and the counter electrode was a Pt wire. For electrode preparation the annealed catalyst was dispersed in 10% IPA and 0.025% Nafion aqueous solution at 1 mg/ml. The mixture was sonicated shortly to allow formation of uniform ink. Then 20 ul of ink was dropped onto the surface of glassy carbon RDE and was dried in air. Figure 1.4.1b in chapter 1 is a photo of typical electrochemistry measurement set up. All current density were normalized by mass of

Pt+Sn acquired from ICP. All potentials discussed were presented against the reversible hydrogen electrode (RHE).

Gas Product Analysis via GC-MS

The selectivity was measured in identical method to Pt/Sn alloy. A 2 cm by 2 cm glassy carbon disk was used as working electrode and 1.5 ml-2 ml of catalyst ink was dropped onto the center and dried in air. Helium was purged into the anodic compartment (directly connected to GC-MS) at 10 sccm. Gas phase products were analyzed by a GCMS-QP2010SE (Shimadzu) installed a Plot-Q column (Restek). Each potential was applied and hold for 30 minutes. Liquid products were identified and quantified by NMR. All potentials discussed were presented against the reversible hydrogen electrode (RHE). Figure 2.2.2 in chapter 2 is experimental set up of novel electrolysis cell and GC-MS adopted. The faradaic efficiency of CO_2 was calculated with equation below:

$$FE_{CO_2}(\%) = \frac{\frac{CO_2\ concentration\ (ppm)}{1000000} \times flow\ rate\ (L/s) \times \frac{nFP}{RT}}{I_{total}} \times 100$$

Here n is electron transfer number with n=6 for EOR and n=5 for EGO. F is faraday constant 96485 C/mol, P is pressure in bar, R is ideal gas constant 0.08314 L·bar/(K·mol), T is temperature in K.

Liquid product analysis via Nuclear Magnetic Resonance (NMR)

A Bruker Advance 300 MHz NMR was implemented to analyze liquid product. Deuterium oxide was added to make solvent 90% H_2O and 10% D_2O. Typically, electrolyte after 30 minutes of amperometry was stored in 2 ml centrifuge vial. 665 ul of electrolyte pending analysis will be added into NMR tube together with 70 ul of 5 mM

dimethyl sulfide (DMSO)/D_2O solution. The NMR tubes were then measured. Figure 2.2.3 in chapter 2 are sample NMR spectra of electrolyte after EOR. The concentration of acetic acid was quantified with relative CH_3 peak area compared to DMSO peak area via external calibration curve. Figure 2.2.4 in chapter 2 is a sample calibration curve of peak area. The faradaic efficiency of acetic acid is calculated in the following way:

$$FE_{acetic\ acid}(\%) = \frac{\frac{acetic\ acid\ concentration\ (M) \times volume\ (L)}{reaction\ time\ (s)} \times nF}{I_{total}} \times 100$$

Here electron transfer number is 4.

6.3 Characterization of Synthesized Pt-Sn heterodimer

Synthesized Pt-Sn heterodimer were first characterized by Transmission Electron Microscopy (TEM) and X-Ray Diffraction (XRD).

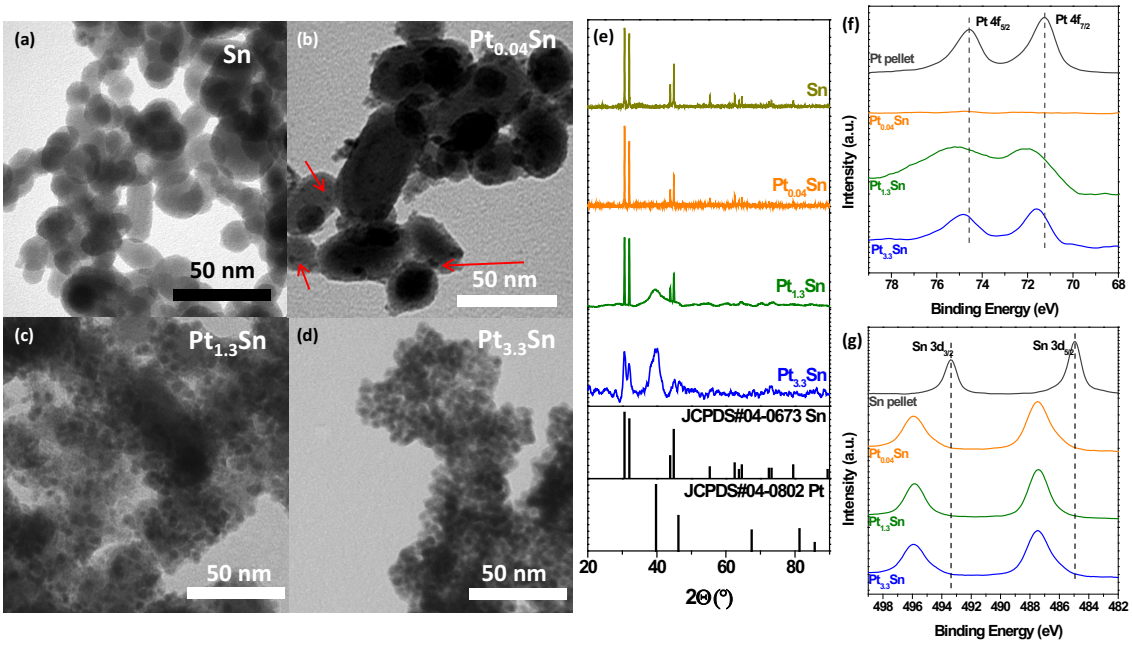

Figure 6.3.1. TEM images of (a) Sn seed, (b) $Pt_{0.04}Sn$, (c) $Pt_{1.3}Sn$ and (d) $Pt_{3.3}Sn$. (e) XRD pattern

As is shown in Figure 6.3.1a, Sn seeds with size from 20 to 40 nm were successfully synthesized. Sn seeds mostly exist in spheres while a minor portion of them are elongated spheres. Their XRD patterns agree with metallic Sn. Three representative Pt-Sn heterodimers were presented in Figure 6.3.1. Figure 6.3.1b shows the morphology of $Pt_{0.04}Sn$ heterodimers. Sn seeds remained their original morphology while Pt clusters of ~3 nm attached to Sn matrix. No visible Pt peak could be observed from XRD pattern, while the existence of Pt was confirmed by both ICP-MS and EDX. The lack of Pt peak on XRD is likely due to amorphous nature of grown Pt cluster or low amount of Pt. $Pt_{1.3}Sn$ exhibited morphology of 5-10 nm Pt nanoparticles attached to Sn nanoparticles. Sn seeds showed minor shrink in size. $Pt_{1.3}Sn$ showed a broad XRD peak at 39.7 degree, corresponding to Pt (111) facet. Sn (200), Sn (101), Sn (220) and Sn (211) peaks also existed in the XRD pattern of $Pt_{1.3}Sn$ and the Sn peaks were sharp. Above XRD pattern indicate the low crystallinity of Pt and high crystallinity of Sn in $Pt_{1.3}Sn$. TEM image of $Pt_{3.3}Sn$ was shown in Figure 6.3.1d and the majority had become Pt nanoparticles of 5-10 nm. Sn seeds, however, shrinked significantly in size and were mostly buried between Pt nanoparticles. $Pt_{3.3}Sn$ exhibited XRD peaks at same position as $Pt_{1.3}Sn$ with sharper Pt peaks and weaker Sn peaks. This could be explained by formation of Pt nanoparticles of higher crystallinity and consumption of Sn during galvanic replacement resulted in lower crystallinity of Sn. The Pt-Sn heterodimers were loaded on carbon and treated under mild thermal conditions for electrochemistry tests. XPS was conducted to investigate surface oxidation state of these catalysts. $Pt_{0.04}Sn/C$ showed nearly no Pt peaks in XPS (Figure 6.3.1f), while $Pt_{1.3}Sn/C$ and $Pt_{3.3}Sn/C$ possess slightly oxidized surface Pt species. In the meantime, all three catalysts possess oxidized Sn surface (Figure 6.3.1g).

Their morphology remained the same after loaded on carbon, as is shown in Figure 6.3.2.

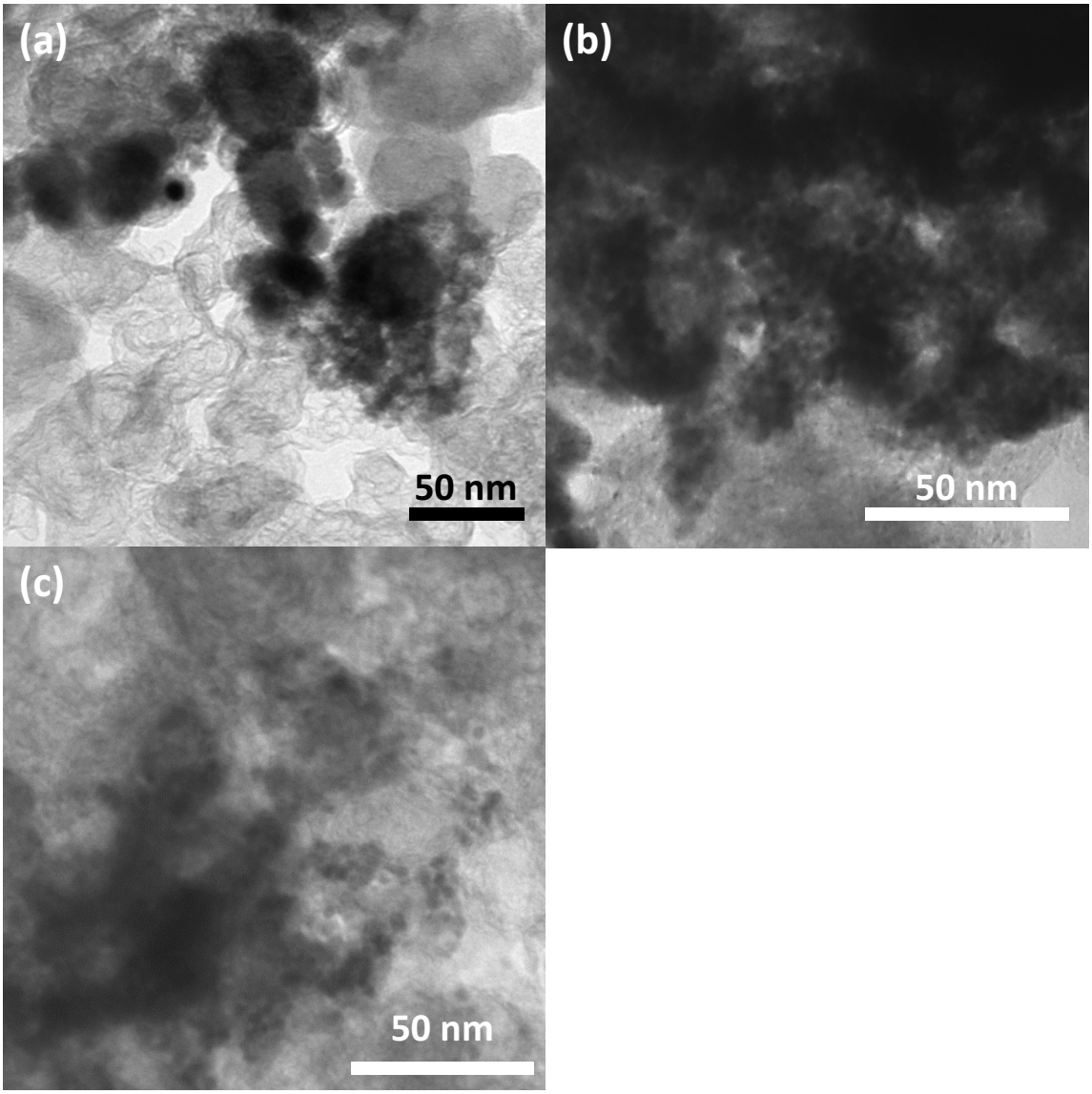

Figure 6.3.2. TEM images of Pt-Sn heterodimers loaded on carbon. (a) $Pt_{0.04}Sn$, (b) $Pt_{1.3}Sn$ and (c) $Pt_{3.3}Sn$.

6.4 Electrocatalytic performance

The EOR performance of Pt-Sn heterodimers were investigated on Rotating Disk Electrode (RDE). Figure 6.4.1 summarizes their catalytic performance. Their voltammogram in 0.1M $HClO_4$ is similar to Pt_3Sn in chapter 2. Hupd peak of platinum

was suppressed for Pt-Sn heterodimers of with all compositions. It is surprising that even $Pt_{3.3}Sn$ showed no Hupd peak, which is likely due to partial alloying of Pt and Sn.

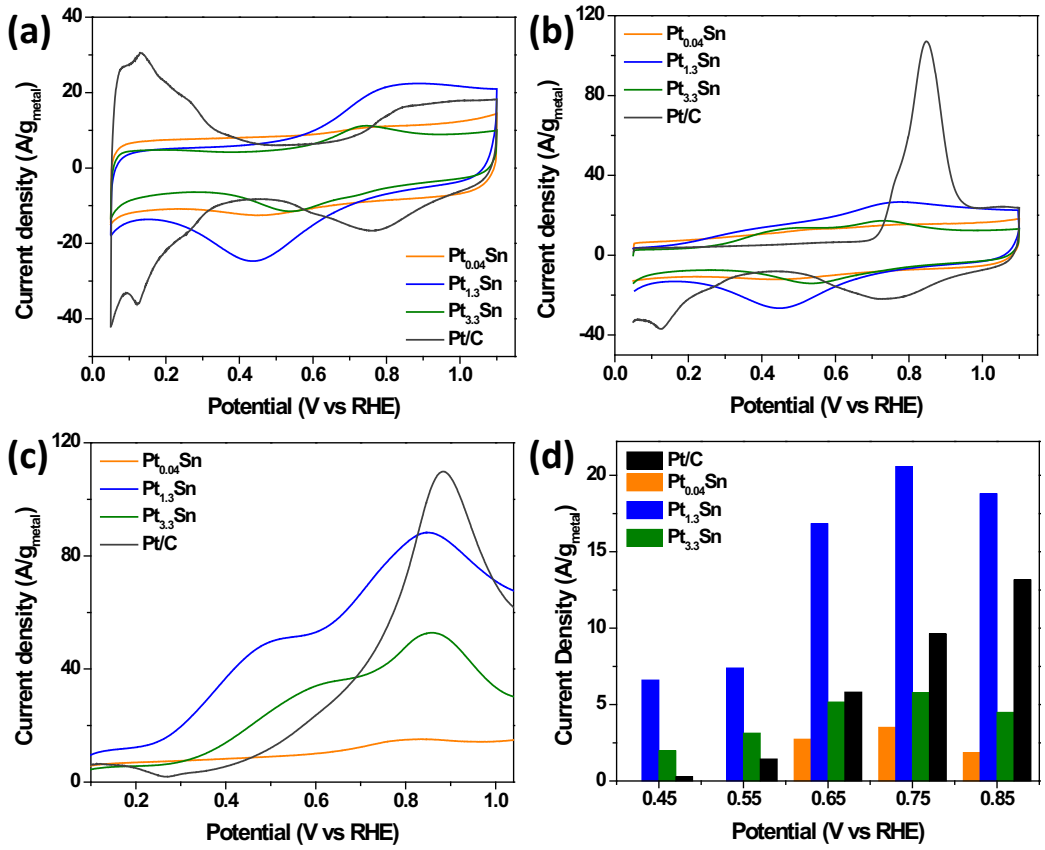

Figure 6.4.1. (a) Voltammogram and (b) CO stripping of Pt-Sn heterodimers in 0.1M $HClO_4$. (c) positive cyclic voltammetry scan and (d) average current density during 30 minutes amperometry in 0.1M $HClO_4$ + 0.1M ethanol.

$Pt_{0.04}Sn$ exhibited a tiny OH adsorption peak at 0.73 V, which is ~100 mV lower than the peak position of 6nm Pt. The ultra-small OH adsorption peak area corresponds to low amount of Pt sites in $Pt_{0.04}Sn$. $Pt_{1.3}Sn$ possess OH adsorption peak at 0.82 V and $Pt_{3.3}Sn$ possess OH adsorption peak at 0.73 V. It should be noted that the OH adsorption peak of $Pt_{1.3}Sn$ is much larger than $Pt_{3.3}Sn$ despite its lower Pt content. This is likely due to

aggregation of Pt nanoparticles on Sn surface resulted in loss of surface area. CO stripping behavior of Pt-Sn heterodimers are also significantly different from Pt. All Pt-Sn heterodimers possess two peaks at ~0.45 V and ~0.72 V, both much lower than the CO stripping peak of pure Pt at ~0.82 V. Similar to Pt/Sn alloys discussed in Chapter 2, the lower peak position of is caused by synergy between Pt and Sn—Sn provides adsorbing site for OH group that assist with CO_{ads} oxidation. Their peak at ~0.72 V could be attributed to Pt sites with high coordination number and the peak at ~0.45 V corresponds to low coordinated Pt sites. The CO stripping peak of $Pt_{0.04}Sn$ is tiny yet visible. The CO stripping peak area of $Pt_{1.3}Sn$ is larger than that of $Pt_{3.3}Sn$, which is consistent as the trend in voltammogram and due to same reason. Pt-Sn heterodimers exhibited enhanced EOR performance. The positive scan of cyclic voltammetry in 0.1M $HClO_4$ + 0.1M ethanol in Figure 6.4.1c shows the onset potential of $Pt_{3.3}Sn$ and $Pt_{1.3}Sn$ is as low as ~0.25 V, compared to ~0.37 V of Pt. $Pt_{1.3}Sn$ possess a shoulder peak at ~0.48 V and $Pt_{3.3}Sn$ possess a shoulder peak at ~0.6 V, showing enhanced EOR activity within potential range between 0.4 V to 0.7 V. The peak current of $Pt_{1.3}Sn$ and $Pt_{3.3}Sn$ is 80% and 47% of Pt respectively, indicating higher activity of Pt at potentials above 0.7 V. $Pt_{0.04}Sn$, however, possessed very low activity. No low potential peak could be observed between 0.4 V and 0.6 V, likely because the current is too low to be visible. A tiny EOR peak corresponding to Pt was observed at 0.8 V with peak current 13 % of Pt. The low total activity of $Pt_{0.04}Sn$ is due to low ensemble of Pt sites in catalyst. Figure 6.4.1d summarizes the average current density during 30 minutes amperometry in 0.1M $HClO_4$ + 0.1M Ethanol. $Pt_{1.3}Sn$ and $Pt_{3.3}Sn$ showed current density much higher than Pt, reaching 24 times and 7 times of Pt at 0.45 V, 5 times and 2 times of Pt at 0.55 V

respectively. $Pt_{1.3}Sn$ still showed higher current density throughout all potentials, with 1.4 to 2.8 times current density of Pt. The enhanced activity of Pt-Sn heterodimers could be attributed to synergy between Pt and Sn. Specifically, $Pt_{1.3}Sn$ showed higher activity than Pt at all potentials because the large amount of Pt-Sn interfaces. $Pt_{0.04}Sn$, however, exhibited very low EOR activity during 30 minutes amperometry. It possessed almost no activity at 0.45 V and 0.55 V, at current 1/10-1/2 of Pt at higher potentials. This is again because of the low ensemble of Pt sites.

6.5 Product selectivity during EOR

The synthesized Pt-Sn heterodimers were tested for product selectivity during EOR. Figure 6.5.1 summarizes their product selectivity.

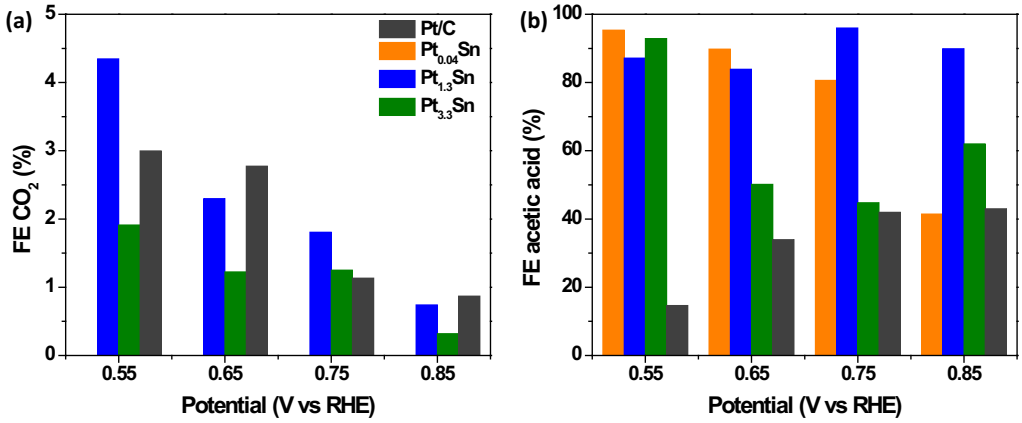

Figure 6.5.1. Faradaic efficiency of (a) CO_2 and (b) acetic acid of Pt-Sn heterodimers during EOR

As is shown in Figure 6.5.1a, the CO_2 faradaic efficiency for Pt-Sn heterodimers during EOR were all below 5 %. The CO_2 faradaic efficiency of $Pt_{1.3}Sn$ was 4.3% at 0.55 V, and slowly decreased to 0.7% at 0.85 V. $Pt_{3.3}Sn$ showed even lower CO_2 faradaic efficiency, with 1.9 % at 0.55 V and decreased to 0.3 % at 0.85 V. These values are similar to that of Pt control sample. The trend of decreasing CO_2 selectivity with potential was same as

that of Pt/Sn alloys and indicate more favorable of C_2 product pathway at high potentials. The current of $Pt_{0.04}Sn$ was very low so no CO_2 signal was detected. The majority of product was still acetic acid, as is shown in Figure 6.5.1b. The faradaic efficiency of acetic acid of $Pt_{0.04}Sn$ decrease from 95 % to 80 % within potential range from 0.55 V – 0.75 V before sharply dropping to 41 % at 0.85 V. The sharp drop could be attributed to favor of acetaldehyde pathway at 0.85 V. $Pt_{1.3}Sn$ exhibited stable acetic acid faradaic efficiency from 83 % to 95 % at all potentials, attributing to highly favorable acetic acid pathway at all potentials. $Pt_{3.3}Sn$ started with acetic acid faradaic efficiency as high as 92 % at 0.55 V, then decreased to 44 % to 62 % between 0.65 V – 0.85 V. Pt-Sn heterodimers exhibited overall very high acetic acid selectivity, which is likely due to lack of close Pt-SnO_x interfaces that is capable of cleaving C-C bond. Our CO_2 selectivity result of Pt-Sn heterodimer exhibited barely any enhancement compared to Pt, and lower performance compared to Pt/Sn alloy. This conclusion agrees with the study reported by Silva et al.[173] and is not consistent with Jiang et al.[129, 169] The minor or no enhancement of CO_2 selectivity could be attributed to two reasons: i) limited number of surface SnOx sites, ii) limited number or lack of subsurface Sn species.

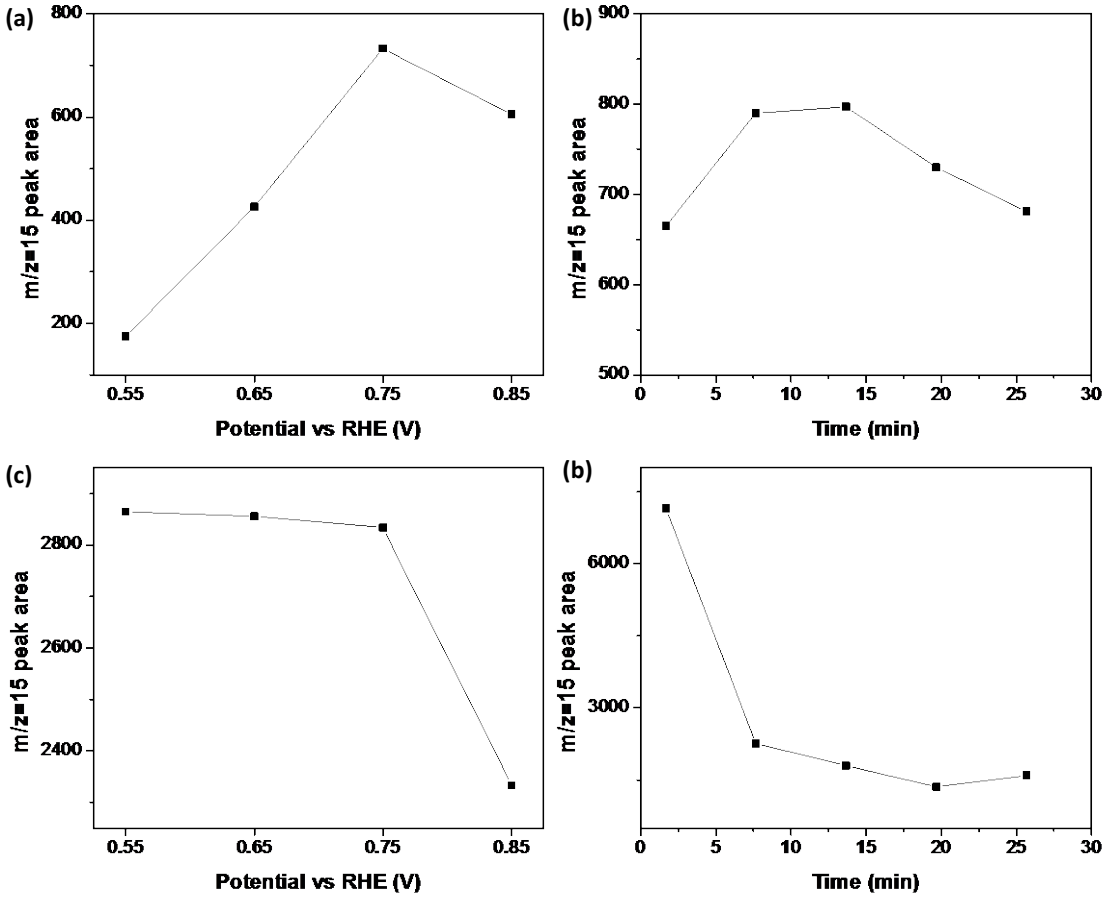

Figure 6.5.2. (a) m/z=15 peak area of $Pt_{1.3}Sn$ during EOR at various potentials. (b) m/z=15 peak area of $Pt_{1.3}Sn$ during 0.75 V EOR at various time. (c) m/z=15 peak area of $Pt_{3.3}Sn$ during EOR at various potentials. (d) m/z=15 peak area of $Pt_{3.3}Sn$ during 0.75 V EOR at various time.

Similar to Pt/Sn alloy, m/z=15 peak attributed to CH_3^+ was also detected during EOR of Pt-Sn heterodimers, indicating formation of methane during EOR. Figure 6.5.2a shows the m/z=15 peak area of $Pt_{1.3}Sn$ at various potentials. The peak area increase from 0.55 V to 0.75 V and decrease at 0.85 V. The methane peak was observed throughout whole 30 minute EOR process and slightly increased between 5 minutes and 15 minutes, as is shown in Figure 6.5.2b. The m/z=15 peak of $Pt_{3.3}Sn$ was much larger compared to

that of $Pt_{1.3}Sn$, likely due to higher ensemble of Pt. As is shown in Figure 6.5.2c, the m/z=15 peak during $Pt_{3.3}Sn$ EOR was rather stable between 0.55 V to 0.75 V and dropped by ~20 % at 0.85 V. The existence of m/z=15 peak was observed throughout whole 30 minutes, as is shown in Figure 6.5.2d. The peak area of methane exhibit rather random trend. The formation of methane and CH_3^+ fragment is complicated and may be affected by many factors, including Pt configuration, Pt-Sn interaction etc.

6.6 Surface change and KOH Treatment

The surface property and structure of Pt-Sn heterodimers could be modified during alcohol electro-oxidation. The mechanism was discussed in Chapter 2. Briefly, Pt possess a stronger CO adsorption energy and migrates to surface at the presence of CO_{ads}. Below is surface change of $Pt_{1.3}Sn$ after ethanol oxidation reaction.

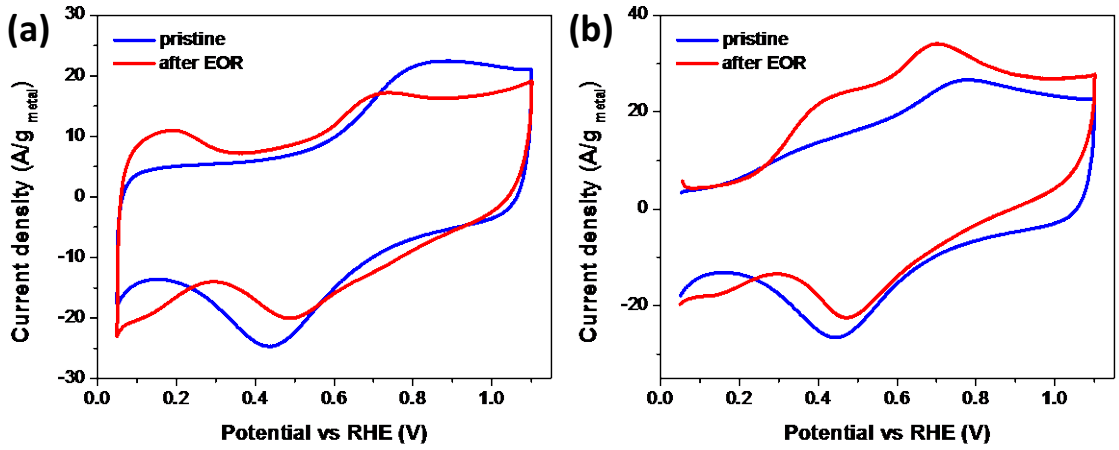

Figure 6.6.1. (a) Voltammogram and (b) CO stripping change of $Pt_{1.3}Sn$ after EOR from 0.45 V to 0.85 V.

Figure 6.6.1 summarizes the surface property change of $Pt_{1.3}Sn$ after ethanol oxidation reaction with chronoamperometry from 0.45 V to 0.85 V. Voltammogram of $Pt_{1.3}Sn$ revealed small Hupd reagion after EOR, while the OH adsorption peak was still at 0.7 V

compared to 0.85 V of pure Pt. CO stripping pattern still possessed two peaks with higher peak area. Above results could be explained by Pt migration onto surface in partially alloyed Pt/Sn region, while a significant portion of Sn particles in heterodimer remain unchanged. The Pt:Sn atomic ratio became 0.56 after EOR. This is a result of Sn slow dissolution that detached some Pt from heterodimers.

The surface property and structure could also be modified via scanning in KOH. The mechanism was discussed in Chapter 2. In short, Sn atoms could dissolve in KOH and leach out. $Pt_{1.3}Sn$ was taken as an example to illustrate the modification.

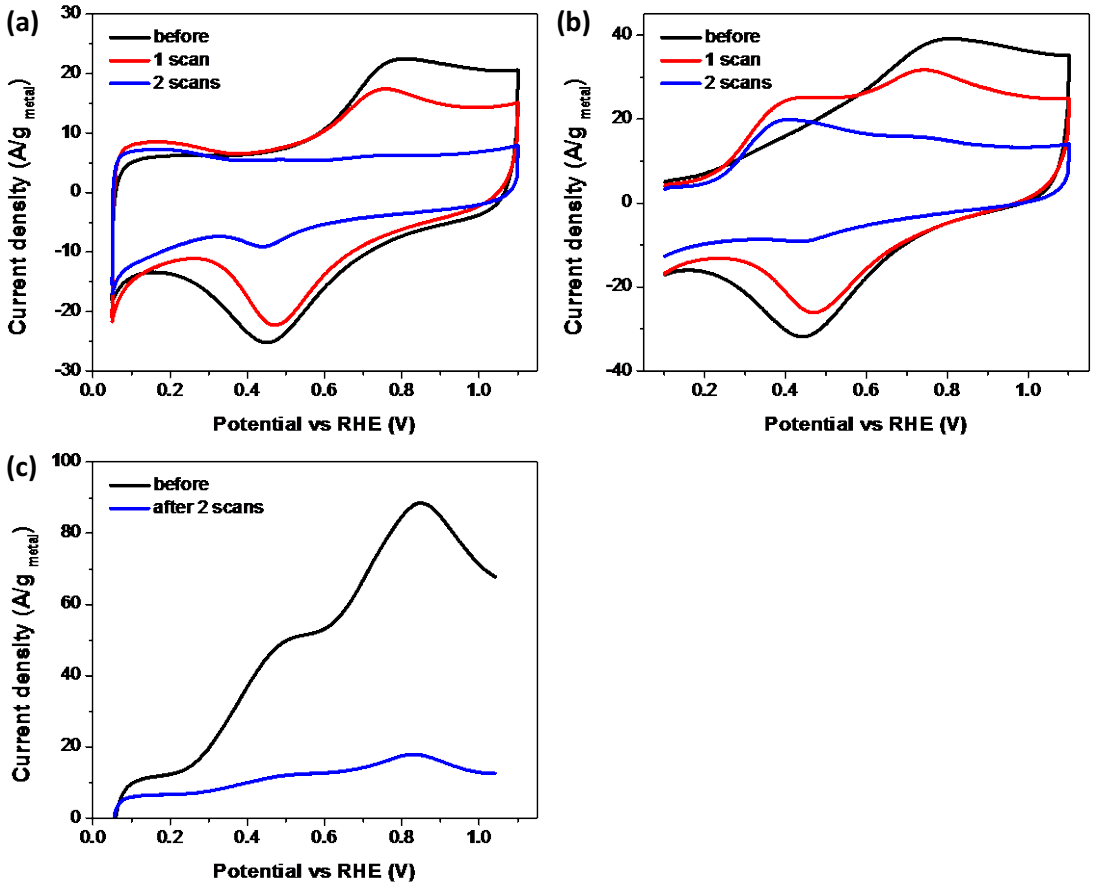

Figure 6.6.2. (a) voltammogram, (b) CO stripping change with scanning in 0.1M KOH. (c) comparison of positive cyclic voltammetry scan in 0.1M $HClO_4$ + 0.1M ethanol before and after KOH scans.

Figure 6.6.2 summarizes the electrochemistry behavior of $Pt_{1.3}Sn$ during KOH treatment. While pristine $Pt_{1.3}Sn$ showed no Hupd peak, it showed a small Hupd peak after one KOH scan, indicating exposure of pure Pt surface with dissolution of Sn. The OH adsorption peak decreased to ~2/3 of original after 1 KOH scan. This indicate loss of Sn atoms on surface. After 2nd scan in KOH, Pt Hupd peak slightly shrinked while OH adsorption peak almost disappeared. This could be attributed to further loss of Sn resulted in loss of almost all Pt attached to Sn nanoparticles. The CO stripping pattern also

exhibited significant change as is shown in Figure 6.6.2b. The peak at ~0.75 V decreased with KOH scan because of loss of surface Pt sites. The peak at ~0.4 V, however, increased after first scan and decreased again after second scan. The increase after first scan was caused by exposure of more Sn dominant surface with detachment of Pt, while the decrease after second scan was due to further loss of total surface area. Figure 6.6.2c shows the significant loss of EOR activity of Pt-Sn heterodimer after KOH scans. The peak current decreased to ~20% of pristine $Pt_{1.3}Sn$ after merely two KOH scans. This could be easily explained by loss of Pt ensemble within Pt-Sn heterodimers. Figure 6.6.3 is a schematic illustration of $Pt_{1.3}Sn$ structure change during KOH scans.

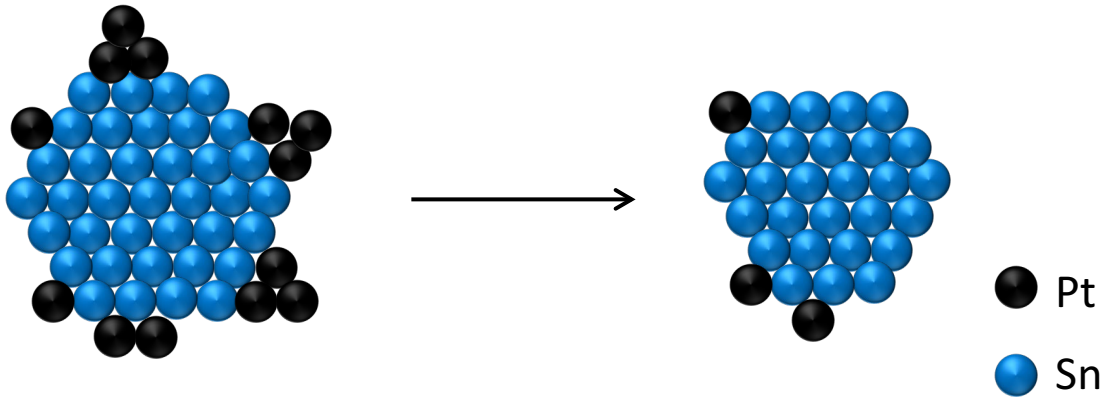

Figure 6.6.3. Schematic illustration of Pt-Sn heterodimer structural change during KOH scans.

6.7 Conclusion

We have successfully synthesized Pt-Sn heterodimers of various morphology and composition. Their catalytic performance for EOR was investigated and all of them exhibited significantly enhanced activity than Pt at 0.45 V and 0.55 V. Specifically $Pt_{1.3}Sn$ showed higher activity than Pt at all potentials. The enhancement of activity could be attributed to existence of Pt-Sn interfaces. The Pt-Sn heterodimers exhibited minor

enhancement in terms of CO_2 selectivity compared to Pt. This is likely due to lack of synergy between surface SnOx and subsurface Sn species. The Pt-Sn heterodimers would experience Sn dissolution and Pt detachment when treated with KOH, which will result in loss of most activity.

Chapter 7. Eletro-Oxidation of Alcohol using Pt/Rh/Sn Ternary Nanomaterials

7.1 Introduction

Binary Pt/Sn nanomaterials exhibited enhancement in catalysis of alcohol electro-oxidation to a certain degree. Another feasible approach to enhance alcohol electro-oxidation catalytic performance is to implement a third element to form ternary composition. Rhodium is a promising element to be implemented and its benefits had been reported by both computational and experimental works. Sheng et al. computed the energy changes during EOR on Pt doped with Ru, Rh, Pd, Os and Ir[174]. They concluded that implementing Rh is beneficial for beta dehydrogenation step ($CH_3CO^* \rightarrow CH_2CO^* + H^*$) thus enhance the selectivity toward CO_2. Li et al. compared the formation of CO_2 on Pt/C and PtRh/C via *in situ* IR and reported that Rh would promote C-C bond breaking on catalyst surface[175]. De Souza et al. further reported that Rhodium not only contribute to C-C bond breaking, but also suppress the formation of acetic acid[176]. The suppression of acetic acid formation could be attributed to obstacle in ethanol adsorption[176] and/or hindered ethanol alpha dehydrogenation on Pt surface[177]. It is, therefore, greatly beneficial to design ternary catalysts with Pt/Rh/Sn composition for alcohol electro-oxidation purpose. Rhodium plays the role of enhancing C-C bond breaking and beta dehydrogenation mentioned above, while tin adsorb OH_{ads} species for oxidation of $CH_{x,ads}$ and CO_{ads} intermediates poisoning catalyst surface[178]. There had been investigations about the EOR performance of ternary Pt/Rh/Sn(O_x) catalysts with enhanced activity and selectivity[179-181]. Here we report the synthesis of novel Pt/Rh/Sn

nanomaterial with various morphology and composition, the investigation of their catalytic performance toward alcohol electro-oxidation, and the assessment of their product selectivity with our novel GC-MS approach. In this work, Pt/Rh/Sn alloy and Pt-Rh-Sn heterodimer were synthesized. Figure 7.1.1 illustrates the structure of the novel nanomaterials. Their enhanced activity toward EOR were demonstrated. Their selectivity toward CO_2, however, exhibited no noticeable enhancement compared to Pt.

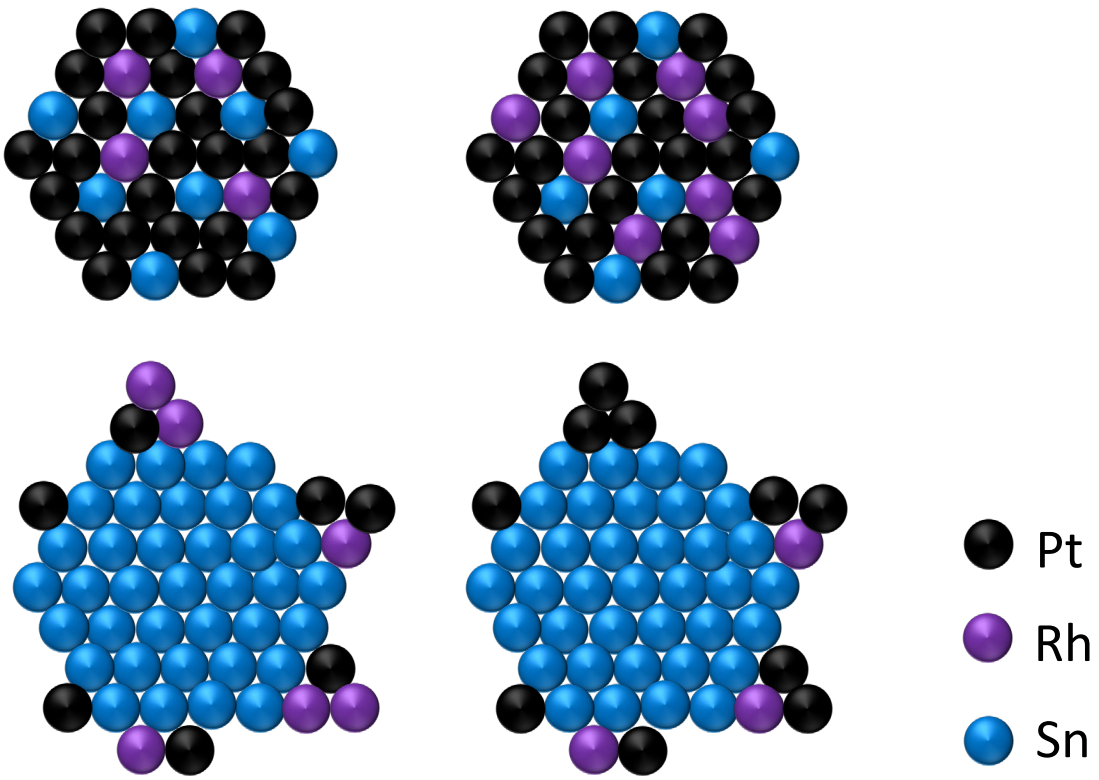

Figure 7.1.1 Illustration of designed structures of Pt/Rh/Sn nanomaterials

7.2 Experimental Method

Materials

Tin Sulfate (>95%, Sigma), polyvinylpyrrolidone (PVP, MW 8000, Alfa Aesar), Sodium borohydride (Sigma), rhodium (III) chloride hydrate (99.98 %, Aldrich) platinum(II)

chloride (98%, alfa aear), 1-octadecene (90%, Alfa Aesar), dodecylamine (98%, Acros Organic), 1,2-hexadecanediol (90%, Aldrich), oleylamine (70%, Sigma), oleic acid (90%, Aldrich), platinum tetrachloride (Acros Organic), tin(II) chloride (Strem Chemicals), borane tert-butylamine complex (Sigma) and perchloric acid (70%, 99.999% trace metal basis from Sigma) were purchased and used as received.

Pt/Rh/Sn nanoparticle synthesis

3nm $Pt_{2.7}Rh_{0.7}Sn$ nanoparticles were synthesized in a novel method. 9ml of oleylamine and 0.4ml of oleic acid was heated to 140 °C. At this temperature the solution was evacuated for 10 minutes before purged with argon for another 10 minutes. Then vacuum and argon flow was repeated twice before the solution was cooled down to 50 °C. 600mg of borane tert-butylamine complex was added into solution. After 10 minutes of stirring at 50 °C the solution was heated to 120 °C when a mixture of 0.6mmol $PtCl_4$, 0.2mmol of $RhCl_3$, 0.2mmol $SnCl_2$ and 1.5ml of ethanol was quickly injected. The dark brown solution was kept at 120 °C for 20 minutes before cooling down to room temperature. The product was precipitated by adding ethanol and centrifuging at 4,000 rpm for 5 minutes. After the sediment was dispersed in toluene, it was centrifuged again with ethanol at 4,000 rpm for 5 minutes. Final product was dispersed in toluene for storage and further usage.

3nm $Pt_{2.7}Rh_{1.3}Sn$ was synthesized in a similar protocol to 3nm $Pt_{2.7}Rh_{0.7}Sn$ except the injection solution consisted of 0.6mmol $PtCl_4$, 0.4mmol of $RhCl_3$, 0.2mmol $SnCl_2$ and 1.5ml of ethanol. Washing procedure is the same as 6nm Pt_3Sn in chapter 2.

Sn seed synthesis

Tin seed nanoparticles could be grown in aqueous or organic solvent. Aqueous solution method was modified from reported synthetic protocol[113]. Briefly, 0.4 mmol $SnSO_4$, 50 mg PVP (MW 8,000) were dissolved in 10 ml de-ionized water. Then 200 mg $NaBH_4$ dissolved in 10 ml water was slowly poured into the $SnSO_4$ and PVP solution. The mixture was stirred in ambient air at room temperature for 2 hours. Product was collected by centrifugation at 10,000 rpm for 20 minutes. The brown sediment was re-dispersed in de-ionized water and centrifuged again at 10,000 rpm for 20 minutes twice to wash off extra PVPs. Acquired product was dispersed in ethanol for further use and storage. Sn seed could also be synthesized in organic solvent with a novel method. In this method, 9 ml of oleylamine and 0.4 ml of oleic acid was heated to 140 – 160 °C and evacuated for 10 minutes in round bottom flask. Then the reaction container was purged with argon for 10 minutes. The evacuation and purge was repeated twice to remove impurities in solvent. The yellow solvent was then cooled down to 50 °C when the flask was opened and 300 mg of BTB was added. When all BTB dissolved, 0.2 mmol of $SnCl_2$ was added into solution. The mixture was quickly heated to 120 °C and was held at there for 5 minutes before cooling down to room temperature. The product was acquired by centrifugation with ethanol added and washed with ethanol for remove excess amount of oleylamine.

Pt-Rh-Sn heterodimer synthesis

Platinum and rhodium was grown onto Sn seed via galvanic replacement. For a typical synthesis of $Pt_{0.35}Rh_{0.83}Sn$ heterodimer, 30 mg of the above Sn nanoparticles were

dispersed in 23 ml of ethanol and heated to 65 °C under inert atmosphere. Then 26.3 mg of $RhCl_3$ dissolved in 1 ml of ethanol was injected dropwise into the Sn dispersion. The solution was kept at 65 °C for 1 hour after injection of $RhCl_3$. Then 28.3 mg of $PtCl_2$ dissolved in 1 ml of ethanol was injected dropwise. The solution was kepted at 65 °C again for 1 hour after injection of $PtCl_2$. The molar ratio of Sn:Rh:Pt was controlled to be 6:3:2. The product was acquired by centrifugation at 10,000 rpm for 5 minutes. The product was then washed by water twice to remove excess amount of metal chloride salts. After washing, product was dispersed in ethanol for further use and storage. Precise Pt:Rh:Sn molar ratio were determined by ICP-MS.

For a typical synthesis of $Pt_{1.06}Rh_{0.06}Sn$ heterodimer, 30 mg of the above Sn nanoparticles were dispersed in 23 ml of ethanol and heated to 65 °C under inert atmosphere. Then 28.3 mg of $PtCl_2$ dissolved in 1 ml of ethanol was injected dropwise into the Sn dispersion. The solution was kept at 65 °C for 1 hour after injection of $PtCl_2$. Then 26.3 mg of $RhCl_3$ dissolved in 1 ml of ethanol was injected dropwise. The solution was kepted at 65 °C again for 1 hour after injection of $RhCl_3$. The molar ratio of Sn:Rh:Pt was controlled to be 6:3:2. The product was acquired by centrifugation at 10,000 rpm for 5 minutes. The product was then washed by water twice to remove excess amount of metal chloride salts. After washing, product was dispersed in ethanol for further use and storage. Precise Pt:Rh:Sn molar ratio were determined by ICP-MS.

For a typical synthesis of $Pt_{0.43}Rh_{0.14}Sn$ heterodimer, 30 mg of the above Sn nanoparticles were dispersed in 23 ml of ethanol and heated to 65 °C under inert atmosphere. Then 14.2 mg of $PtCl_4$ and 8.8mg of $RhCl_3$ dissolved in 1 ml of ethanol was injected dropwise into the Sn dispersion. The solution was kept at 65 °C for 1 hour after injection of $PtCl_4$

and $RhCl_3$. The molar ratio of Sn:Rh:Pt was controlled to be 6:1:1. The product was acquired by centrifugation at 10,000 rpm for 5 minutes. The product was then washed by water twice to remove excess amount of metal chloride salts. After washing, product was dispersed in ethanol for further use and storage. Precise Pt:Rh:Sn molar ratio were determined by ICP-MS.

Catalyst Preparation

The catalyst preparation process for Pt/Rh/Sn alloys and Pt-Rh-Sn heterodimers was similar to Pt/Sn alloys. The as-synthesized Pt/Rh/Sn alloys and Pt-Rh-Sn heterodimers dispersed in ethanol were mixed with carbon black (Ketjenblack, ~900 m^2/g) in a roughly 2:1 mass ratio. After ultra-sonication for 30 minutes the suspension was centrifuged at 10,000 rpm for 5 minutes. To wash away more organic surfactants on the surface of nanoparticles the sediment was re-dispersed in hexane by sonication and centrifuged at 6,000 rpm for 3 minutes. Then the sediment was dispersed in hexane again and dried out in air at 80 °C before being annealed at 185 °C in air overnight. Inductively Coupled Plasma-Mass Spectrometry (ICP-MS) was conducted to determine the precise loading of Pt, Rh and Sn in catalyst.

Characterization

Characterization methods were similar to Pt/Sn alloys. Transmission Electron Microscopy (TEM) images were acquired on an FEI Tecnai 12 microscope operating at 100 kV. X-ray diffraction (XRD) patterns were collected on a PANalytical X'Pert^3 Powder X-Ray Diffractometer equipped with a Cu Kα radiation source (λ=0.15406).

Energy-dispersive X-ray spectroscopy (EDX) was acquired on a JEOL JSM-6700F Field Emission Scanning Electron Microscope. X-ray Photoelectron Spectroscopy (XPS) measurements were done on a PHI 5600 Multi-technique photoelectron spectrometer using a Mg Kα X-ray source. Inductively Coupled Plasma Mass Spectrometry (ICP-MS) was collected with a PerkinElmer Elan DRC II Quadrupole. Nuclear Magnetic Resonance (NMR) was conducted using a Bruker Fourier 300 MHz spectrometer.

Electrochemistry test on Rotating Disk Electrode (RDE)

The EOR activities were measured with same method as Pt/Sn alloys. 5mm glassy carbon rotation disk electrode (RDE) with a Metrohm PGSTAT302N potentiostat was implemented. The reference electrode was an Ag/AgCl electrode and the counter electrode was a Pt wire. For electrode preparation the annealed catalyst was dispersed in 10% IPA and 0.025% Nafion aqueous solution at 1mg/ml. The mixture was sonicated shortly to allow formation of uniform ink. Then 20ul of ink was dropped onto the surface of glassy carbon RDE and was dried in air. Figure 1.4.1b chapter 1 is a photo of typical electrochemistry measurement set up. All current density were normalized by mass of Pt+Rh acquired from ICP. All potentials discussed were presented against the reversible hydrogen electrode (RHE).

Gas Product Analysis via GC-MS

The selectivity was measured in identical method to Pt/Sn alloy. A 2cm by 2cm glassy carbon disk was used as working electrode and 1.5ml-2ml of catalyst ink was dropped onto the center and dried in air. Helium was purged into the anodic compartment

(directly connected to GC-MS) at 10sccm. Gas phase products were analyzed by a GCMS-QP2010SE (Shimadzu) installed a Plot-Q column (Restek). Each potential was applied and hold for 30 minutes. Liquid products were identified and quantified by NMR. All potentials discussed were presented against the reversible hydrogen electrode (RHE). Figure 2.2.2 chapter 2 is experimental set up of novel electrolysis cell and GC-MS adopted. The faradaic efficiency of CO_2 was calculated with equation below:

$$FE_{CO_2}(\%) = \frac{\frac{CO_2\ concentration\ (ppm)}{1000000} \times flow\ rate\ (L/s) \times \frac{nFP}{RT}}{I_{total}} \times 100$$

Here n is electron transfer number with n=6 for EOR and n=5 for EGO. F is faraday constant 96485 C/mol, P is pressure in bar, R is ideal gas constant 0.08314 L·bar/(K·mol), T is temperature in K.

Liquid product analysis via Nuclear Magnetic Resonance (NMR)

A Bruker Advance 300 MHz NMR was implemented to analyze liquid product. Deuterium oxide was added to make solvent 90% H_2O and 10% D_2O. Typically, electrolyte after 30 minutes of amperometry was stored in 2 ml centrifuge vial. 665 ul of electrolyte pending analysis will be added into NMR tube together with 70 ul of 5mM dimethyl sulfide (DMSO)/D_2O solution. The NMR tubes were then measured. Figure 2.2.3 chapter 2 are sample NMR spectra of electrolyte after EOR. The concentration of acetic acid was quantified with relative CH_3 peak area compared to DMSO peak area via external calibration curve. Figure 2.2.4 chapter 2 is a sample calibration curve of peak area. The faradaic efficiency of acetic acid is calculated in the following way:

$$FE_{acetic\ acid}(\%) = \frac{\frac{acetic\ acid\ concentration\ (M) \times volume\ (L)}{reaction\ time\ (s)} \times nF}{I_{total}} \times 100$$

Here electron transfer number is 4.

7.3 Material Characterization

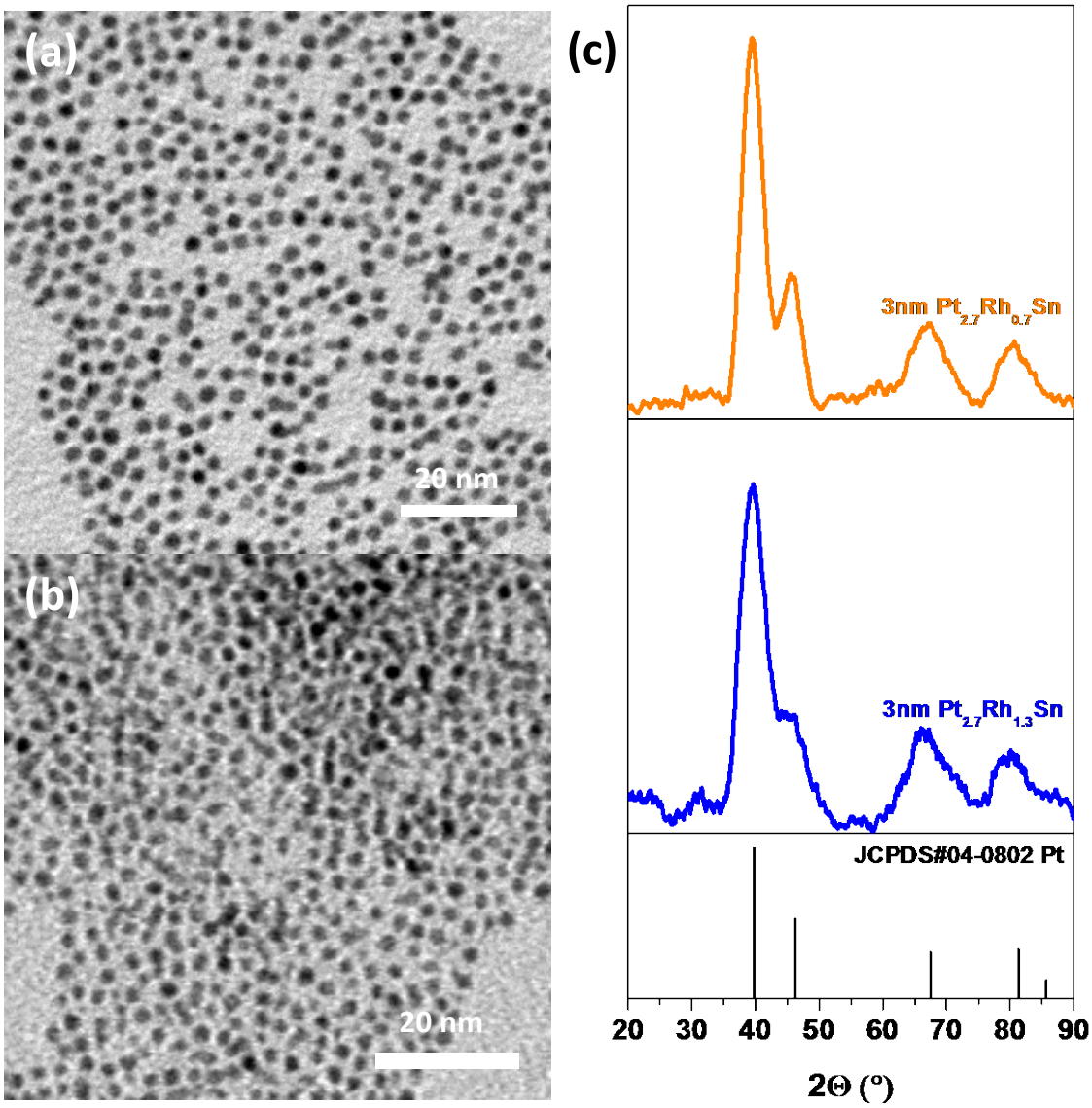

Figure 7.3.1. TEM images of (a) $Pt_{2.7}Rh_{0.7}Sn$ and (b) $Pt_{2.7}Rh_{1.3}Sn$. (c) XRD patterns.

Figure 7.3.1 summarizes the characterization results of Pt/Rh/Sn alloy. Both $Pt_{2.7}Rh_{0.7}Sn$ and $Pt_{2.7}Rh_{1.3}Sn$ are 3 nm spheres. Their XRD pattern reveals the peaks of Pt without peaks attributed to Rh or Sn. This is due to high crystallinity of Pt and low crystallinity of Rh and Sn. The XRD pattern also reveals that Pt are randomly alloyed with Rh and Sn because there is no intermetallic peak.

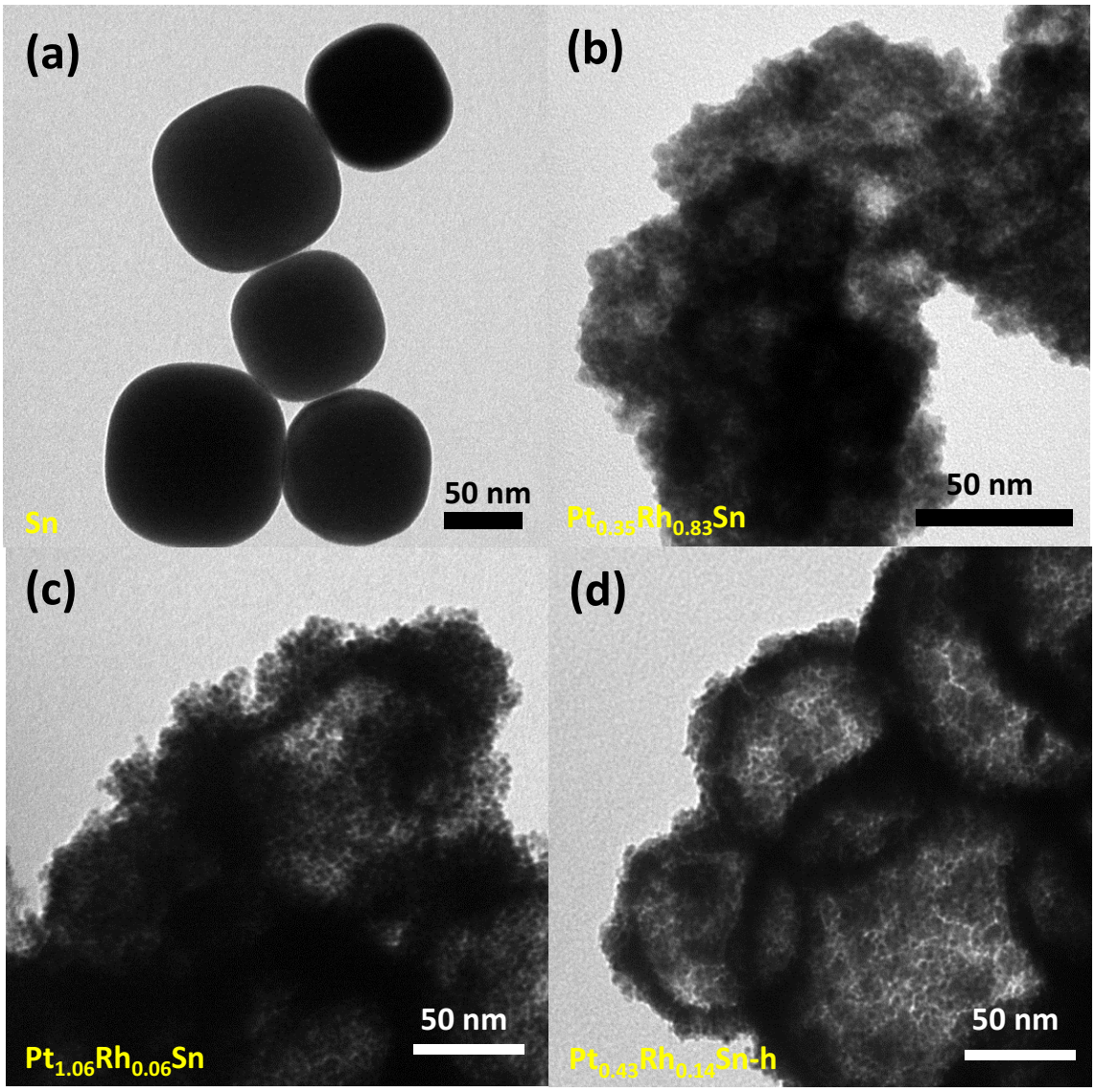

Figure 7.3.2. TEM images of (a) Sn seed, (b) $Pt_{0.35}Rh_{0.83}Sn$ heterodimer, (c) $Pt_{1.06}Rh_{0.06}Sn$ heterodimer and (d) $Pt_{0.43}Rh_{0.14}Sn$ hollow heterodimers

Pt-Rh-Sn heterodimers were also successfully synthesized. Figure 7.3.2 shows the morphology of Sn seeds and three representative Pt-Rh-Sn heterodimers. $Pt_{0.35}Rh_{0.83}Sn$ is a typical heterodimer with Rh more than Pt. $Pt_{1.06}Rh_{0.06}Sn$ is a typical heterodimer with Pt more than Rh. Both of the above heterodimers possess the morphology of small nanoparticles or cluster attach to Sn seeds. $Pt_{0.43}Rh_{0.14}Sn$-h is a representative heterodimers with small clusters attach to hollow Sn or alloyed nanoparticles. The formation of hollow nanoparticle is due to mechanism similar to Kirkendall effect[35, 182]. As is illustrated in Figure 7.3.3, the atoms at inner layers of nanoparticles diffuse out at faster rate than outer layer atoms toward inside, thus void in center is formed.

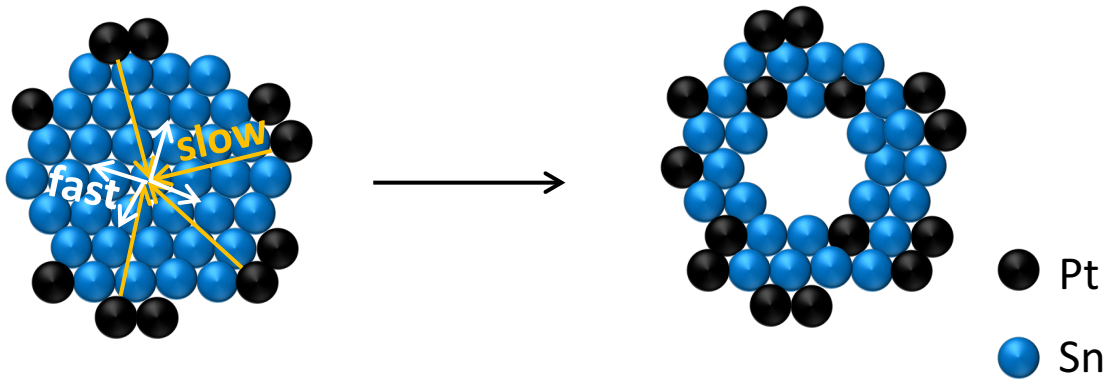

Figure 7.3.3. Schematic illustration of hollow nanoparticle formation.

The XRD patterns of the synthesized material are summarized in Figure 7.3.4. $Pt_{0.35}Rh_{0.83}Sn$ exhibit weak Pt pattern, indicating formation of Pt crystals only after galvanic replacement. Sn and Rh exist in amorphous form in $Pt_{0.35}Rh_{0.83}Sn$ heterodimers. $Pt_{1.06}Rh_{0.06}Sn$ exhibit peaks that could be attributed to (100), (101) and (102) facets of PtSn and (220) facet of $PtSn_2$. Indicating its crystal structure is a mixture of PtSn and $PtSn_2$, which is reasonable considering its Pt/Sn composition. $Pt_{0.43}Rh_{0.14}Sn$-h hollow heterodimers exhibited no XRD peak. Its amorphous crystal structure could likely be

attributed to different orientation of lattice fringes in shells---the lattices cancel out X-ray diffraction of each other and exhibit no total diffraction signal.

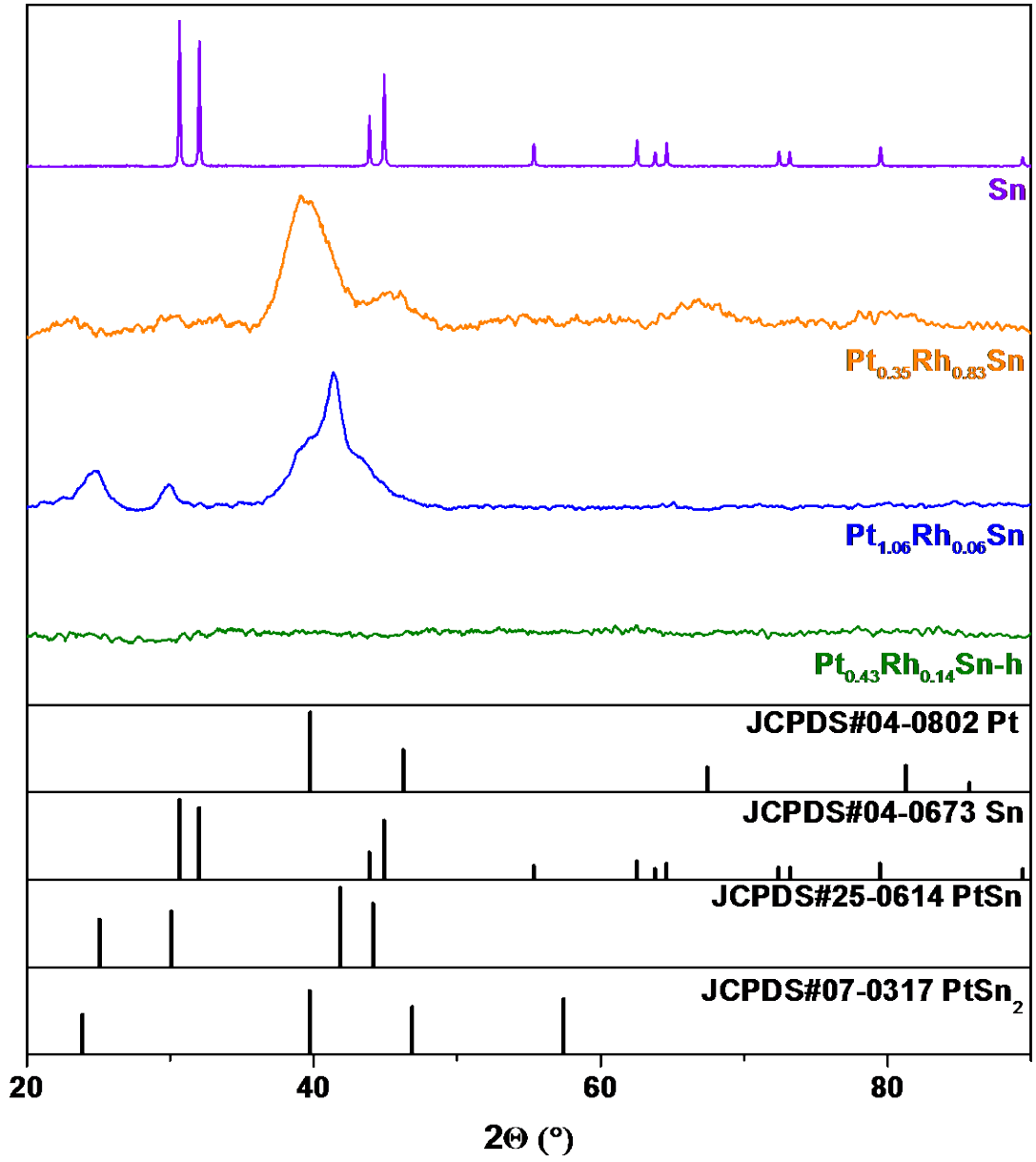

Figure 7.3.4. XRD patterns of Sn seed and various Pt-Rh-Sn heterodimers.

7.4 Catalytic performance for alcohol electro-oxidation

The catalytic performance toward EOR was evaluated for Pt/Rh/Sn alloys and Pt-Rh-Sn heterodimers. All of these ternary nanomaterials exhibited enhanced EOR activity

compared to pure platinum. This confirms the promotion effect of Rh reported by previous investigations[79, 179-180].

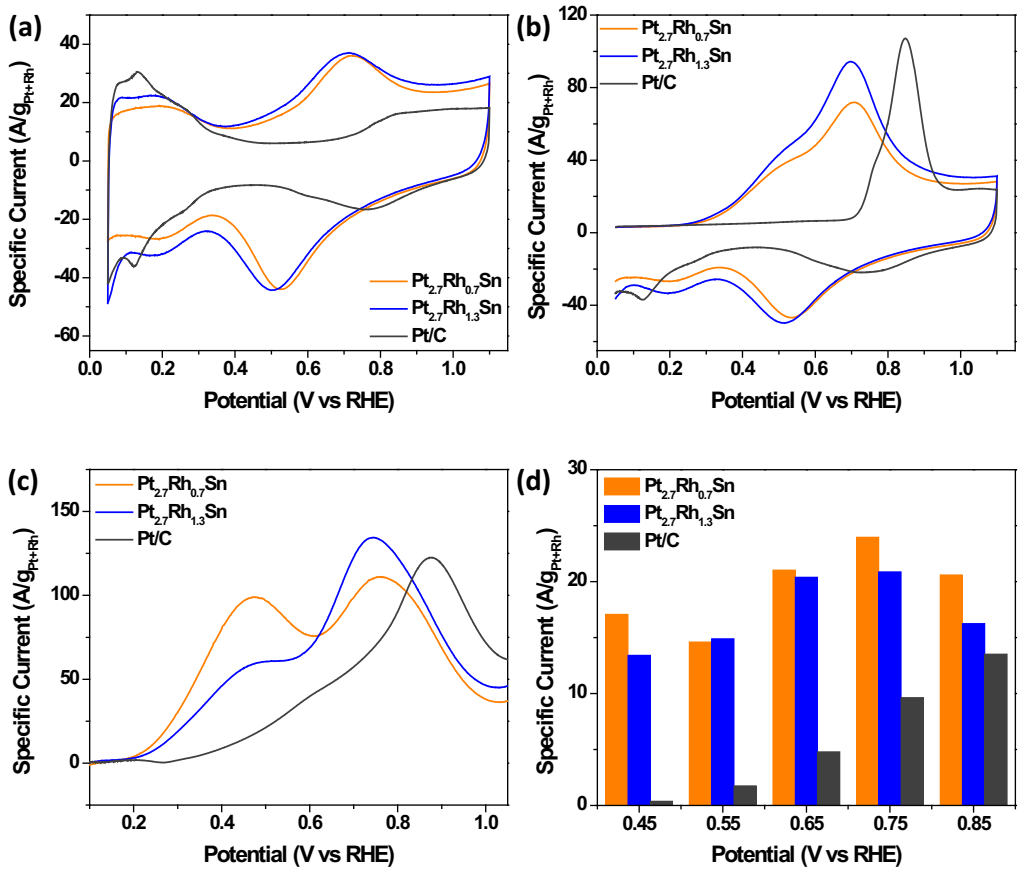

Figure 7.4.1. (a) Voltammogram and (b) CO stripping pattern of $Pt_{2.7}Rh_{0.7}Sn$, $Pt_{2.7}Rh_{1.3}Sn$ and Pt in 0.1M $HClO_4$. (c) positive cyclic voltammetry scan and (d) average chrono amperometry current density in 0.1M $HClO_4$ + 0.1M ethanol

Figure 7.4.1 summarizes the electrocatalytic behavior of $Pt_{2.7}Rh_{0.7}Sn$ and $Pt_{2.7}Rh_{1.3}Sn$. As is shown in Figure 7.4.1a, both $Pt_{2.7}Rh_{0.7}Sn$ and $Pt_{2.7}Rh_{1.3}Sn$ shows Hupd peak between 0.05 V to 0.35 V that could be attributed to Pt and Rh. The Hupd peak of $Pt_{2.7}Rh_{1.3}Sn$ is slightly larger than $Pt_{2.7}Rh_{0.7}Sn$, which is likely due to more Rh composition resulted in more Rh on surface. $Pt_{2.7}Rh_{0.7}Sn$ and $Pt_{2.7}Rh_{1.3}Sn$ exhibited OH adsorption peak almost at

same position with same area, indicating similar structure and configuration of Sn on surface. Their OH adsorption peak is about 120 mV lower than that of Pt due to easier OH_{ads} adsorption on surface induced by Sn. The CO stripping pattern of Pt/Rh/Sn alloy exhibited one major peak at 0.7 V and one shoulder peak at 0.5 V. The peak intensity of shoulder peak is ca. half of major peak. Both peaks exhibit lower peak potential than that of pure Pt (0.85 V), indicating stronger ability of oxidizing CO_{ads}. It's worth mentioning that this pattern is different from Pt/Sn alloys, which has much lower peak intensity. This difference is induced by addition of Rh element and could be attributed to two reasons below: i) the existence of Rh decreased the number of Sn on surface so the blocking effect of Sn is limited, more Pt sites exposed, ii) Rh possess intrinsic CO adsorption and oxidation property. Figure 7.4.1c and d summarizes the EOR performance of Pt/Rh/Sn alloys. The positive cyclic voltammetry scan is shown in Figure 7.4.1c. Both $Pt_{2.7}Rh_{0.7}Sn$ and $Pt_{2.7}Rh_{1.3}Sn$ exhibited an ethanol oxidation peak as low as ~0.48 V, indicating significantly enhanced EOR performance. Their other major peak is located at ~0.75 V which is still lower than the only peak of pure platinum (~0.88 V). In addition to peak position, $Pt_{2.7}Rh_{0.7}Sn$ and $Pt_{2.7}Rh_{1.3}Sn$ alloys also exhibited rather high peak intensity, with their major peak current density 90 % and 109 % of pure Pt respectively even normalized by the mass of Pt+Rh. It's also worth mentioning that the shoulder peak of $Pt_{2.7}Rh_{0.7}Sn$ possessed 80 % current density of Pt peak, which was also rather high. The average current density during 30 minutes amperometry summarized in Figure 7.4.1d provides a more accurate evaluation of EOR activity. $Pt_{2.7}Rh_{0.7}Sn$ and $Pt_{2.7}Rh_{1.3}Sn$ alloys exhibited higher current density than pure Pt at all potentials, reaching 44 and 35 times current density of Pt at 0.45 V, ~8 times of Pt at 0.55 V, ~4 times of Pt at 0.65 V and ~ 2

times at 0.75 V. Therefore the EOR activity of Pt/Rh/Sn alloy is significantly enhanced compared to pure Pt. The enhancement could be attributed to synergy between Rh and Sn introduced in Chapter 7.1. Briefly, Rh assist with C-C bond breaking and beta dehydrogenation while Sn alleviate CO_{ads} and $CH_{x,ads}$ poisoning[174, 178]. To examine the intrinsic EOR activity of Rh, Rh nanoparticles were synthesized and their EOR performance was investigated. As is shown in Figure 7.4.2, Rh nanoparticles possess no EOR activity by themselves. Therefore the enhancement of Pt/Rh/Sn alloy EOR activity is a result of synergistic effect between Pt, Rh and Sn.

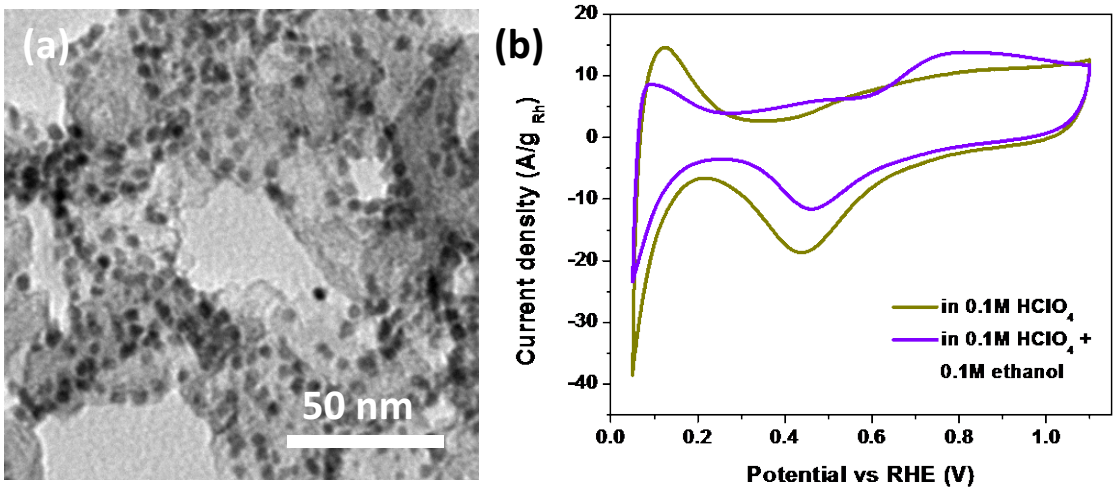

Figure 7.4.2. (a) TEM image of synthesized Rh/C catalyst. (b) cyclic voltammetry curve of Rh/C in 0.1M $HClO_4$ and 0.1M $HClO_4$ + 0.1M ethanol

It's also worth mentioning that the difference of Rh amount in $Pt_{2.7}Rh_{0.7}Sn$ and $Pt_{2.7}Rh_{1.3}Sn$ affected their surface properties. $Pt_{2.7}Rh_{1.3}Sn$ exhibited slightly larger surface area and lower EOR activity. The surface property of Pt/Rh/Sn alloys changed more similar to Pt after EOR, indicated by the Hupd reagion in voltammogram and higher peak at 0.68 V in CO stripping shown in Figure 7.4.3.

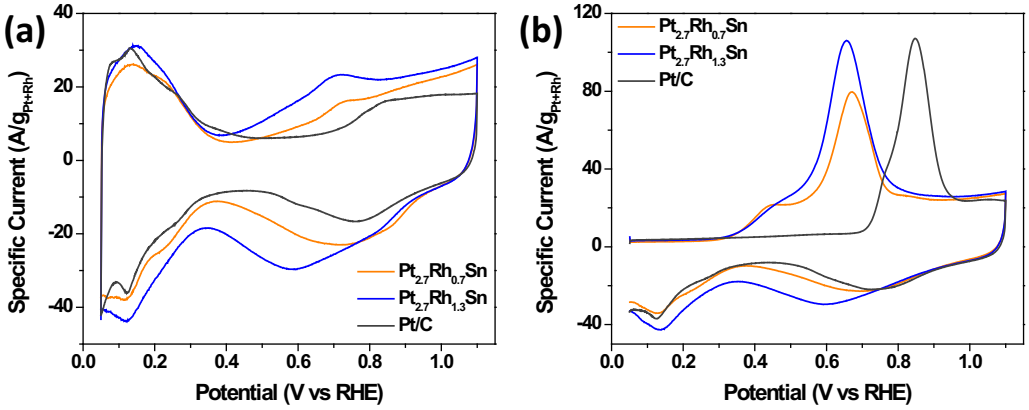

Figure 7.4.3. (a) voltammogram and (b) CO stripping pattern of $Pt_{2.7}Rh_{0.7}Sn$ and $Pt_{2.7}Rh_{1.3}Sn$ after ethanol oxidation reaction.

The surface property and catalytic performance of Pt-Rh-Sn heterodimers were also investigated. Figure 7.4.4 summarizes their surface properties.

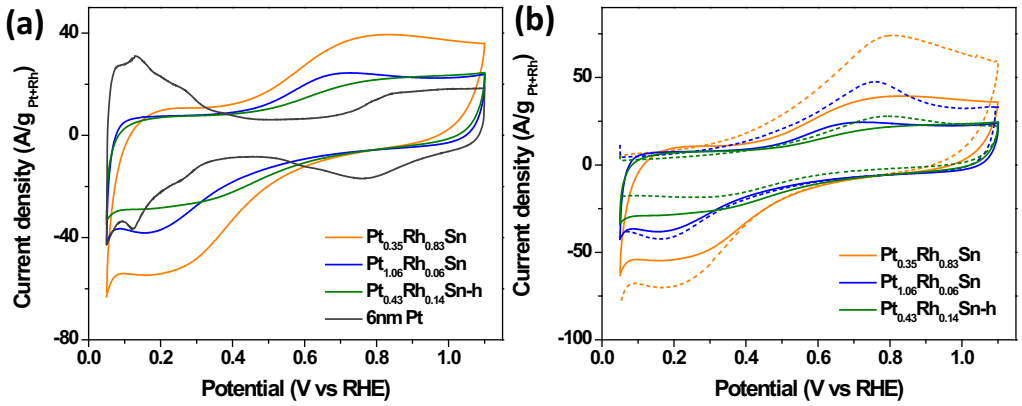

Figure 7.4.4. (a) Voltammogram and (b) CO stripping pattern of various Pt-Rh-Sn heterodimers in 0.1M $HClO_4$.

Figure 7.4.4a shows the voltammogram of various Pt-Rh-Sn heterodimers. All Pt-Rh-Sn heterodimers exhibited no Hupd peak regardless of compositions. They possessed OH adsorption peak centered at 0.7 V – 0.8 V. The voltammogram shows no Pt or Rh signal which could be attributed to two reasons: i) Sn is the only element existing on surface

and/or ii) Sn is blocking proton adsorption on surface Pt and Rh. It's also worth mentioning that the OH desorption peaks of Pt-Rh-Sn heterodimers were centered at 0.2 V – 0.3 V, which was much lower than those observed in Pt/Sn alloy and Pt-Sn heterodimers (~0.5 V). This could be attributed to the synergy of Rh and Sn increased OH affinity on surface and made them hard to desorb. The capacitance current of $Pt_{0.35}Rh_{0.83}Sn$ is significantly larger than the other two (see table 7.4.1, calculated by $\frac{Pt+Rh\ mass\ per\ molecule}{total\ molecular\ mass}$), this could be attributed to its relative lower Pt+Rh relative mass in heterodimers according to composition. $Pt_{0.43}Rh_{0.14}Sn$-h, however, had lowest Pt+Rh relative mass yet exhibited lowest capacitance current. This is likely due to larger cluster size of hollow nanoparticles. The CO stripping pattern of Pt-Rh-Sn heterodimers possessed only one peak centered at 0.75 V – 0.8 V. Although the CO stripping patterns look similar to voltammogram, they possess higher peak that could be attributed to CO oxidation if compared to voltammogram.

Table 7.4.1 Relative Pt+Rh mass in Pt-Rh-Sn heterodimers

Composition	Relative Pt+Rh mass
$Pt_{0.35}Rh_{0.83}Sn$	0.56
$Pt_{1.06}Rh_{0.06}Sn$	0.64
$Pt_{0.43}Rh_{0.14}Sn$-h	0.45

This peak position is slightly lower than pure Pt, indicating stronger ability of oxidizing CO_{ads}. However, the lack of secondary peak ~0.45 V is different from all previously investigated materials. This is likely due to various Pt and Rh sites exhibit CO oxidation peaks all from 0.3 V to 1.1 V and all oxidation signals are connected together. Therefore

no separate peaks were observed. The Pt-Rh-Sn heterodimers also exhibited interesting phenomena: no EOR activity could be observed at all with pristine catalysts. As is shown in Figure 7.4.5, all three Pt-Rh-Sn heterodimers exhibit no or tiny EOR activity since their cyclic voltammetry curve in 0.1M $HClO_4$ + 0.1M ethanol is just slightly higher or same as voltammogram in 0.1M $HClO_4$. Combining the results from voltammogram and CO stripping, it is reasonable to hypothesize that catalyst surface are occupied by Rh and Sn, while Pt all diffused into inner layers of heterodimer during galvanic replacement. In order to migrate Pt atoms onto catalyst surface and reveal EOR activity, scanning in CO saturated electrolyte (so called CO annealing[166]) was first conducted. CO annealing successfully exposed Pt sites in $Pt_{1.06}Rh_{0.06}Sn$ to surface and revealed its EOR activity. However, for the other two Pt-Rh-Sn with less Pt relative content, CO annealing was not sufficient and KOH treatment had to be implemented. After 10 scans in 0.1M KOH a significant portion of surface Sn was dissolved and sufficient Pt sites were exposed, $Pt_{0.35}Rh_{0.83}Sn$ and $Pt_{0.43}Rh_{0.14}Sn$-h revealed EOR activity.

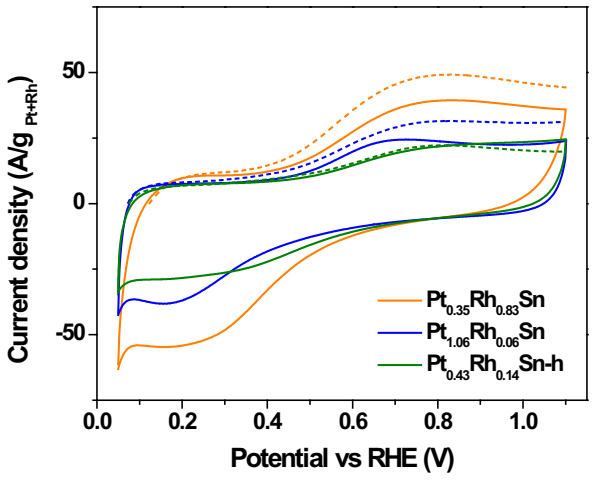

Figure 7.4.5. Positive cyclic voltammetry scan in 0.1M $HClO_4$ + 0.1M ethanol and comparison with voltammogram in 0.1M $HClO_4$

Table 7.4.2 Pt-Rh-Sn composition after treatment

Original	After treatment
$Pt_{0.35}Rh_{0.83}Sn$	$Pt_{1.46}Rh_{4.13}Sn$
$Pt_{1.06}Rh_{0.06}Sn$	$Pt_{1.26}Rh_{0.04}Sn$
$Pt_{0.43}Rh_{0.14}Sn$-h	$Pt_{1.45}Rh_{0.55}Sn$

Table 7.4.2 summarizes the composition of Pt-Rh-Sn heterodimers after treatment. $Pt_{0.35}Rh_{0.83}Sn$ and $Pt_{0.43}Rh_{0.14}Sn$-h both experienced Sn loss of 68% and 49%. Figure 7.4.6 shows the TEM images of Pt-Rh-Sn heterodimers after treatment. $Pt_{1.06}Rh_{0.06}Sn$ exhibited no significant morphology change while $Pt_{0.35}Rh_{0.83}Sn$ and $Pt_{0.43}Rh_{0.14}Sn$-h showed nanoparticle detach from heterodimer matrix. In addition, $Pt_{0.43}Rh_{0.14}Sn$-h lost its hollow sphere morphology likely due to collapse of hollow structure induced by leaching of Sn atoms.

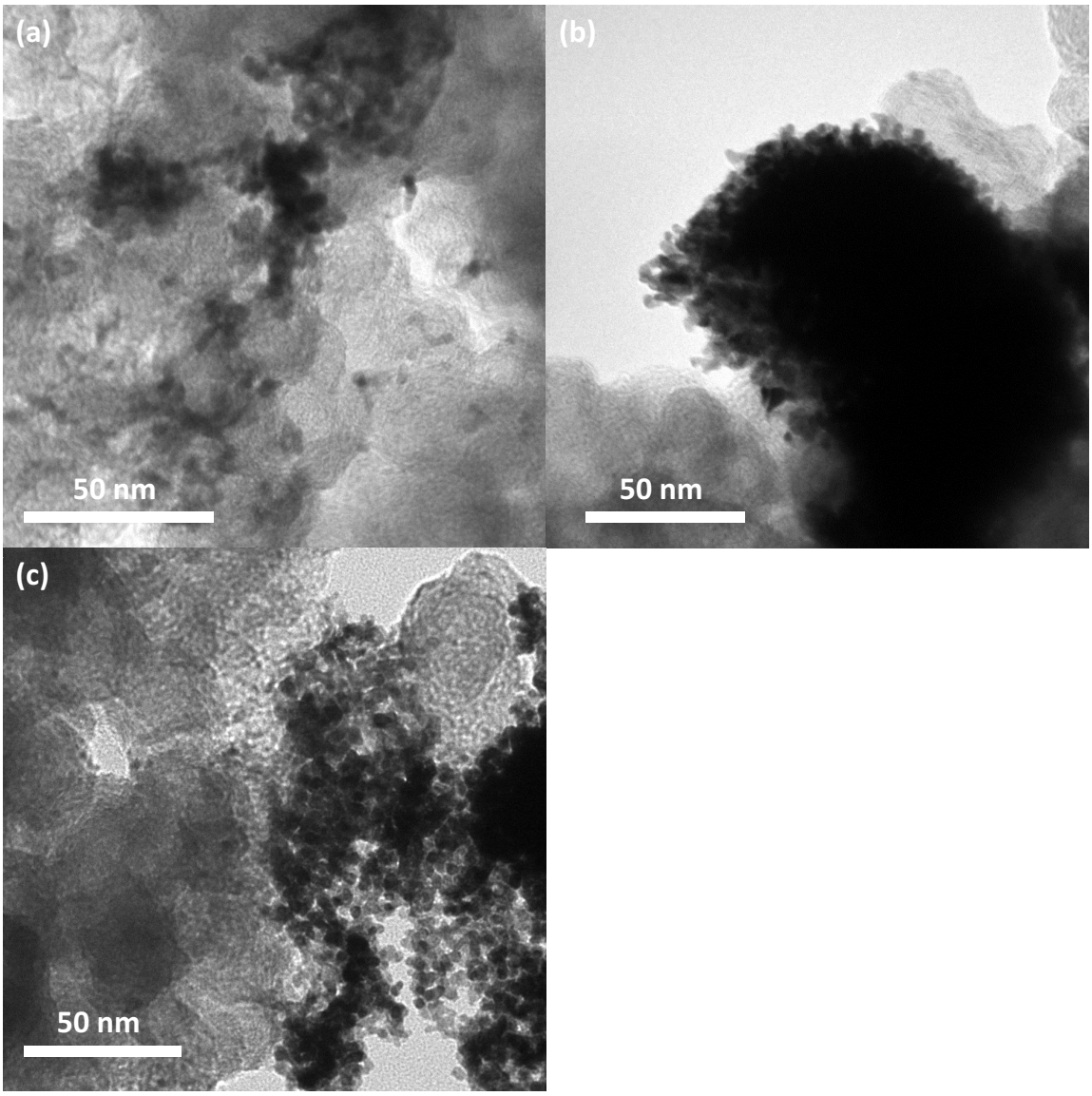

Figure 7.4.6. TEM images of (a) $Pt_{0.35}Rh_{0.83}Sn$, (b) $Pt_{1.06}Rh_{0.06}Sn$ and (c) $Pt_{0.43}Rh_{0.14}Sn$-h catalysts after treatment.

Figure 7.4.7 summarizes the surface property and EOR catalytic performance of treated Pt-Rh-Sn heterodimers. All Pt-Rh-Sn heterodimers exhibited voltammogram consisting of Hupd and OH adsorption region as is shown in Figure 7.4.7a. The Hupd region could be attributed to Pt and Rh on surface while the OH adsorption region is formed via

synergy between Pt, Rh and Sn. $Pt_{0.35}Rh_{0.83}Sn$ exhibited lowest peak position (0.63 V) of OH adsorption region, this is likely due to the high relative Rh content induced voltammogram similar to Rh[183]. $Pt_{1.06}Rh_{0.06}Sn$ and $Pt_{0.43}Rh_{0.14}Sn$-h exhibited OH adsorption peak maximized at 0.75 V, similar to that of Pt/Sn and Pt/Rh/Sn alloys. $Pt_{1.06}Rh_{0.06}Sn$ exhibited higher OH adsorption peak than $Pt_{0.43}Rh_{0.14}Sn$-h because it consisted more Sn after treatment. Figure 4.4.8b presents the CO stripping pattern of three Pt-Rh-Sn heterodimers after KOH/CO treatment. The CO oxidation pattern of Pt-Rh-Sn heterodimers could be divided into three peaks centered at ~ 0.45 V, ~ 0.65 V and ~0.8 V respectively. The lower two peaks could likely be attributed to Sn coordinated Pt and Rh[116, 184]. $Pt_{1.06}Rh_{0.06}Sn$ exhibit CO stripping peak onset potential at 0.2 V, which is ~ 100 mV lower than the other two. This is likely due to higher relative Sn content in composition after treatment.

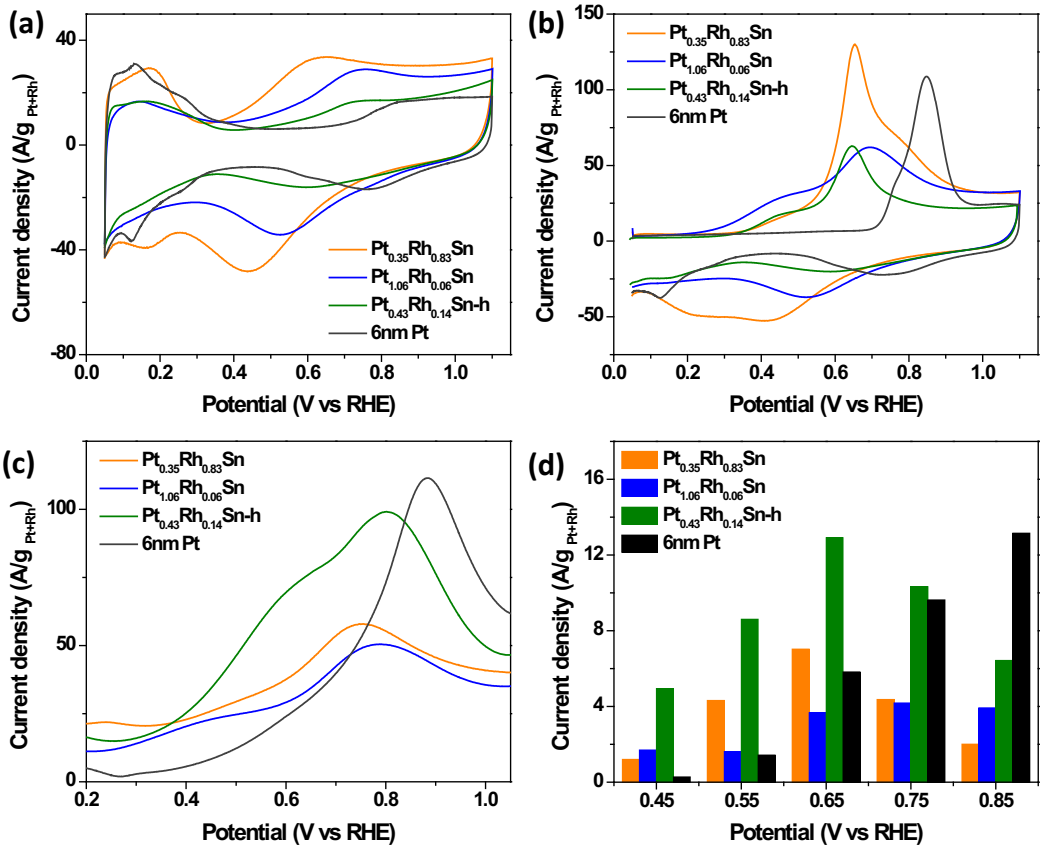

Figure 7.4.7. (a) Voltammogram and (b) CO stripping pattern of various Pt-Rh-Sn heterodimers after treatment in 0.1M $HClO_4$. (c) positive cyclic voltammetry scan and (d) average current density during 30 minutes amperometry in 0.1M $HClO_4$ + 0.1M ethanol.

The EOR activity of Pt-Rh-Sn heterodimers were investigated. As is shown in Figure 7.4.7c, Pt-Rh-Sn heterodimers exhibit lower onset potential (~0.3 V) and shoulder peak (0.4 – 0.6 V), indicating their enhanced EOR activity compared to Pt. Figure 7.4.7d further demonstrated their enhanced EOR activity under steady state environment. All three Pt-Rh-Sn heterodimers exhibited current density 4.3, 6.1, 17.5 times of Pt at 0.45 V and 3.1, 1.1, 6.1 times of Pt at 0.55 V. $Pt_{0.35}Rh_{0.83}Sn$ and $Pt_{0.43}Rh_{0.14}Sn$-h further exhibited superior activity than Pt at 0.65 V. The enhanced activity could be attributed to synergy between Pt, Rh and Sn as is discussed for Pt/Rh/Sn alloys. Among the three Pt-Rh-Sn

heterodimers, $Pt_{0.43}Rh_{0.14}Sn$-h exhibited highest activity, followed by $Pt_{0.35}Rh_{0.83}Sn$. The high activity could be attributed to the appropriate portion of Rh and Sn, providing Rh and Sn to facilitate reaction rate on Pt sites while leaving sufficient Pt ensemble for EOR.

7.5 Product selectivity

The product selectivity of Pt/Rh/Sn alloys and Pt-Rh-Sn heterodimers were investigated.

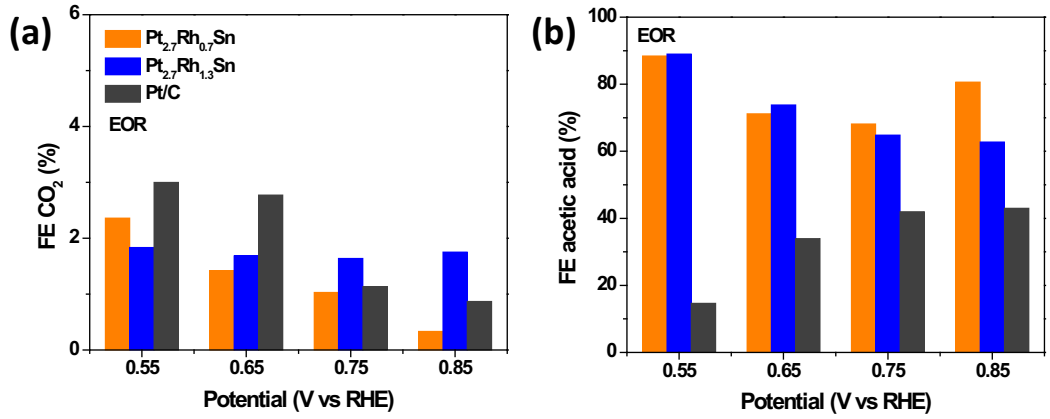

Figure 7.5.1. (a) CO_2 and (b) acetic acid faradaic efficiency during EOR catalyzed with Pt/Rh/Sn alloys

Figure 7.5.1 summarizes the product selectivity of Pt/Rh/Sn alloys during EOR. Both $Pt_{2.7}Rh_{0.7}Sn$ and $Pt_{2.7}Rh_{1.3}Sn$ exhibited overall low CO_2 selectivity. Their CO_2 faradaic efficiencies are 2.3% and 1.8% at 0.55 V, 1.4% and 1.7% at 0.65 V, all slightly lower than 6nm Pt. $Pt_{2.7}Rh_{0.7}Sn$ continued to show lower CO_2 selectivity than Pt at higher potentials, while $Pt_{2.7}Rh_{1.3}Sn$ exhibited CO_2 faradaic efficiency slightly higher than Pt at 0.75 V and 0.85 V. Both Pt/Rh/Sn alloys exhibited rather high acetic acid faradaic efficiency, with $Pt_{2.7}Rh_{0.7}Sn$ between 68% to 88% and $Pt_{2.7}Rh_{1.3}Sn$ decreasing from 89% to 63%. The above results indicate that Pt/Rh/Sn alloys favors C_2 product pathway much more than C_1 product pathway. The CO_2 selectivity during Ethylene Glycol Oxidation (EGO) was also investigated and the results were presented in Figure 7.5.2.

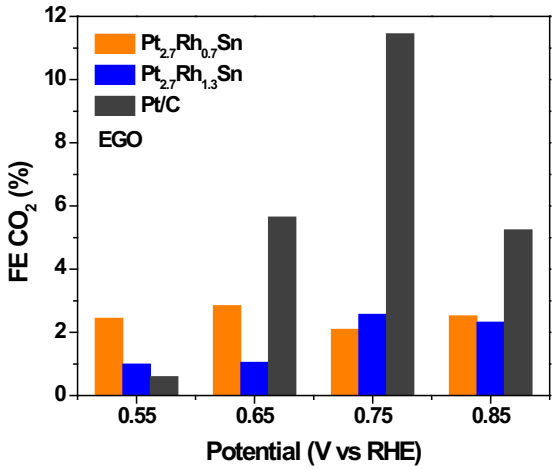

Figure 7.5.2. CO_2 faradaic efficiency of Pt/Rh/Sn alloys during ethylene glycol oxidation. Both Pt/Rh/Sn alloys still exhibited rather low CO_2 selectivity. $Pt_{2.7}Rh_{0.7}Sn$ showed CO_2 faradaic efficiency stable between 2.1% to 2.8%. $Pt_{2.7}Rh_{1.3}Sn$ started from 1% at 0.55 V and reached maximum at 2.6% at 0.75 V. Their CO_2 faradaic efficiency is slightly higher than Pt at 0.55 V and lower than Pt as potential increases.

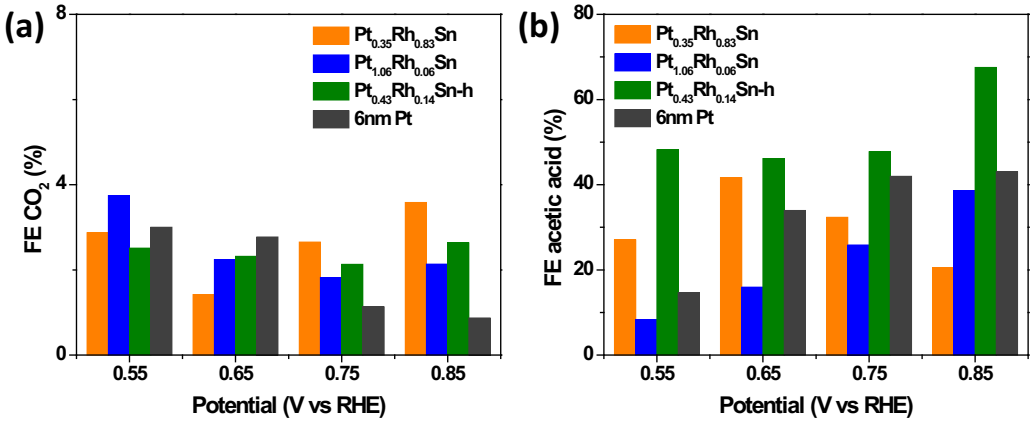

Figure 7.5.3. (a) CO_2 and (b) acetic acid faradaic efficiency of Pt-Rh-Sn heterodimers during EOR.

The product selectivity of Pt-Rh-Sn heterodimers were also investigated. $Pt_{1.06}Rh_{0.06}Sn$ exhibited enhanced CO_2 selectivity compared to Pt, with faradaic efficiency of 8% at

0.55V and around 4% between 0.65 V and 0.85 V. The CO_2 faradaic efficiency of the other two heterodimers were around 2%, similar to that of Pt. The enhanced CO_2 selectivity of $Pt_{1.06}Rh_{0.06}Sn$ could be attributed to the synergy between Pt, Rh and Sn. $Pt_{0.35}Rh_{0.83}Sn$ and $Pt_{0.43}Rh_{0.14}Sn$ lost significant portion of Sn during KOH treatment therefore the synergistic effect was lost.

7.6 Conclusion

Various Pt/Rh/Sn alloys and Pt-Rh-Sn heterodimers were successfully synthesized. According to characterization of XRD, 3nm $Pt_{2.7}Rh_{0.7}Sn$ and $Pt_{2.7}Rh_{1.3}Sn$ possessed crystal structure of Pt and Pt-Rh-Sn exhibited crystal structure of Pt, Pt/Sn alloy or amorphous. Pt/Rh/Sn alloys exhibited significantly enhanced EOR activity compared to Pt. Pristine Pt-Rh-Sn heterodimers possess no EOR activity and requires CO annealing or KOH treatment to reveal activity. Pt/Rh/Sn alloys exhibit no enhancement in CO_2 selectivity likely due to lack of synergistic effect in such small size particles. $Pt_{1.06}Rh_{0.06}Sn$ exhibited enhanced CO_2 selectivity than Pt and the enhancement could be attributed to the synergy between Pt, Rh and Sn. No CO_2 selectivity enhancement was observed for $Pt_{0.35}Rh_{0.83}Sn$ and $Pt_{0.43}Rh_{0.14}Sn$ and this could likely be attributed to their composition is inappropriate for C1 product pathway.

Chapter 8. Electrocatalytic Oxidation of Glycerol on Platinum

Adapted with permission of Liu,Y. *et al.* J. Phys. Chem. C, 2019, 123, 1, 426-432

8.1 Introduction

Glycerol is conventionally used in the food industry as a sweetener or humectant. It is also a byproduct of biodiesel from the transesterification process.[185-186] The fast-growing biodiesel industry over the recent years has resulted in a high surplus of glycerol, owing to the generation of ~1 kg of glycerol per 10 kg of biodiesel produced.[187] In many biodiesel plants, glycerol is treated merely as a waste stream, burned without producing any additional value.[188] Consequently, it is necessary to find alternative applications of glycerol, by either converting it into more valuable chemicals or harvesting the energy to produce hydrogen or electricity.[189]

Prior efforts to utilize glycerol have primarily focused on chemical conversions.[187, 189-191] Besides conventional thermal catalysis approaches, electrochemical methods have also been investigated for transformation reactions.[192-195] However, the electro-oxidation of glycerol to extract out the energy as electricity has received less attention.[196-199] The complete oxidation of glycerol to CO_2 delivers 14 electrons per molecule at an equilibrium potential of −0.01 V (versus the standard hydrogen electrode, SHE; see the section 8.5 for the thermodynamic calculations), giving rise to a high energy density of 6.4 kWh/L. This process is challenged by the lack of efficient electrocatalysts for the complete oxidation of glycerol. Pt is the most studied electrocatalyst for the glycerol oxidation reaction (GOR), but partially oxidized C_2 and C_3 compounds (oxalic

acid, glyceric acid, glyceraldehyde, dihydroxyacetone, glycolic acid, etc.) are commonly found to dominate the products.[193, 200-203] Nevertheless, CO_2 has been detected at potentials above 0.6 V in previous *in situ* infrared spectroscopic studies.[200] It has been proposed that CO_2 could be formed via two different pathways: at low potentials (<0.6 V), CO_2 is generated through oxidation of *CO (* denotes an adsorption site on the catalyst surface) resulting from C-C bond cleavage; at high potentials (>1.1 V), CO_2 can be formed by the direct interaction between adsorbed glycerol and *OH.[196] Meanwhile, alternative electrocatalysts to Pt have also been extensively studied for improved kinetics of GOR, including Pd,[204-205] bimetallics such as Pt-Ru and Pt-Rh,[206] Pt-Bi[207] and Pt-Sb[208], and more sophisticated systems such as Rh-doped Pt-Ir-O_x,[209] but CO_2 is still commonly found to be a minor product on these catalysts. It is noticed that most of these studies employ infrared spectroscopy (IR) for the detection of CO_2 and/or *CO. As a linear spectroscopy technique, IR detects molecules both within the electrolyte and adsorbed on the electrodes, which is usually complicated by the mixing of signals from reaction intermediates and products.

Here, we report the investigation of glycerol electro-oxidation on Pt by combining surface-specific spectroelectrochemical and product-resolved electrocatalytic studies. We first examined the GOR on polycrystalline platinum (Pt-poly) electrodes, where sum frequency generation (SFG) spectroscopy was used to track the potential-dependent adsorption of $^{*}CO$ – the key reaction intermediate for the complete oxidation of glycerol. Further, we performed product-resolved electrocatalytic studies on high-surface-area platinum/carbon (Pt/C) electrocatalysts and used gas chromatography-mass spectrometry (GC-MS) to analyze the product distributions under potentiostatic conditions. We also

conducted comparative studies on isotopically labeled glycerol ($HO^{12}CH_2$-$^{13}CH(OH)$-$^{12}CH_2OH$) to gain further insights into the mechanism of C-C bond cleavage and the complete oxidation pathways for glycerol.

8.2 Experimental Methods

8.2.1 Materials and characterization

Glycerol (>99%) and perchloric acid were purchased from Sigma Aldrich. Commercial Pt/C catalyst was obtained from Tanaka Inc. TEM images were collected with a 120 kV FEI Tecnai-12 TWIN microscope operating at 100 kV.

The Pt-poly electrode was prepared by melting Pt pellets (purchased from Kurt J. Lesker) and casting into an ingot of 5 mm in diameter, 5 mm in height. A Pt wire was attached to its bottom side via laser welding. The Pt ingot and wire was then inserted into a PEEK sleeve (with a through hole in the center) and polished to mirror finish before it was used as the working electrode. The working electrode was connected to a potentiostat by clamping the Pt wire. The electrode was subjected to potential scans in Ar-saturated 0.1 M $HClO_4$ before each spectroscopic measurement until the voltammogram becomes stable.

8.2.2 SFG measurements

SFG measurements were conducted with a home-built spectro-electrochemical cell (see Figure 8.2.1) designed according to a previous report.[210] A Pt wire and $Hg/HgSO_4$ were used as counter and reference electrodes respectively. The polycrystalline Pt electrode was covered with a CaF_2 window. The distance between Pt surface and the window was controlled to be 12 micrometers using a Teflon spacer (purchased from Harrick Corporation). Spectra were collected in the range of 1950 cm^{-1} to 2150 cm^{-1} at steady

potentials from 0.05 V to 0.8 V. The potential was applied using a Metrohm PGSTAT302N potentiostat and was held constant at each point for 3 minutes. All spectra were collected in PPP configuration, which means that the plane of incidence of the generated SFG beam, visible and IR beam are all parallel to electric field vector. Peaks in the SFG spectra were fitted using a Lorentzian function[211-213] and the peak intensities are reported based on the fitting results.

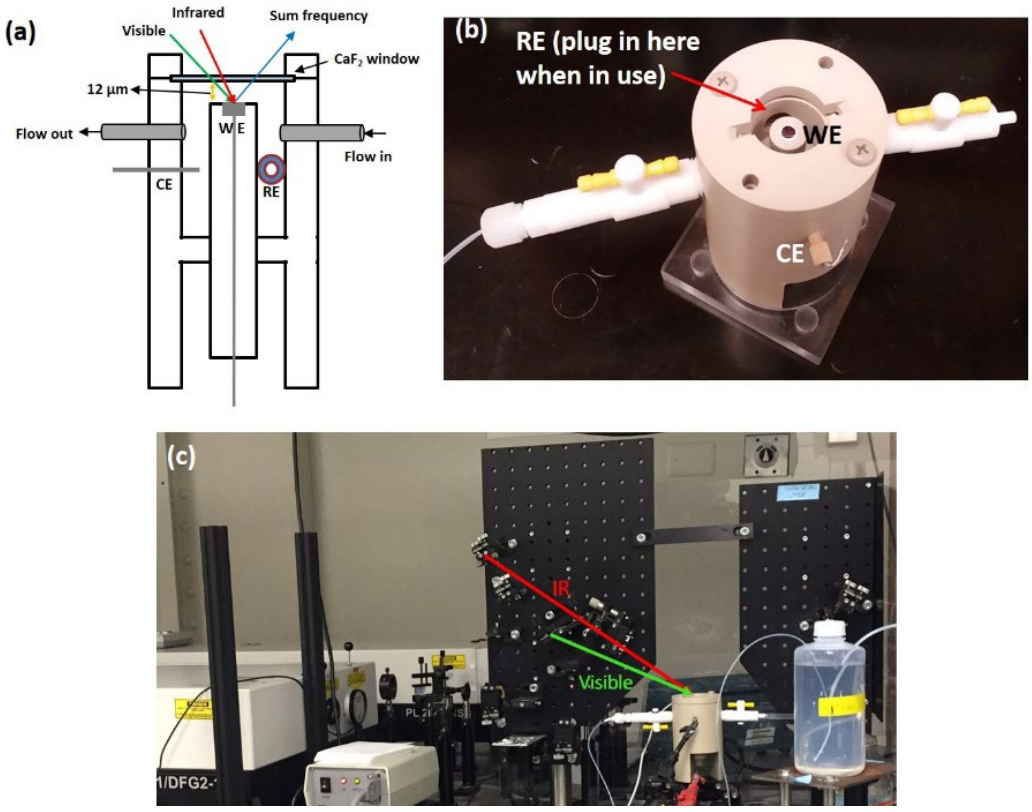

Figure 8.2.1. (a) Schematics, and (b) photo of the electrochemical cell. (c) Photo of the experimental setup for the spectro-electrochemical study.

5.2.3 Electrochemical studies

0.1 M of $HClO_4$ was used as the electrolyte throughout this study. Three-electrode measurements were conducted with a Pt wire as the counter electrode and Ag/AgCl as the reference electrode. All measurements were conducted with iR compensation. A

commercial Pt/C catalyst was dispersed in aqueous solution containing 10% isopropanol and 0.05% weight of Nafion at a concentration of 1 mg/ml. Pt/C loading on rotating disk electrodes was controlled to be ~0.04 mg_{Pt}/cm^2_{disk}. Cyclic voltammogram, CO stripping and GOR polarization curves were all recorded with a scan rate of 50 mV/s.

CO_2 selectivity was measured using a gas-tight electrolysis cell connected to GC-MS.[114] A piece of glassy carbon plate (2×2 cm) was used as the working electrode. One milliliter of Pt/C catalyst ink was drop cast onto the glassy carbon plate and allowed to dry out. Pt mesh and $Hg/HgSO_4$ were used as the counter and reference electrode, respectively. During the measurements, the electrode was held at a given potential with a He flow (10 mL/min) continuously passing through the working electrode compartment. A gas chromatograph equipped with a mass spectrometer (GC – MS, Shimadzu QP2010SE) was used to analyze the gas-phase products periodically.

8.3 Results and discussion

Figure 8.3.1a shows the cyclic voltammogram (CV) and CO stripping pattern recorded on the Pt-poly electrode in 0.1 M of $HClO_4$. We observed that the blank CV exhibits hydrogen underpotential deposition (H_{upd}) peaks at $E < 0.4$ V and hydroxyl adsorption at 0.8 – 1.1 V, with a capacitive double-layer region located in between. We can assign the pronounced peak at ~0.8 V in the cathodic scan to the reduction of surface oxides and the desorption of *OH.[214] We observed that the CO stripping profile exhibits a double-peak feature at 0.74 and 0.77 V (Figure 8.3.1a), which can be assigned to the oxidation of *CO on various types of Pt sites, including low-index facets and stepped surfaces.[215-217] We also observed a weak shoulder peak around ~0.5 V, attributable to the pre-oxidation of *CO on defect sites.[125, 218]

With glycerol added into the electrolyte, the measured voltammogram exhibits anodic peaks in both the positive and negative scans, which can be associated with the GOR (Figure 8.3.1b). Albeit being substantially suppressed, we can still discern H_{upd} features at $E < 0.3$ V. We noticed that the anodic peaks experienced a gradual increase in intensity during the first several scans and became stable after about 10 scans, whereas we observed no significant changes for the H_{upd} region during this process. By comparing the voltammogram to the blank CV, we determined the onset of GOR to be at ca. 0.4 V in the positive scan. After it became stable, the voltammogram exhibits the first anodic peak at 0.55 V with a current density of 0.11 mA/cm^2 and the second peak at 0.80 V with the peak current density reaching 0.39 mA/cm^2 in the positive scan, with the latter also associated with a shoulder feature at 0.74 V (Figure 8.3.1b). Anodic features associated with the GOR are also present in the negative scan, but only with one broad peak spreading from ca. 0.9 to 0.4 V. The peak current density is reached at 0.61 V in the negative scan, the value (0.22 mA/cm^2) of which is much smaller than that found for the positive scan. A shoulder feature around 0.76 V is also discernible.

The GOR polarization behavior shows some interesting correlations to the features exhibited in the CO stripping profile. The first anodic peak at 0.55 V overlaps with the pre-oxidation feature present in CO stripping. The main peak at 0.80 V and its shoulder peak correlates with the double-peak feature exhibited in CO stripping. Such a correlation suggests that the surface coverage of *CO, or the oxidative removal of *CO, is likely a rate-determining factor in the GOR. The appearance of oxidation peak at lower potentials in the negative scan than in the positive scan is well correlated to the behavior of OH_{ad} exhibited in the blank CVs and can be attributed to the blocking of surface sites

by OH_{ad} when the potential was scanned from the high end. The activation of GOR during the initial potential cycles is different from the general scenery with decreasing GOR current densities by scanning seen in the previous studies,[208, 219-220] and it was not observed in our previous study of ethanol and ethylene glycol oxidation on Pt-poly.[221] We can ascribe this phenomenon to the slow process of building up quasi-equilibrium for the GOR. It could be due to the high viscosity and relatively low diffusivity of glycerol, and/or the accumulation of partially oxidized intermediates (glyceraldehyde, glyceric acid, tartonic acid, etc.) on the surface and in the double-layer region of the electrolyte. However, surface restructuring during the scans, such as the formation of more low-coordinated surface sites (such as steps and defects) that are more active for the GOR, cannot be excluded.[222] It should be pointed out that the peak current density of GOR measured here is substantially lower than what we reported before for ethanol and glycerol oxidation (about one third),[221] indicating more sluggish kinetics of the GOR than for the electro-oxidation of C_2 alcohols.[203, 223-224]

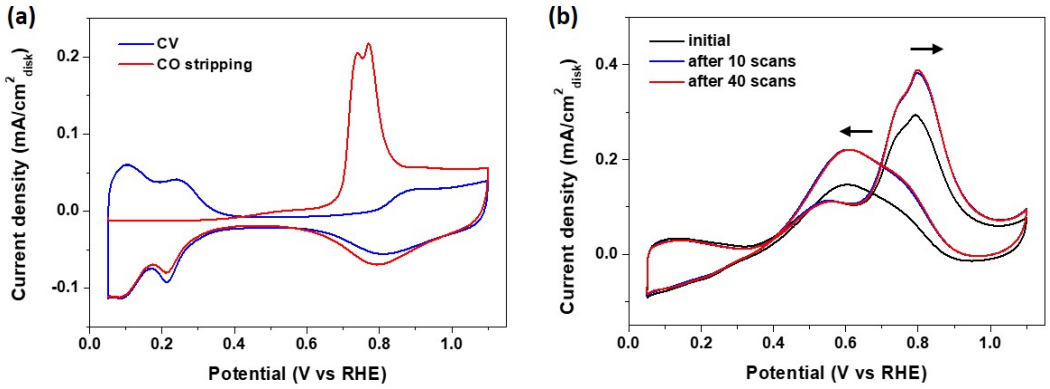

Figure 8.3.1. Electrochemical studies of Pt-poly. (a) Cyclic voltammogram and CO stripping pattern in 0.1 M $HClO_4$. (b) Cyclic voltammogram collected in 0.1 M $HClO_4$ + 0.1 M glycerol.

Considering that *CO is likely the intermediate toward CO_2 formation, we used SFG spectroscopy to track its signal over the course of GOR. Figures 8.3.2a and b present the spectra recorded at various potentials in the wavelength region of 1950 – 2150 cm^{-1} during the positive and negative scans, respectively. The major peak at 2045-2070 cm^{-1} can be assigned to linearly bonded CO (CO_L).[225-226] The CO_L peak appears at potentials as low as 0.05 V, indicating the existence of Pt sites that are capable of cleaving the C-C bond in glycerol at low potentials. Such an observation is consistent with the previous reports using linear IR or differential electrochemical mass spectrometry (DEMS) techniques[203, 227-228] (although some other IR studies did not observe CO_L in the low-potential region[206, 229-231]) and also in line with our previous findings for ethanol and ethylene glycol oxidation[221]. The CO_L peak intensity increases slowly as the potential rises in the positive scan, reaching a maximum at ~0.4 – 0.5 V, and then drops steeply at higher potentials (Figure 8.3.2c). The potential for reaching this maximum is in line with the onset for CO stripping (Figure 8.3.1a) and the first anodic peak of the GOR voltammogram (Figure 8.3.1b), confirming the rate-determining role of *CO oxidation in the GOR electrocatalysis.[203] The CO_L peak intensity disappears at 0.8 V, where *CO is likely completely removed and oxidized into CO_2. The CO_L peak position exhibits a slight shift toward higher wavenumbers at more positive potentials, i.e., from 2050 cm^{-1} at 0.05 V to 2063 cm^{-1} at 0.7 V (Figure 8.3.2a), indicating weaker binding of *CO on the electrode surface at higher potentials, which could be due to the electrical field effects and/or stronger dipole-dipole interactions at higher coverages.[232-235] Our observations to a large extent resemble the report by Martins *et al*.,[227] but do not include the transition from bridge bonded CO (CO_B) to CO_L as seen by Schnaidt *et al.* in the low-potential region

(<0.3 V)[203]. The absence of CO_B feature in the spectro-electrochemical studies using perchloric acid versus the presence of this feature when sulfuric acid is used has been known in the electrocatalysis for ethanol oxidation and ascribed to the relatively low coverages of *CO in the latter case.[77, 147, 236-238] In the negative scan, the CO_L peak intensity increases rather slowly, and is generally much lower than that for the positive scan. This behavior can be correlated to the difference in positive and negative scans exhibited in the voltammograms as shown in Figure 1b and underscores the aforementioned important role of *CO.

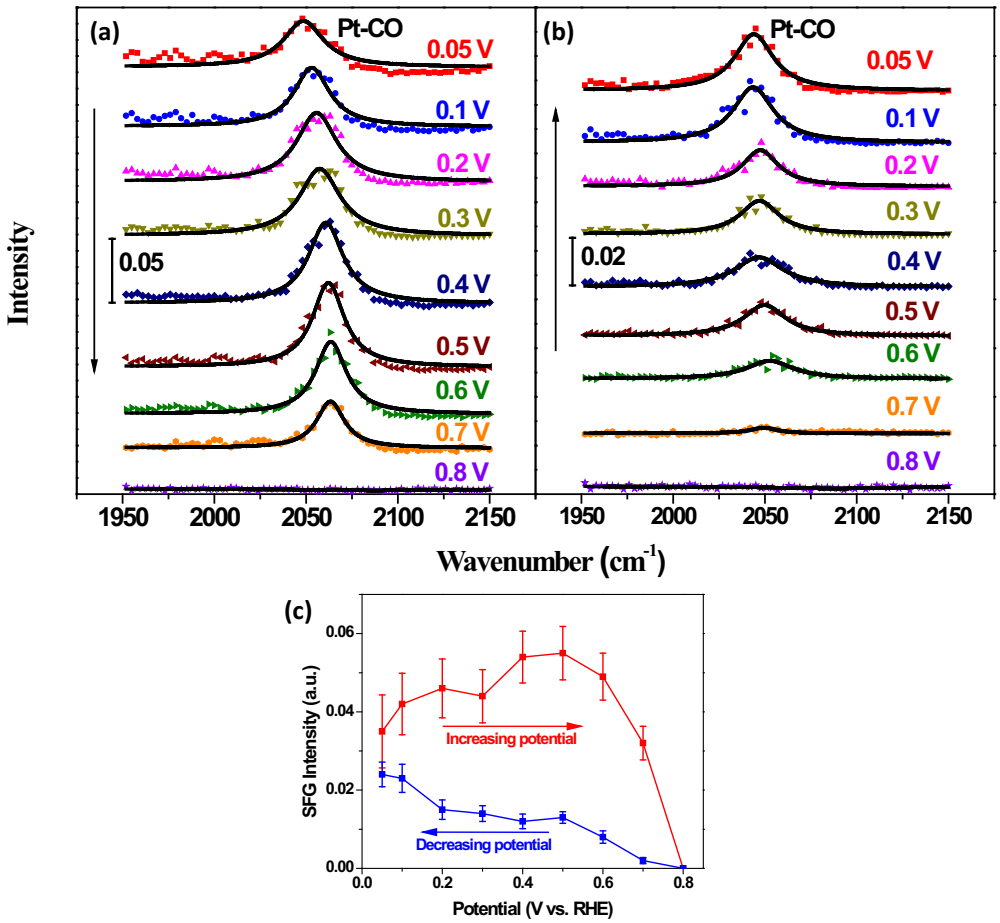

Figure 8.3.2. Spectro-electrochemical studies for the GOR. (a, b) SFG spectra recorded during (a) positive and (b) negative scans. (c) Comparison of CO_L peak intensity at various potentials based on curve fitting of the single peak.

With *CO observed at low potentials (<0.3 V) from the spectro-electrochemical studies, we further conducted product-resolved electrocatalytic studies to examine the capability of Pt for oxidizing glycerol to CO_2. These studies were conducted on high-surface-area Pt/C catalysts under potentiostatic conditions using a H-type electrochemical cell.[221] The employed commercial Pt/C catalyst has an average particle size of ~6 nm (see the inset in Figure 8.3.3a). The CV and CO stripping pattern recorded on Pt/C largely resemble those for Pt-poly, albeit with larger double-layer width due to the presence of

carbon black (Figure 8.3.3a). The polarization curve for GOR exhibits a major peak at 0.75 V, together with two shoulder peaks at 0.5 – 0.6 V and ca. 0.85 V (Figure 8.3.3b). These features mostly reproduce the behavior of Pt-poly as shown in Figure 8.3.1b, except that the peak at ~0.55 V is less visible on Pt/C. The latter difference may not indicate the presence of less low-coordinated sites on the surface, but may be due to the larger double-layer width of the carbon-supported catalyst. Chronoamperometry was also conducted at potentials from 0.45 V to 0.85 V, with averages of the measured current shown in Figure 8.3.3b in comparison to the polarization curve (see Figure 8.3.3d for I-t curve). The smaller amperometric current than the linear polarization can be attributed to the absence of capacitive currents.

Figure 8.3.3c summarizes the Faradaic efficiency (FE_{CO2}) and partial current (J_{CO2}) measured for the GOR by using GC-MS. Overall the selectivity toward CO_2 is low. The highest FE_{CO2} of merely 4.4% is reached at 0.65 V, corresponding to J_{CO2} of 56 mA/g_{Pt}. This observation suggests that the partial oxidation pathways toward C_2 and C_3 products are kinetically more favorable. The low selectivity of CO_2 has been known for the GOR and is usually linked to the large barrier for C-C cleavage and/or the complicated and parallel reaction pathways on catalyst surfaces.[193, 200-202] However, the low CO_2 selectivity contrasts to the capability of Pt for C-C cleavage at low potentials as revealed by our SFG results and many other IR or DEMS studies reported in the literature.[203, 227-228, 239] Martins *et al.* suggest that oxidation of *CO formed at low potentials (ca. <0.5 V, by dissociation of glycerol or its dehydrogenated derivatives) is the primary source of CO_2 production for the GOR at potentials up to 1.0 V.[227] Schnaidt *et al.* ascribe the discrepancy to the blockage of Pt sites required for OH_{ad} formation and further oxidation

of glycerol by *CO, as well as a possible high barrier for C-C cleavage at elevated potentials (ca. 0.6 – 0.7 V).[203] Gomes *et al.* investigated the GOR on single-crystal Pt electrodes and found that C-C cleavage is more favorable on open facets of Pt ((100) and (110)) than on close-packed Pt(111), whereas Pt(111) is less poisoned by the C_1 or C_2 intermediates generated from the dissociation steps.[228] From these discussions and our results, we speculate that only some minor sites on Pt (including both Pt-poly and Pt/C) can cleave the C-C bond in glycerol, which may still be subject to poisoning by strongly binding species such as *CO. The oxidation of *CO requires rather high potentials (>0.5 V) on Pt, where the barrier for C-C cleavage becomes higher due to the presence of *OH on the surface. Noticeably, the rise of the energy barrier for C-C cleavage due to oxygenated adsorbates (*O or *OH) has previously been seen in the electro-oxidation of ethanol by density functional theory (DFT) calculations.[93]

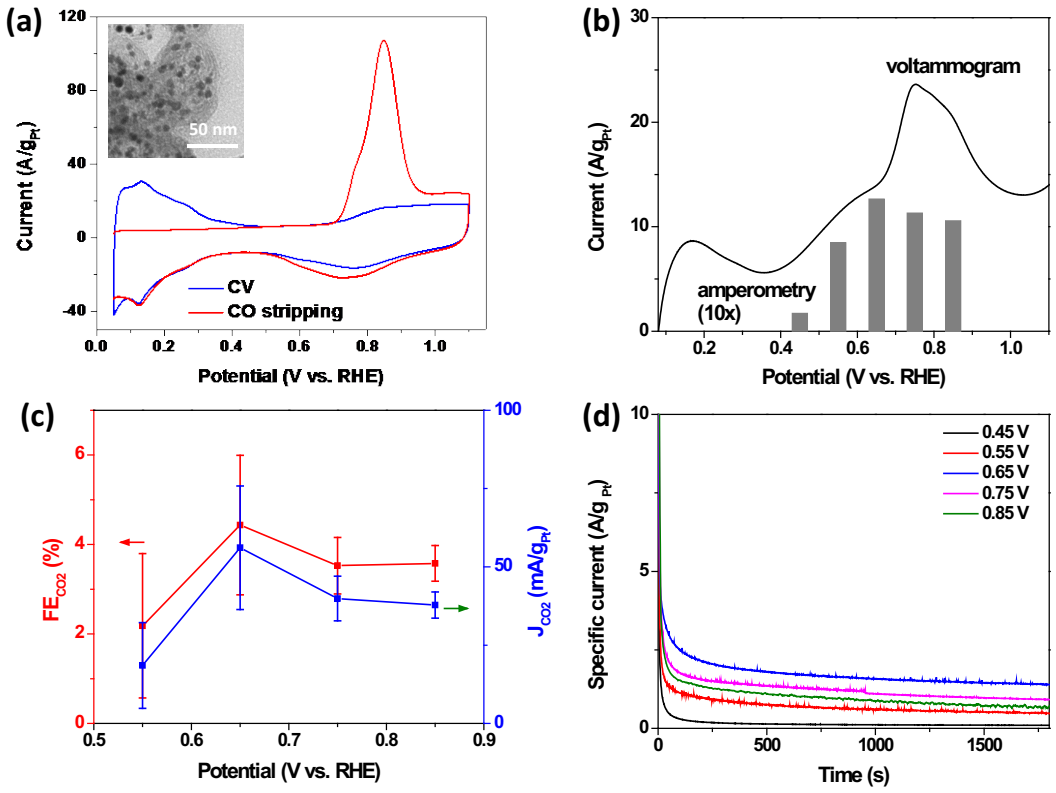

Figure 8.3.3. Product-resolved electrocatalytic studies. (a) Cyclic voltammogram and CO stripping pattern of Pt/C in 0.1 M $HClO_4$. Inset is TEM image of commercial Pt/C. (b) Polarization curve (line) and amperometric specific current (histogram) of Pt/C in 0.1 M $HClO_4$ + 0.1 M glycerol. (c) CO_2 faradaic efficiency and partial current at various potentials during amperometric product analysis. (d) I-t curve of Pt/C during product resolved chronoamperometry tests.

More insights into the reaction mechanism and catalytic selectivity is provided by comparative study of isotopically labeled glycerol ($HO^{12}CH_2$-$^{13}CH(OH)$-$^{12}CH_2OH$). We found that the unlabeled glycerol produces 0.3 % to 3.7 % of $^{13}CO_2$ in the complete oxidation product, which can be considered to be within the range of natural abundance (~1.1%). The reaction using $HO^{12}CH_2$-$^{13}CH(OH)$-$^{12}CH_2OH$ generates 6.2-12.6% of $^{13}CO_2$, which is higher than the natural abundance limit and the case with unlabeled

glycerol (Figure 8.3.4). These results indicate that CO_2 is primarily derived from the terminal carbon in glycerol, albeit with a minor contribution from the central carbon. We also conducted SFG experiments on $HO^{12}CH_2$-$^{13}CH(OH)$-$^{12}CH_2OH$ and found that is *CO peak exhibited a small red shift (~8 cm^{-1}) as compared to $HO^{12}CH_2$-$^{12}CH(OH)$-$^{12}CH_2OH$ (Figure 8.3.5). We did not observe a separate peak for $^{13}CO_L$, which is expected to be red-shifted more significantly (~36 cm^{-1}) due to the isotope effect. The absence of this distinct peak for $^{13}CO_L$ is in contrast to IR studies by Fernandez *et al.*[196, 229], and we presumably attribute this difference to the small fraction of $^{13}CO_L$ produced from the central carbon and the overall rather low surface coverage of *CO in the GOR. Nevertheless, this observation is largely in line with the relatively low abundance of $^{13}CO_2$ in the reaction product as measured by GC-MS (Figure 8.3.4). The findings from the isotope experiments imply that cleavage of the C-C bond in the remaining C_2 intermediates is kinetically more challenging than for the first one. The low but non-zero selectivity of GOR toward CO_2 can thus be ascribed to the rather feasible scission of one terminal carbon in glycerol (or its C_3 derivatives), albeit high potentials still needed to oxidize the generated *CO (one per glycerol molecule), and unfavorable kinetics for further dissociation of the left C_2 moieties toward complete oxidation.

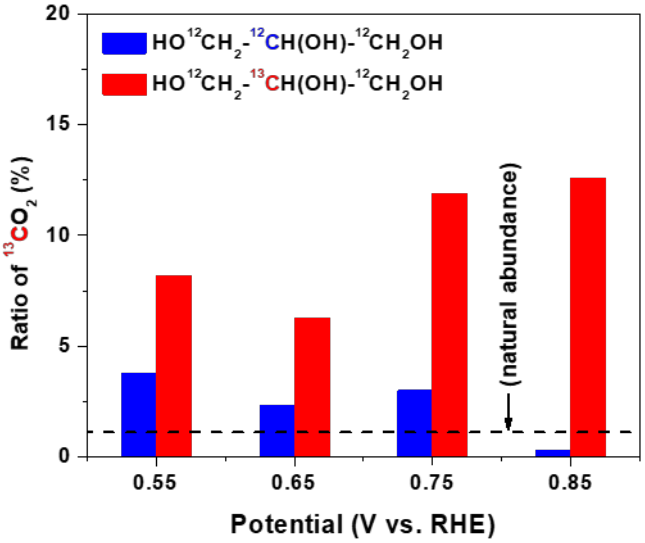

Figure 8.3.4. Electrocatalytic study of GOR using isotopically labeled glycerol. The ratio of $^{13}CO_2$ in the product measured using GC-MS is compared to the result from unlabeled glycerol and the baseline of natural abundance.

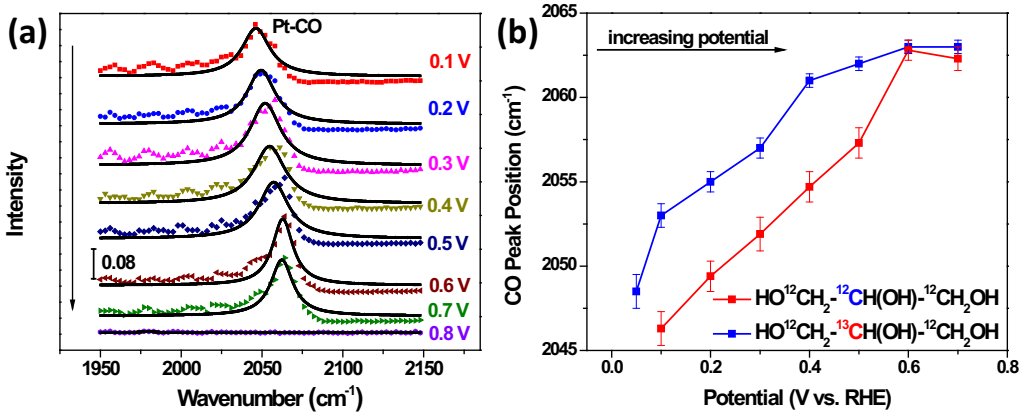

Figure 8.3.5. (a) SFG spectra of $HO^{12}CH_2$-$^{13}CH(OH)$-$^{12}CH_2OH$ during electro-oxidation at various potentials. (b) Comparison of the *CO peak position of $HO^{12}CH_2$-$^{13}CH(OH)$-$^{12}CH_2OH$ and $HO^{12}CH_2$-$^{12}CH(OH)$-$^{12}CH_2OH$.

8.4 Conclusion

In summary, we combined spectro-electrochemical studies of extended surfaces using sum frequency generation (SFG) and product-resolved electrocatalytic measurements on high-surface-area catalysts to investigate the glycerol oxidation reaction (GOR) on Pt. Adsorbing CO as reaction intermediate was observed at potentials as low as 0.05 V on Pt-poly, indicating the capability of Pt to cleave the C-C bond in glycerol at low potentials. The feasibility of C-C cleavage observed in the spectro-electrochemical studies contrasts with the low selectivity toward CO_2 (with a Faradaic efficiency of <4%) measured by the electrocatalytic studies on Pt/C. The discrepancy was ascribed to the rather feasible cleavage of one terminal carbon to form *CO, but kinetically hindered oxidation of *CO and further dissociation of the left C_2 fragments at low potentials, whereas at high potentials partial oxidation pathways become more favorable due to suppressed C-C bond cleavage. Our findings suggest that, to improve the performance of Pt for complete oxidation of glycerol, one would need to enhance the oxidative removal of dissociation residues by, for example, introducing a 3*d* metal to form an alloy[240] or surface metal oxides to enhance the adsorption of hydroxide[98] without obstructing the active sites for C-C cleavage.

Chapter 9. Controllable Synthesis of MoS_2 for Hydrogen Evolution Reaction Purpose

9.1 Introduction

The past decade has witnessed a remarkable growth of research interests in two-dimensional (2D) nanomaterials. Composed of a single layer of carbon atoms in a honeycomb-type of structure, graphene has been intensively studied to show exotic physical properties that are not present in its bulk counterpart (graphite).[241] Besides graphene, many other 2D layered materials have received great attention,[242-243] such as transition metal chalcogenides (TMCs),[244-246] metal oxides (e.g., MnO_2, $LiCoO_2$ and perovskites),[247-250] carbides/nitrides[251-252] and graphene analogues such as boron nitride (BN)[253] and silicene[254]. Among these materials 2D TMCs have received particular attention. With a standard formula of MX_2 (M is a transition metal of groups 4–10 and X is a chalcogen), these materials form layered structures with the hexagonally packed metal atoms sandwiched between two layers of chalcogen atoms. The diverse structures and versatile chemistries of 2D TMCs make them appealing for a variety of applications including electronics, sensors, energy storage and catalysis.[242-245]

2D TMCs can be prepared by either exfoliation of bulk crystals (top-down) or direct chemical synthesis (bottom-up). In the top-down approach, the lamellar layers of TMCs are usually peeled off by micromechanical cleavage,[255-256] liquid exfoliation,[8] and chemical intercalation.[257-261] Direct chemical synthesis of 2D TMCs has also been reported, mostly done by chemical vapor deposition (CVD) on appropriate substrates.[246, 262-266] Alternatively, TMC nanosheets have also been synthesized by solution approaches,

including hydrothermal[267-269] and organic solvothermal synthesis[270-275]. For example, Matte et al. used molybdic or tungstic acid to react with thiourea or selenourea in a hydrothermal process and obtained 2D MoS_2 or WS_2 of one to a few layers.[267] Unlike the top-down and CVD approaches, the solution synthesis produces free-standing, colloidal nanosheets from feasible chemical reactions, which could be advantageous for further modification and functionalization, as well as scaling up. Compared to the overwhelming exfoliation methods, the bottom-up synthesis could provide more robust control over the growth process to tailor the structures of the materials. For example, a recent study by Jung *et al.* showed that the thickness of WSe_2 nanosheets can be tuned by using coordinating ligands of different binding strengths, with monolayer WSe_2 and $MoSe_2$ nanosheets obtained with weakly binding oleic acid.[275] Despite the many advantages, reports on solution synthesis of 2D TMCs are however limited and robust control over the size, including the in-plane (lateral) diameter and degree of stacking,[267-275] still remains challenging, in contrast to the enormous progress that has been made on the development of zero- and one-dimensional nanomaterials by this approach.[276-278] Moreover, the solution processes, particularly in organic phases, usually involve organic ligands for stabilization of the nanocrystals during growth, which might block electrical contact and chemical access to the surface of the materials and hinder functional applications (especially for catalysis[112]) of the products obtained by this approach.

Here we report on the organic solution ultrathin MoS_2 nanosheets in attempt to control the lateral sizes and degrees of stacking. Ultrathin MoS_2 nanosheets of a few (<3) layers in thickness were synthesized by thermal decomposition of molybdenum carbonyl and subsequent sulfurization with element sulfur (Figure 9.1.1, and also see the

Experimental Method section). The in-plane size of the nanosheets was tuned from <5 to 20 nm by controlling the temperature and time of growth. Thermal annealing of the nanosheets at various temperatures was applied to manipulate the degree of stacking without causing significant agglomeration in-plane. The obtained nanosheets were further applied as electrocatalysts for the hydrogen evolution reaction (HER) and the effects of lateral size and stacking on the catalytic activity were examined.

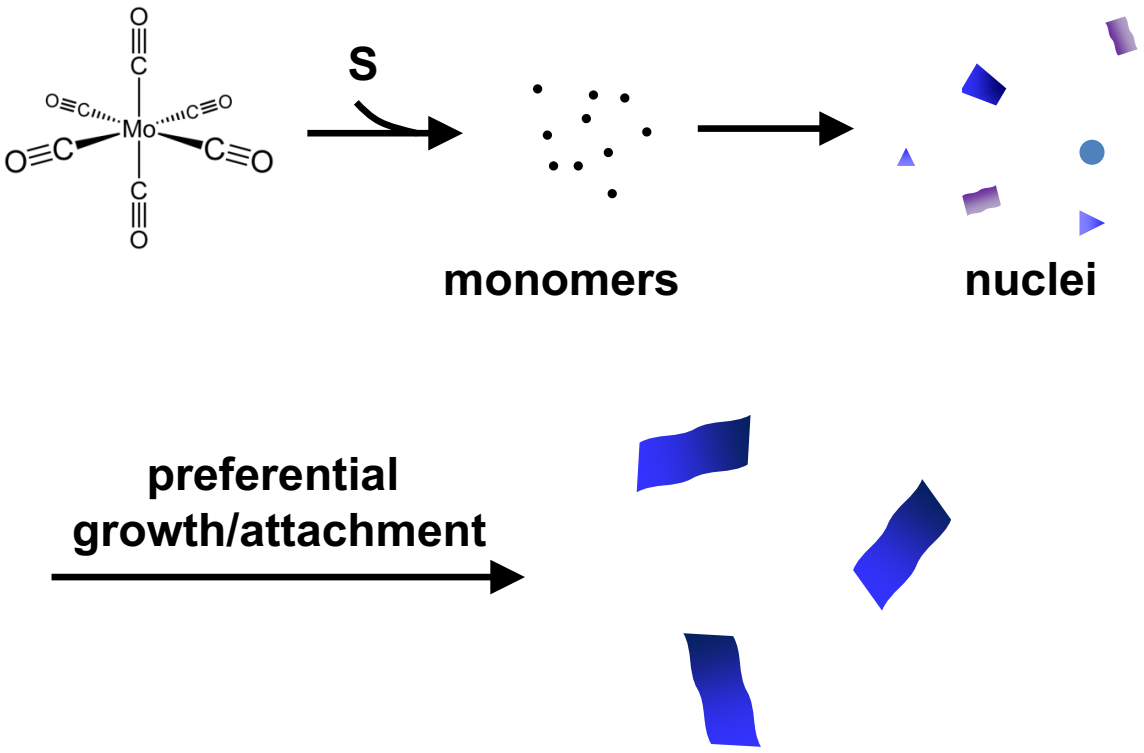

Figure 9.1.1. Schematic illustration of MoS_2 synthesis process.

9.2 Experimental Method

Synthesis

In a typical synthesis, 1 mmol of molybdenum hexacarbonyl ($Mo(CO)_6$) was dissolved in 10 ml of 1-octadecene and 1 ml of oleylamine with a three-neck flask. Under nitrogen flow the formed solution was heated up to 120 $^{\circ}$C, where $Mo(CO)_6$ started to decompose

as indicated by the change of solution color from light yellow to dark brown. To this hot solution 2 mmol of elemental sulfur dissolved in 1ml of oleylamine and 1ml of 1-octadecene was injection quickly. The temperature was further raised to 300 $^{\circ}$C for growth. After the reaction, the product was collected by adding iso-propanol and centrifuge. The product was further washed with acetone and re-dispersed in toluene.

Characterization

Transmission electron microscopy (TEM) images were collected on a 120 kV, FEI Tecnai 12 TWIN microscope operated at 100 kV. A 300 kV, field emission Phillips CM300-FEG was used for high-resolution TEM (HRTEM) imaging. X-ray diffraction (XRD) patterns were collected on a PANalytical X'Pert Powder X-Ray Diffractometer equipped with a Cu Kα radiation source (λ=0.15406). High-angle annular dark field scanning transmission electron microscopy (HAADF-STEM) was conducted on a JEOL 2200FS TEM/STEM equipped with a CEOS aberration (probe) corrector. The microscope was operated at 200 kV, and the electron beam size was ~0.7 Å for imaging. Fourier Transformed Infrared Spectroscopy (FTIR) was performed on the nanoparticles with a Varian 640 Spectrophotometer. X-ray photoelectron spectroscopy (XPS) measurements were done on a PHI 5600 Multi-technique photoelectron spectrometer using a Mg Kα X-ray source. The X-ray source was operated at 15kV, 300W and a pass energy of 5.85eV was used to sample ejected photoelectrons from the Mo(3d) and S(2s) regions. Peak fitting of the Re(4f) region was performed using the CasaXPS software and a *Gaussian-Lorentzian (30)* line-shape. Raman spectra were measured with HORIBA Jobin Yvon LabRAM HR Raman System at room temperature with 514-nm excitation and 1-μm spatial resolution, the spectrum resolution of the system is <0.4 cm^{-1}.

Inductively Coupled Plasma Mass Spectrometry (ICP-MS) was collected with a PerkinElmer Elan DRC II Quadrupole.

Electrochemistry

For electrocatalytic studies, the MoS_2 nanosheets were mixed with carbon black (~900 m^2/g) at 2:1 mass ratio by sonication. After drying in air, the obtained powder was annealed at 185^oC in air overnight. The obtained catalyst was dispersed in deionized water by sonication. An aliquot of the formed suspension was deposited onto a glassy carbon disk electrode at a loading of ~100 $\mu g_{cata}/cm^2_{disk}$. The HER activities were measured with a three compartment electrochemical cell in rotational disk electrode (RDE, 5 mm diameter) configuration and an Autolab 302 potentiostat. A saturated Ag/AgCl electrode and a platinum wire were used as reference and counter electrodes, respectively. A solution of 0.1 M $HClO_4$ was used as electrolyte. All the potentials discussed in the main text were given against the reversible hydrogen electrode (RHE). All current densities are normalized by mass of Mo unless noted otherwise.

9.3 Results and Discussion

Synthesis and Characterization. Sulfur could directly react with Mo, or fast react with oleylamine to generate H_2S at elevated temperatures (>130 ^oC) which then reacts with Mo (meanwhile release H_2),[279] to produce MoS_2 monomers. Transmission electron microscopy (TEM) images show that small clusters (<2 nm in diameter) formed at 200 ^oC after the addition of S (Figure 9.3.1a, corresponding to the "nuclei" stage in Figure 9.1.1). When the temperature reached 300 ^oC, single-layer nanosheets appeared with lateral sizes smaller than 5 nm (Figure 9.3.1b), likely formed through preferential growth or oriented attachment[280] of the previously formed nuclei species laterally (Figure 9.1.1).

These small nanosheets were found to undergo further growth and reach a lateral size of 10 nm after 15 min, and 15 – 20 nm after 30 – 60 min of growth at 300 ^{o}C, respectively (Figure 9.3.1c, d and e). During this process the degree of stacking in c-axis direction merely increased, and the nanosheets finally obtained has a thickness of 1 – 3 layers. It is noticed that this observation is different from the recently reported synthesis of $MoSe_2$ nanosheets by using oleylamine as both the surfactant and solvent where thick slabs (4 – 8 layers) were obtained, which is probably owing to the different reaction conditions used in the present study.

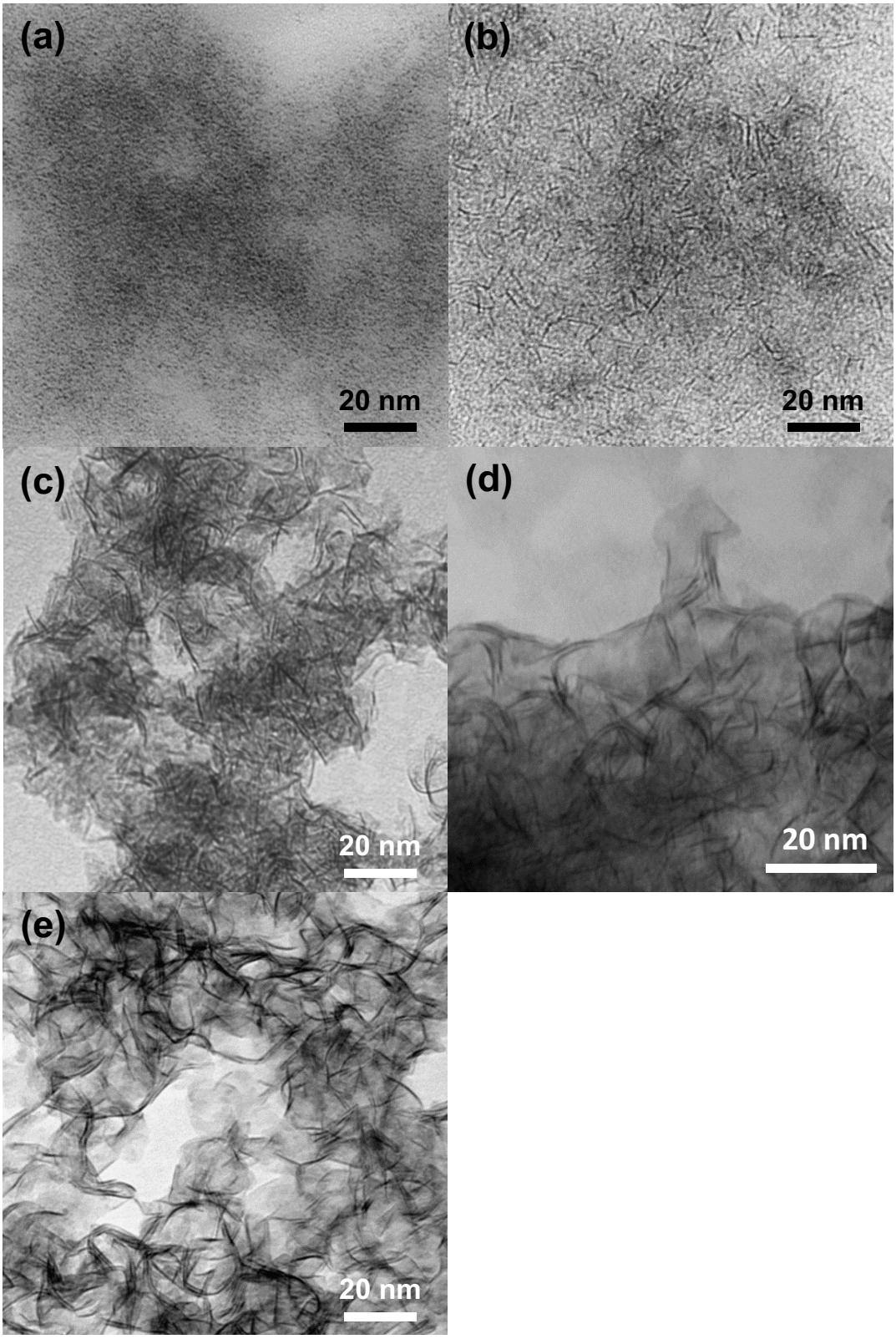
(a)
20 nm
(b)
20 nm
(c)
20 nm
(d)
20 nm
(e)
20 nm

Figure 9.3.1. TEM images of products collected at (a) 200 °C and (b) 0 min, (c) 5 min and (d) 60 min at 300 °C.

The anisotropic growth likely originates from the layered crystal structure of MoS_2. The Mo–S bond within the MoS_2 layer is covalent, while the interlayer coupling is through weak van der Waals forces. Monomers deposited on the edge thus possess lower free energy than deposited on the basal plane of the MoS_2 layer. Similar energy difference is also present between the attachment of nanosheets in plane and the stacking along c-axis.

The as-synthesized MoS_2 nanosheets exhibit a polycrystalline nature, as revealed by high-resolution TEM (HRTEM) imaging and X-ray diffraction (XRD) analysis. The lattice fringes in the HRTEM images are not well defined, probably owing to the low contrast of the ultrathin nanosheets and presence of organic surfactants (Figure 9.3.2a). Correspondingly, the XRD pattern shows only two weak, broad peaks at 33^o and 59^o, which could be assigned to the (100) and (110) planes of MoS_2 in the 2H phase (Figure 9.3.3a).[245] The absence of (002) peak at ~14^o indicates that the MoS_2 nanosheets are of low degree of stacking in *c*-axis direction, which is consistent with the observation of <3 layer in thickness from TEM images (Figure 9.3.1 d and e). Raman spectrum of the as-synthesized nanosheets exhibits two broad peaks at 383 and 406 cm^{-1}, corresponding to the in-plane $E_{2g}{}^1$ and A_{1g} modes of Mo–S phonons, respectively (Figure 9.3.3b). The rather broad peaks could be due to the polycrystalline nature or varying thickness of the nanosheets, while the spacing between the two peaks (23 cm^{-1}) indicates the thickness of the nanosheets is two to three molecular layers.[255] X-ray photoemission spectroscopy (XPS) analysis of the as-synthesized MoS_2 nanosheets shows Mo, S, O and C lines in the

spectrum (Figure 9.3.3d). The Mo 3*d* peaks were de-convoluted and MoS_2 was found to be the major component (~84 atom %) albeit the presence a small amount of MoO_3. The peaks observed at 229.1 eV and 232.5 eV correspond to Mo $3d_{5/2}$ and $3d_{3/2}$ in MoS_2,[281-282] while the peaks at 232.2 eV and 235.6 eV for Mo $3d_{5/2}$ and $3d_{3/2}$ in MoO_3; The peak located at 226.4 eV can be attributed to S 2s. The presence of a small ratio (16%) of MoO_3 could be due to the existence of a small amount of oxygen or moisture in the synthesis that reacted with Mo or oxidation of MoS_2 edges in air.

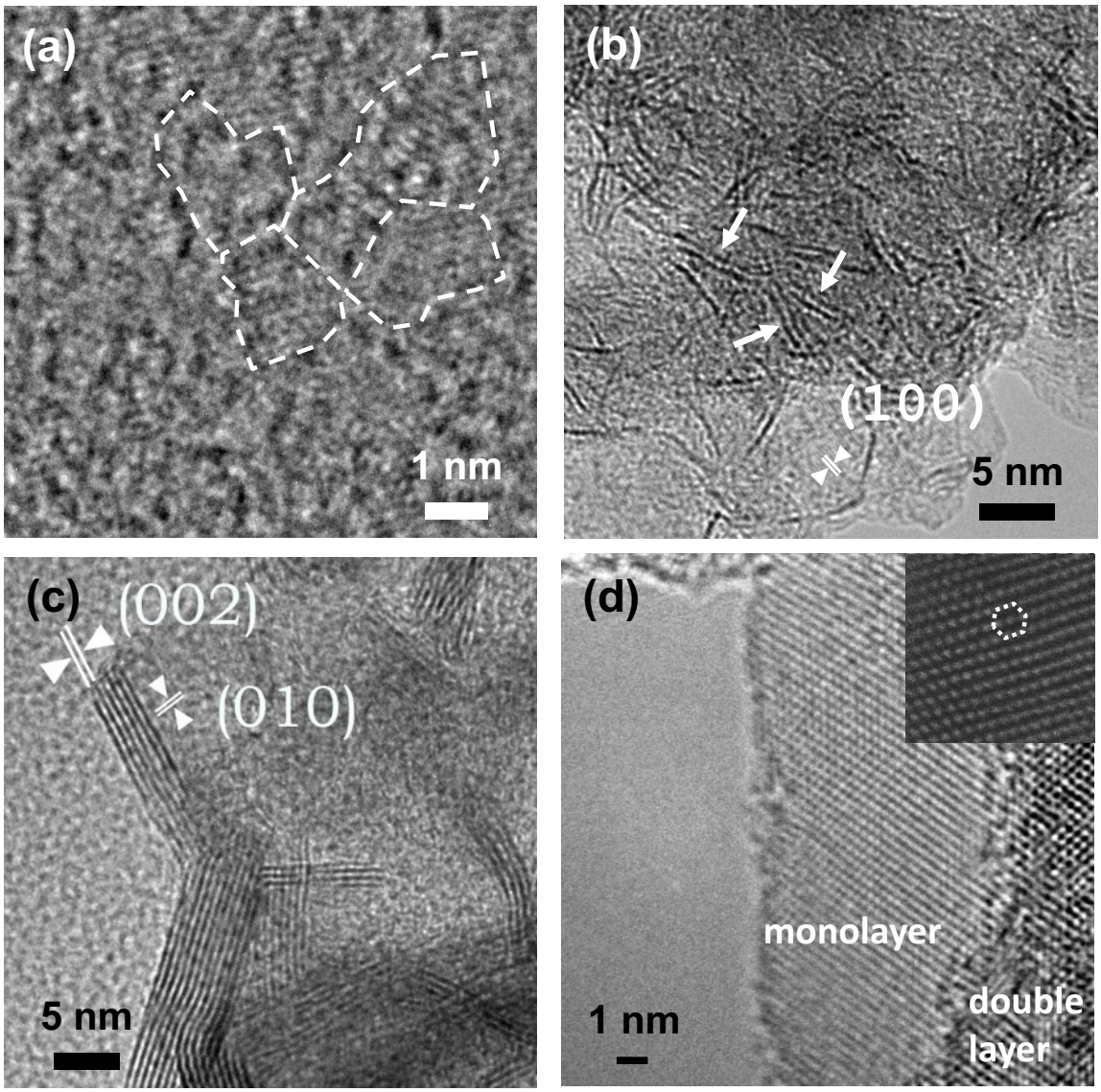

Figure 9.3.2. HRTEM images of the (a) as-synthesized, (b) 500°C annealed and (c) 1000°C annealed MoS_2 nanosheets. (d) Atomically resolved images of a MoS_2 monolayer from the annealed nanosheets. The arrows in (b) label the stacked double layers of nanosheets. The insert in (d) shows a STEM image indicating the six-fold symmetry of the Mo atoms.

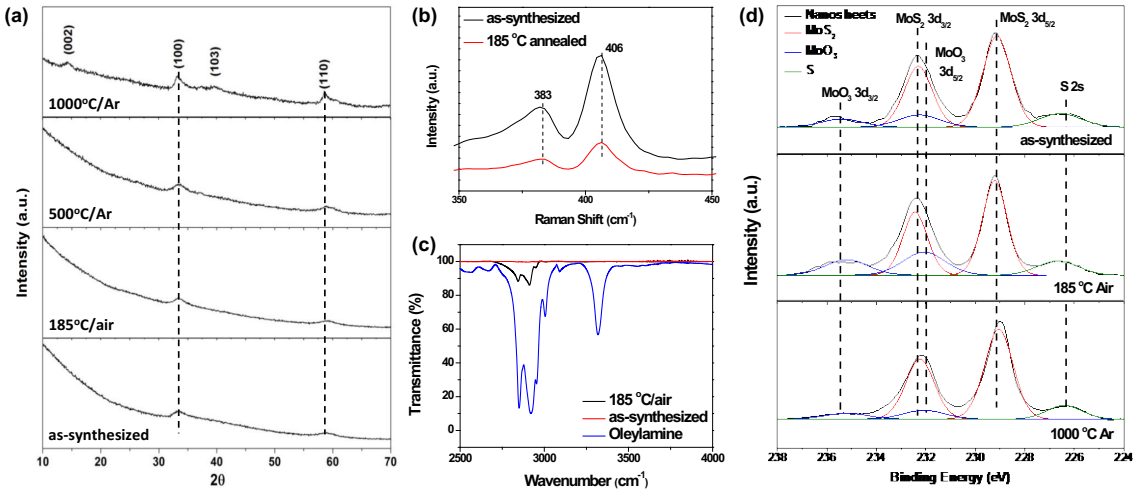

Figure 9.3.3. (a) XRD pattern of MoS_2 treated under various temperature. (b) Raman spectra of as-synthesized and 185 °C annealed MoS_2. (c) FT-IR spectra of oleylamine, as-synthesized and 185 °C annealed MoS_2. (d) XPS spectra of MoS_2 treated under various temperature.

Thermal Treatments. To remove the organic ligands for catalytic applications, the as-synthesized MoS_2 nanosheets were annealed in air at 185 °C. This treatment was previously applied to clean metal nanoparticles obtained from organic solution synthesis, and the treated nanoparticles were found to be catalytically active.[112] The Fourier Transform Infrared Spectroscopy (FTIR) analysis of the as-synthesized MoS_2 nanosheets show the characteristic peaks of oleylamine, including the two strong peaks at 2800–3000

cm^{-1} for the symmetric and asymmetric stretching of $–CH_2$ or $–CH_3$ groups and the stretching mode of (=)C–H at 3004 cm^{-1} (Figure 9.3.3c). The absence of the peak associated with $–NH_2$ at ~3300 cm^{-1} could be due to the binding of oleylamine to MoS_2 through the amine group. These peaks were found to disappear in the spectrum for the nanosheets after annealing at 185 ^oC, demonstrating that the thermal treatment was sufficient to remove the surfactants on the nanosheets.

For the 20 nm MoS_2 nanosheets, chemical nature of the nanosheets was largely preserved after the surfactant removal, although the molibdite content increased slightly from 16% to 29% (Figure 9.3.3d). Crystal structure of the treated nanosheets was found to be still hexagonal (Figure 9.3.3a), and Raman spectrum shows the E_{2g}^1 and A_{1g} peaks preserved (despite broadening due to more disordering[268]), indicating that the MoS_2 nanosheets were reasonably stable under the conditions of thermal treatment in air (Figure 9.3.3b). The increase of molibdite after annealing in air might be owing to oxidation of the edges of the nanosheets, which was confirmed by the higher extent of oxidation observed on the MoS_2 nanosheets of smaller sizes. The 10 nm nanosheets were found to preserve ~55% content as MoS_2 after the annealing at 185 ^oC in air, compared to ~51% for the 5 nm ones (Figure 9.3.4). For all of the nanosheets, the Raman scattering peaks were found to preserve after this treatment, indicating the preservation of 2D crystalline planes (Figure 9.3.5). It is noticed that the edge oxidation observed here could be different from the case in the previous report on the MoS_2 nanosheets obtained by the hydrothermal reaction of ammonium molybdate with thiourea, where the oxygen in small content, ~1 – 4 atom %, was incorporated into the basal plane of MoS_2 due to incomplete sulfurization.[268]

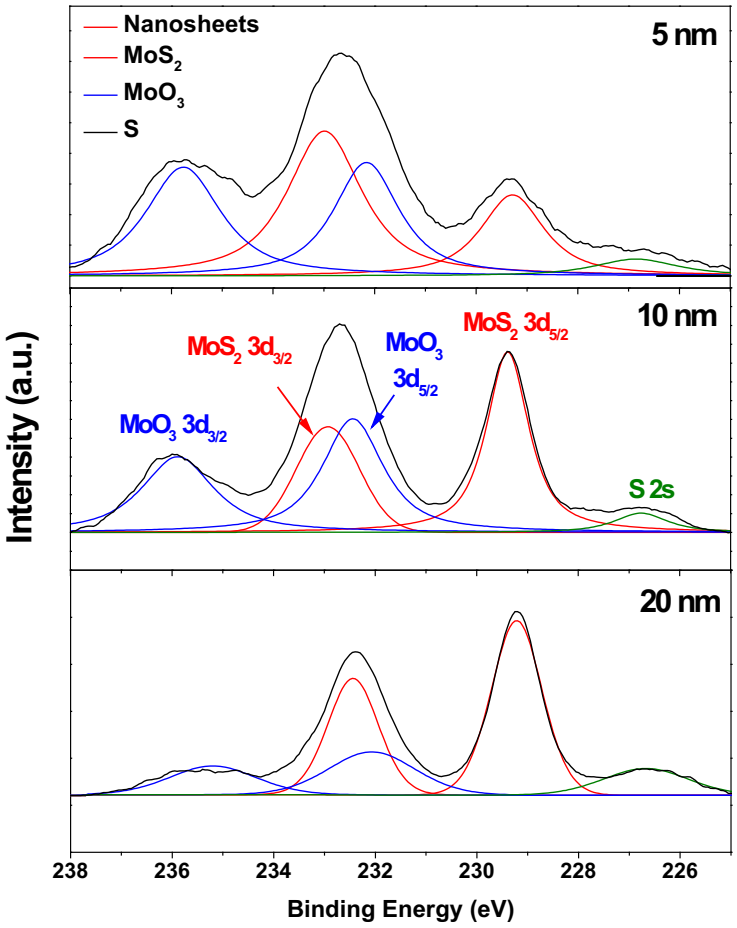

Figure 9.3.4. XPS spectra of the MoS_2 nanosheets of different sizes annealed at 185 ^oC in air. The contents of MoS_2 were estimated to be 51%, 55% and 84% for the 5, 10 and 20 nm MoS_2 nanosheets.

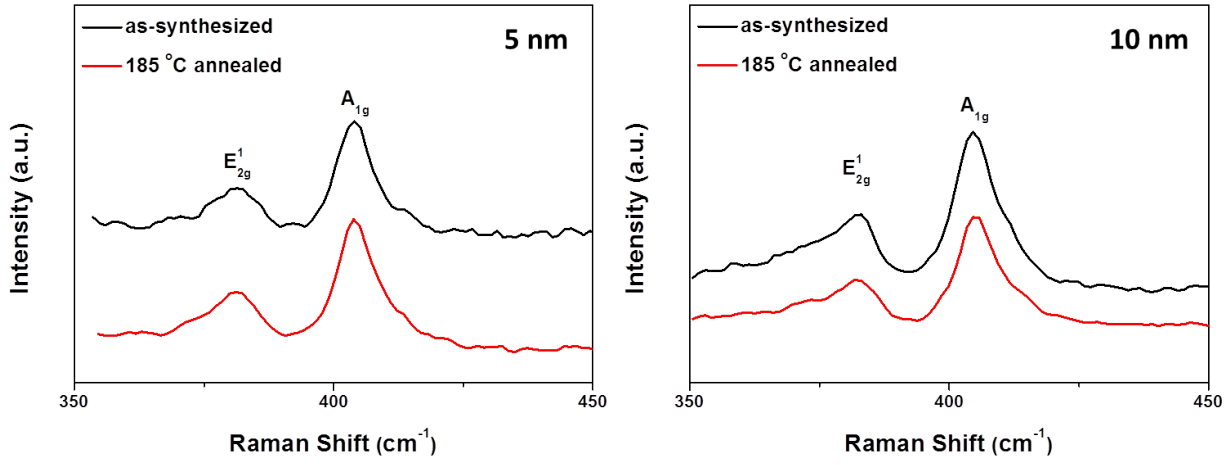

Figure 6.3.5. Raman spectra of the 5 and 10 nm MoS_2 nanosheets before and after the annealing at 185 ^oC.

Further thermal annealing at higher temperatures in Ar could reduce the content of oxidized molybdenum in the nanosheets after the treatment in air. For example, after annealing at 1000 ^oC, the MoO_3 content in the 20 nm MoS_2 nanosheets was reduced to 12.6% (Figure 9.3.3d). Such high-temperature treatments also improve the crystallinity of the nanosheets and cause stacking of the nanosheets along *c* axis. HRTEM images show that after annealing up to 500 ^oC, no substantial stacking occurred (Figure 9.3.2b), which is consistent with the observation from XRD (Figure 9.3.3a). It was found that the degree of stacking increased up to ~10 MoS_2 layers after annealing at 1000 ^oC, whereas the lateral size was largely preserved despite some aggregation (Figure 9.3.2c). The preservation of lateral size upon annealing could be due to the small probability of alignment in plane for the 2D morphology in the powder form with random orientations, which is in contrast to the stacking in *c* axis and the substantial aggregation and agglomeration of nanoparticles upon high-temperature annealing[283]. Two sets of lattice fringes were observed in the annealed nanosheets with inter-layer spacing measured to be 0.62 and 0.27 nm, which can be assigned to the (002) and (010) planes of hexagonal MoS_2, respectively (Figure 9.3.2 b and c). After annealing above 500 ^oC the nanosheets exhibited a single-crystalline nature, with the Mo atoms showing six-fold symmetry in scanning transmission electron microscopy (STEM) images (Figure 9.3.2d).

Electrocatalysis. MoS_2 has recently received great attention as electrocatalysts for the hydrogen evolution reaction (HER), mainly owing to its potential as an earth-abundant, low-cost alternative to precious metals such as platinum (Pt).[245-246, 284] The previous work

on Au(111)-supported MoS_2 monolayers shows that metallic edge states associated with the coordinatively unsaturated Mo edges are active sites for the HER.[246] Substantial effort has thus been dedicated to the nanostructure engineering of MoS_2 catalysts in order to maximize the exposure of these active sites, including intercalation of lithium,[260-261, 284] controlling the crystal plane orientation,[285-286] incorporation of oxygen,[268] tuning the degree of stacking,[265], forming composites with conductive polymer[287] or graphene[288-289], and so on. Our synthesis has provided a novel approach to control and tune the lateral size and stacking of MoS_2 nanosheets. With the demonstrated surfactant removal, this approach thus enabled us to systematically study the structure-property relationship of the solution derived 2D MoS_2 nanomaterials.

Figure 9.3.6 summarizes the electrochemical studies of MoS_2 nanosheets of different in-plane sizes but with similar degree of stacking (<3 layer in thickness). All the nanosheets (5, 10 and 20 nm, corresponding to the TEM images shown in Figure 6.3.2 b–d, respectively) have a similar onset potential of about –0.2 V (vs. reversible hydrogen electrode (RHE); the same in the following discussion), compared to −0.27 V of commercial MoS_2 slabs (Figure 9.3.6 a and b, also see Figure 9.3.7 for TEM images of commercial MoS_2). This implies that the MoS_2 nanosheets of different sizes likely have active sites of similar chemical nature.[290] At −0.3 V, the current density reaches 0.39, 0.49 and 0.97 A/mg_{Mo} for the 20, 10 and 5 nm nanosheets, respectively (Figure 9.3.6a), representing improvement factors of 10-25 compared to the commercial MoS_2 (0.036 A/mg_{Mo}). Tafel slopes of the nanosheets was found to be slightly dependent on the lateral size, dropping from 76 to 63 mV/dec as the size decreases from 20 to 5 nm, compared to 195 mV/dec for commercial MoS_2 and 46 mV/dec for Pt/C (Figure 9.3.6b), indicating the

nanosheets of smaller size are more active. These values of Tafel slopes approach those previously reported results for oxygen-incorporated[268] or Li-intercalated MoS_2 nanohseets of high HER activities[260-261, 284], indicating the potential of simply tailoring the geometry of the 2D nanomaterials for catalytic enhancement. Amperometry studies at −0.3 V over a period of 3 minutes showed that the 20, 10 and 5 nm nanosheets reached steady-state current densities of 0.29, 0.36 and 0.70 A/mg_{Mo}, respectively (Figure 9.3.6c). The 20 and 10 nm nanosheets exhibited durable HER activities and the drop in current density was not more than 10%, versus 15% for the 5 nm nanosheets which turned out to be less stable. The result reported here shows the activity increases as the lateral size decreases which could be attributed to the increase in edge site number and this agrees with previous reports[6].

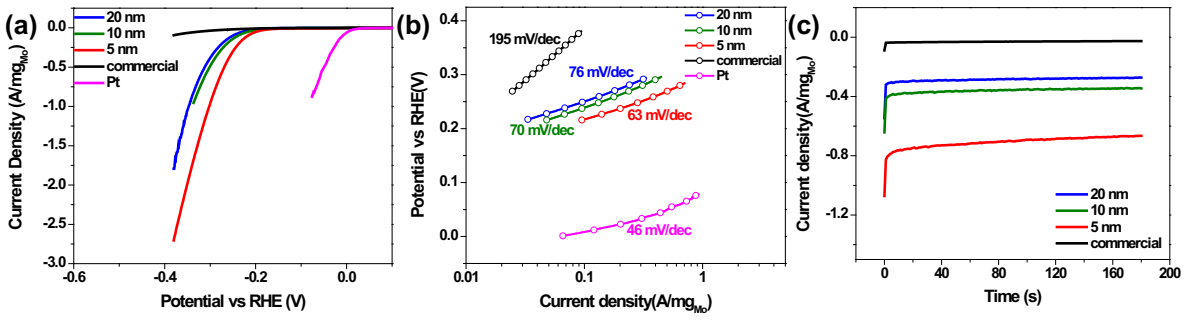

Figure 9.3.6. Summary of electrochemical studies for the MoS_2 nanosheets of different lateral sizes. (a) Polarization curves recorded at 10 mV/s in 0.1 M $HClO_4$ and (b) corresponding Tafel plots. (c) Amperometry measured at –0.3 V vs. RHE.

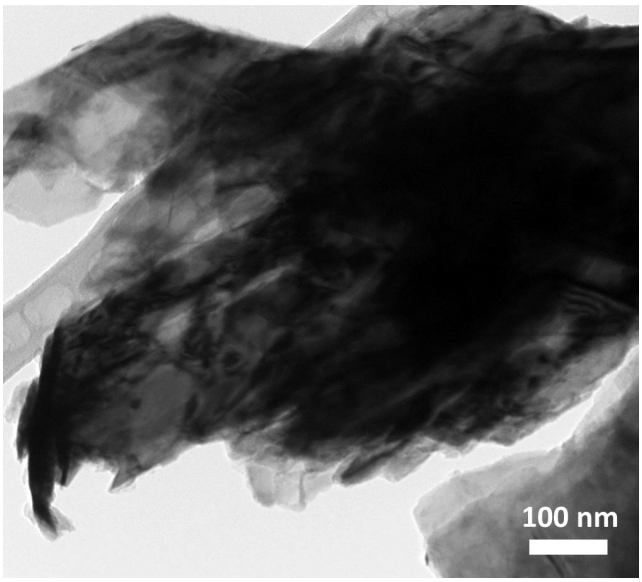

Figure 9.3.7. TEM image of the commercial MoS_2 from Alfa Aesar.

Besides the lateral size, the HER activity was also found to be dependent on the degree of stacking for MoS_2 nanohseets. As discussed above, the annealing in Ar at high temperatures had induced stacking of the nanosheets whereas the lateral size had been kept rather consistent (Figure 9.3.2). For the 20 nm MoS_2 nanosheets annealed at 500 and 1000 ^{o}C, the current density at –0.3 V dropped from 0.39 to 0.21 and 0.02 A/mg_{Mo}, respectively (Figure 9.3.8a). Correspondingly, the Tafel slope increased from 76 to 92 and 97 mV/dec (Figure 9.3.8b) and the steady-state current densities decreased from 0.29 to 0.18 and 0.02 A/mg_{Mo} after the annealing at 500 and 1000 ^{o}C, respectively. The observation that thinner nanosheets were more active for the HER and Tafel slope increase as stacking degree increase is consistent with the previously reported stacking-dependent electrocatalytic properties for MoS_2[265]. Such a trend could be ascribed to the smaller resistances for charge conduction between adjacent layers, which is via tunneling and weak van der Waals interactions.[265]

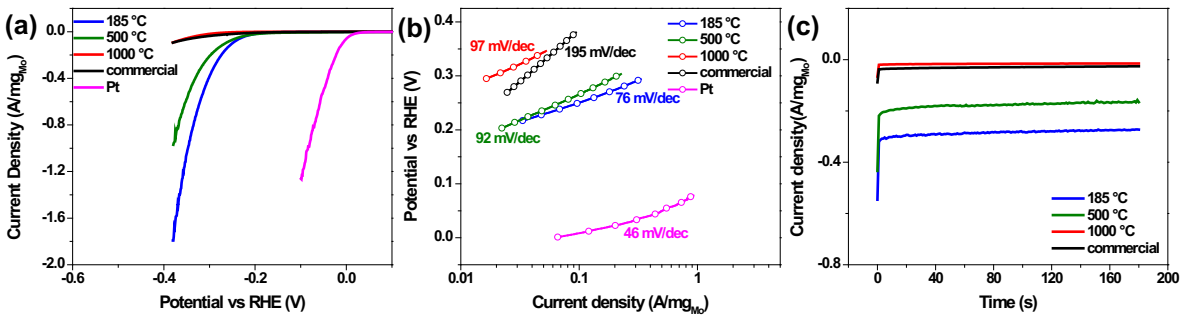

Figure 9.3.8. Summary of electrochemical studies for the 20 nm MoS_2 nanosheets annealed at different temperatures. (a) Polarization curves recorded at 10 mV/s in 0.1 M $HClO_4$ and (b) corresponding Tafel plots. (c) Amperometry measured at –0.3 V vs. RHE.

9.4 Conclusion

We have developed an organic solution approach for the synthesis of ultrathin MoS_2 nanosheets by subsequent thermal decomposition of molybdenum carbonyl and sulfurization with elemental sulfur. The lateral size of the nanosheets was tunable in the range of 5 – 20 nm by controlling the reaction conditions, while the stacking along *c* axis was manipulated from <3 to ~10 molecular layers by applying post-synthetic thermal annealing at different temperatures. Surfactant removal by thermal treatments was also demonstrated for the nanosheets without causing significant changes to the chemical composition or morphology. Electrochemical studies showed that the MoS_2 nanosheets were highly active for the HER with improvement factors of 10-25 compared to commercial MoS_2, and the Tafel slopes were in line with the previous reports on oxygen incorporated or lithium intercalated MoS_2 nanosheets. The catalytic activity was further found to improve as the lateral size increases and the degree of stacking reduces. The former dependence can be ascribed to the edge sites being the active sites and improved chemical stability of the nanosheets with larger in-plane sizes during the treatment for

surfactant removal, whereas the latter is likely a result of smaller resistance in thinner nanosheets, respectively. Our approach could be generalized to the synthesis of other transition metal chalcogenides, and the capability of synthetically tuning the materials dimensions at the nanoscale possesses great potential for tailoring the 2D nanomaterials for catalytic improvement.

Chapter 10. Outlook

In previous chapters, various materials had been investigated for their catalytic behavior toward alcohol electro-oxidation. Significant enhancement in activity and CO_2 selectivity had been accomplished by Pt/Sn binary nanomaterials. However, to achieve commercially viable direct alcohol fuel cells (DAFCs), current CO_2 selectivity (11 % for ethanol electro-oxidation, 28 % for ethylene glycol and 4 % for glycerol) is still not satisfactory and would need to be further enhanced. Considering the unsuccessful attempts of tailoring catalyst composition and structure in Chapters 6 and 7, it might be more worthwhile to investigate DAFCs operating at elevated temperature. Otomo *et al.* investigated electro-oxidation of ethanol, ethylene glycol and glycerol at 230 – 260 °C and reported C-C bond dissociation ratio above 90 %.[291-293] However, thermal decomposition of alcohol also contribute to reaction and a considerable amount of product would be H_2, CH_4. Wang *et al.* characterized the product of DEFC operating at 150 – 190 °C and reported CO_2 selectivity reaching 20 – 40 %.[294] Alcohol electro-oxidation showed a higher tendency toward complete oxidation and intermediate temperature DAFCs may be a promising energy conversion device. The future direction of this research project is, thus, investigate DAFCs operating at elevated temperature, including its catalyst, electrolyte, membrane etc.

References

1. Rizo, R.; Sebastián, D.; Rodríguez, J. L.; Lázaro, M. J.; Pastor, E., Influence of the Nature of the Carbon Support on the Activity of Pt/C Catalysts for Ethanol and Carbon Monoxide Oxidation. *Journal of Catalysis* **2017**, *348*, 22-28.

2. Badwal, S. P. S.; Giddey, S.; Kulkarni, A.; Goel, J.; Basu, S., Direct Ethanol Fuel Cells for Transport and Stationary Applications – a Comprehensive Review. *Applied Energy* **2015**, *145*, 80-103.

3. Goldemberg, J., Ethanol for a Sustainable Energy Future. *Science* **2007**, *315*, 808.

4. Akhairi, M. A. F.; Kamarudin, S. K., Catalysts in Direct Ethanol Fuel Cell (Defc): An Overview. *International Journal of Hydrogen Energy* **2016**, *41*, 4214-4228.

5. Zou, X.; Zhang, Y., Noble Metal-Free Hydrogen Evolution Catalysts for Water Splitting. *Chemical Society Reviews* **2015**.

6. Alivisatos, A. P., Nanocrystals: Building Blocks for Modern Materials Design. *Endeavour* **1997**, *21*, 56-60.

7. Novoselov, K. S.; Geim, A. K.; Morozov, S. V.; Jiang, D.; Zhang, Y.; Dubonos, S. V.; Grigorieva, I. V.; Firsov, A. A., Electric Field Effect in Atomically Thin Carbon Films. *Science* **2004**, *306*, 666.

8. Coleman, J. N., et al., Two-Dimensional Nanosheets Produced by Liquid Exfoliation of Layered Materials. *Science* **2011**, *331*, 568-71.

9. Qian, W.; Hao, R.; Hou, Y.; Tian, Y.; Shen, C.; Gao, H.; Liang, X., Solvothermal-Assisted Exfoliation Process to Produce Graphene with High Yield and High Quality. *Nano Research* **2009**, *2*, 706-712.

10. Smith, R. J., et al., Large-Scale Exfoliation of Inorganic Layered Compounds in Aqueous Surfactant Solutions. *Adv Mater* **2011**, *23*, 3944-8.

11. Abdellaoui, M.; Mokbli, S.; Cuevas, F.; Latroche, M.; Percheron-Guégan, A.; Zarrouk, H., Structural and Electrochemical Properties of Amorphous Rich Mgxni100−X Nanomaterial Obtained by Mechanical Alloying. *Journal of Alloys and Compounds* **2003**, *356-357*, 557-561.

12. Rao, C. N.; Sood, A. K.; Subrahmanyam, K. S.; Govindaraj, A., Graphene: The New Two-Dimensional Nanomaterial. *Angew Chem Int Ed* **2009**, *48*, 7752-77.

13. Yin, Y.; Alivisatos, A. P., Colloidal Nanocrystal Synthesis and the Organic-Inorganic Interface. *Nature* **2005**, *437*, 664-70.

14. Frey, N. A.; Peng, S.; Cheng, K.; Sun, S., Magnetic Nanoparticles: Synthesis, Functionalization, and Applications in Bioimaging and Magnetic Energy Storage. *Chem Soc Rev* **2009**, *38*, 2532-42.

15. Murray, C. B.; Kagan, C. R.; Bawendi, M. G., Synthesis and Characterization of Monodisperse Nanocrystals and Close-Packed Nanocrystal Assemblies. *Annual Review of Materials Science* **2000**, *30*, 545-610.

16. Peng, Z.; Yang, H., Designer Platinum Nanoparticles: Control of Shape, Composition in Alloy, Nanostructure and Electrocatalytic Property. *Nano Today* **2009**, *4*, 143-164.

17. van der Vliet, D. F.; Wang, C.; Li, D.; Paulikas, A. P.; Greeley, J.; Rankin, R. B.; Strmcnik, D.; Tripkovic, D.; Markovic, N. M.; Stamenkovic, V. R., Unique Electrochemical Adsorption Properties of Pt-Skin Surfaces. *Angew Chem Int Ed* **2012**, *51*, 3139-42.

18. Wang, C.; Daimon, H.; Onodera, T.; Koda, T.; Sun, S., A General Approach to the Size- and Shape-Controlled Synthesis of Platinum Nanoparticles and Their Catalytic Reduction of Oxygen. *Angew Chem Int Ed* **2008**, *120*, 3644-3647.

19. Wang, C.; Daimon, H.; Lee, Y.; Kim, J.; Sun, S., Synthesis of Monodisperse Pt Nanocubes and Their Enhanced Catalysis for Oxygen Reduction. *Journal of the American Chemical Society* **2007**, *129*, 6974-6975.

20. Ren, J.; Tilley, R. D., Preparation, Self-Assembly, and Mechanistic Study of Highly Monodispersed Nanocubes. *Journal of the American Chemical Society* **2007**, *129*, 3287-3291.

21. Elghanian, R.; Storhoff, J. J.; Mucic, R. C.; Letsinger, R. L.; Mirkin, C. A., Selective Colorimetric Detection of Polynucleotides Based on the Distance-Dependent Optical Properties of Gold Nanoparticles. *Science* **1997**, *277*, 1078.

22. Chang, C.-C.; Wu, H.-L.; Kuo, C.-H.; Huang, M. H., Hydrothermal Synthesis of Monodispersed Octahedral Gold Nanocrystals with Five Different Size Ranges and Their Self-Assembled Structures. *Chemistry of Materials* **2008**, *20*, 7570-7574.

23. Link, S.; El-Sayed, M. A., Spectral Properties and Relaxation Dynamics of Surface Plasmon Electronic Oscillations in Gold and Silver Nanodots and Nanorods. *The Journal of Physical Chemistry B* **1999**, *103*, 8410-8426.

24. Smith, P. F., et al., Coordination Geometry and Oxidation State Requirements of Corner-Sharing Mno6 Octahedra for Water Oxidation Catalysis: An Investigation of Manganite (Γ-Mnooh). *ACS Catalysis* **2016**, *6*, 2089-2099.

25. Callejas, J. F.; McEnaney, J. M.; Read, C. G.; Crompton, J. C.; Biacchi, A. J.; Popczun, E. J.; Gordon, T. R.; Lewis, N. S.; Schaak, R. E., Electrocatalytic and

Photocatalytic Hydrogen Production from Acidic and Neutral-Ph Aqueous Solutions Using Iron Phosphide Nanoparticles. *ACS Nano* **2014**, *8*, 11101-11107.

26. Popczun, E. J.; Read, C. G.; Roske, C. W.; Lewis, N. S.; Schaak, R. E., Highly Active Electrocatalysis of the Hydrogen Evolution Reaction by Cobalt Phosphide Nanoparticles. *Angew Chem Int Ed* **2014**, *53*, 5427-30.

27. Chen, K.; Huang, X.; Wan, C.; Liu, H., Efficient Oxygen Reduction Catalysts Formed of Cobalt Phosphide Nanoparticle Decorated Heteroatom-Doped Mesoporous Carbon Nanotubes. *Chem Commun* **2015**, *51*, 7891-4.

28. Vrubel, H.; Hu, X., Growth and Activation of an Amorphous Molybdenum Sulfide Hydrogen Evolving Catalyst. *ACS Catalysis* **2013**, *3*, 2002-2011.

29. Li, W.; Yang, Y.; Weber, J. K.; Zhang, G.; Zhou, R., Tunable, Strain-Controlled Nanoporous Mos2 Filter for Water Desalination. *ACS Nano* **2016**, *10*, 1829-1835.

30. Xie, J.; Zhang, H.; Li, S.; Wang, R.; Sun, X.; Zhou, M.; Zhou, J.; Lou Xiong, W.; Xie, Y., Defect-Rich Mos2 Ultrathin Nanosheets with Additional Active Edge Sites for Enhanced Electrocatalytic Hydrogen Evolution. *Advanced Materials* **2013**, *25*, 5807-5813.

31. Altavilla, C.; Sarno, M.; Ciambelli, P., A Novel Wet Chemistry Approach for the Synthesis of Hybrid 2d Free-Floating Single or Multilayer Nanosheets of Ms2@Oleylamine (M═Mo, W). *Chemistry of Materials* **2011**, *23*, 3879-3885.

32. Ma, R.; Zhou, Y.; Chen, Y.; Li, P.; Liu, Q.; Wang, J., Ultrafine Molybdenum Carbide Nanoparticles Composited with Carbon as a Highly Active Hydrogen-Evolution Electrocatalyst. *Angew Chem Int Ed* **2015**, *54*, 14723-7.

33. Hunt, S. T.; Nimmanwudipong, T.; Roman-Leshkov, Y., Engineering Non-Sintered, Metal-Terminated Tungsten Carbide Nanoparticles for Catalysis. *Angew Chem Int Ed* **2014**, *53*, 5131-6.

34. Chen, J.; Wu, X. J.; Yin, L.; Li, B.; Hong, X.; Fan, Z.; Chen, B.; Xue, C.; Zhang, H., One-Pot Synthesis of Cds Nanocrystals Hybridized with Single-Layer Transition-Metal Dichalcogenide Nanosheets for Efficient Photocatalytic Hydrogen Evolution. *Angew Chem Int Ed* **2015**, *54*, 1210-4.

35. Yin, Y.; Erdonmez, C. K.; Cabot, A.; Hughes, S.; Alivisatos, A. P., Colloidal Synthesis of Hollow Cobalt Sulfide Nanocrystals. *Advanced Functional Materials* **2006**, *16*, 1389-1399.

36. Feng, Y.; He, T.; Alonso-Vante, N., In Situ Free-Surfactant Synthesis and Orr-Electrochemistry of Carbon-Supported Co3s4 and Cose2 Nanoparticles. *Chemistry of Materials* **2008**, *20*, 26-28.

37. Wang, H.; Liang, Y.; Li, Y.; Dai, H., Co(1-X)S-Graphene Hybrid: A High-Performance Metal Chalcogenide Electrocatalyst for Oxygen Reduction. *Angew Chem Int Ed* **2011**, *50*, 10969-72.

38. Sun, Y.; Lei, F.; Gao, S.; Pan, B.; Zhou, J.; Xie, Y., Atomically Thin Tin Dioxide Sheets for Efficient Catalytic Oxidation of Carbon Monoxide. *Angew Chem Int Ed* **2013**, *52*, 10569-72.

39. Jun, Y. W.; Choi, J. S.; Cheon, J., Shape Control of Semiconductor and Metal Oxide Nanocrystals through Nonhydrolytic Colloidal Routes. *Angew Chem Int Ed* **2006**, *45*, 3414-39.

40. Liu, W.; Li, X.; Zhu, M.; He, X., High-Performance All-Solid State Asymmetric Supercapacitor Based on Co 3 O 4 Nanowires and Carbon Aerogel. *Journal of Power Sources* **2015**, *282*, 179-186.

41. Seo, J.-w.; Jun, Y.-w.; Ko, S. J.; Cheon, J., In Situ One-Pot Synthesis of 1-Dimensional Transition Metal Oxide Nanocrystals. *The Journal of Physical Chemistry B* **2005**, *109*, 5389-5391.

42. Dubau, L.; Asset, T.; Chattot, R.; Bonnaud, C.; Vanpeene, V.; Nelayah, J.; Maillard, F., Tuning the Performance and the Stability of Porous Hollow Ptni/C Nanostructures for the Oxygen Reduction Reaction. *ACS Catalysis* **2015**, *5*, 5333-5341.

43. Lu, S.; Zhuang, Z., Investigating the Influences of the Adsorbed Species on Catalytic Activity for Hydrogen Oxidation Reaction in Alkaline Electrolyte. *J Am Chem Soc* **2017**.

44. Hoang, T. T. H.; Gewirth, A. A., High Activity Oxygen Evolution Reaction Catalysts from Additive-Controlled Electrodeposited Ni and Nife Films. *ACS Catalysis* **2016**, *6*, 1159-1164.

45. Xiong, H.; Lin, S.; Goetze, J.; Pletcher, P.; Guo, H.; Kovarik, L.; Artyushkova, K.; Weckhuysen, B. M.; Datye, A. K., Thermally Stable and Regenerable Platinum-Tin Clusters for Propane Dehydrogenation Prepared by Atom Trapping on Ceria. *Angew Chem Int Ed* **2017**, *56*, 8986-8991.

46. Wang, X.; Altmann, L.; Stöver, J.; Zielasek, V.; Bäumer, M.; Al-Shamery, K.; Borchert, H.; Parisi, J.; Kolny-Olesiak, J., Pt/Sn Intermetallic, Core/Shell and Alloy Nanoparticles: Colloidal Synthesis and Structural Control. *Chemistry of Materials* **2013**, *25*, 1400-1407.

47. Stamenkovic, V. R.; Mun, B. S.; Mayrhofer, K. J. J.; Ross, P. N.; Markovic, N. M., Effect of Surface Composition on Electronic Structure, Stability, and Electrocatalytic Properties of Pt-Transition Metal Alloys: Pt-Skin Versus Pt-Skeleton Surfaces. *Journal of the American Chemical Society* **2006**, *128*, 8813-8819.

48. Vayssieres, L., Growth of Arrayed Nanorods and Nanowires of Zno from Aqueous Solutions. *Advanced Materials* **2003**, *15*, 464-466.

49. Zhang, X.; Ai, Z.; Jia, F.; Zhang, L., Generalized One-Pot Synthesis, Characterization, and Photocatalytic Activity of Hierarchical Biox (X = Cl, Br, I) Nanoplate Microspheres. *The Journal of Physical Chemistry C* **2008**, *112*, 747-753.

50. Yoo, E.; Kim, J.; Hosono, E.; Zhou, H.-s.; Kudo, T.; Honma, I., Large Reversible Li Storage of Graphene Nanosheet Families for Use in Rechargeable Lithium Ion Batteries. *Nano Letters* **2008**, *8*, 2277-2282.

51. Boisselier, E.; Astruc, D., Gold Nanoparticles in Nanomedicine: Preparations, Imaging, Diagnostics, Therapies and Toxicity. *Chemical Society Reviews* **2009**, *38*, 1759-1782.

52. Jain, R. K.; Stylianopoulos, T., Delivering Nanomedicine to Solid Tumors. *Nat Rev Clin Oncol* **2010**, *7*, 653-64.

53. Manto, M. J.; Xie, P.; Wang, C., Catalytic Dephosphorylation Using Ceria Nanocrystals. *ACS Catalysis* **2017**, *7*, 1931-1938.

54. Manto, M. J.; Xie, P.; Keller, M. A.; Liano, W. E.; Pu, T.; Wang, C., Recovery of Inorganic Phosphorus Using Copper-Substituted Zsm-5. *ACS Sustainable Chemistry & Engineering* **2017**, *5*, 6192-6200.

55. Guo, S.; Wang, E., Synthesis and Electrochemical Applications of Gold Nanoparticles. *Analytica Chimica Acta* **2007**, *598*, 181-192.

56. Wan, C.; Regmi Yagya, N.; Leonard Brian, M., Multiple Phases of Molybdenum Carbide as Electrocatalysts for the Hydrogen Evolution Reaction. *Angewandte Chemie International Edition* **2014**, *53*, 6407-6410.

57. Bagotsky, V. S., Fundamentals of Electrochemistry. *John Wiley & Sons Inc.* **2006**.

58. Haring, M. M., The Theory of Rate Processes (Glasstone, Samuel; Laidler, Keith J.; Eyring, Henry). *Journal of Chemical Education* **1942**, *19*, 249.

59. Villagrasa, J. P.; Colomer-Farrarons, J.; Miribel, P. L., Bioelectronics for Amperometric Biosensors. In *State of the Art in Biosensors - General Aspects*, Rinken, T., Ed. InTech: Rijeka, 2013; p Ch. 10.

60. Kwan, J. T. H.; Bonakdarpour, A.; Afonso, G.; Wilkinson, D. P., Bridging Fundamental Electrochemistry with Applied Fuel Cell Testing: A Novel and Economical Rotating Disk Electrode Tip for Electrochemical Assessment of Catalyst-Coated Membranes. *Electrochimica Acta* **2017**, *258*, 208-219.

61. Liu, C.-W.; Chen, W.-E.; Sun, Y. T. A.; Lin, C.-R., Fabrication and Electrochemistry Characteristics of Nickel-Doped Diamond-Like Carbon Film toward Applications in Non-Enzymatic Glucose Detection. *Applied Surface Science* **2018**, *436*, 967-973.

62. Moore Colin, E.; Gyenge Előd, L., Tuning the Composition of Electrodeposited Bimetallic Tin–Lead Catalysts for Enhanced Activity and Durability in Carbon Dioxide Electroreduction to Formate. *ChemSusChem* **2017**, *10*, 3512-3519.

63. Shehnaz; Wu, D.; Guo, Y.; Song, X.; Yang, Y.; Mao, Q.; Ren, S.; Hao, C., Synergistic Effect of Heat Treatments and Koh Activation Enhances the Electrochemistry Performance of Polypyrrole Nanochains (Ppy-Ncs). *Electrochimica Acta* **2018**, *266*, 151-160.

64. Bard, A.; Faulkner, L., *Electrochemical Methods: Fundamentals and Applications*; John Wiley & Sons, Inc, 2001.

65. Li, C. W.; Kanan, M. W., Co2 Reduction at Low Overpotential on Cu Electrodes Resulting from the Reduction of Thick Cu2o Films. *J Am Chem Soc* **2012**, *134*, 7231-4.

66. Waszczuk, P.; Zelenay, P.; Sobkowski, J., Surface Interaction of Benzoic Acid with a Copper Electrode. *Electrochimica Acta* **1995**, *40*, 1717-1721.

67. Pozio, A.; De Francesco, M.; Cemmi, A.; Cardellini, F.; Giorgi, L., Comparison of High Surface Pt/C Catalysts by Cyclic Voltammetry. *Journal of Power Sources* **2002**, *105*, 13-19.

68. Carrette, L.; Friedrich, K. A.; Stimming, U., Fuel Cells – Fundamentals and Applications. *Fuel Cells* **2001**, *1*, 5-39.

69. Barbir, F.; Gómez, T., Efficiency and Economics of Proton Exchange Membrane (PEM) Fuel Cells. *International Journal of Hydrogen Energy* **1997**, *22*, 1027-1037.

70. Sun, Y.; Cheng, J., Hydrolysis of Lignocellulosic Materials for Ethanol Production: A Review. *Bioresource Technology* **2002**, *83*, 1-11.

71. Farrell, A. E.; Plevin, R. J.; Turner, B. T.; Jones, A. D.; Hare, M.; Kammen, D. M., Ethanol Can Contribute to Energy and Environmental Goals. *Science* **2006**, *311*, 506.

72. Wang, H.; Jusys, Z.; Behm, R. J., Ethanol Electrooxidation on a Carbon-Supported Pt Catalyst: Reaction Kinetics and Product Yields. *The Journal of Physical Chemistry B* **2004**, *108*, 19413-19424.

73. Zhou, W. J.; Zhou, B.; Li, W. Z.; Zhou, Z. H.; Song, S. Q.; Sun, G. Q.; Xin, Q.; Douvartzides, S.; Goula, M.; Tsiakaras, P., Performance Comparison of Low-Temperature Direct Alcohol Fuel Cells with Different Anode Catalysts. *Journal of Power Sources* **2004**, *126*, 16-22.

74. Kavanagh, R.; Cao, X. M.; Lin, W. F.; Hardacre, C.; Hu, P., Origin of Low CO2 Selectivity on Platinum in the Direct Ethanol Fuel Cell. *Angew Chem Int Ed* **2012**, *51*, 1572-5.

75. Wang, H.-F.; Liu, Z.-P., Comprehensive Mechanism and Structure-Sensitivity of Ethanol Oxidation on Platinum: New Transition-State Searching Method for Resolving the Complex Reaction Network. *Journal of the American Chemical Society* **2008**, *130*, 10996-11004.

76. Ferre-Vilaplana, A.; Buso-Rogero, C.; Feliu, J. M.; Herrero, E., Cleavage of the C–C Bond in the Ethanol Oxidation Reaction on Platinum. Insight from Experiments and Calculations. *The Journal of Physical Chemistry C* **2016**, *120*, 11590-11597.

77. Lai, S. C. S.; Kleyn, S. E. F.; Rosca, V.; Koper, M. T. M., Mechanism of the Dissociation and Electrooxidation of Ethanol and Acetaldehyde on Platinum as Studied by Sers. *The Journal of Physical Chemistry C* **2008**, *112*, 19080-19087.

78. Lai, S. C. S.; Koper, M. T. M., Electro-Oxidation of Ethanol and Acetaldehyde on Platinum Single-Crystal Electrodes. *Faraday Discussions* **2009**, *140*, 399-416.

79. Kowal, A.; Li, M.; Shao, M.; Sasaki, K.; Vukmirovic, M. B.; Zhang, J.; Marinkovic, N. S.; Liu, P.; Frenkel, A. I.; Adzic, R. R., Ternary Pt/Rh/Sno2 Electrocatalysts for Oxidizing Ethanol to CO2. *Nat Mater* **2009**, *8*, 325-30.

80. Holladay, J. D.; Hu, J.; King, D. L.; Wang, Y., An Overview of Hydrogen Production Technologies. *Catalysis Today* **2009**, *139*, 244-260.

81. Conway, B. E.; Tilak, B. V., Interfacial Processes Involving Electrocatalytic Evolution and Oxidation of H2, and the Role of Chemisorbed H. *Electrochimica Acta* **2002**, *47*, 3571-3594.

82. Li, Y.; Wang, H.; Xie, L.; Liang, Y.; Hong, G.; Dai, H., Mos2 Nanoparticles Grown on Graphene: An Advanced Catalyst for the Hydrogen Evolution Reaction. *Journal of the American Chemical Society* **2011**, *133*, 7296-7299.

83. Jaramillo, T. F.; Jørgensen, K. P.; Bonde, J.; Nielsen, J. H.; Horch, S.; Chorkendorff, I., Identification of Active Edge Sites for Electrochemical H2 Evolution from Mos2 Nanocatalysts. *Science* **2007**, *317*, 100-102.

84. Badwal, S. P. S.; Giddey, S.; Kulkarni, A.; Goel, J.; Basu, S., Direct Ethanol Fuel Cells for Transport and Stationary Applications - a Comprehensive Review. *Appl Energ* **2015**, *145*, 80-103.

85. Lamy, C.; Lima, A.; LeRhun, V.; Delime, F.; Coutanceau, C.; Leger, J. M., Recent Advances in the Development of Direct Alcohol Fuel Cells (Dafc). *J Power Sources* **2002**, *105*, 283-296.

86. Wang, H.; Jusys, Z.; Behm, R. J., Ethanol Electrooxidation on a Carbon-Supported Pt Catalyst: Reaction Kinetics and Product Yields. *J Phys Chem B* **2004**, *108*, 19413-19424.

87. Colmati, F.; Tremiliosi-Filho, G.; Gonzalez, E. R.; Berna, A.; Herrero, E.; Feliu, J. M., Surface Structure Effects on the Electrochemical Oxidation of Ethanol on Platinum Single Crystal Electrodes. *Faraday Discuss* **2008**, *140*, 379-397.

88. Lai, S. C. S.; Koper, M. T. M., Electro-Oxidation of Ethanol and Acetaldehyde on Platinum Single-Crystal Electrodes. *Faraday Discuss* **2008**, *140*, 399-416.

89. Braunchweig, B.; Hibbitts, D.; Neurock, M.; Wieckowski, A., Electrocatalysis: A Direct Alcohol Fuel Cell and Surface Science Perspective. *Catal Today* **2013**, *202*, 197-209.

90. Lai, S. C. S.; Kleyn, S. E. F.; Rosca, V.; Koper, M. T. M., Mechanism of the Dissociation and Electrooxidation of Ethanol and Acetaldehyde on Platinum as Studied by Sers. *Journal of Physical Chemistry C* **2008**, *112*, 19080-19087.

91. Colmati, F.; Tremiliosi, G.; Gonzalez, E. R.; Berna, A.; Herrero, E.; Feliu, J. M., The Role of the Steps in the Cleavage of the C-C Bond During Ethanol Oxidation on Platinum Electrodes. *Physical Chemistry Chemical Physics* **2009**, *11*, 9114-9123.

92. Ferre-Vilaplana, A.; Buso-Rogero, C.; Feliu, J. M.; Herrero, E., Cleavage of the C-C Bond in the Ethanol Oxidation Reaction on Platinum. Insight from Experiments and Calculations. *J. Phys. Chem. C* **2016**, *120*, 11590-11597.

93. Kavanagh, R.; Cao, X. M.; Lin, W. F.; Hardacre, C.; Hu, P., Origin of Low Co2 Selectivity on Platinum in the Direct Ethanol Fuel Cell. *Angewandte Chemie-International Edition* **2012**, *51*, 1572-1575.

94. Lai, S. C. S.; Koper, M. T. M., The Influence of Surface Structure on Selectivity in the Ethanol Electro-Oxidation Reaction on Platinum. *The Journal of Physical Chemistry Letters* **2010**, *1*, 1122-1125.

95. Dewan, S.; Raciti, D.; Liu, Y. F.; Gracias, D. H.; Wang, C., Comparative Studies of Ethanol and Ethylene Glycol Oxidation on Platinum Electrocatalysts. *Topics in Catalysis* **2018**, *61*, 1035-1042.

96. Du, W.; Yang, G.; Wong, E.; Deskins, N. A.; Frenkel, A. I.; Su, D.; Teng, X., Platinum-Tin Oxide Core–Shell Catalysts for Efficient Electro-Oxidation of Ethanol. *Journal of the American Chemical Society* **2014**, *136*, 10862-10865.

97. Rizo, R.; Lázaro, M. J.; Pastor, E.; Koper, M. T. M., Ethanol Oxidation on Sn-Modified Pt Single-Crystal Electrodes: New Mechanistic Insights from on-Line Electrochemical Mass Spectrometry. *ChemElectroChem* **2016**, *3*, 2196-2201.

98. Kowal, A.; Li, M.; Shao, M.; Sasaki, K.; Vukmirovic, M. B.; Zhang, J.; Marinkovic, N. S.; Liu, P.; Frenkel, A. I.; Adzic, R. R., Ternary Pt/Rh/Sno2 Electrocatalysts for Oxidizing Ethanol to CO2. *Nature Materials* **2009**, *8*, 325-330.

99. St John, S.; Boolchand, P.; Angelopoulos, A. P., Improved Electrocatalytic Ethanol Oxidation Activity in Acidic and Alkaline Electrolytes Using Size-Controlled Pt-Sn Nanoparticles. *Langmuir* **2013**, *29*, 16150-9.

100. Antolini, E., Catalysts for Direct Ethanol Fuel Cells. *Journal of Power Sources* **2007**, *170*, 1-12.

101. Rousseau, S.; Coutanceau, C.; Lamy, C.; Leger, J. M., Direct Ethanol Fuel Cell (Defc): Electrical Performances and Reaction Products Distribution under Operating Conditions with Different Platinum-Based Anodes. *J Power Sources* **2006**, *158*, 18-24.

102. Zhu, M. Y.; Sun, G. Q.; Xin, Q., Effect of Alloying Degree in Ptsn Catalyst on the Catalytic Behavior for Ethanol Electro-Oxidation. *Electrochimica Acta* **2009**, *54*, 1511-1518.

103. Kim, J. H.; Choi, S. M.; Nam, S. H.; Seo, M. H.; Choi, S. H.; Kim, W. B., Influence of Sn Content on Ptsn/C Catalysts for Electrooxidation of C-1-C-3 Alcohols: Synthesis, Characterization, and Electrocatalytic Activity. *Appl Catal B-Environ* **2008**, *82*, 89-102.

104. Jin, J. M., et al., The Origin of High Activity but Low Co2 Selectivity on Binary Ptsn in the Direct Ethanol Fuel Cell. *Physical Chemistry Chemical Physics* **2014**, *16*, 9432-9440.

105. Wang, Q.; Sun, G. Q.; Jiang, L. H.; Xin, Q.; Sun, S. G.; Jiang, Y. X.; Chen, S. P.; Jusys, Z.; Behm, R. J., Adsorption and Oxidation of Ethanol on Colloid-Based Pt/C, Ptru/C and Pt3Sn/C Catalysts: In Situ FTIR Spectroscopy and on-Line DEMS Studies. *Physical Chemistry Chemical Physics* **2007**, *9*, 2686-2696.

106. El-Shafei, A. A.; Eiswirth, M., Electrochemical Activity of Sn-Modified Pt Single Crystal Electrodes for Ethanol Oxidation. *Surf Sci* **2010**, *604*, 862-867.

107. Paulino, M. E.; Nunes, L. M. S.; Gonzalez, E. R.; Tremiliosi-Filho, G., In Situ Ftir Spectroscopic Study of Ethanol Oxidation on Pt(111)/Rh/Sn Surface. The Anion Effect. *Electrochemistry Communications* **2015**, *52*, 85-88.

108. Jablonski, A.; Kulesza, P. J.; Lewera, A., Oxygen Permeation through Nafion 117 Membrane and Its Impact on Efficiency of Polymer Membrane Ethanol Fuel Cell. *J Power Sources* **2011**, *196*, 4714-4718.

109. Rao, V.; Hariyanto; Cremers, C.; Stimming, U., Investigation of the Ethanol Electro-Oxidation in Alkaline Membrane Electrode Assembly by Differential Electrochemical Mass Spectrometry. *Fuel Cells* **2007**, *7*, 417-423.

110. Jiang, L. H.; Sun, G. Q.; Sun, S. G.; Liu, J. G.; Tang, S. H.; Li, H. Q.; Zhou, B.; Xin, Q., Structure and Chemical Composition of Supported Pt-Sn Electrocatalysts for Ethanol Oxidation. *Electrochimica Acta* **2005**, *50*, 5384-5389.

111. Simoes, F. C., et al., Electroactivity of Tin Modified Platinum Electrodes for Ethanol Electrooxidation. *J Power Sources* **2007**, *167*, 1-10.

112. Li, D. G.; Wang, C.; Tripkovic, D.; Sun, S. H.; Markovic, N. M.; Stamenkovic, V. R., Surfactant Removal for Colloidal Nanoparticles from Solution Synthesis: The Effect on Catalytic Performance. *ACS Catal* **2012**, *2*, 1358-1362.

113. Fan, X.; Tang, X.; Ma, D.; Bi, P.; Jiang, A.; Zhu, J.; Xu, X., Novel Hollow Sn–Cu Composite Nanoparticles Anodes for Li-Ion Batteries Prepared by Galvanic Replacement Reaction. *Journal of Solid State Electrochemistry* **2014**, *18*, 1137-1145.

114. Raciti, D.; Livi, K. J.; Wang, C., Highly Dense Cu Nanowires for Low-Overpotential CO2 Reduction. *Nano Lett* **2015**, *15*, 6829-35.

115. House, C. I.; Kelsall, G. H., Potential—Ph Diagrams for the Sn/H2O-Cl System. *Electrochimica Acta* **1984**, *29*, 1459-1464.

116. Rizo, R.; Sebastián, D.; Lázaro, M. J.; Pastor, E., On the Design of Pt-Sn Efficient Catalyst for Carbon Monoxide and Ethanol Oxidation in Acid and Alkaline Media. *Applied Catalysis B: Environmental* **2017**, *200*, 246-254.

117. Antoniassi, R. M.; Silva, J. C. M.; Oliveira Neto, A.; Spinacé, E. V., Synthesis of Pt+SnO2/C Electrocatalysts Containing Pt Nanoparticles with Preferential (100) Orientation for Direct Ethanol Fuel Cell. *Applied Catalysis B: Environmental* **2017**, *218*, 91-100.

118. De Souza, R. F. B.; Parreira, L. S.; Rascio, D. C.; Silva, J. C. M.; Teixeira-Neto, E.; Calegaro, M. L.; Spinace, E. V.; Neto, A. O.; Santos, M. C., Study of Ethanol Electro-Oxidation in Acid Environment on Pt3Sn/C Anode Catalysts Prepared by a Modified Polymeric Precursor Method under Controlled Synthesis Conditions. *Journal of Power Sources* **2010**, *195*, 1589-1593.

119. Peng, S.; Lee, Y. M.; Wang, C.; Yin, H. F.; Dai, S.; Sun, S. H., A Facile Synthesis of Monodisperse Au Nanoparticles and Their Catalysis of Co Oxidation. *Nano Res.* **2008**, *1*, 229-234.

120. Goksu, H.; Ho, S. F.; Metin, O.; Korkmaz, K.; Garcia, A. M.; Gultekin, M. S.; Sun, S. H., Tandem Dehydrogenation of Ammonia Borane and Hydrogenation of Nitro/Nitrile Compounds Catalyzed by Graphene-Supported Nipd Alloy Nanoparticles. *ACS Catalysis* **2014**, *4*, 1777-1782.

121. Guo, D. J., Electrooxidation of Ethanol on Novel Multi-Walled Carbon Nanotube Supported Platinum-Antimony Tin Oxide Nanoparticle Catalysts. *J Power Sources* **2011**, *196*, 679-682.

122. Subbaraman, R.; Tripkovic, D.; Chang, K. C.; Strmcnik, D.; Paulikas, A. P.; Hirunsit, P.; Chan, M.; Greeley, J.; Stamenkovic, V.; Markovic, N. M., Trends in Activity for the Water Electrolyser Reactions on 3d M(Ni,Co,Fe,Mn) Hydr(Oxy)Oxide Catalysts. *Nat. Mater.* **2012**, *11*, 550-557.

123. by John, F. M.; edited by Jill Chastain, R. C. K., Jr., *Handbook of X-Ray Photoelectron Spectroscopy : A Reference Book of Standard Spectra for Identification and Interpretation of XPS Data*; Eden Prairie, Minn. : Physical Electronics, [1995] ©1995, 1995.

124. Garcia, G.; Koper, M. T. M., Carbon Monoxide Oxidation on Pt Single Crystal Electrodes: Understanding the Catalysis for Low Temperature Fuel Cells. *ChemPhysChem* **2011**, *12*, 2064-2072.

125. Strmcnik, D. S.; Tripkovic, D. V.; van der Vliet, D.; Chang, K. C.; Komanicky, V.; You, H.; Karapetrov, G.; Greeley, J.; Stamenkovic, V. R.; Markovic, N. M., Unique Activity of Platinum Adislands in the Co Electrooxidation Reaction. *J. Am. Chem. Soc.* **2008**, *130*, 15332-15339.

126. Wang, L., et al., Core-Shell Nanostructured Cobalt-Platinum Electrocatalysts with Enhanced Durability. *ACS Catalysis* **2018**, *8*, 35-42.

127. Rudi, S.; Cui, C. H.; Gan, L.; Strasser, P., Comparative Study of the Electrocatalytically Active Surface Areas (ECSAs) of Pt Alloy Nanoparticles Evaluated by H-Upd and Co-Stripping Voltammetry. *Electrocatalysis* **2014**, *5*, 408-418.

128. Kutz, R. B.; Braunschweig, B.; Mukherjee, P.; Behrens, R. L.; Dlott, D. D.; Wieckowski, A., Reaction Pathways of Ethanol Electrooxidation on Polycrystalline Platinum Catalysts in Acidic Electrolytes. *J. Catal.* **2011**, *278*, 181-188.

129. Jiang, L.; Colmenares, L.; Jusys, Z.; Sun, G. Q.; Behm, R. J., Ethanol Electrooxidation on Novel Carbon Supported Pt/Snox/C Catalysts with Varied Pt:Sn Ratio. *Electrochimica Acta* **2007**, *53*, 377-389.

130. Li, M.; Cullen, D. A.; Sasaki, K.; Marinkovic, N. S.; More, K.; Adzic, R. R., Ternary Electrocatalysts for Oxidizing Ethanol to Carbon Dioxide: Making Ir Capable of Splitting C-C Bond. *Journal of the American Chemical Society* **2013**, *135*, 132-141.

131. Lin, Q.; Wei, Y.; Liu, W.; Yu, Y.; Hu, J., Electrocatalytic Oxidation of Ethylene Glycol and Glycerol on Nickel Ion Implanted-Modified Indium Tin Oxide Electrode. *International Journal of Hydrogen Energy* **2017**, *42*, 1403-1411.

132. Matsumoto, T.; Sadakiyo, M.; Ooi, M. L.; Kitano, S.; Yamamoto, T.; Matsumura, S.; Kato, K.; Takeguchi, T.; Yamauchi, M., Co2-Free Power Generation on an Iron Group Nanoalloy Catalyst Via Selective Oxidation of Ethylene Glycol to Oxalic Acid in Alkaline Media. *Scientific Reports* **2014**, *4*, 5620.

133. Livshits, V.; Peled, E., Progress in the Development of a High-Power, Direct Ethylene Glycol Fuel Cell (Degfc). *Journal of Power Sources* **2006**, *161*, 1187-1191.

134. Rebsdat, S.; Mayer, D., Ethylene Glycol. *Ullmann's Encyclopedia of Industrial Chemistry* **2000**.

135. T. Teunissen, H.; J. Elsevier, C., Ruthenium Catalysed Hydrogenation of Dimethyl Oxalate to Ethylene Glycol. *Chemical Communications* **1997**, 667-668.

136. Zhang, S.; Liu, Q.; Fan, G.; Li, F., Highly-Dispersed Copper-Based Catalysts from Cu–Zn–Al Layered Double Hydroxide Precursor for Gas-Phase Hydrogenation of Dimethyl Oxalate to Ethylene Glycol. *Catalysis Letters* **2012**, *142*, 1121-1127.

137. Yang, J.; Yang, Y.; Wu, W.-M.; Zhao, J.; Jiang, L., Evidence of Polyethylene Biodegradation by Bacterial Strains from the Guts of Plastic-Eating Waxworms. *Environmental Science & Technology* **2014**, *48*, 13776-13784.

138. Bombelli, P.; Howe, C. J.; Bertocchini, F., Polyethylene Bio-Degradation by Caterpillars of the Wax Moth Galleria Mellonella. *Current Biology* **2017**, *27*, R292-R293.

139. Peled, E.; Livshits, V.; Duvdevani, T., High-Power Direct Ethylene Glycol Fuel Cell (Degfc) Based on Nanoporous Proton-Conducting Membrane (Np-Pcm). *Journal of Power Sources* **2002**, *106*, 245-248.

140. Chatterjee, M.; Chatterjee, A.; Ghosh, S.; Basumallick, I., Electro-Oxidation of Ethanol and Ethylene Glycol on Carbon-Supported Nano-Pt and -Ptru Catalyst in Acid Solution. *Electrochimica Acta* **2009**, *54*, 7299-7304.

141. Fan, Y.-J.; Zhou, Z.-Y.; Zhen, C.-H.; Fan, C.-J.; Sun, S.-G., Kinetics of Dissociative Adsorption of Ethylene Glycol on Pt(1 0 0) Electrode Surface in Sulfuric Acid Solutions. *Electrochimica Acta* **2004**, *49*, 4659-4666.

142. Wang, H.; Zhao, Y.; Jusys, Z.; Behm, R. J., Ethylene Glycol Electrooxidation on Carbon Supported Pt, Ptru and Pt3sn Catalysts—a Comparative Dems Study. *J. Power Sources* **2006**, *155*, 33-46.

143. Wang, H.; Jusys, Z.; Behm, R. J., Electrochemical Oxidation Kinetics and Mechanism of Ethylene Glycol on a Carbon Supported Pt Catalyst: A Quantitative Dems Study. *Journal of Electroanalytical Chemistry* **2006**, *595*, 23-36.

144. Wang, H.; Jusys, Z.; Behm, R. J., Adsorption and Electrooxidation of Ethylene Glycol and Its C2 Oxidation Products on a Carbon-Supported Pt Catalyst: A Quantitative Dems Study. *Electrochimica Acta* **2009**, *54*, 6484-6498.

145. Schnaidt, J.; Heinen, M.; Jusys, Z.; Behm, R. J., Electro-Oxidation of Ethylene Glycol on a Pt-Film Electrode Studied by Combined in Situ Infrared Spectroscopy and Online Mass Spectrometry. *The Journal of Physical Chemistry C* **2012**, *116*, 2872-2883.

146. Wieland, B.; Lancaster, J. P.; Hoaglund, C. S.; Holota, P.; Tornquist, W. J., Electrochemical and Infrared Spectroscopic Quantitative Determination of the Platinum-

Catalyzed Ethylene Glycol Oxidation Mechanism at Co Adsorption Potentials. *Langmuir* **1996**, *12*, 2594-2601.

147. Kutz, R. B.; Braunschweig, B.; Mukherjee, P.; Behrens, R. L.; Dlott, D. D.; Wieckowski, A., Reaction Pathways of Ethanol Electrooxidation on Polycrystalline Platinum Catalysts in Acidic Electrolytes. *J Catal* **2011**, *278*, 181-188.

148. Salciccioli, M.; Yu, W.; Barteau, M. A.; Chen, J. G.; Vlachos, D. G., Differentiation of O-H and C-H Bond Scission Mechanisms of Ethylene Glycol on Pt and Ni/Pt Using Theory and Isotopic Labeling Experiments. *J Am Chem Soc* **2011**, *133*, 7996-8004.

149. Schnaidt, J.; Heinen, M.; Jusys, Z.; Behm, R. J., Mechanistic Aspects of the Electro-Oxidation of Ethylene Glycol on a Pt-Film Electrode: A Combined in Situ Ir Spectroscopy and Online Mass Spectrometry Study of Kinetic Isotope Effects. *Catalysis Today* **2013**, *202*, 154-162.

150. Schnaidt, J.; Heinen, M.; Jusys, Z.; Behm, R. J., Oxidation of the Partly Oxidized Ethylene Glycol Oxidation Products Glycolaldehyde, Glyoxal, Glycolic Acid, Glyoxylic Acid, and Oxalic Acid on Pt Electrodes: A Combined Atr-Ftirs and Dems Spectroelectrochemical Study. *The Journal of Physical Chemistry C* **2013**, *117*, 12689-12701.

151. Neto, A. O.; Vasconcelos, T. R. R.; Silva, R. W. R. V. D.; Linardi, M.; Spinacé, E. V., Electro-Oxidation of Ethylene Glycol on Ptru/C and Ptsn/C Electrocatalysts Prepared by Alcohol-Reduction Process. *J. Appl. Electrochem.* **2005**, *35*, 193-198.

152. Shi, Y.-C.; Feng, J.-J.; Lin, X.-X.; Zhang, L.; Yuan, J.; Zhang, Q.-L.; Wang, A.-J., One-Step Hydrothermal Synthesis of Three-Dimensional Nitrogen-Doped Reduced

Graphene Oxide Hydrogels Anchored Ptpd Alloyed Nanoparticles for Ethylene Glycol Oxidation and Hydrogen Evolution Reactions. *Electrochimica Acta* **2019**, *293*, 504-513.

153. Huang, X.-Y.; Wang, A.-J.; Zhang, X.-F.; Zhang, L.; Feng, J.-J., One-Step Synthesis of Ptcu Alloyed Nanocages with Highly Open Structures as Bifunctional Electrocatalysts for Oxygen Reduction and Polyhydric Alcohol Oxidation. *ACS Applied Energy Materials* **2018**, *1*, 5779-5786.

154. Yu, Z.-N.; Zhang, Z.; Lv, Z.-S.; Liu, M.-T.; Zhang, L.; Wang, A.-J.; Jiang, L.-Y.; Feng, J.-J., Platinum69-Cobalt31 Alloyed Nanosheet Nanoassemblies as Advanced Bifunctional Electrocatalysts for Boosting Ethylene Glycol Oxidation and Oxygen Reduction. *Journal of Colloid and Interface Science* **2018**, *525*, 216-224.

155. Leticia L. de Souza, A. O. N., Christiana A. L. G. de O. Forbicini, Direct Oxidation of Ethylene Glycol on Ptsn/C for Application in Alkaline Fuel Cell. *Int. J. Electrochem. Sci.* **2017**, *12*, 11855 - 11874.

156. Liu, Y.; Wei, M.; Raciti, D.; Wang, Y.; Hu, P.; Park, J. H.; Barclay, M.; Wang, C., Electro-Oxidation of Ethanol Using Pt3sn Alloy Nanoparticles. *ACS Catalysis* **2018**, 10931-10937.

157. Rudi, S.; Cui, C.; Gan, L.; Strasser, P., Comparative Study of the Electrocatalytically Active Surface Areas (ECSAs) of Pt Alloy Nanoparticles Evaluated by Hupd and Co-Stripping Voltammetry. *Electrocatalysis* **2014**, *5*, 408-418.

158. Mayrhofer, K. J. J.; Strmcnik, D.; Blizanac, B. B.; Stamenkovic, V.; Arenz, M.; Markovic, N. M., Measurement of Oxygen Reduction Activities Via the Rotating Disc Electrode Method: From Pt Model Surfaces to Carbon-Supported High Surface Area Catalysts. *Electrochim. Acta* **2008**, *53*, 3181-3188.

159. Garrick, T. R.; Moylan, T. E.; Carpenter, M. K.; Kongkanand, A., Electrochemically Active Surface Area Measurement of Aged Pt Alloy Catalysts in Pem Fuel Cells by Co Stripping. *J. Electrochem. Soc.* **2017**, *164*, F55-F59.

160. Moniri, S.; Van Cleve, T.; Linic, S., Pitfalls and Best Practices in Measurements of the Electrochemical Surface Area of Platinum-Based Nanostructured Electro-Catalysts. *J. Catal.* **2017**, *345*, 1-10.

161. Wang, L.; Holewinski, A.; Wang, C., Prospects of Platinum-Based Nanostructures for the Electrocatalytic Reduction of Oxygen. *Acs Catalysis* **2018**, *8*, 9388-9398.

162. Wu, F.; Zhang, D.; Peng, M.; Yu, Z.; Wang, X.; Guo, G.; Sun, Y., Microfluidic Synthesis Enables Dense and Uniform Loading of Surfactant-Free Ptsn Nanocrystals on Carbon Supports for Enhanced Ethanol Oxidation. *Angewandte Chemie International Edition* **2016**, *55*, 4952-4956.

163. González-Quijano, D.; Pech-Rodríguez, W. J.; Escalante-García, J. I.; Vargas-Gutiérrez, G.; Rodríguez-Varela, F. J., Electrocatalysts for Ethanol and Ethylene Glycol Oxidation Reactions. Part I: Effects of the Polyol Synthesis Conditions on the Characteristics and Catalytic Activity of Pt–Sn/C Anodes. *International Journal of Hydrogen Energy* **2014**, *39*, 16676-16685.

164. Sieben, J. M.; Duarte, M. M. E., Methanol, Ethanol and Ethylene Glycol Electro-Oxidation at Pt and Pt–Ru Catalysts Electrodeposited over Oxidized Carbon Nanotubes. *International Journal of Hydrogen Energy* **2012**, *37*, 9941-9947.

165. Ma, X.-Y.; Chen, Y.; Wang, H.; Li, Q.-X.; Lin, W.-F.; Cai, W.-B., Electrocatalytic Oxidation of Ethanol and Ethylene Glycol on Cubic, Octahedral and

Rhombic Dodecahedral Palladium Nanocrystals. *Chemical Communications* **2018**, *54*, 2562-2565.

166. Mayrhofer, K. J.; Juhart, V.; Hartl, K.; Hanzlik, M.; Arenz, M., Adsorbate-Induced Surface Segregation for Core-Shell Nanocatalysts. *Angew Chem Int Ed* **2009**, *48*, 3529-31.

167. Wang, H.; Jusys, Z.; Behm, R. J., Ethanol Electro-Oxidation on Carbon-Supported Pt, Ptru and Pt3sn Catalysts: A Quantitative Dems Study. *Journal of Power Sources* **2006**, *154*, 351-359.

168. Rizo, R.; Lazaro, M. J.; Pastor, E.; Garcia, G., Spectroelectrochemical Study of Carbon Monoxide and Ethanol Oxidation on Pt/C, Ptsn(3:1)/C and Ptsn(1:1)/C Catalysts. *Molecules* **2016**, *21*.

169. Jiang, L.; Zhou, Z.; Li, W.; Zhou, W.; Song, S.; Li, H.; Sun, G.; Xin, Q., Effects of Treatment in Different Atmosphere on Pt3sn/C Electrocatalysts for Ethanol Electro-Oxidation. *Energy & Fuels* **2004**, *18*, 866-871.

170. Antolini, E.; Colmati, F.; Gonzalez, E. R., Ethanol Oxidation on Carbon Supported (PtSn)Alloy/SnO2 and (PtSnPd)Alloy/SnO2 Catalysts with a Fixed Pt/SnO2 Atomic Ratio: Effect of the Alloy Phase Characteristics. *Journal of Power Sources* **2009**, *193*, 555-561.

171. Silva, J. C. M.; De Souza, R. F. B.; Parreira, L. S.; Neto, E. T.; Calegaro, M. L.; Santos, M. C., Ethanol Oxidation Reactions Using SnO2@Pt/C as an Electrocatalyst. *Applied Catalysis B: Environmental* **2010**, *99*, 265-271.

172. Godoi, D. R. M.; Perez, J.; Villullas, H. M., Alloys and Oxides on Carbon-Supported Pt–Sn Electrocatalysts for Ethanol Oxidation. *Journal of Power Sources* **2010**, *195*, 3394-3401.

173. Silva, J. C. M.; Parreira, L. S.; De Souza, R. F. B.; Calegaro, M. L.; Spinacé, E. V.; Neto, A. O.; Santos, M. C., PtSn/C Alloyed and Non-Alloyed Materials: Differences in the Ethanol Electro-Oxidation Reaction Pathways. *Applied Catalysis B: Environmental* **2011**, *110*, 141-147.

174. Sheng, T.; Lin, W. F.; Hardacre, C.; Hu, P., Significance of Beta-Dehydrogenation in Ethanol Electro-Oxidation on Platinum Doped with Ru, Rh, Pd, Os and Ir. *Phys Chem Chem Phys* **2014**, *16*, 13248-54.

175. Li, M.; Zhou, W. P.; Marinkovic, N. S.; Sasaki, K.; Adzic, R. R., The Role of Rhodium and Tin Oxide in the Platinum-Based Electrocatalysts for Ethanol Oxidation to CO2. *Electrochimica Acta* **2013**, *104*, 454-461.

176. de Souza, E. A.; Giz, M. J.; Camara, G. A.; Antolini, E.; Passos, R. R., Ethanol Electro-Oxidation on Partially Alloyed Pt-Sn-Rh/C Catalysts. *Electrochimica Acta* **2014**, *147*, 483-489.

177. Xu, Z.-F.; Wang, Y., Effects of Alloyed Metal on the Catalysis Activity of Pt for Ethanol Partial Oxidation: Adsorption and Dehydrogenation on Pt3m (M = Pt, Ru, Sn, Re, Rh, and Pd). *The Journal of Physical Chemistry C* **2011**, *115*, 20565-20571.

178. Du, W.; Yang, G.; Wong, E.; Deskins, N. A.; Frenkel, A. I.; Su, D.; Teng, X., Platinum-Tin Oxide Core-Shell Catalysts for Efficient Electro-Oxidation of Ethanol. *J Am Chem Soc* **2014**, *136*, 10862-5.

179. Erini, N.; Loukrakpam, R.; Petkov, V.; Baranova, E. A.; Yang, R.; Teschner, D.; Huang, Y.; Brankovic, S. R.; Strasser, P., Ethanol Electro-Oxidation on Ternary Platinum–Rhodium–Tin Nanocatalysts: Insights in the Atomic 3d Structure of the Active Catalytic Phase. *ACS Catalysis* **2014**, *4*, 1859-1867.

180. Erini, N.; Krause, P.; Gliech, M.; Yang, R.; Huang, Y.; Strasser, P., Comparative Assessment of Synthetic Strategies toward Active Platinum–Rhodium–Tin Electrocatalysts for Efficient Ethanol Electro-Oxidation. *Journal of Power Sources* **2015**, *294*, 299-304.

181. Yang, G.; Frenkel, A. I.; Su, D.; Teng, X., Enhanced Electrokinetics of C−C Bond Splitting During Ethanol Oxidation by Using a Pt/Rh/Sn Catalyst with a Partially Oxidized Pt and Rh Core and a SnO2 Shell. *ChemCatChem* **2016**, *8*, 2876-2880.

182. Yin, Y.; Rioux, R. M.; Erdonmez, C. K.; Hughes, S.; Somorjai, G. A.; Alivisatos, A. P., Formation of Hollow Nanocrystals through the Nanoscale Kirkendall Effect. *Science* **2004**, *304*, 711.

183. Łukaszewski, M.; Siwek, H.; Czerwiński, A., Electrochemical Behavior of Thin Polycrystalline Rhodium Layers Studied by Cyclic Voltammetry and Quartz Crystal Microbalance. *Electrochimica Acta* **2007**, *52*, 4560-4565.

184. Bach Delpeuch, A.; Maillard, F.; Chatenet, M.; Soudant, P.; Cremers, C., Ethanol Oxidation Reaction (EOR) Investigation on Pt/C, Rh/C, and Pt-Based Bi- and Tri-Metallic Electrocatalysts: A DEMS and in situ FTIR Study. *Applied Catalysis B: Environmental* **2016**, *181*, 672-680.

185. Pagliaro, M.; Ciriminna, R.; Kimura, H.; Rossi, M.; Della Pina, C., From Glycerol to Value-Added Products. *Angewandte Chemie International Edition* **2007**, *46*, 4434-4440.

186. Daniel Oliver, M.; DeLaRiva, A.; Kunkes Edward, L.; Datye Abhaya, K.; Dumesic James, A.; Davis Robert, J., X-Ray Absorption Spectroscopy of Bimetallic Pt–Re Catalysts for Hydrogenolysis of Glycerol to Propanediols. *ChemCatChem* **2010**, *2*, 1107-1114.

187. Behr, A.; Eilting, J.; Irawadi, K.; Leschinski, J.; Lindner, F., Improved Utilisation of Renewable Resources: New Important Derivatives of Glycerol. *Green Chem.* **2008**, *10*, 13-30.

188. Gholami, Z.; Abdullah, A. Z.; Lee, K. T., Dealing with the Surplus of Glycerol Production from Biodiesel Industry through Catalytic Upgrading to Polyglycerols and Other Value-Added Products. *Renewable & Sustainable Energy Reviews* **2014**, *39*, 327-341.

189. Dodekatos, G.; Schunemann, S.; Tuysuz, H., Recent Advances in Thermo-, Photo-, and Electrocatalytic Glycerol Oxidation. *ACS Catal.* **2018**, *8*, 6301-6333.

190. Du, L.; Shao, Y. Y.; Sun, J. M.; Yin, G. P.; Du, C. Y.; Wang, Y., Electrocatalytic Valorisation of Biomass Derived Chemicals. *Catal. Sci. Tech.* **2018**, *8*, 3216-3232.

191. Skrzynska, E.; Wondolowska-Grabowska, A.; Capron, M.; Dumeignil, F., Crude Glycerol as a Raw Material for the Liquid Phase Oxidation Reaction. *Applied Catalysis A-General* **2014**, *482*, 245-257.

192. Kwon, Y.; Birdja, Y.; Spanos, I.; Rodriguez, P.; Koper, M. T. M., Highly Selective Electro-Oxidation of Glycerol to Dihydroxyacetone on Platinum in the Presence of Bismuth. *ACS Catal.* **2012**, *2*, 759-764.

193. Huang, L., et al., Combined EC-NMR and in situ FTIR Spectroscopic Studies of Glycerol Electrooxidation on Pt/C, PtRu/C, and PtRh/C. *ACS Catal.* **2016**, *6*, 7686-7695.

194. Zhou, Y. F.; Shen, Y.; Piao, J. H., Sustainable Conversion of Glycerol into Value-Added Chemicals by Selective Electro-Oxidation on Pt-Based Catalysts. *Chemelectrochem* **2018**, *5*, 1636-1643.

195. Garcia, A. C.; Birdja, Y. Y.; Tremiliosi, G.; Koper, M. T. M., Glycerol Electro-Oxidation on Bismuth-Modified Platinum Single Crystals. *J. Catal.* **2017**, *346*, 117-124.

196. Fernández, P. S.; Martins, M. E.; Camara, G. A., New Insights About the Electro-Oxidation of Glycerol on Platinum Nanoparticles Supported on Multi-Walled Carbon Nanotubes. *Electrochimica Acta* **2012**, *66*, 180-187.

197. Martins, C. A.; Ibrahim, O. A.; Pei, P.; Kjeang, E., Towards a Fuel-Flexible Direct Alcohol Microfluidic Fuel Cell with Flow-through Porous Electrodes: Assessment of Methanol, Ethylene Glycol and Glycerol Fuels. *Electrochimica Acta* **2018**, *271*, 537-543.

198. Simoes, M.; Baranton, S.; Coutanceau, C., Electro-Oxidation of Glycerol at Pd Based Nano-Catalysts for an Application in Alkaline Fuel Cells for Chemicals and Energy Cogeneration. *App. Catal. B: Environ.* **2010**, *93*, 354-362.

199. Marchionni, A.; Bevilacqua, M.; Bianchini, C.; Chen, Y. X.; Filippi, J.; Fornasiero, P.; Lavacchi, A.; Miller, H.; Wang, L. Q.; Vizza, F., Electrooxidation of

Ethylene Glycol and Glycerol on Pd-(Ni-Zn)/C Anodes in Direct Alcohol Fuel Cells. *Chemsuschem* **2013**, *6*, 518-528.

200. Gomes, J. F.; Tremiliosi-Filho, G., Spectroscopic Studies of the Glycerol Electro-Oxidation on Polycrystalline Au and Pt Surfaces in Acidic and Alkaline Media. *Electrocatalysis* **2011**, *2*, 96.

201. Kwon, Y.; Schouten Klaas Jan, P.; Koper Marc, T. M., Mechanism of the Catalytic Oxidation of Glycerol on Polycrystalline Gold and Platinum Electrodes. *ChemCatChem* **2011**, *3*, 1176-1185.

202. Roquet, L.; Belgsir, E. M.; Leger, J. M.; Lamy, C., Kinetics and Mechanisms of the Electrocatalytic Oxidation of Glycerol as Investigated by Chromatographic Analysis of the Reaction-Products - Potential and Ph Effects. *Electrochim. Acta* **1994**, *39*, 2387-2394.

203. Schnaidt, J.; Heinen, M.; Denot, D.; Jusys, Z.; Behm, R. J., Electrooxidation of Glycerol Studied by Combined in Situ Ir Spectroscopy and Online Mass Spectrometry under Continuous Flow Conditions. *J Electroanal Chem* **2011**, *661*, 250-264.

204. Guima, K.-E.; Alencar, L. M.; da Silva, G. C.; Trindade, M. A. G.; Martins, C. A., 3d-Printed Electrolyzer for the Conversion of Glycerol into Tartronate on Pd Nanocubes. *ACS Sustainable Chemistry & Engineering* **2018**, *6*, 1202-1207.

205. Almeida, T. S. D.; Guima, K.-E.; Silveira, R. M.; da Silva, G. C.; Martines, M. A. U.; Martins, C. A., A Pd Nanocatalyst Supported on Multifaceted Mesoporous Silica with Enhanced Activity and Stability for Glycerol Electrooxidation. *RSC Advances* **2017**, *7*, 12006-12016.

206. Huang, L., et al., Combined Ec-Nmr and in Situ Ftir Spectroscopic Studies of Glycerol Electrooxidation on Pt/C, Ptru/C, and Ptrh/C. *ACS Catalysis* **2016**, *6*, 7686-7695.

207. González-Cobos, J.; Baranton, S.; Coutanceau, C., A Systematic in Situ Infrared Study of the Electrooxidation of C3 Alcohols on Carbon-Supported Pt and Pt–Bi Catalysts. *The Journal of Physical Chemistry C* **2016**, *120*, 7155-7164.

208. Caneppele, G. L.; Almeida, T. S.; Zanata, C. R.; Teixeira-Neto, É.; Fernández, P. S.; Camara, G. A.; Martins, C. A., Exponential Improving in the Activity of Pt/C Nanoparticles Towards Glycerol Electrooxidation by Sb Ad-Atoms Deposition. *Applied Catalysis B: Environmental* **2017**, *200*, 114-120.

209. Zanata, C. R.; Fernández, P. S.; Troiani, H. E.; Soldati, A. L.; Landers, R.; Camara, G. A.; Carvalho, A. E.; Martins, C. A., Rh-Decorated Ptirox Nanoparticles for Glycerol Electrooxidation: Searching for a Stable and Active Catalyst. *Applied Catalysis B: Environmental* **2016**, *181*, 445-455.

210. Baldelli, S.; Markovic, N.; Ross, P.; Shen, Y. R.; Somorjai, G., Sum Frequency Generation of Co on (111) and Polycrystalline Platinum Electrode Surfaces: Evidence for Sfg Invisible Surface Co. *J. Phys. Chem. B* **1999**, *103*, 8920-8925.

211. Wang, H.-F.; Gan, W.; Lu, R.; Rao, Y.; Wu, B.-H., Quantitative Spectral and Orientational Analysis in Surface Sum Frequency Generation Vibrational Spectroscopy (SFG-VS). *International Reviews in Physical Chemistry* **2005**, *24*, 191-256.

212. Lambert, A. G.; Davies, P. B.; Neivandt, D. J., Implementing the Theory of Sum Frequency Generation Vibrational Spectroscopy: A Tutorial Review. *Applied Spectroscopy Reviews* **2005**, *40*, 103-145.

213. Gautam, K. S.; Schwab, A. D.; Dhinojwala, A.; Zhang, D.; Dougal, S. M.; Yeganeh, M. S., Molecular Structure of Polystyrene at Air/Polymer and Solid/Polymer Interfaces. *Physical Review Letters* **2000**, *85*, 3854-3857.

214. Markovic, N. M.; Ross, P. N., Surface Science Studies of Model Fuel Cell Electrocatalysts. *Surf. Sci. Rep.* **2002**, *45*, 121-229.

215. Lopez-Cudero, A.; Cuesta, A.; Gutierrez, C., Potential Dependence of the Saturation Co Coverage of Pt Electrodes: The Origin of the Pre-Peak in Co-Stripping Voltammograms. Part 1: Pt(111). *J. Electroanal. Chem.* **2005**, *579*, 1-12.

216. Cuesta, A.; Couto, A.; Rincon, A.; Perez, M. C.; Lopez-Cudero, A.; Gutierrez, C., Potential Dependence of the Saturation Co Coverage of Pt Electrodes: The Origin of the Pre-Peak in CO-Stripping Voltammograms. Part 3: Pt(Poly). *J. Electroanal. Chem.* **2006**, *586*, 184-195.

217. Lopez-Cudero, A.; Cuesta, A.; Gutierrez, C., Potential Dependence of the Saturation Co Coverage of Pt Electrodes: The Origin of the Pre-Peak in Co-Stripping Voltammograms. Part 2: Pt(100). *J. Electroanal. Chem.* **2006**, *586*, 204-216.

218. Farias, M. J. S.; Camara, G. A.; Feliu, J. M., Understanding the Co Preoxidation and the Intrinsic Catalytic Activity of Step Sites in Stepped Pt Surfaces in Acidic Medium. *J. Phys. Chem. C* **2015**, *119*, 20272-20282.

219. Teles, R.; Arenillas, A.; da Silva, G. C.; Fernández, P. S.; Cardoso, E. S. F.; Maia, G.; Martins, C. A., Understanding the Influence of the Biomass-Derived Alcohols on the Activity and Stability of Pt Nanoparticles Supported on Graphene Nanoribbons. *Electrocatalysis* **2017**, *8*, 151-163.

220. Fernández Pablo, S.; Martins Cauê, A.; Angelucci Camilo, A.; Gomes Janaina, F.; Camara Giuseppe, A.; Martins Maria, E.; Tremiliosi-Filho, G., Evidence for Independent Glycerol Electrooxidation Behavior on Different Ordered Domains of Polycrystalline Platinum. *ChemElectroChem* **2014**, *2*, 263-268.

221. Dewan, S.; Raciti, D.; Liu, Y.; Gracias, D. H.; Wang, C., Comparative Studies of Ethanol and Ethylene Glycol Oxidation on Platinum Electrocatalysts. *Topics in Catalysis* **2018**.

222. Fernandez, P. S.; Tereshchuk, P.; Angelucci, C. A.; Gomes, J. F.; Garcia, A. C.; Martins, C. A.; Camara, G. A.; Martins, M. E.; Da Silva, J. L. F.; Tremiliosi-Filho, G., How Do Random Superficial Defects Influence the Electro-Oxidation of Glycerol on Pt(111) Surfaces? *Physical Chemistry Chemical Physics* **2016**, *18*, 25582-25591.

223. Kwon, Y.; Schouten, K. J. P.; Koper, M. T. M., Mechanism of the Catalytic Oxidation of Glycerol on Polycrystalline Gold and Platinum Electrodes. *Chemcatchem* **2011**, *3*, 1176-1185.

224. Falase, A.; Garcia, K.; Lau, C.; Atanassov, P., Electrochemical and in Situ Ir Characterization of Ptru Catalysts for Complete Oxidation of Ethylene Glycol and Glycerol. *Electrochem. Commun.* **2011**, *13*, 1488-1491.

225. Baldelli, S.; Markovic, N.; Ross, P.; Shen, Y.-R.; Somorjai, G., Sum Frequency Generation of Co on (111) and Polycrystalline Platinum Electrode Surfaces: Evidence for Sfg Invisible Surface Co. *The Journal of Physical Chemistry B* **1999**, *103*, 8920-8925.

226. Dederichs, F.; Friedrich, K. A.; Daum, W., Sum-Frequency Vibrational Spectroscopy of Co Adsorption on Pt(111) and Pt(110) Electrode Surfaces in Perchloric

Acid Solution: Effects of Thin-Layer Electrolytes in Spectroelectrochemistry. *The Journal of Physical Chemistry B* **2000**, *104*, 6626-6632.

227. Martins, C. A.; Giz, M. J.; Camara, G. A., Generation of Carbon Dioxide from Glycerol: Evidences of Massive Production on Polycrystalline Platinum. *Electrochim Acta* **2011**, *56*, 4549-4553.

228. Gomes, J. F.; de Paula, F. B. C.; Gasparotto, L. H. S.; Tremiliosi-Filho, G., The Influence of the Pt Crystalline Surface Orientation on the Glycerol Electro-Oxidation in Acidic Media. *Electrochim. Acta* **2012**, *76*, 88-93.

229. Fernández, P. S.; Martins, M. E.; Martins, C. A.; Camara, G. A., The Electro-Oxidation of Isotopically Labeled Glycerol on Platinum: New Information on C–C Bond Cleavage and CO2 Production. *Electrochemistry Communications* **2012**, *15*, 14-17.

230. Fernández, P. S.; Fernandes Gomes, J.; Angelucci, C. A.; Tereshchuk, P.; Martins, C. A.; Camara, G. A.; Martins, M. a. E.; Da Silva, J. L. F.; Tremiliosi-Filho, G., Establishing a Link between Well-Ordered Pt(100) Surfaces and Real Systems: How Do Random Superficial Defects Influence the Electro-Oxidation of Glycerol? *ACS Catalysis* **2015**, *5*, 4227-4236.

231. Gomes, J. F.; Martins, C. A.; Giz, M. J.; Tremiliosi-Filho, G.; Camara, G. A., Insights into the Adsorption and Electro-Oxidation of Glycerol: Self-Inhibition and Concentration Effects. *Journal of Catalysis* **2013**, *301*, 154-161.

232. Gomes, J. F.; Busson, B.; Tadjeddine, A., Sfg Study of the Ethanol in an Acidic Medium−Pt(110) Interface: Effects of the Alcohol Concentration. *The Journal of Physical Chemistry B* **2006**, *110*, 5508-5514.

233. Lambert, D. K., Vibrational Stark Effect of Adsorbates at Electrochemical Interfaces. *Electrochimica Acta* **1996**, *41*, 623-630.

234. Chang, S.-C.; Weaver, M. J., In-Situ Infrared Spectroscopy of Co Adsorbed at Ordered Pt(110)-Aqueous Interfaces. *Surface Science* **1990**, *230*, 222-236.

235. Bare, S. R.; Hofmann, P.; King, D. A., Vibrational Studies of the Surface Phases of CO on Pt{110} at 300 K. *Surface Science* **1984**, *144*, 347-369.

236. Iwasita, T.; Dalbeck, R.; Pastor, E.; Xia, X., Progress in the Study of Electrocatalytic Reactions of Organic Species. *Electrochimica Acta* **1994**, *39*, 1817-1823.

237. Vigier, F.; Coutanceau, C.; Hahn, F.; Belgsir, E. M.; Lamy, C., On the Mechanism of Ethanol Electro-Oxidation on Pt and Ptsn Catalysts: Electrochemical and in Situ Ir Reflectance Spectroscopy Studies. *Journal of Electroanalytical Chemistry* **2004**, *563*, 81-89.

238. Camara, G. A.; Iwasita, T., Parallel Pathways of Ethanol Oxidation: The Effect of Ethanol Concentration. *Journal of Electroanalytical Chemistry* **2005**, *578*, 315-321.

239. Gomes, J. F.; Tremiliosi-Filho, G., Spectroscopic Studies of the Glycerol Electro-Oxidation on Polycrystalline Au and Pt Surfaces in Acidic and Alkaline Media. *Electrocatalysis* **2011**, *2*, 96-105.

240. van der Vliet, D. F.; Wang, C.; Li, D. G.; Paulikas, A. P.; Greeley, J.; Rankin, R. B.; Strmcnik, D.; Tripkovic, D.; Markovic, N. M.; Stamenkovic, V. R., Unique Electrochemical Adsorption Properties of Pt-Skin Surfaces. *Angew. Chem. Int. Ed.* **2012**, *51*, 3139-3142.

241. Geim, A. K.; Novoselov, K. S., The Rise of Graphene. *Nat. Mater.* **2007**, *6*, 183-191.

242. Butler, S. Z., et al., Progress, Challenges, and Opportunities in Two-Dimensional Materials Beyond Graphene. *ACS Nano* **2013**, *7*, 2898-2926.

243. Rao, C. N. R.; Matte, H. S. S. R.; Maitra, U., Graphene Analogues of Inorganic Layered Materials. *Angew. Chem. Int. Ed.* **2013**, *52*, 13162-13185.

244. Wang, Q. H.; Kalantar-Zadeh, K.; Kis, A.; Coleman, J. N.; Strano, M. S., Electronics and Optoelectronics of Two-Dimensional Transition Metal Dichalcogenides. *Nat. Nanotechnol.* **2012**, *7*, 699-712.

245. Chhowalla, M.; Shin, H. S.; Eda, G.; Li, L. J.; Loh, K. P.; Zhang, H., The Chemistry of Two-Dimensional Layered Transition Metal Dichalcogenide Nanosheets. *Nature Chem.* **2013**, *5*, 263-275.

246. Jaramillo, T. F.; Jorgensen, K. P.; Bonde, J.; Nielsen, J. H.; Horch, S.; Chorkendorff, I., Identification of Active Edge Sites for Electrochemical H-2 Evolution from MoS2 Nanocatalysts. *Science* **2007**, *317*, 100-102.

247. Osada, M.; Sasaki, T., Two-Dimensional Dielectric Nanosheets: Novel Nanoelectronics from Nanocrystal Building Blocks. *Adv. Mater.* **2012**, *24*, 210-228.

248. de la Cruz, C., et al., Magnetic Order Close to Superconductivity in the Iron-Based Layered Lao(1-X)F(X)Feas Systems. *Nature* **2008**, *453*, 899-902.

249. Omomo, Y.; Sasaki, T.; Wang, L. Z.; Watanabe, M., Redoxable Nanosheet Crystallites of Mno2 Derived Via Delamination of a Layered Manganese Oxide. *J. Am. Chem. Soc.* **2003**, *125*, 3568-3575.

250. Amatucci, G. G.; Tarascon, J. M.; Klein, L. C., Coo2, the End Member of the Lixcoo2 Solid Solution. *J. Electrochem. Soc.* **1996**, *143*, 1114-1123.

251. Khazaei, M.; Arai, M.; Sasaki, T.; Chung, C. Y.; Venkataramanan, N. S.; Estili, M.; Sakka, Y.; Kawazoe, Y., Novel Electronic and Magnetic Properties of Two-Dimensional Transition Metal Carbides and Nitrides. *Adv. Fun. Mater.* **2013**, *23*, 2185-2192.

252. Mashtalir, O.; Naguib, M.; Mochalin, V. N.; Dall'Agnese, Y.; Heon, M.; Barsoum, M. W.; Gogotsi, Y., Intercalation and Delamination of Layered Carbides and Carbonitrides. *Nature Communications* **2013**, *4*.

253. Sutter, P.; Lahiri, J.; Zahl, P.; Wang, B.; Sutter, E., Scalable Synthesis of Uniform Few-Layer Hexagonal Boron Nitride Dielectric Films. *Nano Lett.* **2013**, *13*, 276-281.

254. Vogt, P.; De Padova, P.; Quaresima, C.; Avila, J.; Frantzeskakis, E.; Asensio, M. C.; Resta, A.; Ealet, B.; Le Lay, G., Silicene: Compelling Experimental Evidence for Graphenelike Two-Dimensional Silicon. *Phys. Rev. Lett.* **2012**, *108*.

255. Lee, C.; Yan, H.; Brus, L. E.; Heinz, T. F.; Hone, J.; Ryu, S., Anomalous Lattice Vibrations of Single- and Few-Layer MoS2. *ACS Nano* **2010**, *4*, 2695-2700.

256. Radisavljevic, B.; Radenovic, A.; Brivio, J.; Giacometti, V.; Kis, A., Single-Layer Mos2 Transistors. *Nat. Nanotechnol.* **2011**, *6*, 147-150.

257. Zeng, Z. Y.; Yin, Z. Y.; Huang, X.; Li, H.; He, Q. Y.; Lu, G.; Boey, F.; Zhang, H., Single-Layer Semiconducting Nanosheets: High-Yield Preparation and Device Fabrication. *Angew. Chem. Int. Ed.* **2011**, *50*, 11093-11097.

258. Eda, G.; Yamaguchi, H.; Voiry, D.; Fujita, T.; Chen, M. W.; Chhowalla, M., Photoluminescence from Chemically Exfoliated Mos2. *Nano Lett.* **2011**, *11*, 5111-5116.

259. Zeng, Z. Y.; Sun, T.; Zhu, J. X.; Huang, X.; Yin, Z. Y.; Lu, G.; Fan, Z. X.; Yan, Q. Y.; Hng, H. H.; Zhang, H., An Effective Method for the Fabrication of Few-Layer-Thick Inorganic Nanosheets. *Angew. Chem. Int. Ed.* **2012**, *51*, 9052-9056.

260. Wang, H. T., et al., Electrochemical Tuning of Vertically Aligned Mos2 Nanofilms and Its Application in Improving Hydrogen Evolution Reaction. *Proc. Natl. Acad. Sci.* **2013**, *110*, 19701-19706.

261. Voiry, D.; Salehi, M.; Silva, R.; Fujita, T.; Chen, M. W.; Asefa, T.; Shenoy, V. B.; Eda, G.; Chhowalla, M., Conducting Mos2 Nanosheets as Catalysts for Hydrogen Evolution Reaction. *Nano Lett.* **2013**, *13*, 6222-6227.

262. Han, J. H.; Lee, S.; Cheon, J., Synthesis and Structural Transformations of Colloidal 2d Layered Metal Chalcogenide Nanocrystals. *Chem. Soc. Rev.* **2013**, *42*, 2581-2591.

263. Zhou, W.; Zou, X. L.; Najmaei, S.; Liu, Z.; Shi, Y. M.; Kong, J.; Lou, J.; Ajayan, P. M.; Yakobson, B. I.; Idrobo, J. C., Intrinsic Structural Defects in Monolayer Molybdenum Disulfide. *Nano Lett.* **2013**, *13*, 2615-2622.

264. Wang, X. S.; Feng, H. B.; Wu, Y. M.; Jiao, L. Y., Controlled Synthesis of Highly Crystalline Mos2 Flakes by Chemical Vapor Deposition. *J. Am. Chem. Soc.* **2013**, *135*, 5304-5307.

265. Yu, Y. F.; Huang, S. Y.; Li, Y. P.; Steinmann, S. N.; Yang, W. T.; Cao, L. Y., Layer-Dependent Electrocatalysis of Mos2 for Hydrogen Evolution. *Nano Lett.* **2014**, *14*, 553-558.

266. Shi, Y. M., et al., Van Der Waals Epitaxy of Mos2 Layers Using Graphene as Growth Templates. *Nano Lett.* **2012**, *12*, 2784-2791.

267. Matte, H. S. S. R.; Gomathi, A.; Manna, A. K.; Late, D. J.; Datta, R.; Pati, S. K.; Rao, C. N. R., Mos2 and Ws2 Analogues of Graphene. *Angew. Chem. Int. Ed.* **2010**, *49*, 4059-4062.

268. Xie, J. F.; Zhang, J. J.; Li, S.; Grote, F.; Zhang, X. D.; Zhang, H.; Wang, R. X.; Lei, Y.; Pan, B. C.; Xie, Y., Controllable Disorder Engineering in Oxygen-Incorporated Mos2 Ultrathin Nanosheets for Efficient Hydrogen Evolution. *J. Am. Chem. Soc.* **2013**, *135*, 17881-17888.

269. Yan, Y.; Xia, B. Y.; Ge, X. M.; Liu, Z. L.; Wang, J. Y.; Wang, X., Ultrathin Mos2 Nanoplates with Rich Active Sites as Highly Efficient Catalyst for Hydrogen Evolution. *ACS Appl. Mater. Interfaces* **2013**, *5*, 12794-12798.

270. Seo, J. W.; Jun, Y. W.; Park, S. W.; Nah, H.; Moon, T.; Park, B.; Kim, J. G.; Kim, Y. J.; Cheon, J., Two-Dimensional Nanosheet Crystals. *Angew. Chem. Int. Ed.* **2007**, *46*, 8828-8831.

271. Jeong, S.; Yoo, D.; Jang, J. T.; Kim, M.; Cheon, J., Well-Defined Colloidal 2-D Layered Transition-Metal Chalcogenide Nanocrystals Via Generalized Synthetic Protocols. *J. Am. Chem. Soc.* **2012**, *134*, 18233-18236.

272. Cunningham, G.; Lotya, M.; Cucinotta, C. S.; Sanvito, S.; Bergin, S. D.; Menzel, R.; Shaffer, M. S. P.; Coleman, J. N., Solvent Exfoliation of Transition Metal Dichalcogenides: Dispersibility of Exfoliated Nanosheets Varies Only Weakly between Compounds. *ACS Nano* **2012**, *6*, 3468-3480.

273. Altavilla, C.; Sarno, M.; Ciambelli, P., A Novel Wet Chemistry Approach for the Synthesis of Hybrid 2d Free-Floating Single or Multilayer Nanosheets of Ms2@Oleylamine (M=Mo, W). *Chem. Mater.* **2011**, *23*, 3879-3885.

274. Zhuang, A.; Li, J. J.; Wang, Y. C.; Wen, X.; Lin, Y.; Xiang, B.; Wang, X. P.; Zeng, J., Screw-Dislocation-Driven Bidirectional Spiral Growth of Bi2se3 Nanoplates. *Angew. Chem. Int. Ed.* **2014**, *53*, 6425-6429.

275. Jung, W.; Lee, S.; Yoo, D.; Jeong, S.; Miro, P.; Kuc, A.; Heine, T.; Cheon, J., Colloidal Synthesis of Single-Layer Mse_2 (M = Mo, W) Nanosheets Via Anisotropic Solution-Phase Growth Approach. *J. Am. Chem. Soc.* **2015**, *137, 23, 7266-7269.*

276. Cushing, B. L.; Kolesnichenko, V. L.; O'Connor, C. J., Recent Advances in the Liquid-Phase Syntheses of Inorganic Nanoparticles. *Chem. Rev.* **2004**, *104*, 3893-3946.

277. Xia, Y. N.; Xia, X. H.; Wang, Y.; Xie, S. F., Shape-Controlled Synthesis of Metal Nanocrystals. *MRS Bull* **2013**, *38*, 335-344.

278. Jun, Y. W.; Choi, J. S.; Cheon, J., Shape Control of Semiconductor and Metal Oxide Nanocrystals through Nonhydrolytic Colloidal Routes. *Angew. Chem. Int. Ed.* **2006**, *45*, 3414-3439.

279. Thomson, J. W.; Nagashima, K.; Macdonald, P. M.; Ozin, G. A., From Sulfur-Amine Solutions to Metal Sulfide Nanocrystals: Peering into the Oleylamine-Sulfur Black Box. *J. Am. Chem. Soc.* **2011**, *133*, 5036-5041.

280. Schliehe, C., et al., Ultrathin Pbs Sheets by Two-Dimensional Oriented Attachment. *Science* **2010**, *329*, 550-553.

281. Baker, M. A.; Gilmore, R.; Lenardi, C.; Gissler, W., Xps Investigation of Preferential Sputtering of S from Mos2 and Determination of Mosx Stoichiometry from Mo and S Peak Positions. *Appl. Surf. Sci.* **1999**, *150*, 255-262.

282. Rumble, J. R.; Bickham, D. M.; Powell, C. J., The Nist X-Ray Photoelectron-Spectroscopy Database. *Surf. Interface Anal.* **1992**, *19*, 241-246.

283. Wang, C.; Wang, G. F.; van der Vliet, D.; Chang, K. C.; Markovic, N. M.; Stamenkovic, V. R., Monodisperse Pt3co Nanoparticles as Electrocatalyst: The Effects of Particle Size and Pretreatment on Electrocatalytic Reduction of Oxygen. *Phys. Chem. Chem. Phys.* **2010**, *12*, 6933-6939.

284. Lukowski, M. A.; Daniel, A. S.; Meng, F.; Forticaux, A.; Li, L. S.; Jin, S., Enhanced Hydrogen Evolution Catalysis from Chemically Exfoliated Metallic Mos2 Nanosheets. *J. Am. Chem. Soc.* **2013**, *135*, 10274-10277.

285. Kibsgaard, J.; Chen, Z. B.; Reinecke, B. N.; Jaramillo, T. F., Engineering the Surface Structure of Mos2 to Preferentially Expose Active Edge Sites for Electrocatalysis. *Nat. Mater.* **2012**, *11*, 963-969.

286. Wang, H. T.; Kong, D. S.; Johanes, P.; Cha, J. J.; Zheng, G. Y.; Yan, K.; Liu, N. A.; Cui, Y., Mose2 and Wse2 Nanofilms with Vertically Aligned Molecular Layers on Curved and Rough Surfaces. *Nano Lett.* **2013**, *13*, 3426-3433.

287. Wang, T. Y.; Zhuo, J. Q.; Du, K. Z.; Chen, B. B.; Zhu, Z. W.; Shao, Y. H.; Li, M. X., Electrochemically Fabricated Polypyrrole and Mosx Copolymer Films as a Highly Active Hydrogen Evolution Electrocatalyst. *Adv. Mater.* **2014**, *26*, 3761-3766.

288. Li, Y. G.; Wang, H. L.; Xie, L. M.; Liang, Y. Y.; Hong, G. S.; Dai, H. J., Mos2 Nanoparticles Grown on Graphene: An Advanced Catalyst for the Hydrogen Evolution Reaction. *J. Am. Chem. Soc.* **2011**, *133*, 7296-7299.

289. Worsley, M. A.; Shin, S. J.; Merrill, M. D.; Lenhardt, J.; Nelson, A. J.; Woo, L. Y.; Gash, A. E.; Baumann, T. F.; Orme, C. A., Ultralow Density, Monolithic Ws2, Mos2, and Mos2/Graphene Aerogels. *ACS Nano* **2015**, *9*, 4698-705.

290. Benck, J. D.; Hellstern, T. R.; Kibsgaard, J.; Chakthranont, P.; Jaramillo, T. F., Catalyzing the Hydrogen Evolution Reaction (Her) with Molybdenum Sulfide Nanonnaterials. *ACS Catal* **2014**, *4*, 3957-3971.

291. Ishiyama, K.; Kosaka, F.; Shimada, I.; Oshima, Y.; Otomo, J., Glycerol Electro-Oxidation on a Carbon-Supported Platinum Catalyst at Intermediate Temperatures. *Journal of Power Sources* **2013**, *225*, 141-149.

292. Kosaka, F.; Oshima, Y.; Otomo, J., Electrochemical Performance for the Electro-Oxidation of Ethylene Glycol on a Carbon-Supported Platinum Catalyst at Intermediate Temperature. *Electrochimica Acta* **2011**, *56*, 10093-10100.

293. Shimada, I.; Oshima, Y.; Otomo, J., Acceleration of Ethanol Electro-Oxidation on a Carbon-Supported Platinum Catalyst at Intermediate Temperatures. *Journal of The Electrochemical Society* **2011**, *158*, B369-B375.

294. Wang, J.; Wasmus, S.; Savinell, R. F., Evaluation of Ethanol, 1-Propanol, and 2-Propanol in a Direct Oxidation Polymer-Electrolyte Fuel Cell: A Real-Time Mass Spectrometry Study. *Journal of The Electrochemical Society* **1995**, *142*, 4218-4224.

Biblography

Yifan Liu was born in Hulan, a small town in the very north of China and lived there until 11 years old. He then lived in Guangzhou in the very south for another 6 years. In 2009, he attended college in central China and was later awarded with BS degree in physical chemistry. Since 2013 he started working toward his PhD degree at Johns Hopkins University located at east coast United States, with research interest focusing on developing nanomaterial for electrocatalysis.